Closure Assessment and Overload Transient Behaviour in Damage Tolerant Airframe Materials

A thesis submitted to the School of Engineering Sciences, University of Southampton for the degree of Doctor of Philosophy.

By

Yigeng Xu

Materials Research Group

School of Engineering Sciences

University of Southampton, 2001

UNIVERSITY OF SOUTHAMPTON

ABSTRACT

FACULTY OF ENGINEERING SCIENCES
MATERIALS RESEARCH GROUP

Doctor of Philosophy

Closure Assessment and Overload Transient Behaviour in Damage Tolerant Airframe Materials

by Yigeng Xu

Most engineering structures are subjected to variable amplitude fatigue (*VA*) loading. For ductile engineering alloys, various mechanisms have been proposed to rationalise *VA* fatigue behaviour. Their influences may vary with loading conditions and material characteristics. Whilst considerable knowledge has been built up in the area of fatigue analysis of aerospace Al-alloys, quantitative understanding of *VA* fatigue behaviour remains disappointing, with basic understanding remaining controversial in a number of areas. Crack closure effects in particular remain open to debate, even for simple single overload conditions and constant amplitude (*CA*) loading.

Systematic material characterisation has been carried out on two high strength heat-treatable damage tolerant airframe aluminium alloys: 2024- & 2024A-T351. Given a lack of consensus in closure measurement methods within the literature, significant effort was made in establishing sensitive, non-subjective curve fitting methods to measure crack closure under *CA* and *VA* loading conditions for the specific specimen geometry tested in this work. These methods are identified as more accurate and meaningful than current accepted methods, including recommendations by the American Society for Testing and Materials (*ASTM*). *CA* and single overload tests showed that alloy influence on crack growth can be closely attributed to crack closure (i.e. extrinsic) processes. *CA* closure benefits in 2024A over 2024 were seen to be carried through to overload behaviour. Reduced dispersoid content was particularly considered to promote crystallographic crack growth in 2024A, enhancing crack closure levels in this alloy. Crack closure behaviour, approaching threshold at least, was insensitive to the absolute scale of fracture surface asperities, suggesting other characteristics such as deflection angle may be more significant in controlling crack closure as suggested by certain models within the literature. Stress state effects were investigated for both alloys through the use of 12*mm* thick side-grooved and 2*mm* thick centre cracked tension (*CCT*) samples, with measured crack closure levels again providing a clear rationalisation of crack growth behaviour.

A modified strip-yield analytical model has been developed to simulate plasticity-induced crack closure (*PICC*). The importance of the crack closure concept in controlling near-tip material behaviour is demonstrated by the analytic results. The incidence of two transition points on post-overload local compliance curves (as noted experimentally) is seen to be consistent with the model's behaviour. The model has been extended into a multi-mechanistic form by introducing an effective surface roughness concept. Further understanding of the effect of stress state, roughness-induced crack closure (*RICC*), and oxide-induced crack closure (*OICC*) on fatigue behaviour under *CA* and *VA* loading has thus been obtained. It is found analytically that *RICC* has a stronger influence in plane strain than in plane stress. Overall closure levels and prolonged post-overload retardation distances under plane strain loading have been successfully rationalised via first order approximations of how *RICC* effects may vary with crack tip conditions during an overload.

CONTENTS

ACKNOWLEDGEMENTS

All the work reported here is under the efficient and very active supervisions of my two supervisors: Professor P. J. Gregson and Dr I. Sinclair. It is from them that I acquire a further understanding of what the right research attitude and the true meaning of research activity is. Comprehensive academic training in the area of material sciences was also acquired through their active supervision. I am sure that I'll benefit from it all my life. Particularly, I'd like to express my sincere appreciation to Dr I. Sinclair for his many inspiring instructions as well as lots of detailed help. I will not forget those late evenings we spent together to have a final polish on my presentations and reports.

The financial and technical support of Pechiney, Centre de Recherches de Voreppe (Voreppe, France) and British Aerospace, Airbus Division (Filton, UK) are gratefully acknowledged. I'd like to express my deep appreciation to Drs Jean-Christophe Ehrstrom, Timothy Warner, John Haddock, and Richard Collins for their stimulating questions and warm discussions in the process of my presentations.

Dr Philippa Reed gave me lots of precious advice and detailed help. The papers on overload studies you recommended are the main references in my work. Dr Marco Starink's help in *DSC* tests as well as the discussions on material characterisation is gratefully acknowledged. Dr P. Prangnell (Manchester University/UMIST) is gratefully acknowledged for arranging the *FEG-SEM* analysis. I'd also like to give my thanks to Matthew Parry, Martin Browne, Nick Hide, Julien Boselli, Tim Austin, Ching Hsin Ku, Yangmeng Xu, Aihui Wu and all the other friends in our materials research group for their help.

I'd like to thank Mrs Sue Walker, Gill Rood, Hazel Douglas, and Gwyneth Skiller for their kindly help. The work of Dave Beckett, Eric Bonner, Sheila Cleary, Chris, and Ray is essential to my research and is gratefully acknowledged.

Finally I'd like to express my deep gratitude to my wife, Jun Tong, and my parents. Without their full understanding and support, it is impossible for me to sit here and write my thesis.

NOMENCLATURE

a	the half crack length
A	material constant
a_{aff}	crack growth length affected by a variation in load condition
a_d	crack growth delay distance
a_o	half the physical crack length
b	modulus of the Burgers vector
b_1, b_2	intermediate parameter used in stress intensity factor calculation
B	material constant
B_1, B_2	intermediate parameters used in stress intensity factor calculation
C	scaling constant in the Paris law
C_o	specimen compliance above estimated crack opening load
C_s	secant compliance of the specimen
d	precipitate diameter or distance from the current crack tip to the overload plastic zone boundary due to the most severe overload (in the Wheeler model) or half the fictitious crack length
d_g	grain size
D	distance over which a tilted crack advances along a kink
da/dN	crack growth increment per cycle
$(da/dN)_{CA}$	constant amplitude crack growth rate
$(da/dN)_{VA}$	variable amplitude crack growth rate
$(da/dN)_t$	transient crack growth rate
E	Young's modulus
E'	Young's modulus in plane strain
f	volume fraction of precipitates
G	shear modulus
h	effective roughness of crack surfaces
k	exponent in Coffin-Manson type damage law or in-plane stress ratio
K_c	fracture toughness
K_{cl}	maximum stress intensity factor value under which first crack surface contact occurs
K_I	mode-I stress intensity factor
K_{max}	maximum stress intensity factor value in a fatigue cycle

K_{min}	minimum stress intensity factor value in a fatigue cycle
K_{op}	minimum stress intensity factor value which fully opens a crack
K_{red}	stress intensity factor used in the Willenborg model to reduce the applied crack tip stress intensity
K_t	theoretical stress concentration factor
K_∞	stress intensity factor due to remote tensile stress
$K_{\sigma i}$	stress intensity factor due to the uniform stress on element i
l^*	microstructural size scale of interest, e.g. grain size
L_j	length of element j
$L_j^{(k)}$	length of element j at k^{th} iteration
m	scaling constant in the Paris law
m_{local}	local slope of the compliance curve
m_o	slope of the upper part of the compliance curve
n	strain hardening exponent
N	fatigue cycle number
N_a	dispersoid number per unit area
n_c	cyclic strain hardening exponent
N_d	delayed crack growth cycles after a variation of the load condition
n_i	load cycles with the same mean load and load amplitude in a *VA* loading spectrum
N_i	life to failure in a *CA* test with the same mean stress and amplitude of n_i cycles
n_m	monotonic strain hardening exponent
N'	program fatigue life
P_{cl}	closure load level
P_{max}	maximum load of the loading cycle
P_{min}	minimum load of the load cycle
P_{max1}	one of the maximum load values in a load shedding procedure
P_{max2}	another maximum load value in a load shedding procedure
R	stress ratio ($\sigma_{min}/\sigma_{max}$)
r_b	baseline monotonic plastic zone size
r_a^p	local average plastic strain amplitude
r_f^p	true plastic strain for monotonic fracture
r_{OL}	overload ratio (K_{2max}/K_{1max})

$r_{overload}$	overload plastic zone size corresponding to its practical stress state
r_p	plastic zone size
$r_{p.OL}$	monotonic plane strain plastic zone size at the maximum load of the overload cycle
r_s	size of the slip band zone ahead of the crack tip
S	distance over which the plane of the growing crack is normal to the far field tensile direction
$S_{a,max}$	maximum stress amplitude of a standardized load spectrum
S_m	mean stress
S_{max}	maximum stress of the fatigue cycle
$S_{max,1}$	maximum stress value of the first block in a high-low block load history
$S_{max,2}$	maximum stress value of the second block in a high-low block load history
S_{min}	minimum stress of the fatigue cycle
S_{op}	crack opening stress in a fatigue cycle
S_{op}^{n}	opening stress level in *CORPUS* at which hump n breaks contact
t	plate thickness
T_z	out-of-plane stress constraint factor
U	closure level ($\Delta K_{eff}/\Delta K_{app}$ or S_{op}/S_{max})
u_I	mode-I displacement from the peak load to the point of first contact of the fatigue cycle
u_{II}	mode-II displacement from the peak load to the point of first contact of the fatigue cycle
V_j	crack surface opening displacement at point j
$V_j^{(k)}$	crack surface opening displacement at point j at k^{th} iteration
W	width of a center-cracked tension sample
x_i	x co-ordinate of the center of element i
α	constraint factor
β	parameter associated with yield strength, cyclic strain hardening exponent, the efficiency of crack blunting and re-sharpening in fatigue
η	material constant associated with stress state
χ	u_{II}/u_I
δ	elongation
δ_{max}	crack tip opening at maximum load of the load cycle

δ_{min}	crack tip opening at minimum load of the load cycle
δ_R	plastic stretch to be appended to crack faces
δ_o, δ_t	crack tip opening displacement at maximum load level
Δ_2	mean nearest neighbor separation in 2 dimensions
Δa	crack length increment
$\Delta\delta_t$	cyclic crack tip opening displacement
ΔK	stress intensity factor range
ΔK_{app}	applied (nominal) stress intensity factor range
ΔK_b	baseline stress intensity factor range
ΔK_{eff}	effective stress intensity factor range
ΔK_i	stress intensity factor range in the i^{th} cycle of a load sequence
ΔK_I	mode-I stress intensity factor range
ΔK_{rms}	root-mean-square value of the stress intensity factor range in a load spectrum
ΔK_{RP}	effective stress intensity range corresponding to the load when re-tensile plastic zone is generated
ΔK_{th}	stress intensity factor range threshold
ε	strain
θ	crack deflection angle
ϕ	empirical retardation factor in the Wheeler model
ω_j	half the width of element j
κ	slope factor in fatigue life interpolation equation
ν	Poisson's ratio
λ_L	linear intercept grain dimension in longitudinal direction
λ_S	linear intercept grain dimension in short transverse direction
λ_T	linear intercept grain dimension in transverse direction
σ	Stress
σ_a	stress amplitude
σ_i	uniform stress acting on a segment of the crack surface
σ_j	uniform stress on element j
$\sigma_j^{(k)}$	uniform stress on element j at k^{th} iteration
σ_{max}	maximum stress of the load cycle

σ_{min}	minimum stress of the load cycle
σ_o	average of yield strength and ultimate tensile strength
σ_{UTS}	Ultimate Tensile Strength
σ_{xx}	normal stress in x direction
σ_y	flow stress of the material
σ_y', $(\sigma_y)_c$	cyclic yield strength
$(\sigma_y)_m$	monotonic yield strength
σ_{ys}	yield strength
σ_{yy}	normal stress in y direction
σ_{zz}	normal stress in z direction
σ_∞	remote uniform tensile stress
AE	Acoustic Emission
APFIM	Atom Probe Field Ion Microscopy
BFS	Back Face Strain
CA	Constant Amplitude
CCT	Center-Cracked Tension
CCZT	Constant Closure Zero Threshold
COD	Crack Opening Displacement
CT	Compact Tension
CTOD	Crack Tip Opening Displacement
DSC	Differential Scanning Calorimetry
EDS	Energy Dispersive Spectoscopy
FCG	Fatigue Crack Growth
FCGR	Fatigue Crack Growth Rate
FE	Finite Element
FEG	Field Emission Gun
GP	Guinier-Preston
HRR	Hutchinson, Rice & Rosengren
IADS	International Alloy Designation System
MST	Multiple-Step Test
PD	Potential Drop
PFZ	Precipitate Free Zone
PICC	Plasticity-Induced Crack Closure

OICC	Oxide-Induced Crack Closure
RPG	Re-tensile Plastic zone's Generated
SAXS	Small Angle *X*-ray Scattering
SEM	Scanning Electron Microscope
SS	Surface Strain
TEM	Transmission Electron Microscope
VA	Variable Amplitude
XRD	*X*-Ray Diffraction

1. INTRODUCTION

The study of constant amplitude (*CA*) fatigue behaviour provides valuable insights into the mechanisms of fatigue failure. Investigations over the years have identified various micromechanical and microstructural influences on fatigue crack growth. It is widely recognised that resistance to fatigue crack growth may be differentiated into: (i) '*intrinsic*' behaviour, representing the inherent material resistance to fatigue crack propagation, which may then vary with parameters such as deformation heterogeneity, environment, and the extent of crack tip plasticity in relation to characteristic micro-structural dimensions such as grain size, secondary phase particle separation and/or dislocation cell size, and (ii) '*extrinsic*' behaviour, which may be described as localised mechanical influences tending to attenuate or shield the crack driving force experienced at a crack tip, that may or may not be dependent on microstructure[1]. The separation of intrinsic and extrinsic crack growth resistance has of course constituted a major theme of fatigue research in the last 30 years, with the concept of crack closure or crack tip shielding being used to rationalise a wide range of micro-structural and mechanical influences on fatigue crack growth behaviour. It is clear that an accurate quantitative understanding of intrinsic and extrinsic effects on crack growth is essential to directed alloy development for improved fatigue resistance, and/or improved structural service life predictions. While numerous papers address such issues, the experimental measurement of crack closure levels remains problematic, with no physically proven, non-subjective methodology being established as yet [2-4]. Detailed information on this issue is given in Section 2.1 & 2.3.

Most engineering structures are subjected to variable amplitude (*VA*) loading. For ductile engineering alloys, factors thought to influence *VA* fatigue behaviour include plasticity-induced crack closure, crack tip blunting, residual stresses ahead of the crack tip, static tearing, crack deflection and associated roughness-induced crack closure processes, variations in crack front profile, strain hardening, mean stress relaxation, and the activation of near-threshold crack growth mechanisms. Their influences on crack growth behaviour may vary with both loading conditions and material characteristics. Section 2.2 gives a detailed literature survey on this issue.

Accurate, quantitative fatigue analysis is of course vital for efficient engineering design. It is however due to the complexity of the problem that current *VA* life prediction algorithms (such as *FASTRAN[5]*) remain simplistic (normally single mechanism-based) and to a significant extent empirical in nature. Given recent BAe - Airbus identification of regimes where, even for quite simple load excursions, current predictive methods may be highly inaccurate (by up to an order of magnitude in fatigue lives) [6], it is obvious that an improved micro-mechanical quantification of *VA* fatigue behaviour is required. Such an understanding of *VA* loading effects will benefit both end users and material suppliers by providing a solid physical basis for improved life prediction and microstructural optimisation of advanced damage tolerant materials. Clearly, microstructure is the principal independent variable which will influence fatigue crack growth behaviour once the loading and environmental conditions are established. It is significant to note that whilst many reports exist in the literature on *VA* crack growth in *Al*-alloy, detailed and systematic correlation between microstructure and *VA* performance is not widely available. A multi-mechanism based analytical model which accounts for both the microstructural and micromechanical influences on fatigue crack growth is highly desirable for the accurate and reliable prediction of the fatigue life of engineering structures.

This thesis presents my work in the period of October 1997—October 2000 on the above issues. Detailed literature reviews on fatigue behaviour under *CA* loading, fatigue behaviour under *VA* loading, and the microstructural features of high strength heat-treatable *Al*-alloys are presented in Chapter 2. Chapter 3 presents the results of microstructural and general mechanical characterisation of two high strength heat-treatable damage tolerant airframe aluminium alloys, namely *Pechiney* 2024- & 2024A-T351. Given the problems that may be identified with much of the closure data within the literature, Chapter 4 presents a systematic assessment and validation of compliance-based crack closure measurements. Detailed assessment of crack growth behaviour under *CA* loading (Chapter 5) and single overloads (Chapter 6) has then been carried out for the two *Pechiney* alloys under various loading and specimen conditions. Key issues including the separation of intrinsic and extrinsic contributions of materials to the crack growth resistance and stress state effects on fatigue behaviour are addressed. In Chapter

7, a modified Dugdale-type strip-yield model has been developed to analytically simulate plasticity-induced crack closure under various loading conditions. The modelling approach is extended to multimechanistic situations via the use of an equivalent plastic strain approach. Finally, Chapter 8 highlights the main results achieved in the project and the areas where further work is needed.

References

[1] I. Sinclair and P. J. Gregson, (1998), *Proc. ICAA6*, Toyohashi, JILM, Vol. 4, pp.2091-2104.

[2] Yigeng Xu, P. J. Gregson and I. Sinclair, (2000), *Mater. Sci. Eng. A.*, Vol.284, pp.114-120.

[3] E. P. Phillips, (1989), *NASA Technical Memorandum 101601*, Langley Research Centre, Hampton, Virginia.

[4] E. P. Phillips, (1993), *NASA Technical Memorandum 109032*, Langley Research Centre, Hampton, Virginia.

[5] J. C. Newman, Jr., (1992), *NASA TM 104159,* Langley research Center, Hampton, Virginia.

[6] R. A. Collins, (1996), private communication, BAe Airbus, UK.

2. LITERATURE REVIEW

— *The present chapter consists of three sections. These are based on a detailed literature review on fatigue behaviour under constant amplitude loading, fatigue behaviour under variable amplitude loading, and material characteristics of high strength heat-treatable aluminium alloys.*

2.1. Fatigue Behaviour under Constant Amplitude (*CA*) Loading

There are two major design approaches to the prediction in fatigue life in engineering components. One is the classical total-life approach which considers simply the total cycles to failure of a component, independent of relative crack initiation and propagation contributions. The other is the more modern damage-tolerant design approach which assumes that all engineering components are inherently flawed. The useful fatigue life is then the number of cycles to propagate a dominant crack of an assumed or measured initial size to a critical dimension where catastrophic failure occurs. The assumed initial crack size may be estimated from the resolution of a given flaw detection technique (such as visual, dye-penetrant, *X*-ray techniques, ultrasonic, and electro-magnetic methods) if no flaw is found during inspection. Various methods are available to account for the effects of stress ratios, stress concentrations, environments, variable amplitude loading spectra and multi-axial stresses in the estimation of useful crack growth life. This approach to fatigue has been widely used in fatigue-critical applications, such as the design of military and civil aircraft. It is the objective of this section to review basic fracture mechanics concepts, along with micro- and macro-mechanics models and theories available for describing crack growth behaviour in metallic materials under constant amplitude fatigue loading.

2.1.1. Regimes of Crack Growth

For most engineering alloys, crack growth rate behaviour as a function of the stress intensity factor range (ΔK) can be characterised by three distinctive regimes (see Figure 2.1). In regime A, known as the near-threshold regime, the average crack growth increment per cycle, da/dN, falls below a single lattice spacing ($\sim 2 - 4$ Å) for common

engineering alloys. The apparent asymptotic character of this regime has been associated with the existence of a threshold stress intensity factor range, ΔK_{th}. Below this threshold, cracks may be essentially dormant; above this value, growth rates increase rapidly with ΔK. Regime B exhibits an approximately linear variation of $log(da/dN)$ with $log(\Delta K)$. Since this was first identified by Paris *et al.* [1], regime B is commonly known as the Paris regime. Regime C pertains to the rapid acceleration in growth rates that tends to occur as the peak stress intensity (K_{max}) approaches quasi-static catastrophic failure levels (*i.e.* the fracture toughness K_C or K_{IC}).

2.1.1.1. Near-Threshold Fatigue Crack Growth

- *Definition and Measurement*

Within this regime it is commonly asserted that crack growth behaviour is characterised by a fatigue threshold, ΔK_{th}, below which crack growth no longer occurs. The existence of such a fatigue crack growth threshold was first postulated by McClintock in 1963 [2]. He used the criterion that crack propagation occurs when local strain or accumulated damage over a certain characteristic distance ahead of the crack tip reaches a critical value. Using elastic-plastic analyses, McClintock argued that fatigue cracks may cease to advance when the extent of near-tip plasticity becomes comparable to some characteristic microstructural scale. Frost [3] presented the first experimental evidence supporting the existence of a fatigue threshold. He correlated the existence of threshold with the critical value of an empirical characterisation parameter, $\sigma_a^3 a$, where σ_a is the stress amplitude and a is the crack length. Later, it was found that the threshold for the non-propagation of long fatigue cracks could be more generally associated with a critical stress intensity factor range [4]. Whilst some discussion exists regarding the existence of an absolute threshold, a common practical definition is taken as $da/dN \leq 10^{-8}$ *mm/cycle*. Experimentally, ΔK_{th} values are usually obtained by so-called load-shedding techniques [5]. As such, a fatigue pre-crack is initiated ahead of a starter notch at ΔK values corresponding to the Paris regime. The value of ΔK may then be successively reduced: whilst different ΔK shedding procedures exist, stepwise reductions in ΔK of about 5 – 10% are commonly adopted, with the fatigue crack being extended over distances at least 0.5*mm* or five times the maximum current plastic zone

size, whichever is larger, to eliminate transient effects at each load-step. The test is continued until the crack growth rate is smaller than 10^{-8} *mm/cycle*.

A number of problems may be encountered with load shedding tests, *e.g.* plasticity-induced crack closure effects (see Section 2.1.2.1) due to the greater prior plastic deformations associated with previous higher load levels, potentially causing artificial retardation or even complete arrest of fatigue crack growth if the load is dropped too rapidly. The ΔK_{th} value thus obtained may then be higher than the "*intrinsic*" one leading to non-conservative fatigue life predictions. However, if ΔK values are reduced too slowly, other kinds of crack closure, such as oxide-induced crack closure, may be actuated [6] and may then result in a higher value of ΔK_{th}. The choice of a particular gradient of ΔK is somewhat arbitrary and can lead to experimental uncertainties and errors in the detection of fatigue threshold. Another significant point to consider is that the fatigue threshold so obtained is actually the crack growth arrest threshold rather than the one for the onset of crack growth. However, it is the latter value that is of significance in most practical applications. Phillips [7] measured a threshold ΔK_{th} value for a stress ratio R ($R=\sigma_{min}/\sigma_{max}$, where σ_{min} and σ_{max} are the minimum and maximum stress of the load cycle) of *0.7* using load-shedding on a 2024-T3 material. An surprising discovery was that ΔK level had to be raised by up to 20% to re-start the crack growing once the no-growth condition was achieved. Cracks would not grow at the same loads at which they grew during the load-shedding test.

To overcome the above shortcomings, several alternative threshold test methods have been suggested. One was proposed by Suresh [8] and Christman & Suresh [9], where self-arresting fatigue pre-cracks are introduced under compressive cyclic loads. Subsequently, the specimen is subjected to tensile loads beginning at ΔK levels below the anticipated ΔK_{th} value. If no crack growth is detected, the value of ΔK is raised by a small percentage. This procedure is repeated until the onset of crack growth is detected. Another method was proposed by Herman, Hertzberg & Jaccard [10] which involves raising the R ratio to measure the intrinsic fatigue threshold. In this method, K_{max} is held fixed and ΔK is progressively reduced by raising R. The argument here is that when the maximum stress intensity factor is held fixed, the size of the maximum

plastic zone at the crack tip remains unaltered. Therefore, load reductions would not be expected to cause retardation effects typical of variable amplitude fatigue. Furthermore, closure of the crack faces is virtually eliminated for the high R ratio levels at which ΔK_{th} is then measured.

- *Modelling Approaches*

Apart from the experimental determination of ΔK_{th}, theoretical models have been developed for the prediction of fatigue thresholds. A common approach [11] is that crack growth occurs when the crack tip opening displacement attains a value comparable to a critical micro-structural dimension. A representative model developed by Donahue *et al.* [11] predicts

$$\Delta K_{th} \propto \left(\sigma_{ys} E' l^*\right)^{1/2} \tag{2-1}$$

where σ_{ys} is the yield strength, E' is Young's modulus in plane strain and l^* is the micro-structural size scale of interest, such as grain size. The prediction that the threshold values increase with yield stress is, however, inconsistent with many experimental observations.

Similarly, Yoder *et al.* [12] assume that the size of the cyclic plastic zone size ahead of the crack tip is comparable to a characteristic micro-structural dimension in the near-threshold regime and predict the threshold ΔK_{th} for ferritic-pearlitic steels to be of the form

$$\Delta K_{th} = A + B\sqrt{d_g} \tag{2-2}$$

where d_g is the ferrite grain size, and A and B are material constants. This model predicts that ΔK_{th} increases with d_g, which is consistent with many experimental observations. A similar model was proposed by Taira *et al.* [13]. They assumed that the crack growth threshold is determined by whether the critical slip band near the crack tip propagates into an adjacent grain or not. When the size of the slip band zone

ahead of the crack tip, r_s, which is analogous to the cyclic plastic zone size, becomes greater than the grain size, d_g, the slip band can traverse the grain boundary and propagate into the adjacent grain. Experimental support for this approach was found in low carbon steels [13].

In the near-threshold regime, the plastic zone size ahead of a crack tip is commonly confined to within a single grain diameter. As such, crack growth may then occur predominantly by single shear in the direction of the primary slip system. This single slip mechanism may then lead to crystallographic cracking and a zig-zag crack path [14-16] depending on heat-treatments and chemical composition, *etc.* of the material. The tendency to grow along crystallographic planes may lead to geometrical incompatibilities along the crack path. To maintain a coherent main crack front from grain to grain, crack branching and other complex failure modes may then occur. Crack growth will become more structurally sensitive because of different local barriers to cyclic slip and may then behave in a discontinuous manner. Since crack tip opening displacements in the near-threshold regime are comparable to the characteristic micro-structural dimension of the materials and of the order of local surface asperities, significant effects of crack closure may be expected, the details of which are considered in Section 2.1.2.

2.1.1.2. Paris Regime

- *Definition and Measurement*

The intermediate or Paris regime of fatigue crack growth has been widely studied. In this regime, crack growth rates commonly range from 10^{-6} *to* 10^{-4} *mm/cycle.* With higher stress intensity factor values compared to threshold, the plastic zone at the crack tip usually encompasses several grains of the material. The attendant crack growth processes may then involve simultaneous or alternating flow on two or more slip systems. This multiple slip mechanism favours a planar crack path, normal to the far-field tensile stress axis, which has been termed "Stage II" by Forsyth [17], in contrast to the "Stage I" crystallographic crack growth behaviour seen in the near-threshold regime. In many engineering alloys, including high strength heat-treatable aluminium

alloys, "Stage II" crack growth may be associated with the formation of striations on fracture surfaces which were first noted by Zappfe & Worden [18]. For certain values of imposed cyclic loads in the Paris regime it has been shown that the spacing between adjacent striations can be correlated with the experimentally measured average crack growth rate per cycle. Since the crack growth resistance in this regime usually depends on the average effect of many micro-structural features (plastic zone sizes are larger), and the crack opening displacements are increased, cracks propagate steadily and are considered to be relatively insensitive to stress ratio and microstructure.

- *Modelling Approaches*

Paris, Gomez & Anderson [1] were the first to suggest that the fatigue crack growth increment *da/dN* could be related to the ΔK by the power law relationship

$$da/dN = C \cdot (\Delta K)^m \tag{2-3}$$

where C and m are scaling constants that are related to material microstructure, cyclic frequency, waveform, environment, load ratio, *etc.* For most engineering alloys, m usually falls between 2 to 4. Whilst simplistic, the Paris equation has been widely adapted for characterising the growth of fatigue cracks under conditions of small-scale plastic deformation and remains one of the most useful expressions in the analyses of fatigue crack growth for a vast spectrum of materials and fatigue test conditions.

Laird [19] and Lardner [20] have proposed similar geometrical models based on the relationship between the crack tip opening displacement and the crack length increment per cycle in the Paris regime. The physical basis for these models is the experimental correlation between striation spacing and crack growth rates, and the geometrical relationship between the striation spacing and the crack tip blunting. The crack growth rate is then given by

$$da/dN \cong \Delta\delta_t = \beta \cdot (\Delta K)^2 / (\sigma_y' E') \tag{2-4}$$

where $\Delta\delta_t$ is the cyclic crack tip opening displacement, σ_y' is the cyclic yield strength, E' is Young's modulus in plane strain, and β is a function of yield strain, cyclic strain hardening exponent, the efficiency of blunting and re-sharpening in fatigue, etc. *Eq.(2-4)* indicates a Paris exponent m of 2, which is reasonable for some alloys. The prediction that crack growth rate is inversely proportional to E' is generally true for metallic materials. However, the prediction that *da/dN* is also inversely proportional to σ_y' is usually not true. Furthermore, it has been found that the quantitative prediction of fatigue behaviour using *Eq. (2-4)* is good only in some parts of the supposed Paris regime, *i.e.* the linear region of a $da/dN \sim \Delta K$ curve may be limited.

McClintock[2] first proposed a damage accumulation model using a Coffin-Manson type damage law. In his model, crack growth occurs when the following function of the local average plastic strain amplitude, r_a^p, and the true plastic strain for monotonic fracture r_f^p, integrated over the number of fatigue cycles, N, reaches unity:

$$\int_0^N 4\left(\frac{r_a^p}{r_f^p}\right)^k dn = 1 \qquad (2\text{-}5)$$

where k is an exponent taken to be 1 or 2. This damage theory, along with later developed damage accumulation models such as those of Weertman [21] and Rice [22], predicts that crack growth is proportional to the square of the plastic zone size, corresponding to a Paris exponent of 4, which is in agreement with experimental observations for many metals.

The development of crack growth models is still under the way. Some correlate fatigue crack growth with cyclic crack tip plastic deformations (*e.g.* [23]) under both constant and variable amplitude loading conditions. Some use variable index (m) values to account for the effects of microstructural characteristics on crack growth (*e.g.* [24]). Fatemi *et al.* [25] recently reviewed cumulative fatigue damage and life prediction theories for homogeneous materials. They concluded that although many damage models have been developed, none of them enjoys universal acceptance. Each damage

model can only account for a limited number of phenomenological factors, such as load dependence, multiple damage stages, non-linear damage evolution, *VA* effects, and mean stress.

2.1.1.3. High Growth Rate Regime

In this regime, the major factors affecting crack growth rate are microstructure, load ratio and stress state. Accelerated growth rates are obtained as the maximum stress intensity factor of the fatigue cycle approaches the fracture toughness of the material. As such, static fracture modes (cleavage or void growth) occur in addition to cyclic crack growth. The inherent sensitivity of static failure modes to microstructures and stress state are then reflected in overall crack growth behaviour [26, 27]. Since the vast majority of the useful fatigue life of most components is consumed in the low to moderate growth rate regimes, attention will be particularly paid to the associated micro-mechanical and micro-structural influences on fatigue behaviour in these regimes in the present study

2.1.2. Closure Effects on Crack Propagation

The application of linear elastic fracture mechanics to characterise fatigue crack growth is essentially based on the assumption that a fatigue crack can be idealised as a "*cut*" of zero thickness. Such an assumption has the implication that the K_I fields ahead of the crack tip uniquely determine the conditions for the propagation of the crack in small-scale yielding. However, the experimental observation made by Elber [28, 29] that a fatigue crack can close even at a far-field tensile load established that crack growth rates are not only influenced by the conditions ahead of the crack tip, but also by the nature of crack face contact behind the crack tip. This kind of premature contact between the upper and lower surface of a fatigue crack with load transmission through the contact area is generally described as crack closure, which may be expected to reduce (or shield) the *range* of the externally applied stress transmitted to the crack tip. It implies that the fatigue crack growth rate might no longer be determined by the nominal stress intensity factor range, ΔK, but rather by an effective value of ΔK which

accounts for fracture surface contact in the wake of the fatigue crack tip. Elber's work focused on the influence of prior plastic deformation on crack closure during fatigue fracture. However, it soon became clear from the studies of a number of researchers [30,31,32] in the 1970s and early 1980s that Elber's assertion represented just one potential closure mechanism - specifically plasticity-induced closure. Other sources of crack closure include fracture surface oxidation, mismatch between crack surfaces exhibiting surface asperities, viscous effects for fluid trapped within the crack walls, and stress-induced phase transformations (see Figure 2.2). The fatigue crack closure effect has been one of the most intensively studied parameters associated with fatigue crack growth in the past thirty years. The concept of crack closure has widely been applied to rationalise various aspects of the fatigue behaviour of materials, e.g. the effects of material properties, microstructures, sample geometry, loading conditions, and environments.

2.1.2.1. Plasticity-Induced Crack Closure (PICC)

- *Definition and Measurement*

It has been generally demonstrated that permanent tensile displacements formed due to the plastic deformation at a plane stress crack tip may result in premature contact between crack faces as the crack tip advances through the prior plastic zone. With an increase in the stress intensity factor and the size of the plastic zone due to crack advance, the material which has previously been deformed within the plastic zone now forms a gradually enlarging envelope of plastic zones in the wake of the crack front for constant load amplitude conditions.

Elber [28,29] argued that a fatigue crack can propagate only when the crack faces are fully open. The effective stress intensity factor range, ΔK_{eff}, which is responsible for crack growth, is then given by

$$\Delta K_{eff} = K_{\max} - K_{\min}, if \quad K_{\min} > K_{op}$$
$$= K_{\max} - K_{op}, if \quad K_{\min} < K_{op}$$

$$U = \frac{\Delta K_{eff}}{\Delta K_{app}} \tag{2-6}$$

where $(\Delta K)_{app}$ is the applied stress intensity factor range, K_{op} refers to the minimum stress intensity factor which fully opens the crack faces, K_{min} and K_{max} are the minimum and maximum stress intensities of the fatigue load cycle, and U is the crack closure (or opening) level. The corresponding characterisation of fatigue crack growth based on linear elastic fracture mechanics becomes

$$da/dN = C \cdot (\Delta K_{eff})^n = C \cdot [U \cdot (\Delta K)_{app}]^n \tag{2-7}$$

Using a specially designed clip gauge which was carefully positioned (2*mm* behind the crack tip) on a centre-cracked tension (*CCT*) specimen surface to record the compliance curve of the specimen, Elber established the following crack closure variations of 2024-T3 sheet alloy in terms of the stress ratio R:

$$K_{op} / K_{\max} = 0.5 + 0.1 \cdot R + 0.4 \cdot R^2 \tag{2-8}$$

Compliance curve-based crack closure measurement details are given in Section 2.1.3. It was found by Elber that crack growth behaviour under different R values could then be described by a single curve in terms of the effective stress intensity factor range, ΔK_{eff}. Today, it is recognised that, in addition to its dependence on R, U is also influenced by the material, specimen geometry, stress state, stress intensity factor range and environment. Many empirical relationships between K_{op} and R have since been established by different investigators for different materials and loading conditions.

- *Modelling Approaches*

Numerous finite element (*FE*) simulations of *PICC* have been reported in the literature. Among them, the early *FE* models of *PICC* developed by Newman, *et al.* [33] predict a similar dependence of crack closure on R ratio to the experimental observations of Elber for aluminium alloys [29]. A general observation among finite element results is the reduced level of crack closure in plane strain compared to plane stress, which is

reflected in the three-dimensional elastic-plastic finite element analysis of fatigue crack closure in thick centre-cracked plates [34]. The numerically predicted trend is in qualitative agreement with the experimental measurements of crack closure by Fleck & Smith [35] where a strain gauge and a push-rod compliance gauge were used to measure the closure levels at the surface (close to plane stress condition) and the mid-thickness section (close to plane strain condition) of a thick compact tension specimen.

Parallel to the extensive experimental and *FE* investigations of *PICC*, analytical simulations, based mainly on Dugdale-type strip-yield model, have been carried out and found to be reasonably successful, especially in the parametric study of *PICC* (more straight-forward than in *FE*). Details of such *PICC* models are given in Section 2.2.2.5.

A key issue in *PICC* investigations are how to account for three-dimensional aspects, particularly plane stress/plane strain transitions along the crack front and the incidence of shear lips. Pure plane stress and plane strain are of course idealisations of the real situation in an engineering component. The free surface of a component is only under the quasi-plane stress state due to the existence of a significant stress gradient in the through-thickness direction. The size of the plastic zone relative to the thickness of the cracked body can may be considered to dictate whether the crack tip stress state is essentially plane stress, plane strain, or a combination of the two. Under constant loading amplitude conditions, newly initiated fatigue cracks are often small in length and thus exhibit small plastic zones, thereby inducing predominantly plane strain condition. During fatigue crack propagation, as the crack length increases, the corresponding increase in plastic zone size results in a transition from plane strain to plane stress. The change of stress state has a significant influence on fatigue crack growth behaviour via its effects on crack tip plastic zone sizes, crack opening displacements, and associated closure mechanisms (not necessarily *PICC*). Also worth noting is that *PICC* alone cannot explain the influence of various mechanical, micro-structural and environmental factors on fatigue crack growth, especially in the near-threshold regime.

2.1.2.2. Oxide-Induced Crack Closure (OICC)

It has long been suggested that crack face oxides may influence the fatigue behaviour of engineering alloys. Endo *et al.* [30] reported the first observations of slower crack growth in aqueous media than in gaseous environments and attributed the effect to the presence of oxide layers. Suresh *et al.* [31] reported the first experimental attempts to quantify the role of crack face oxidation in influencing fatigue crack growth rates, especially in the near-threshold regime where relatively small crack tip opening displacements could undergo substantial reductions in effective magnitude due to the presence of foreign debris. Using secondary ion mass spectroscopy to measure the oxide layer thickness, Vasudevan & Suresh [32] validated the potential effect of *OICC* in near-threshold fatigue fracture in 7xxx series aluminium alloys.

For *OICC* to occur, oxide deposits may be enlarged in thickness near threshold due to repeated contact (fretting) between the fracture surfaces. Fretting can lead to the build-up of oxide layers up to $0.2\mu m$ at threshold in lower strength steels tested in moist laboratory air. Since corresponding maximum crack tip opening displacements are of the order of a small fraction of a micron, it is possible for effective wedging of the crack to be produced.

The extent of oxidation may be strongly dictated by microstructure, environment, ΔK level, and load ratio. Near-threshold corrosion fatigue crack growth rates may be influenced by mutually competitive processes: *OICC* and conventional embrittling effects (*i.e.* corrosion – fatigue). Dominance of these processes is strongly dependent on alloy composition and ageing treatment even for alloys with similar yield strengths. Studies of high temperature oxidation of 2xxx series aluminium alloys [36] reveal that increasing the *Cu* content of the alloy causes a reduction in the oxide crystal nucleation density and in the depth of intrusion of the crystal into the base metal, as compared to the behaviour in pure aluminium. Moreover, '*tenacity*' of the oxide layer to the base metal affects the amount of oxide build-up since a fretting process is essential for enlarged oxide debris formation at low growth rates.

In terms of *Al*-alloys, *OICC* has been identified to influence certain 7xxx alloys [31, 32] and 2xxx alloys where the extents of oxidation are comparable to the crack tip opening displacements. Experimental studies of the influence of load ratio R on the near-threshold crack growth behaviour in the 2024-T3 *Al*-alloy by Schmidt & Paris [4] showed that ΔK_{th} decreased with increasing R up to a certain value of R, beyond which ΔK_{th} was load-ratio-independent. This may suggest that *OICC* effects play a role in influencing near-threshold crack growth behaviour in this case.

At high R ratios the possibility of crack face contact is minimised by increased crack tip opening displacements and *OICC* effects may be expected to be reduced significantly, even in the near-threshold regime. Similar conclusions can also be drawn in regimes B and C where crack growth rates are generally too rapid to promote excessive oxide formation and crack tip opening displacements are large.

2.1.2.3. Crack Deflection and Roughness-Induced Crack Closure (RICC)

Periodical crack deflection from the nominal growth plane may cause apparent benefits to crack growth resistance. Theoretical analyses of periodic two-dimensional deflections in the path of a fatigue crack show the following general influences [6]:

(a) When the crack tip is deflected from its nominal mode I growth direction, the effective driving force (expressed via equivalent strain energy release rates, for example) for crack growth is typically smaller than that of a straight crack of the same projected length which is subjected to the same far-field loading. Therefore, a deflected crack may propagate at an apparently slower rate than the corresponding straight crack under the same nominal driving force.

(b) Shear mismatch between the mating crack faces can lead to premature contact under a far-field tensile stresses. This crack closure effect would further reduce the growth rate of a deflected crack.

As mentioned earlier, in the near-threshold regime, the crack driving force is marginal and only one slip system may be operative. Associated Stage I growth may then lead to a highly serrated fracture morphology. It is also suggested that permanent plastic

deformation ahead of the crack tip can cause mismatch between fracture surface asperities: *in situ* observations in the scanning electron microscope of the opening and closing of surface fatigue cracks in aluminium alloys have shown strong mode II displacements associated with fatigue crack opening and the occurrence of premature contact between crack face asperities [37, 38].

Experimental studies on 7xxx series alloys show that the over-aged condition in heat treatable *Al*-alloys leads to a predominantly straight fatigue crack profile over a wide range of growth rates, while the under-aged heat treatment of the same alloy under identical test conditions promote a highly serrated and crystallographic crack path [39]. The differences in the path of the crack for the two ageing conditions are promoted by the differences in their strengthening precipitate characteristics (*i.e.* shearable as opposed to non-shearable) [14]. The under-aged tempers exhibit markedly lower fatigue crack growth in the near-threshold regime compared to the over-aged alloys, with observed increases in threshold ΔK_{th} with increasing grain size being attributed to increased asperity size and hence *RICC* effects.

Overall, it has been suggested that *RICC* is enhanced by [40-43]:

(a) plastic zone dimensions at the crack tip that are smaller than an average grain dimension, promoting crystallographic cracking,

(b) crack tip opening displacements that are somewhat smaller than the average height of fracture surface asperities,

(c) microstructures containing shearable precipitates which generally promote planar, crystallographic slip band formation,

(d) enhanced slip irreversibility, *e.g.* due to environmental interactions.

- *Modelling Approaches*

A simple geometrical approach due to Suresh [40,43] (which includes deflection shielding as well as *RICC*) suggests that the ratio of the nominal to effective stress intensity factor range for a regularly deflecting crack may be given by:

$$\Delta K_I / \Delta K_{eff} \cong \frac{D+S}{\left[D \cdot \cos^2\left(\frac{\theta}{2}\right)+S\right]\cdot\left[1-\sqrt{\frac{\chi \tan\theta}{1+\chi \tan\theta}}\right]} \tag{2-9}$$

where D is the distance over which the tilted crack advances along the kink, θ is the kink angle, S is the distance over which the plane of the growing crack is normal to the far-field tensile axis, $\chi=u_{II}/u_I$ and u_I and u_{II} are the mode I and mode II displacements from the peak stress of the fatigue cycle to the point of first contact (see Figure 2.3). Thus, the nominal mode I stress intensity factor range ΔK_I required to propagate a deflected crack at the same rate as a straight crack is always greater than that for the undeflected crack by a factor equal to the right-hand side of *Eq.(2-9)*. Numerical analyses by Llorca [44, 45] of fatigue crack propagation have been suggested to show comparable closure levels to those predicted by *Eq.(2-9)* for a constant value of the tilt angle θ. The analyses also point out that much higher levels of crack closure can be induced if the tilt angle is not constant during crack propagation. It is worth noting that further results of the finite difference modelling of Llorca indicate the primary sensitivity of *RICC* to asperity angles rather than the absolute scale of the asperities, which is in keeping with the model formulation of Suresh in *Eq.*(2-9).

Beevers *et al.* [46] developed an analytical mode I and mixed mode asperity model which evaluated the effects of asperity heights and the relative distance of the asperity from the crack tip on crack closure. The mode I variant provides a basis for focusing on the micro-structural parameters (asperity width, height, and distribution, for example) which are related to closure interference. It can also be used to reveal the effects of asperity welding on the effective range of the stress intensity factor. The mixed mode model discloses the importance of local interference loading near the crack tip, as well as the global, external loading. Both components of loading contribute to a complex stress state at the crack tip and combine to produce conditions which may promote crack branching on a microscopic scale. High shielding effects are predicted by the model for high elastic moduli for both matrix and fatigue surface asperities, large asperities near the crack tip, and high yield stress for the material in the

process zone ahead of the crack tip. The model is however an essentially elastic solution, and may not fully reflect the fatigue behaviour of ductile engineering alloys.

2.1.3. Closure Measurements

Crack closure measurement methods may be broadly divided into four groups, based on: (1) direct observations of the crack tip, (2) indirect indications derived from crack growth observations, (3) physical compliance measurements, and (4) mechanical compliance measurements [42,47,48]. A comparison of conventional closure measurements from the first round robin tests organised by the *ASTM Task Group E24.04.04* in 1989 on a fixed material and specimen geometry combination exhibited large differences in closure results, dependent on the laboratory, the investigator and the techniques used [49]. One of the conclusions drawn from this work was that "*Scatter of this magnitude would make it very difficult to develop a clear picture of closure effects and to verify quantitative models of closure effects using data from the literature*". While the second round robin on opening load measurement conducted by the same group in 1993 [50] reduced the scatter in the opening load results by more than 50 percent when some of the test results were excluded from the analysis population based on an accept/reject criterion for raw data '*quality*', the difference in closure results among the fourteen laboratories was still significant and dependent upon the adopted measures of the quality of the raw load and displacement/strain data. It is the purpose of this part of the literature review to present a general picture of various closure measurement techniques.

2.1.3.1. Direct Observations of Crack Tip

The most direct observation of crack closure is to study the fatigue crack through a microscope during loading. Staal *et al.* [51], for example, utilized an optical microscope with a TV camera, with a maximum magnification of X800. Larger magnifications can of course be obtained under a scanning electron microscopy (*SEM*). Observations of the crack tip profile can also be made with replica techniques, but then a number of replicas are required to arrive at a crack opening stress level. Nisitani *et*

al. [52] have adopted this method for small cracks. Fellows *et al.* [53] have used Moire interferometry to obtain high resolution near-tip displacement fields. The closure point on the surface of the sample is obtained through the careful monitoring of the variations of the displacement fields during unloading. Davidson [54] used a stereo-imaging technique on pictures obtained in the *SEM.* Photographs in the region of the crack made at minimum load may be compared in a stereoscope with photographs of the same region made at progressively larger loads. By this comparative technique, the open portion of the crack may be seen and directly measured. As the open portion of the crack approaches the crack tip, higher magnification photographs may increase the accuracy of the measurement. Three-dimensional information on crack closure can be obtained by testing transparent plastics [55]. Interferometric measurements of the crack opening in such a sample over the full area of a fatigue crack has revealed that the crack opening stress level may be relatively high at the surface, and decrease towards the interior of the material, with a minimum then occurring at the specimen mid-thickness. Another approach for three-dimensional crack closure measurements was developed by Fleck *et al.* [35] as noted earlier. In a relatively thick compact tension *(CT)* specimen (24*mm* thick), two small holes (diameter of 1.5*mm*) were drilled at mid-thickness, parallel to the loading direction, just behind the crack front. The depth of one hole terminated 1*mm* above the crack and the other hole went to 1*mm* below the crack. With a push-rod displacement gage the crack opening level at the mid-thickness of the specimen was then measured. This work also indicated a lower crack closure stress level in the mid-thickness compared to that on the specimen surface. In terms of more sophisticated experimental methods, Guvenilir *et al.* [56] has recently used high resolution X-ray computed tomography to image fatigue cracks within the interior of metallic specimens, with crack opening as a function of position across the crack face being measured and related to the three-dimensional crack face geometry. Whilst direct observations of crack opening are attractive in their immediacy to closure behaviour, they are inevitably time-consuming, mainly surface-based, and are not directly related to the up-take of load along the crack path.

2.1.3.2. Indirect Observations Based on Fatigue Crack Growth

Based on the assumption adopted by De Koning [57] that crack growth does not occur in a load cycle of a variable amplitude load cycle history of $S_{max}<S_{op}$ (S_{max} is the peak load of the load cycle and S_{op} is the load level to open the crack), the crack opening stress level may be determined in tests with simple *High-Low* block load histories. The maximum stress value of the second block, $S_{max,2}$, which does not lead to further crack growth, is then supposed to be equal to S_{op} associated with the last cycle of the first block. This method assumes that the smallest amount of crack opening is sufficient for further growth. A disadvantage of the method is the extensive experimental effort required. Since striations on fatigue crack fracture surfaces may provide direct evidence of crack growth in individual cycles, they may also be used to give information on S_{op}. Pelloux *et al.* [58] employed this in tests of two-block load sequences. 10 smaller cycles were introduced in the second block, with S_{max} being kept the same as that in the first block. Different minimum load values (S_{min}) of the second block were used in the tests. When the striation spacing of the small cycles was the same as that of the large cycles, it was assumed that this S_{min} was equal to S_{op} of the larger cycles. The problem with such techniques is also the extensive experimental effort.

2.1.3.3. Physical Compliance Measurements

These methods cover a variety of physical indications of effective crack length that may be monitored during loading and unloading. The electrical potential drop (*PD*) method has been successfully applied for automatic crack growth monitoring in fatigue tests, however, the experience with the potential drop method for measuring crack closure is not encouraging. Bachmann *et al.* [59] indicate the significance of oxide layers on the fracture surfaces, which can act as insulators. The application of the eddy current method to measure crack closure was reported by Lal *et al.* [60]. The eddy current probe was put in close proximity to the crack tip. There is some control on the depth of penetration of the eddy currents by adjusting the frequency. The possibilities have not yet been fully explored, but the argument against the potential drop method

may be seen to apply to this method as well. An acoustic technique was adopted by Ho *et al.* [61]. The transmission of ultrasonic surface waves through a crack was supposed to indicate whether closure was present. One of the problems associated with this method is the difficulty in distinguishing hydraulic noises and other physical processes from the real closure events. Uncertainties may also exist regarding the relationship between acoustic properties during crack face contact and the actual take-up of load in the crack wake.

2.1.3.4. Mechanical Compliance Measurements

Mechanical compliance curves of cracked specimens can be simply recorded with clip gauges and strain gauges. Clip gauges mounted at a crack mouth or on the specimen side surface behind the crack tip may be used to monitor the response of crack opening displacement (*COD*) to the applied fatigue load. Strain gauges mounted on the side surface of a specimen near the crack tip may be used to record variations in the near tip surface strain (*SS*) with the fatigue load. Crack closure loads are considered to be associated with initial deviation from linearity in mechanical compliance of a specimen when unloading. Given their experimental ease, mechanical compliance measurements have become established the most widely used methods to assess closure. In the *SS* method, the shapes of load-displacement curves may be found to vary with the relative locations of the crack tip with the strain gages [62]. Elber [28] first used a clip gage (*COD* meter) on the side surface of a specimen to obtain crack closure data. A popular position for clip gages nowadays is at the centre line of a *CCT* specimen, or at the notch mouth of a *CT* specimen. The advantage of such an approach is that one does not have to reposition the gauge as the crack grows. A similar argument applies to the use of back face strain (*BFS*) measurement in *CT* specimens. On the other hand, it has been stated that more accurate measurements can be made if a clip gage or a strain gauge is positioned closer to the crack tip in view of the larger apparent changes in compliance. Some authors, however, have warned against a location too close to the crack tip, because of crack tip plasticity, which may give misleading results. Vasudevan *et al.* [63] indicate that a change in compliance slope can occur if plastic relaxation (reverse plastic flow) occurs during unloading. This is not consistent with, for example, the

incidence of high apparent closure levels (from crack mouth compliance data analysis) in the near threshold regime, where the extent of plasticity will be very small in relation to any typical fatigue specimen format.

Methods commonly used to determine fatigue crack opening point from mechanical compliance curves [50, 64] include the slope variation and tangent line intersection methods. In the slope variation method, the slope of the upper part of the curve is obtained first by linear regression analysis; then, going down along the compliance curve, local averaged slopes are obtained for each point by considering a number of neighbouring points on both sides of a data point. The criterion to determine S_{op} may then be based on some nominal difference in local & upper slope values (*e.g.* 5%). Closure point estimations via visual checks are based essentially on this slope variation principle. In the tangent line intersection method, two tangent lines are drawn for the upper part and the lower part of the compliance curve respectively. The fatigue crack opening stress S_{op} is defined as the intersection point of the tangent lines.

2.1.3.5. Evaluation of Various Closure Measuring Methods

Yisheng *et al.* [64] have studied the effect of *COD* gage position and the data processing methods on crack closure measurements. It was found that closure results measured with the tangent line intersection method are not sensitive to clip gage position. It was considered that the crack opening stress determined by this method may be a median stress level between the crack just fully open and the crack just fully closed, although there is limited physical justification for this. For the slope variation method, the position of the clip gage had a systematic effect on the S_{op} results. The S_{op} values obtained by the slope variation method increased if the clip gage was located closer to the crack tip, and became higher than the S_{op} values obtained by the tangent line intersection method. A particular issue in using the slope variation method is the selection of the nominal difference in local & upper slope values (say, *2% or 5%*). The selection will of course affect the level and stability of the closure measurement results. A rigorous physical basis for the selection of the nominal difference is difficult to establish at present. It is interesting to consider that different closure mechanisms may

influence the form of initial deviation from linearity, making the 'correct' choice of slope variation value a function of material and load conditions.

Vasudevan *et al.* & Louat *et al.* [63, 65] have evaluated several conventional closure measurement methods via a dislocation model and concluded that the closure effect is much less than conventionally believed. Specifically they argue that asperity-induced closure loads are only about one quarter of those computed from slope change points on load-displacement curves. The argument was based on their theoretical evaluation using a dislocation crack model (Louat *et al.* [65]) in which a sharp asperity was located near the crack tip. It should however be noted that Louat *et al.* [66] have only evaluated an extreme case in which the asperity width is ignored. Shan *et al.* [72] evaluate crack closure when the asperity width varies from a point to finite values using a dislocation model, in order to obtain more realistic estimation of asperity-induced crack closure during crack propagation. They conclude that although the effect of asperity-induced crack closure on crack growth may still be less than conventional estimations based on the slope change of load-displacement curves, the consideration of the width effect of an asperity near the crack tip will raise the corresponding crack closure level.

It is claimed by several investigators that pre-processing specimen compliance data via a displacement-offset analysis can assist in the accurate deduction of crack closure points. In the displacement-offset method, displacement data is presented as an offset from a straight line approximation of the upper part of the compliance curve. Offset data in the region where the crack is fully open will then fall into a narrow vertical band, whilst at lower loads, the onset of non-linearity should become more obvious. The compliance offset method is suggested by the *ASTM E647* Standard [5] for data analysis. However, Lee *et al.* [67] pointed out that identifying the crack opening point is still ambiguous (the non-linearity point is still identified qualitatively), and there are additional uncertainties in selecting the upper portion of the curve for the linear fit.

Lee [62] employed an acoustic emission *(AE)* technique to measure crack closure of *CT* samples during fatigue tests of 2024 and compared the results with those obtained by

COD, BFS, and *SS* methods. They concluded that the *COD* and *BFS* methods gave relatively good agreement with each other and measured the through-thickness mean value of the crack closure loads, while the *SS* and *AE* methods were sensitive to local crack tip behaviour on a microscopic scale that resulted in higher closure levels. The *SS* method, though it was thought to precisely measure the local closure event, could give inaccurate data since the sensitivity varied significantly, being dependent on the relative distance between the strain gage and the crack tip. The intrinsic fatigue crack growth curve obtained by the *AE* technique fitted well with the curve of high stress ratio (R=0.8) test, suggesting that the *AE* technique could be considered as a convenient and reliable method for crack closure, which is, however, not supported by the observations of *Ho et al.* [61].

In terms of global and crack tip specimen behaviour, Hudak *et al.* [68] reported that local closure measurements with a stereo-imaging technique gave significantly higher crack opening loads than the global closure measurements performed by Minakawa *et al.* [69] for the same material by using a crack opening displacement clip gage. Ward-Close *et al.* [70] measured crack closure values of a titanium alloy IMI 550 subjected to tensile overloads by using *BFS* technique (global measurements) and *SS* method (local measurements). They found that the overload retardation could not be explained by global compliance measurements. On the contrary, the near-tip local closure measurements provided a superior interpretation of the significantly delayed retardation in crack propagation that typically occurs after an overload. Davidson *et al.* [71] also reported that the opening load measured at a crack mouth seriously under-estimated that measured at the crack tip by direct observation. However, Allison *et al.* [72] reported that the closure measurements obtained by global closure measurements and local closure measurements, *i.e., COD & BFS vs.* replicas, are equivalent.

The above closure analyses essentially consider crack closure as a simple, single definable point in the load cycle. Chen *et al.* [73] proposed a new consideration of the closure effect and a re-definition of the effective driving force for crack propagation, taking into account the role of the lower portion of loading cycle below the fully open load. Based on local crack tip strain measurements, Donald [74] observed significant

crack tip strain occurring below the conventionally defined K_{op} load. It was found that the re-distribution of stresses associated with a partially open crack and the effect of this re-distribution on the stress field in front of the crack could not be determined simply on the basis of a change in the slope of the load-displacement curve. He proposed a compliance ratio technique to determine the effective stress intensity from the local crack tip strain measurement. The compliance ratio is the ratio of the secant compliance (C_s) divided by the compliance (C_o) above the estimated opening load. C_s is the inverse slope of the secant drawn between minimum load-displacement and maximum load-displacement. C_o is the inverse slope of the load-displacement curve above the estimated opening load. A modification of this technique (adjusted compliance ratio technique) allows the use of remote compliance measurements to account for the effect of crack tip strain below the fully opening load. The *'adjusted compliance ratio'* is determined by subtracting the compliance prior to the initiation of a crack from both the C_s and C_o. It is however worth noting that whilst this method gives more consistent closure results from the same strain gauge, the results may be crack length dependent and reflect more or less the in-between closure levels. Difficulties may also be expected in applying this technique to more complex loading conditions such as post-overload crack growth, where the proposed geometrical construction may not be *'rational'* for the complex compliance curve shapes that may arise.

From the above discussion, it is not surprising for the *ASTM Task Group E24.04.04* to have reached a disappointing conclusion on the validity of closure measurements in light of the variety of methods used with different underlying principles, sensitivities and accuracy, coupled with different measurement locations relative to the crack tip and overall specimen geometries. Obviously, an improved understanding of the significance of crack closure is still required.

2.2. Fatigue Behaviour under Variable Amplitude (*VA*) Loading

The study of constant amplitude fatigue behaviour provides valuable insights into the mechanistic understanding of fatigue failures. However, most engineering structures are subjected to variable amplitude loading. Investigations over the years have identified various micromechanical and microstructural influences on crack advance under variable amplitude conditions. For most ductile engineering alloys, the major factors influencing variable amplitude fatigue include *PICC*, crack tip blunting, residual stresses ahead of the crack tip, crack deflection and the associated *RICC*, *OICC*, variations of the crack front profiles, strain hardening, mean stress relaxation, and the activation of near-threshold crack closure effects. Their influences on crack growth behaviour may vary with both loading conditions and material system. Due to the complexity of the problem, none of the existing predictive models can encompass all of these factors. Current variable amplitude life prediction algorithms (such as *FASTRAN* [75]) remain simplistic and to a significant extent empirical in nature. It is clear that an improved micro-mechanical quantification of variable amplitude fatigue behaviour is required.

As real variable amplitude loading spectra can be highly complex, simple loading spectra are preferred for basic studies since successive transient effects may be impossible to systematically de-convolute. It is only via the systematic break down of the key elements of such load conditions that a direct scientific understanding and optimisation of performance may be achieved. In this section, transient effects following a single overload and underload and the basic load interactions of periodically applied overloads and/or underloads are reviewed. General models available for describing variable amplitude fatigue behaviour are presented at the end of this section.

2.2.1. Transient Effects Following Single Overloads

It is well established that the application of a single overload will generally cause transient crack growth retardation or sometimes even complete crack arrest. For most

ductile engineering alloys, a typical overload transient involves an initial brief acceleration in crack growth (stretch zone) immediately after the overload, followed by a prolonged period of retardation until crack arrest occurs or growth rates return to their pre-overload levels [70]. The magnitude of the delay following the overload may be measured in terms of either crack length, i.e. the delay distance (a_d), or the crack length affected by the delay (a_{aff}), or the number of delay cycles (N_d). Delay behaviour may be a function of the baseline stress intensity range (ΔK_B), baseline load ratio R, overload ratio r_{OL} ($r_{OL}=K_{2max}/K_{1max}$, where K_{2max} is the peak stress intensity of the overload cycle and K_{1max} is the peak stress intensity of the baseline fatigue cycle), specimen thickness, material microstructure, and environment [76]. The incidence of the minimum in crack growth rate occurring sometime after the application of the single overload is usually known as delayed retardation. Arguments which have been proposed over the years to rationalise post-overload fatigue behaviour in ductile alloys are considered in the following subsections.

2.2.1.1. Enhanced PICC

Since enhanced *PICC* may occur following the application of an overload due to the larger plastic stretch left in the wake of the advancing crack, it is reasonable to expect a transient retardation of post-overload crack growth. This argument also predicts a delayed retardation based on the fact that a certain amount of crack growth through the overload plastic zone is required to activate enhanced *PICC*, which is consistent with many experimental observations. Experimental work [77] on aluminium alloys shows that crack surface striations formed prior to the overload may be abraded with no striations left behind after the overload. Von Euw *et al.* [77] argued that it was the increased *PICC* and the subsequent increased frictional contact between the crack faces following the overload that obliterated the crack surface striations. Using the push-rod compliance system described earlier, Fleck [78] also experimentally measured higher levels of crack closure in plane stress following an overload, indicating enhanced *PICC*. Based on Dugdale's original work [79], a modified *'strip yield' PICC* model was developed by Newman [80] and used for fatigue life predictions during *VA* loading. Newman [80,81] compared the predicted fatigue lives with the experimental

ones for notched 2024-T3 aluminium alloy sheet specimens under some load sequences. The predicted lives agreed well with the test data via the use of a fitting constraint factor to account for the influence of finite thickness of the sample. Details of the *PICC* modelling can be found in Section 2.2.2.5. It is generally agreed that enhanced *PICC* mechanism is one of the major factors influencing post-overload fatigue behaviour.

2.2.1.2. Crack Tip Blunting

For ductile alloys it is unrealistic to assume that the crack tip remains sharp under far-field tensile loads. Such blunting of the crack tip may lead to crack growth retardation due to the less severe stress concentration ahead of the crack tip. Whilst the shielding effect caused by crack tip blunting is stable during constant amplitude fatigue, the enhanced crack tip blunting following an overload could be taken into account to rationalise post-overload transient crack growth retardation. Christensen [82] and Rice [22] have suggested that crack tip blunting after an overload can persist during post-overload crack growth leading to growth retardation. Lankford *et al.* [83] have combined *SEM* observations with a fatigue machine and observed crack tip blunting processes dynamically during testing. It is worth noting that crack tip blunting can sometimes be used to account for crack growth acceleration. Based on experimental studies of transient fatigue crack growth behaviour following single overloads in a *2090-T8E41* aluminium-lithium alloy, Rao *et al.* [76] argued that the immediate, yet brief, acceleration in growth rate after the overload was associated with a small decrease in crack closure (measured via *BFS* compliance techniques), due to crack tip blunting and consequent increased crack opening displacements at the overload. This is contrary to the conventional viewpoint that crack tip blunting cannot explain delayed retardation. As a result, it is possible for us to rationalise the transient post-overload crack growth behaviour if we use the crack tip blunting argument together with other effects such as crack closure.

2.2.1.3. Residual Stresses Ahead of the Crack Tip

A residual compressive stress zone is set up ahead of a crack tip on unloading during cyclic tensile loading. The interaction of the advancing crack tip with this compressive stress zone may be considered to reduce the driving force for crack growth and provide a mechanism for the retardation of fatigue cracks. As such, it is logical to anticipate that a larger compressive stress zone ahead of a crack tip after the overload may influence transient post-overload crack growth behaviour. Enlarged residual compressive zones following tensile overloads have been measured by various investigators [84, 85] by X-ray diffraction. Since the compressive stresses ahead of the crack tip have to be overcome before the crack can propagate, crack growth retardation is expected after the overload. Mainly due to its feasibility for analytical analysis, various fatigue life prediction models have been established on this argument. The well-known Willenborg retardation model [86] and Wheeler model [87] are based on the assumption that compressive stresses ahead of the crack tip lead to the retarded crack growth (see details in Section 2.2.2.3). More recently, from the viewpoint of damage occurrence, Toyasada *et al.* [88] proposed a new parameter ΔK_{RP}, which is the effective stress intensity factor range corresponding to the excess *RPG* (Re-tensile Plastic zone's Generated) load in which the '*re-tensile*' plastic zone appears during the loading process.

Crack tip residual stress effects have also been used in *FE* modelling of variable amplitude fatigue behaviour. In most conventional investigations, the crack opening stress is identified as the applied stress at which the crack becomes fully open (the last released node) and the crack closing stress is defined as the applied stress at which any part of the crack first contacts (the first node making contact) [33, 89]. However, since the implication of '*opening*' should be that the crack has a potential capability to extend, while '*closing*' must imply that the crack cannot propagate, conventionally defined crack opening and closing stress concepts may not answer following two questions clearly. Firstly, if the displacement of the node immediately behind the current crack tip becomes positive, is the crack then fully open? While this is a necessary condition, it is not a sufficient one, because a positive displacement of this

node only implies that the crack is open at this node without guaranteeing that it is open between this node and the current crack tip node. Secondly, when a part of the crack has closed first, but the crack tip node still carries a tensile force which may be the case following a single overload, can it be said that the crack is closed? Conversely, when all of the finite element nodes on the crack surface have a positive displacement, but the crack tip node carries a compressive stress during unloading, is the crack still open? To address the above uncertainties, Wu *et al.* [90] proposed a new definition of crack opening and closing stresses based on the consideration of crack tip residual stresses. They argued that the crack is deemed to be fully open when the compressive stress borne by the crack tip node from the connected truss elements changes to a tensile one. They define this corresponding far field applied stress as the crack opening stress. Similarly, the initiation of crack closure occurs when the tensile stress borne by the crack tip node from the connected truss elements is changed to a compressive one. The corresponding applied far field stress is taken to be the crack closing stress. Obviously, the newly defined crack opening and closing stresses are useful to clarify the ambiguity of the physical basis of conventionally defined ones. From comparison of the *FE* predictions with experimental results, the authors concluded that the proposed definitions of the crack opening and closing stresses describe the opening and closing of cracks more accurately, and can be generalised to stationary cracks and overload cases. It may however be noted that the significance of loads at a specific node in an *FE* model would leave such a method rather dependent upon the exact model formation (*e.g.*, the use of specialised crack tip nodes). Also worth noting is that varying crack tip strains contribute directly to crack growth, and not stresses, as implied by this approach.

Wei and James [91] have also studied the effects of crack closure definition on crack growth by comparing finite element predictions with experimental results. In their *FE* models, crack opening load was taken either as corresponding to full opening of the two crack faces (Definition 1), or identified by the instant when the near tip principal stress perpendicular to the crack propagating direction becomes tensile (Definition 2). Their results show that higher crack closure levels are predicted from Definition 2. The

FE predictions of crack closure using Definition 1 were better than those obtained from Definition 2, which is not consistent with the above results of Wu *et al.* [90].

Overall, it should be noted that the effect of residual compressive stresses in themselves cannot explain the experimentally observed delayed retardation of post-overload crack growth since the largest residual compressive stress exist at the crack tip immediately after an overload. Suresh [92] also found that retardation can persist even when the post-overload crack has passed through the zone of residual compressive stresses. It is obvious that residual stresses ahead of the crack tip are not the only factor affecting transient post-overload crack growth behaviour.

2.2.1.4. Crack Deflection and RICC

Post-overload crack deflections from the nominal mode I crack growth plane have been observed by various investigators [83,93]. As discussed earlier, a deflected crack tip may be subjected to a lower effective ΔK than a straight crack of the same projected length under the same far-field loading condition. Based on experimental results and theoretical analyses of aluminium alloys, Suresh [92] has shown that a reduction in effective ΔK of approximately 25% can be realised in the post-overload regime solely from the crack deflection process. Therefore, the crack deflection following an overload can be used to explain the transient retardation of post-overload crack growth. It is worth noting that immediate acceleration rather than retardation of post-overload crack growth may occur because of the lower fracture resistance along the deflecting plane (crack growth does occur preferentially along this path). Considering the subsequent lower effective ΔK at the deflected crack tip, it is possible for us to rationalise the delayed retardation. However, there is still dispute over the ability of crack deflection to account for retardation after overload. Lankford *et al.* [83] have provided experimental evidence to suggest that retardation following a single overload is not due to crack tip deflection. Their observations of 7075-T6, 2024-T4 and 6061-T6 *Al*-alloys show that crack tip deflection after the overload leads to an initial acceleration in crack growth rate. Retardation occurs only after the fatigue crack has grown out of the influence of the deflection and has re-oriented itself normal to the

loading axis. But, even in this case, the retardation may be linked to the enhanced roughness-induced crack closure due to the wedging of the crack by enlarged fracture surface asperities after the crack deflection. Rao *et al.* [76] have observed greater crack growth retardation in the *Al-Li* alloy 2090-T8E41 after overload, compared to 2124-T351 and 7150-T651, attributing this to the higher levels of crack deflection and associated roughness-induced closure in the 2090 material.

2.2.1.5. Variations of Crack Front Profiles

Trockels *et al.* [94] compared constant amplitude tests with periodically applied overload tests of high strength *Al*-alloys at R=0.1 and 0.5 in vacuum. Since no closure could be detected at R=0.5, and since crack growth behaviour was quantitatively similar at low and high R ratios, crack closure effects could not explain the observed post-overload crack growth retardation behaviour observed in coarse and the fine grained X-7075 alloys compared to corresponding constant amplitude tests. They suggest that crack front profile variations after overload are the main reason for overload retardation. Crack front geometry variations were also linked to higher crack growth resistance of under-aged *Al*-alloys compared to over-aged ones. It was thought that higher crack growth resistance was due to the greater extent of the crack front geometry variations associated with under-aged *Al*-alloys. The influence of crack front geometry variations on crack growth is thought to result from crack advance occurring preferentially in some grains, leaving unfractured ligaments between those fractured grains. In order to propagate the overall crack front these ligaments must be fractured, reducing the overall crack propagation rates. Microstructural or external parameters which increase the deviations of the crack front from a smooth line may then contribute to a higher propagation resistance [95].

Other important features of crack front geometry variations include through-thickness crack front incompatibility and the formation of shear lips, which are not unique to overload situations. Through-thickness crack front incompatibility can be attributed to the larger extent of the plastic deformation near the specimen surfaces (plane stress condition), the loss of out-of-plane constraint on mode *III* deformation, and the

irreversible mode *III* deformation in the through thickness direction. The development of shear lips is a well known phenomenon for aluminium alloys. The shear lips are usually associated with plane stress conditions at the specimen surfaces, involving a mixed mode *I/III* crack opening. They may be expected to be the first parts where mating crack surfaces will touch during unloading: Lindley *et al.* [96] have shown for mild steel that closure contacts start at the shear lips. The contribution of shear lips to the crack closure was also indicated by Ewalds *et al.* [97]. They reduced the thickness of plate specimens containing fatigue cracks in order to remove the shear lips. As a result, the crack closure level was reduced. The influence of shear lips on crack growth may also be seen in the work of McEvily [98] who observed significant crack growth retardation after an overload in an *Al*-alloy: a much smaller retardation was found when the thickness of the specimen was reduced immediately after the overload. Environmental influences on the formation of shear lips and fatigue behaviour of aluminium alloys are also discussed in reference [99].

Although the effect of crack front geometry variations on crack growth has been recognised, quantitative evaluation of this effect is difficult due to its three dimensional nature and the difficulties in separating stress state and shear lip effects.

2.2.1.6. Activation of Near-Threshold Crack Closure Effects

Various studies of the post-overload activation of near-threshold crack closure effects have been presented in the literature [92, 100-102]. Following a single overload, the aforementioned effects can result in a much lower post-overload effective stress intensity range than the nominal baseline value, ΔK_B. As a result, even if the post-overload ΔK_B is well into the Paris regime of crack growth, crack growth after the overload may be characterised by near-threshold crack growth behaviour. In such cases, additional near-threshold retardation mechanisms may be activated (typically involving Stage I crack growth, along with oxide-induced and roughness-induced crack closure), enhancing the transient post-overload crack growth retardation. Bucci *et al.* [100] observed uniformly distributed dark bands of oxide on the fracture surface of a 7010-T7 aluminium alloy which was subjected to a single tensile overload after every

8000 cycles of constant amplitude fatigue crack growth at $\Delta K_B = 7 \sim 10\ MPam^{1/2}$ and $R=0.33$. This is a regime of growth in which oxide-induced closure is not significant during constant amplitude fatigue in the associated moist air environment. These dark bands of oxide, however, where considered to correspond to retarded crack growth after each overload, enhanced by the activation of oxide-induced crack closure. Influences of various loading and alloy heat treatment conditions on the activation of near-threshold crack closure effects are presented in references [100-102].

2.2.1.7. Strain Hardening

Skorupa [103] presents a detailed literature review on strain hardening effects on post-overload transient crack growth behaviour. Reduced crack tip opening due to overload induced plastic strain hardening was used to rationalise post-overload retardation in reference [104], which is also supported by experimental results [102]. However, other experimental investigations [105] suggest that the more pronounced retardation in a more strain-hardening under-aged *Al*-alloy compared to a less strain hardening over-aged *Al*-alloy is associated with the crack profile geometry rather than strain hardening. Controversial experimental observations are also reported in references [106,107] where faster crack growth was measured in pre-strained, and therefore strain hardened material, than was found in the as-received state. It is worth noting that the role of strain hardening on fatigue crack growth behaviour is not straightforward. The crack growth conditions in a homogeneously strain hardened sample may be different from those within a small localised zone of strain hardened material ahead of the crack tip surrounded by 'soft' un-strain-hardened material. Furthermore, since the strain hardening will affect both the residual deformation in the crack wake and the crack tip opening displacement, the influence of strain hardening on plasticity-induced crack closure may then be twofold [106,108,109]. Finite element results [110] indicate that at lower applied stress levels more strain hardening materials show higher closure levels than less strain hardening material, whilst the reverse occurs at higher applied stress levels, highlighting the complexity of strain hardening effects on crack growth.

It is worth noting that the effect of *cyclic* hardening or softening on fatigue crack growth may be different under *CA* loading and under *VA* loading conditions. Under the same baseline loading conditions, regions which are penetrated with higher transient growth rates undergo less cyclic strain hardening or softening than those penetrated with lower transient growth rates under *VA* loading. This suggests that crack growth behaviour during the application of a single overload and the initial post-overload acceleration stage of crack growth may be better described by monotonic strain hardening, except for a relatively small region of the reversed plastic zone generated by the preceding baseline cycles. Cyclic strain hardening/softening may then be more significant when delayed retardation occurs, *i.e.* cyclic stress/strain responses may be more important. Controversial test results supporting or refuting the use of different stress strain responses to rationalise the transient crack growth behaviour are reported [102,108,109,111].

2.2.2. Fatigue Models under Variable Amplitude Loading

The practical importance of fatigue crack growth under variable amplitude loading is well recognised. Many predictive models have been developed over the years as a result. In general, they can be divided into five categories: (a) cumulative fatigue damage models, (b) interpolation methods, (c) similarity approaches, (d) plastic zone- and residual stress-related models, and (e) fatigue crack closure models.

2.2.2.1. Cumulative Fatigue Damage Models

The most well known cumulative damage model is the Palmgren-Miner linear damage rule [112].

$$\sum_{i=1}^{N} \frac{n_i}{N_i} = 1 \qquad (2\text{-}10)$$

Palmgren assumed that n_i load cycles with the same mean load and load amplitude will consume a portion of the fatigue life equal to n_i/N_i, where N_i is the life to failure in a

constant amplitude test with the same mean stress and amplitude. Failure will then occur when the sum of the consumed life portions reaches 100%. Despite the major shortcoming of its inability to account for load interaction effects, this treatment of cumulative fatigue damage has received significant attention and many modified damage models have been developed since then. Different improvements have been made by considering non-linear damage curves and two-stage linearisation, life curve modifications to account for load interactions, crack initiation and propagation concepts, continuum damage mechanics theories, and energy-based damage theories. Detailed information can be found in a recent review made by Fatemi and Yang [25]. However, since these models are essentially associated with total-life design, they will not be discussed in further detail here.

2.2.2.2. Interpolation Methods

Interpolation methods seem to be the most direct approach to *VA* modelling in a sense of using available fatigue data and are preferred in engineering evaluation of structural components under complex load spectra. However, the interpolation procedure is a critical issue. Interpolation can be made for a large variety of parameters, such as mean stress (S_m), theoretical stress concentration factor (K_t), load spectrum shape, etc. Gassner *et al.* [113] proposed an interpolation equation as:

$$\log(N') + \kappa \cdot \log(S_{a,\max}) = C \tag{2-11}$$

where N' is the program fatigue life, $S_{a,max}$ is the maximum stress amplitude of the standardised load spectrum applied in the test and C is a constant. The slope factor κ usually has a value of the order of 6. This linear relation has been confirmed by many tests [113-115]. The program fatigue life N' can thus be obtained for any value of $S_{a.max}$, either by interpolation or extrapolation. Obviously, if it can be based on realistic variable amplitude test data, the interpolation approach may well give a reasonable life prediction. The problem at present is that such data are still largely to be collected and need to be validated. Applications of interpolation methods are mainly based on past experience. As a result, the quality of the results obtained will depend heavily on the

amount of information and subjective ability in interpreting and judging the validity of the data.

2.2.2.3. *Similarity Approaches*

Based on the similarity concept, which presumes that similar stress-strain conditions at the fatigue-critical locations in two different specimens should produce similar fatigue lives, several life prediction models have been established. Paris [116] proposed a model for variable amplitude fatigue, which assumes that variations of the crack tip fields are describable in terms of the root-mean-square value of the stress intensity factor range, ΔK_{rms}. The variable amplitude crack growth rates are then given by a Paris-type equation:

$$da/dN = C \cdot (\Delta K_{rms})^m \tag{2-12}$$

$$\Delta K_{rms} = \frac{\left[\sum_{i=1}^{n} (\Delta K_i)^2\right]^{1/2}}{n} \tag{2-13}$$

where C and m are constants depending on materials and loading conditions, and ΔK_i is the stress intensity factor range in the i^{th} cycle in a sequence consisting of n stress cycles. Although this model is empirical and does not account for load sequence effects, this approach has been used in a variety of fatigue-critical applications such as variable amplitude fatigue of steel bridges [117]. However, in some applications, such as flight simulation of gust loading spectra for aircraft, random loading and statistically equivalent program loading are known to provide different results [118].

2.2.2.4. *Plastic Zone- and Residual Stress-Related Models*

It is established that plastic zones and the residual stresses ahead of a crack tip may have an influence on fatigue behaviour under variable amplitude loading. Several life prediction models have been established on this basis. Among them, the Willenborg

[86] and Wheeler models [87] are the best known. The Wheeler model assumes that the variable amplitude crack growth rate, $(da/dN)_{VA}$, due to the current load cycle, ΔK, of a load sequence is equal to the constant amplitude growth rate corresponding to ΔK, $(da/dN)_{CA}$, multiplied by an empirical retardation factor, ϕ, so that

$$(da/dN)_{VA} = \phi \cdot (da/dN)_{CA} \tag{2-14}$$

$$\phi = \left(\frac{r_p}{d} \right)^m \tag{2-15}$$

where r_p is the plastic zone size associated with the current load cycle, d is the distance from the current crack tip to the overload plastic zone boundary due to the most severe previous overload, and m (the Wheeler index) depends on material properties and the load spectrum. The Willenborg model is based on consideration of the effect of residual compressive stresses ahead of the crack tip. This model uses an effective stress intensity factor K_{red} to reduce the applied crack tip stress intensity factor. K_{red} depends on the plastic zone size of the current cycle and the maximum plastic zone size induced by the largest previous load cycle in the load sequence. The model predicts crack growth retardation when the baseline minimum stress intensity is less than K_{red}. Unlike the Wheeler model, the Willenborg model does not require an empirical index. A major shortcoming for both models is that they do not account for underload effects and are essentially single-mechanism models in origin.

2.2.2.5. Fatigue Crack Closure Models

Since fatigue crack closure can physically account for load interaction effects, many attempts have been made to develop life prediction models for variable amplitude fatigue. It is obvious that a more physically realistic life prediction procedure can be reached if crack closure behaviour under variable amplitude loading can be presented in a quantitative way. Consequently, much attention has been paid to crack closure behaviour under variable amplitude loading.

Elber [119] measured experimentally crack opening points under random loading, reporting that crack opening stresses are nearly constant irrespective of crack length during random loading tests. He then proposed an equivalent constant amplitude concept for fatigue life prediction under spectrum loading. On the other hand, Newman [80,120] analysed crack opening behaviour under flight simulation loading and reported that crack opening points vary in an irregular pattern, oscillating about a mean value. Based on this result, he introduced an equivalent crack opening stress concept for crack growth prediction under variable amplitude loading. Kikukawa *et al.* [121,122] have extensively measured crack opening behaviour under random loading sequences and reported that the crack opening point is controlled by the largest load cycle and is identical with the crack opening result for constant amplitude loading corresponding to the largest load cycle. Based on this crack opening behaviour, they proposed a simple prediction procedure for crack growth under variable amplitude loading. Based on their fatigue tests on *CCT* specimens of 2024-T351, Kim *et al.* [123] observed a similar trend in that the crack opening stress intensity factor under random loading was linearly proportional to the maximum stress intensity factor of the largest load cycle in a random load history. However, whilst the crack opening load was mainly governed by the largest load cycle, they found that the crack opening load under random loading was different from that under constant amplitude loading, indicating that the crack closure behaviour under random loading cannot be estimated from constant amplitude tests. They found that the crack closure behaviour under random loading could be estimated from single overloading or periodic single overloading tests. A relatively simple method was proposed to predict crack growth under random loading based on the above suggestion.

Sunder [124] predicted crack growth under a variety of flight simulation loading using a *CCZT* (constant closure zero threshold) model which assumes that the crack opening level is constant and there is no threshold stress intensity range under random loading. This model is similar to the method proposed by Kikukawa *et al.* [121,122] with the difference in determining the crack opening point.

Much analytical fracture mechanics modelling of crack closure for both *CA* and *VA* loading conditions has been based on an extension of the Dugdale [79] or '*strip yield*' model. Budiansky & Hutchinson [125] provided the first comprehensive analytical treatment for the influence of *PICC* on crack propagation on this basis. In their rigorous mathematical approach, the crack opening displacements estimated from the Dugdale analysis describe the opening profile of the fatigue crack at K_{max} with the exception that a residual stretch of previously yielded material is attached to the crack faces. Upon unloading, this residual stretch leads to contact over the entire length of the fatigue crack. The effects of crack closure on crack opening and closing loads are calculated by complex function methods for a range of loading ratios. The model leads to the result that

$$K_{op} / K_{\max} = 1 - \left[1.37 E \sigma_y \left(\delta_t - \delta_R\right)\right]^{1/2} / K_{\max} \tag{2-16}$$

where σ_y is the flow stress, E is the Young's modulus, δ_t is the crack tip opening displacement at K_{max}, and $\delta_R/2$ is the plastic stretch to be appended to the upper and lower crack faces.

Since the crack growth rate for a particular material ought to be a function of the cyclic crack tip displacements $(\delta_t - \delta_R)$ and this kind of cyclic displacement is found to be closely related to the effective stress intensity range, as defined by $\Delta K_{eff} = K_{max} - K_{op}$ (as described by *Eq.2-16*), this analytical closure model provides a theoretical justification for the use of ΔK_{eff} to characterise fatigue crack growth. The results rationalise the effect of R ratio on crack growth in the Paris regime as described by Elber. It was found that, for plane stress *PICC*, K_{op}/K_{max} is primarily a function of load ratio R (and not ΔK) which is consistent with experimental observations of Elber and of subsequent researchers where *PICC* is dominant. The calculations provide valuable insights into the development of monotonic and reversed plastic zones and plastic stretch during steady-state fatigue crack growth and into the effects of cyclic strain hardening on closure. It was also found that cyclic strain hardening enhanced the effects of crack closure, whereas cyclic softening reduced closure levels.

Lo [126] extended the Budiansky/Hutchinson model to study crack closure processes following a step-increase in the cyclic load amplitude. The influence of crack closure on the development of active plastic deformation at the crack tip was incorporated. It was shown that the effect of previous history of loading on crack growth is significant only when the extent of crack growth is within about one plastic zone size. Russell [127] details a similar theoretical development of a model for fatigue crack growth retardation following an overload. The variations of plastic zone size as the crack tip advances through the overload plastic zone are calculated. Delayed retardation effects and other experimentally observed transient growth characteristics following the overload were predicted.

De Koning [128] developed a crack growth model (*CORPUS*) based on the so-called hump opening behaviour. The model describes effects of overloads and underloads on the average crack growth rate. The peak load excursion results in a plastic deformation, which becomes visible as ridges on the fracture surfaces during subsequent fatigue crack growth. The height and width of the ridges depend on the magnitude of the peak load and the associated plastic zone size. The ridges cause a local increase in crack opening stress. A subsequent underload flattens the ridges over a distance corresponding to the reversed plastic zone size (leading to the formation of hump) and therefore decreases the crack opening stress. This peak overload-underload effect on the crack opening stress is approximated in *CORPUS* by changing the crack opening stress immediately after a peak load or underload. The effect of each peak load and its associated opening stress are also lost once the fatigue crack and its current plastic zone have grown through the plastic zone caused by the peak load. Variable amplitude loading will lead to the formation of a series of humps. The crack is assumed to be closed as long as one or more of the humps is in contact with its counterpart on the opposite crack surface. The crack is opened if all humps have lost contact. The hump that last lost contact determines the crack opening stress, σ_{op}, that is

$$\sigma_{op} = \max\left(S_{op}^{n}\right) \tag{2-17}$$

where S_{op}^{n} is the opening stress level at which hump n breaks contact. Opening stress levels of the humps will influence each other. In general, it can be concluded that the effect of a previous hump, j, on the crack opening behaviour is overruled by the application of a more severe maximum load S_{max}^{n}. As a result, this model is of limited memory capability.

A popular boundary element model was particularly developed by Newman [80]. While the physical basis of Newman model was similar to Budiansky and Hutchinson's approach, the formulation employed was different (Newman adopts a fracture mechanics approach). This model also removed the semi-infinite crack idealisation in Budiansky & Hutchison's work [125]. The corresponding fatigue life prediction code, *FASTRAN,* was conceived and developed as a crack closure analysis tool based on *PICC.* The associated computer program was originally developed for a central through crack in a finite-width specimen subjected to remote applied stress and called *FAST* (Fatigue crack growth Analysis of STructures). Later the use of 'small-crack' concepts was incorporated into *FASTRAN* [129]. In the model, the flow stress σ_o is taken as the average between the yield stress and ultimate tensile strength to account for possible strain hardening effects. As with the original Dugdale model [79], and with the mathematical analyses of Budiansky and Hutchinson, the Newman model is appropriate under the plane stress conditions. The model is however also applied to plane strain. A constraint factor, α, is used to elevate the flow stress (σ_{ys}) within the plastic zone to account for the influence of stress state on plastic zone sizes and crack surface displacements. For plane stress conditions, α is equal to unity (original Dugdale model): for simulated plane strain conditions, α is equal to 3. Although the strip-yield model does not model the correct yield-zone pattern for plane strain conditions, the model with a high constraint factor is able to produce crack surface displacements and crack opening stresses similar to those calculated from elastic-plastic finite element analyses of crack growth and closure for finite-thickness plate [130]. As the crack grows under cyclic loading, residual plastic deformation is left on the crack surfaces. During unloading, these surfaces contact each other at the minimum applied stress. The material in the plastic zone and along the contacting surfaces was assumed to yield at $-\sigma_{ys}$. Using the contact stresses, the crack opening stress is calculated. The crack

opening stress is the applied stress level at which the crack surfaces are fully open and is denoted as S_{op}. The model is able to predict crack opening stresses as a function of crack length and load history. The crack opening stress is then used to calculate the effective stress-intensity factor range, ΔK_{eff}. In turn, the crack growth rate is calculated using a ΔK_{eff} *vs.* crack growth rate relation.

Newman [80,81,120,129-131] compared the predicted fatigue lives with experimental values for notched 2024-T3 aluminium alloy sheet specimens under a variety of load sequences. The predicted lives agreed well with the test data although the constraint factor α must be calibrated to account for the influence of finite thickness of the samples. The model is easily adapted to various loading and sample geometry conditions. The most uncertain issue about this model is the use of the constraint factor α. At present, this factor is essentially used as a fitting parameter.

Similar models of *PICC* have been developed by Dill and Saff [132], Fuhring and Seeger [133], Blom *et al.* [134], Daniewicz *et al.* [135], Chen *et al.* [136-137], Nowell [138], and Atkinson *et al.* [139], *etc.* The general principle is the same. Plastically deformed material is left in the wake of the crack tip to simulate propagating fatigue cracks. The compatibility requirement between the elastic plate and the elements along the crack surface and plastic zone boundary is used to calculate plastic deformations of the elements and residual stresses ahead of and behind the crack tip. The crack opening stress, S_{op}, is normally calculated from the contact stresses behind the crack tip by equating the applied stress intensity factor at S_{op} to the stress intensity factor caused by the contact stresses at the minimum stress, S_{min}. Daniewicz *et al.* [135] used their strip-yield model to predict fatigue crack propagation in an edge-cracked panel under the combined effects of crack closure and residual stress fields. Nowell [138] used piecewise-constant displacement discountinuity boundary elements to model the crack and yield zone with quadratic programming techniques to efficiently establish the correct boundary condition. Atkinson *et al.* [139] developed an inclined strip yield super-dislocation model to represent crack tip plasticity, as such this approach might be more appropriate to simulate crack closure phenomenon under plane strain conditions.

In general, reasonably satisfactory comparisons are observed between fatigue crack closure models and experimental observations under certain constant amplitude and variable amplitude fatigue loading conditions. Crack closure based models offer the great potential in accurately predicting cycle-by-cycle crack growth under complex *VA* fatigue load spectra. It should be noted however that improvements are required for closure based fatigue models. Experimentally established closure models are essentially semi-empirical and depend heavily on the calibrating closure measurements. Closure based *FE* modelling of *VA* crack growth can be computationally expensive and there are issues in representing the crack tip region. Existing analytical models are essentially single mechanism-based and mainly applicable under plane stress conditions. Any single mechanism approach is in contradiction to the known impact of many different physical processes during variable amplitude fatigue crack growth.

2.3. Material Characteristics

2.3.1. Metallurgical Characteristics of High Strength Heat-Treatable *Al*-Alloys

Depending on whether or not they respond to precipitation hardening, *Al*-alloys can be classified as heat-treatable or non-heat-treatable. 2xxx series and 7xxx series are the two major kinds of heat-treatable *Al*-alloys used for aerospace applications. 7xxx series alloys are mainly for high-strength applications, whilst 2xxx series alloys are mainly for damage-tolerant applications due to their good crack growth resistance.

A normal heat-treatment cycle usually involves a solutionising soak at a high temperature within the single-phase region to dissolve the alloying elements, followed by rapid cooling or quenching to a low temperature to obtain a solid solution supersaturated with both solute elements and vacancies. The final stage of the heat treatment cycle is the controlled decomposition of the supersaturated solid solution to produce dispersed precipitates by ageing at either room temperature (natural ageing) or some intermediate temperature (artificial ageing). Three types of precipitates can be produced for aircraft *Al*-alloys during ageing. They are Guinier-Preston *(GP)* zones, intermediate meta-stable phases, and equilibrium precipitates. *GP* zones are coherent and finely dispersed within the matrix. They are ordered, solute-rich clusters of atoms which may be only one or two atom planes in thickness with densities possibly as high as 10^{17} to 10^{18} cm^{-3} [140]. *GP* zones are formed in the early stages of ageing and may be the precursors of intermediate precipitates. They are the major strengthening precipitates for naturally aged materials. Intermediate precipitates may nucleate homogeneously, or heterogeneously at vacancy clusters, *GP* zones, dislocations, or sub-boundaries [141]. The shape and habit plane of these intermediate precipitates depends on the balance between strain energy and interfacial free energy. Intermediate precipitates normally have a crystal structure which is different from that of the matrix but are completely coherent with the matrix on at least one interface. Their composition and crystal structure may differ only slightly from that of the equilibrium precipitates. Equilibrium precipitates are generally larger still and more widely spaced. They may form by transformation of intermediate precipitates. They can also nucleate

at dislocations and at interfaces such as grain boundaries and sub-grain boundaries, and at the interfaces between other particles and the matrix. They form at relatively high ageing temperatures/times and are largely incoherent with the matrix.

Apart from the above three precipitates formed during ageing, intermetallic constituent particles and dispersoids are the other two important particle types found in heat-treatable *Al*-alloys. Coarse intermetallic constituent particles form inter-dendritically during solidification, primarily from iron and silicon impurities. Because the low solubility of iron in pure aluminium is further reduced by alloying elements, constituents containing iron are essentially insoluble. Silicon has appreciable solubility in aluminium, but its solubility is decreased by other alloying elements, particularly magnesium. Consequently, while soluble in some alloys, Mg_2Si is virtually insoluble in alloys such as 7075. The size and distribution of insoluble constituent particles are controlled by the rate of ingot solidification, the chemical composition, and the extent and nature of bulk deformation. Constituent size decreases as solidification rate increases, as iron and/or silicon content decreases, and as the amount of working deformation increases. Generally, the insoluble constituents are coarsest and most heterogeneously distributed in thick plates and are finer and more homogeneously distributed in thin sheets. Soluble constituents consist of equilibrium intermetallic compounds of the major alloying elements. Typical examples are Al_2Cu, Al_2CuMg, and sometimes Mg_2Si. Both soluble and insoluble constituents may form as lacy networks surrounding as-cast grains, with one purpose of the preheating or ingot homogenisation process being to dissolve the soluble constituents. During the subsequent fabrication of the cast ingots, the largest of the remaining particles usually fracture, which reduces their sizes to the range of 0.5 - 10μm and causes them to become aligned as stringers in the direction of working or metal flow, promoting anisotropy in tensile and other mechanical properties. Sub-micron dispersoids (typically 0.05 - 0.5μm) form during the homogenisation of ingots by solid state precipitation of compounds containing the transition elements chromium, manganese or zirconium which have modest solubility and diffuse slowly in solid aluminium. They are present by design to control grain structure and degree of re-crystallisation of the alloys concerned. All of these particles are sufficiently stable that their size remains stable after ingot preheating. Typical

dispersoids in *Al*-alloys are $Al_{12}Mg_2Cr$, $Al_{20}Mn_3Cu_2$ and Al_3Zr. The first two dispersoids are larger (up to $0.5\mu m$ in the longest dimension) and develop an incoherent interface with the matrix. In contrast, Al_3Zr forms as significantly smaller coherent particles (typically around 50 *nm* in diameter).

Another important metallurgical feature in heat-treatable *Al*-alloys is the development of precipitate free zones (*PFZ*) adjacent to grain boundaries (along with sub-grain boundaries and dispersoid-matrix interfaces to varying extents). There are two types of *PFZ*. One is the vacancy-depleted *PFZ* which may arise when vacancies have been lost to an interface prior to ageing, being reduced to levels below that which is needed to assist with the formation of precipitates. The other is solute-depleted, which arises when solute elements near grain boundaries are depleted due to the ready diffusion of solute atoms into the boundary where relatively large particles of equilibrium phase are formed. Since *PFZs* almost always have a detrimental effect on the mechanical properties of *Al*-alloys, processing procedures such as low temperature ageing, duplex ageing and/or deformation prior to ageing are frequently used [140].

2.3.2. Metallurgical Characteristics of 2xxx *Al*-Alloys

The first heat-treatable *Al*-alloy was based on the *Al-Cu* system. Wrought *Al*-alloys having copper as the main alloying element are designated as 2xxx alloys by the International Alloy Designation System *(IADS)*. For the classical high copper-content 2xxx series alloys, the ageing sequence is usually described as:

$$Supersaturated \quad \alpha \Rightarrow GP \quad zones \Rightarrow \theta' \Rightarrow \theta \quad (Al_2Cu) \tag{2-18}$$

Copper atoms may cluster into two-dimensional disc-shaped *GP* zones on {100} matrix planes during ageing. These zones are thought to be 30—50 *Å* in diameter and are probably single layers of copper atoms [140,141]. At temperatures of *373 K* and higher, three-dimensional *GP* zones may form. Depending on the ageing time and temperature, they may transform into the intermediate precipitate θ' on {100} matrix planes, which has the same chemical composition as the equilibrium precipitate θ

(Al_2Cu), but which has a primative tetragonal crystal structure (*a=0.404nm, c=0.580nm*) and is only partially incoherent with the matrix. θ' is fully coherent with the matrix along the broad faces, and its {001} planes and <001> directions are parallel to the {001} planes and <001> directions of the matrix. θ' precipitates often nucleate directly on dislocations since the dislocations can relieve the misfit associated with the precipitate. The distribution of θ', therefore, may be very heterogeneous and reflects the distribution of dislocations. Deformation prior to ageing can increase the dislocation density and thereby the number of nucleating sites for heterogeneous precipitation of θ'. The final equilibrium precipitate θ formed during ageing treatment may nucleate at the surface of θ'. θ has a body-centred tetragonal crystal structure Al_2Cu (*a=0.606 nm, c=0.487 nm*) and is incoherent with the matrix.

For the higher magnesium-content 2xxx series *Al*-alloys such as 2024, the decomposition process can be described as:

$$Supersaturated \quad \alpha \Rightarrow GP(B) \quad zones \Rightarrow S' \Rightarrow S \quad (Al_2CuMg) \tag{2-19}$$

The addition of magnesium to *Al*-alloys enhances both the rate and the magnitude of natural ageing. *GP (B)* zones are *Cu-* and *Mg*-rich zones that have been reported to form as thin rods along <100> directions of the matrix. It is however worth noting that some uncertainty and controversy concerning the nature of the zones/clusters exists in the literature on monolithic *AlCuMg* alloys [142-146]. *Mg-Mg, Cu-Cu* as well as *Cu-Mg* clusters have been identified in an *Al-Cu-Mg* alloy [143] by atom probe field ion microscopy (*APFIM*). *X*-ray diffraction (*XRD*) data have been interpreted as indicating the formation of cylindrical structures with diameter about 1-2 *nm* and length in the order of 10 *nm* which were termed *GPB1* zones [144], but small angle *X*-ray scattering (*SAXS*) has been interpreted in terms of disk-shaped structures with radius of about 1 *nm* which were termed *GPB* zones [145], and the mottled appearance of underaged *Al-Cu-Mg* alloys in conjunction with the appearance of diffraction rings in the selected area diffraction pattern has been related to *GPB2* zones [146].

The intermediate precipitate *S'* has the same chemical composition and basic orthorhombic crystal structure (*a=0.404nm, b=0.925nm, c=0.718nm*) as the equilibrium precipitate *S* (Al_2CuMg). The [100], [010], and [001] directions of *S'* are respectively parallel to the [001], [021] and [012] directions of the matrix. The *S'* precipitates normally nucleate at dislocations and grow as laths on {210} planes along <100> directions of the matrix. As growth continues, the laths of *S'* may form corrugated sheets on {210} planes with {110} composite planes. The final incoherent equilibrium precipitate *S* (Al_2CuMg) has an orthorhombic crystal structure (*a=0.400nm, b=0.923nm, c=0.714nm*) and probably transform from *S'* [147].

The *Al-Cu-Mg-Mn* alloy 2024 was developed in 1938 and is widely used as a damage-tolerant airframe material (in the naturally aged T3 condition) in primary aerospace structures. It may exhibit fatigue crack growth rates of the order of one third those observed in the 7xxx series alloys [148]. On the *Airbus A320*, fuselage skins and stringers, bottom wing skin and stringers and wing spars and slate are fabricated from 2024-T3. Nominal chemical compositions for 2024-T351 (solution, cold work/stress relieved by stretching, and then naturally aged) and its improved 2024A-T351 variant [149,150], which are the research materials in this project, are listed in Table 2.1.

Table 2.1 Nominal compositions (wt%) of 2024 & 2024A.

Alloy	*Cu*	*Mg*	*Mn*	*Fe (max)*	*Si (max)*
2024	3.8-4.9	1.2-1.8	0.30-0.90	0.50	0.50
2024A	3.7-4.5	1.2-1.5	0.15-0.80	0.20	0.15

For 2024-T351, the major strengthening precipitates are *GP(B)* zones. The usual intermetallic forming phases are Al_7Cu_2Fe, $Al_{12}(Fe, Mn)_3Si$, Al_2CuMg, Al_2Cu, and $Al_6(Fe, Cu)$. $Al_{20}Cu_2Mn_3$ is the main form of dispersoids found in 2024-T351. 2024A-T351 is the higher purity version of 2024-T351. Due to its reduced level of *Mn, Si,* and *Fe* contents, a decrease in volume fraction of intermetallic constituents and manganese-containing dispersoids is expected. Not all of the above insoluble constituents may be present.

2.3.3. Correlation between Mechanical Properties and Microstructure

2.3.3.1. Strength and Microstructure

The strength of a heat-treatable alloy is mainly controlled by the interaction of moving dislocations with precipitates. When the precipitates are small, such as *GP* zones and intermediate precipitates, they may be sheared by moving dislocations, which will reduce the precipitate-associated strengthening mechanisms. This results, successively, in a local decrease in resistance to further dislocation movement. Deformation therefore tends to be heterogeneous and work-hardening is comparatively limited. The strength associated with these shearable precipitates can be described as:

$$\Delta\sigma_p \cong c \cdot f^m \cdot d^n \tag{2-20}$$

Where $\Delta\sigma_p$ is the contribution of the particles to the yield strength of the alloys, c is an alloy constant that depends on the properties of the strengthening particles and matrix, m and n are positive exponents, f is the volume fraction of the precipitates and d is the precipitate diameter. *Eq.(2-20)* shows that strength increases with volume fraction and size of the shearable precipitates.

If precipitates are large and widely spaced, then they may resist cutting and the dislocations are forced to bow out and rejoin by the classical Orowan mechanism. The yield strength of the alloy may be low but the rate of work-hardening is high, and plastic deformation ends to be spread more uniformly throughout the grains. This is the normal situation of over-aged alloys. This strengthening mechanism may be described by the modified Orowan equation:

$$\Delta\sigma_p \cong G \cdot b \cdot \left(\frac{f}{d}\right)^{1/2} \tag{2-21}$$

where G is the shear modulus, b is the modulus of the Burgers vector of the matrix dislocations. Obviously, a high volume fraction of very small non-shearable precipitates is desired, although this is usually difficult to obtain in age-hardening

systems. It is worth noting that the alloy strength increases with decreasing the precipitate size, which is contrary to the shearable precipitate strengthening mechanism of *Eq.(2-20).*

2.3.3.2. Fracture Toughness and Microstructure

As strength increases, ductility and fracture toughness usually decrease. This is the typical relationship during ageing for 2xxx and 7xxx series alloys [151]. A variety of microstructural effects may arise, with, for example, shearable precipitates favouring the development of concentrated slip bands, which may then become preferential failure paths. Heterogeneous precipitation occurring at grain and sub-grain boundaries may also result in soft, solute-depleted *PFZs* in the matrix adjacent to the boundaries. These soft zones can cause strain localisation and thus lead to early crack initiation and low fracture toughness.

Coarse intermetallic constituents do not contribute to strength, but they have a detrimental effect on the fracture toughness of *Al*-alloys [152,153]. Constituent particles participate in the fracture process through void formation at particle/matrix interfaces, or by fracturing, at relatively low stress/strain levels.

Depending on their size and details of their interface with the matrix, dispersoids may also play an unfavorable role in the fracture process. Specifically, void coalescence within shear bands may occur by the formation of void sheets associated with the nucleation of fine voids at dispersoids [154]. However, Lutjering *et al.* [155] found that small 0.1 to 0.2 micron sized dispersoids which are normally presented in commercial high strength *Al*-alloys such as 2024 may also be beneficial for fracture toughness due to their contributions to slip homogeneity (*i.e.* if they do not fail too readily during deformation).

Alloy design for high fracture toughness generally focuses on reducing the volume fraction of void nucleating particles, by minimising *Fe* and *Si* contents, optimising solute content to prevent the formation of coarse phases, and using *Zr* as the dispersoid

forming addition to control the grain size and degree of re-crystallisation. Table 2.2 shows the longitudinal mechanical properties of *Pechiney* 2024-T351 and 2024A-T351 in 1.6 – 3.2*mm* sheet. Compared with 2024-T351, 2024A-T351 has significantly greater toughness (over 20% on K_c (*T-L*)) with equivalent or very slightly reduced static strengths. The increase in toughness is associated with a decrease in the manganese, iron and silicon content of the alloy, which allows a decrease in volume fraction of constituent particles and manganese-containing dispersoids [149, 156]

Table 2.2 Nominal longitudinal monotonic properties of Pechiney 2024-T351 & 2024A-T351.

Alloy	Yield Strength (*MPa*)	Tensile Strength (*MPa*)	Elongation (%)	Toughness K_c (*T-L*) $MPam^{1/2}$
2024-T351	345	465	19	130
2024A-T351	340	455	22	160

2.3.3.3. Fatigue Crack Growth Resistance and Microstructure

Microstructure is the principal independent variable which can be used to control fatigue crack growth rate (*FCGR*) once loading and environmental conditions are established. Detailed discussions were given by Sinclair and Gregson [157] in a recent survey on fatigue optimisation in aerospace aluminium alloys. Table 2.3 presents a survey of basic micro-structural influences on fatigue resistance in high strength monolithic Al-alloys.

Much work, such as that in Refs.[14, 37-43, 100, 158], has shown that the effect of microstructure on *FCG* behaviour changes as the stress intensities vary from near-threshold to near-final failure. For example, over-ageing from a T6 temper to a T7 temper can reduce *FCGR* by a factor of two at intermediate stress intensities, but can increase *FCGR* by a factor of ten at low stress intensities. In terms of intrinsic fatigue crack growth resistance, major factors may be identified in slip character, slip length and slip reversibility [14, 37-39, 159]. Each of these factors may be affected by both alloy composition and microstructure.

Table 2.3 Basic micro-structural influences on fatigue resistance in high strength monotonic Al-alloys [157].

Regime	Relevant Mechanisms	Desirable Micro-structural Features
Initiation	Slip band formation	Non-shearable precipitates, dispersoids, reduced grain size, reduced texture
	Particle failure	Uniform spatial distributions, small equiaxed particles
	Porosity	Improved processing procedures
	Grain boundary failure	'Remove' boundary *PFZs* & particles, limit slip band activity
Short Crack Growth	Slip band/Stage I	Small grain size, high angle boundaries
	Grain boundary growth	Triple points, large boundary particles
	Slip band/extended Stage I	Shearable precipitates, fewer dispersoids, increased grain size, in creased texture
Long Crack Growth	Roughness induced closure	Shearable precipitates, fewer dispersoids, increased grain size, increased texture-texture effects vary with orientation
	Deflection shielding	Shearable precipitates, fewer dispersoids, increased grain size, increased texture-texture effects vary with orientation
	Plasticity induced closure	Lower strength, increasing cyclic work hardening

The effects of planar slip deformation, enhanced by shearable precipitates and larger grain size, are twofold. On the one hand, strain localisation caused by planar slip may lead to early crack initiation and low fracture toughness. This may reduce the fatigue life of uncracked specimens and increase *FCGR* in the fast crack growth regime where the influence of fracture toughness is large. On the other hand, planar slip may reduce *FCGR* in the near-threshold and lower part of the Paris regime through enhanced crack tip shielding promoted by crystallographically deflected and tortuous crack path morphologies. Based on their experimental results, many researchers (e.g. [32, 159-

161]) have attributed the excellent crack growth resistance of commercial aluminium-lithium alloys in conventional long-crack tests to crack tip shielding due to their propensity for planar slip (crack tip shielding mechanism discussed in detail in Section I of the literature review). Planar slip associated with shearable precipitates may also decrease *FCGR* by enhancing slip reversibility which results in less damage in the crack tip plastic zone [141].

Chanani *et al.* [162] observed improved *FCG* behaviour in high purity alloys 2124-T851 and 7475-T7351 at high stress intensities under both constant amplitude and variable amplitude loading spectra compared with that of corresponding low purity 2024-T851 and 7075-T7351. This was associated with the reduction of the volume fraction of constituents in the matrix. However, little effect of the volume fraction of the constituents was found on crack growth resistance at intermediate and low stress intensities. Detailed fracture surface examination of 2024-T851 and 7075-T7351 under variable amplitude loading indicated that crack growth occurred by striation formation and void nucleation and growth, while the higher purity alloys 2124-T851 and 7475-T7351 showed striation formation occurred with much more limited evidence of particle-initiated fracture and void growth on the fracture surfaces under high stress intensities.

Dispersoids have been reported to homogenise slip and inhibit the propensity for crystallographic, tortuous fatigue crack paths. They may also reduce fatigue fracture surface roughness by their retardation effect on grain growth during processing. Both of these factors may increase the *FCGR* by reducing deflection shielding and roughness-induced crack closure. As a result, dispersoid-strengthened alloys are often less attractive than those hardened by shearable precipitates for damage-tolerant applications. However, dispersoids may be beneficial for *FCG* resistance (at intermediate to high stress intensities) and under aggressive environments due to reduced strain localisation (slip bands being preferred environmental damage sites) [155].

2.3.3.4. Mechanical Properties of 2x24 Alloys

Natural ageing in 2xxx alloys is attributable to complex interactions between *GP* zones, solute atoms, and vacancies. Although the rate and extent of natural ageing vary from one alloy to another, most of the strengthening occurs during the first day, and stability is reached after about four days. While the maximum strength cannot normally be realised during natural ageing, many 2xxx alloys are used in the natural ageing tempers such as T3 (solutionised, cold work & natural ageing) and T4 (solutionised & natural ageing) due to their good combination of strength, ductility, fracture toughness, and fatigue crack growth resistance. Good fracture properties can be related to the lack of coarse grain boundary phases and *PFZs* during room temperature ageing. 2xxx alloys also respond well to deformation prior to ageing. For 2024 type alloys, cold work after the quench from the solution heat-treatment increases strength by increasing dislocation density in natural aged materials (T3 & T4 tempers) and by refining the size of the *S'* (Al_2CuMg) produced during subsequent artificial ageing (T8 temper: solution, cold work & artificial ageing) [163].

Depending on temper, AA2024 can either strain harden or soften on cyclic loading [163]. In general, cyclic hardening occurs in strain-controlled tests of aluminium alloys by dislocation multiplication and interaction, but this hardening can be reduced by softening associated with dislocation/precipitate interactions (particularly precipitate shearing). Cyclic stress-strain tests on 2024-T351 *(GP (B)* zone strengthened) and 2024-T851 (*S'* strengthened) after one cycle and after saturation demonstrate that, despite its considerably lower monotonic yield strength, 2024-T351 develops a relatively high cyclic flow stress. 2024-T851, which is overaged to develop *S'* precipitates and a higher level of monotonic yield strength, cyclically hardens to a much lesser extent, *i.e.* the nature of the precipitates, not the level of monotonic yield strength, may strongly determine the character of the cyclic response.

Fatigue crack growth resistance of 2024 in T3 (natural ageing) and T8 (overaged) tempers under intermediate ΔK levels progressively decreases as monotonic yield strength increases either by artificial ageing or by stretching up to about 5% [130]. The

superior fatigue crack growth performance at intermediate ΔK of 2024 in T3 temper relative to that in T8 temper is attributed in part to the ability of *GP* zones to promote a higher degree of cyclic hardening, in addition to effects such as the ease of planar deformation which will promote greater roughness-induced crack closure, and more slip reversibility which will lessen damage accumulation [39]. In keeping with the previous discussion of 2024 and 2124 purity effects the effect of the volume fraction of inter-metallic constituents on fatigue crack growth rate of alloy 2024 under constant amplitude loading depends on temper as well as the level of ΔK [151]. At a ΔK level near 18 $MPam^{1/2}$, decreasing the volume fraction of inter-metallic constituents from 2.2 to 1.4% has been shown to approximately double the resistance to fatigue crack growth of sheet in the higher strength T86 temper but had negligible effect on fatigue resistance of sheet in the lower-strength T31 temper. On the other hand, at a ΔK level near 7 $MPam^{1/2}$, volume fraction of constituents had a negligible effect on fatigue resistance of sheet in either temper.

In conjunction with issues raised in previous sections it may be recognised that fatigue resistance in high strength aluminium alloys such as 2024 is determined by a complex collection of microstructural and mechanical effects.

References

[1] P. C. Paris, M. P. Gomez, and W. P. Anderson, (1961), *The Trend In Engineering,* Vol.13, pp.9-14.

[2] F. A. McClintock, (1963), In: *Fracture of Solids* (eds. D.C. Drucker & J. J. Gilman), Vol.20, pp.65-102, New York: Wiley.

[3] N. E. Frost, (1966), In: *Proc. of the First Int. Conf. On Fracture* (ed. T. Yokobori), pp.1433-59, Sendai: The Japan Society for Strength and Fracture of Materials.

[4] R. A. Schmidt and P. C. Paris, (1973), *ASTM STP 536*, American Society for Testing and Materials, pp.79-94.

[5] *ASTM E647*, (1995), Annual Book of ASTM Standards, Section 3, Vol.03.01, pp.578-614.

[6] S. Suresh, (1996), *Fatigue of Materials*, Cambridge Solid State Science Series, (eds. D.R.Clarke, S.Suresh, and I.M.Ward), Cambridge.

[7] E. P. Phillips, (1988), *ASTM STP982*, American Society for Testing and Materials, pp.505-515.

[8] S. Suresh, (1985), *Engineering Fracture Mechanics,* Vol.21, pp.453-63.

[9] T. Christman and S. Suresh, (1986), *Engineering Fracture Mechanics*, Vol.23, pp.953-64.

[10] W. A. Herman, R. W. Hertzberg, and R. Jaccard, (1988), *Fatigue & Fracture of Engineering Materials & Structures*, Vol.4, pp.303-20.

[11] R. J. Donahue, H. M. Clark, P. Atanmo, R. Kumble, and A. J. MvEvily, (1972), *Int. J. of Fracture*, Vol.8, pp209-19.

[12] G. R. Yoder, Y. A. Cooley, T. W. Crooker, (1983), *ASTM STP791*, American Society for Testing and Materials, pp.348-65.

[13] S. Taira, K. Tanaka, and M. Hoshina, (1979), *ASTM STP675*, American Society for Testing and Materials, pp.135-73.

[14] *C. P. Blankenship and E. A. Starke, (1991), Fatigue & Fracture of Engineering Materials & Structures,* Vol.14, pp.103-114.

[15] E. Hornbogen and K. –H. Zum Gahr, (1976), *Acta Metallurgica*, Vol.24, pp.581-92.

[16] P. E. Irving and C. J. Beevers, (1974), Materials Science and Engineering A, Vol.14, pp229-38.

[17] P. J. E. Forsyth, (1962), In*: Crack Propagation: Proc. of Cranfield Symposium*, pp76-94.

[18] C. A. Zappfe and C. O. Worden, (1951), *Transactions of the American Society for Metals*, Vol.43, pp.958-69.

[19] C. Laird, (1967), *ASTM STP415*, American Society for Testing and Materials, pp.131-68.

[20] R. W. Lardner, (1967), *Philosophical Magazine*, Vol.17, pp71-82.

[21] J. Weertman, (1966), *Int. J. of Fracture*, Vol.2, pp.460-7.

[22] J. R. Rice, (1967), *ASTM STP415*, American Society for Testing and Materials, pp.247-309.

[23] M.M.I. Hammouda, B. M. El-Sheily, H.E.M. Sallam, S.S.E. Ahmed, and M.H. Seleem, (1999), *Engineering Against Fatigue,* J. H. Beynon et al Eds., A.A. Balkema Publisher, pp.113-121.

[24] P. E. Magnusen, R. J. Bucci, A. J. Hinkle, J. R. Brockenbrough, and H. J. Konish, (1997), *Int. J. of Fatigue,* Vol.19, pp.S275-S283.

[25] A. Fatemi and L. Yang, (1998), *Int. J. of Fatigue,* Vol.20, pp.9-34.

[26] R. G. Forman, V. E. Kearney, and R. M. Engle, (1967), *J. of Basic Engineering*, Vol.89, pp.459-64.

[27] K.Walker, (1970), *ASTM STP462*, American Society for Testing and Materials , pp1-14.

[28] W. Elber, (1970), *Engineering Fracture Mechanics*, Vol.2, pp. 37-45.

[29] W. Elber, (1971), *ASTM STP486*, American Society for Testing and Materials, pp.230-42.

[30] K. Endo, T. Okada and T. Hariya, (1972), *Bulletin of the Japan Society of Mechanical Engineers*, Vol.15, pp.439-45.

[31] S. Suresh, G. F. Zamiski, and R. O. Ritchie, (1981), *Metallurgical Transactions*, Vol.12A, pp.1435-43.

[32] A. K. Vasudevan and S. Suresh, (1982), *Metallurgical Transactions*, Vol.13A, pp.2271-80.

[33] J. C. Newman, (1976), *ASTM STP590*, American Society for Testing and Materials, pp.281-301.

[34] R. G. Chermahini, K. N. Shivakumar, J. C. Newman, and A. F. Blom, (1989), *Engineering Fracture Mechanics,* Vol.34, pp.393-402.

[35] N. A. Fleck and R. A. Smith, (1982), *Int. J. of Fatigue*, Vol.4, pp.157-60.

[36] A. F. Beck, M. A. Heine, E. J. Caule, and M. J. Pryor, (1967), *Corros. Sci.,* Vol.7, p.1.

[37] H. Nowack, K. H. Trautmann, K. Schulte, and G. Lutjering, (1979), *ASTM STP677*, American Society for Testing and Materials, pp.36-53.

[38] D. L. Davidson, (1981), *Fatigue & Fracture of Engineering Materials & Structures*, Vol.3, pp.229-36.

[39] T. H. Sanders, Jr. and J. T. Staley, (1979), In: *Fatigue and Microstructure*, American Society for Metals, Metals Park, pp.467-522.

[40] S. Suresh, (1983), *Metallurgical Transactions*, Vol.14A, pp.2375-85.

[41] E. A. Starke, Jr. and J. C. Williams, (1989), *ASTM STP 1020,* American Society for Testing and Materials, pp.184-205.

[42] R. D. Carter, E. W. Lee, E. A. Starke, and C. J. Beevers, (1984), *Metallurgical Transactions*, Vol.15A, pp555-63.

[43] S. Suresh, (1985), *Metallurgical Transactions*, vol.16A, pp.249-60.

[44] J. Llorca, In: *Numerical Methods in Fracture Mechanics* (eds. D. R. Luxmoore and D. R. J. Owen), Swansea: Pineridge, pp.211-23.

[45] J. Llorca, (1992), *Fatigue & Fracture of Engineering Materials & Structures*, Vol.15, p.655.

[46] C. J. Beevers and R. L. Carlson, (1984), *Fatigue Crack Growth, 30 Years of Progress*, (Ed. R. A. Smith), Pergamon Press, pp.89-102.

[47] J. Schijve, (1988), *ASTM STP982*, American Society for Testing and Materials, pp.5-34.

[48] R. Kumar, (1992), *Engineering Fracture Mechanics*, Vol.42, pp.389-400.

[49] E. P. Phillips, (1989), *NASA Technical Memorandum 101601*, Langley Research Center, Hampton, Virginia.

[50] E. P. Phillips, (1993), *NASA Technical Memorandum 109032*, Langley Research Center, Hampton, Virginia.

[51] H. U. Staal and J. D. Elen, (1979), *Engineering Fracture Mechanics*, Vol.11, pp.275-83.

[52] H. Nisitani and M. Kagi, (1979), *Fracture 1979 (ICF 4),* Vol.2, University of Waterloo Pres., pp.1099-1108.

[53] L. J. Fellows, D. Nowell and D. A. Hills, (1997), In: *Advances in Fracture Research, Proc. 9th Int. Conf. On Fracture,* Sydney, Australia, pp.2552-2558.

[54] D. L. Davidson, (1991), *Engineering Fracture Mechanics*, Vol.38, pp393-402.

[55] F. J. Pitionak, A. F. Grandt, L. T. Montulli, and P. F. Packman, (1974), *Engineering Fracture Mechanics,* Vol.6, pp.663-70.

[56] A. Guvenilir, T. M. Breunig, J. H. Kinney, and S. R. Stock, (1997), *Acta Meter.,* Vol.45, pp.1977-1987.

[57] A. U. De Koning, (1982), *NLR TR 81141 L,* National Aerospace Lab., NLR, Amsterdam, The Netherlands.

[58] R. M. Pelloux, M. Faral, and W. M. McGee, (1980), *ASTM STP700*, American Society for Testing and Materials, pp.35-48.

[59] V. Bachmann and D. Munz, (1976), *J. of Testing and Evaluation*, Vol.4, pp.257-60.

[60] K. M. Lal, S. B. L. Gary, and I. Lemay, (1980), *J. of Engineering Materials and Technology*, Vol.102, pp.147-52.

[61] C. L. Ho, O. Buck, and H. L. Marcus, (1973), *ASTM STP536*, American Society for Testing and Materials, pp.5-21.

[62] C. S. Lee, C. G. Park, and Y. M. Chang, (1996), *Materials Science and Engineering*, A216, pp131-38.

[63] A. K. Vasudevan, K. Sadananda, annd N. Louat, (1994), *Materials Science and Engineering,* A188, pp.1-22.

[64] W. Yisheng and J. Schijve, (1995), *Fatigue & Fracture of Engineering Materials & Structures*, Vol.18, pp.917-21.

[65] N. Louat, K. Sadananda, M. Duesberg, and A. K. Vasudevan, (1993), *Metall. Trans.*, Vol.24A, p.2225.

[66] Zhaohui Shan and Yang Leng, (1997), *Scripta Materialia*, Vol.36, pp.137-43.

[67] J. J. Lee and W. N. Sharpe, Jr., (1988), *ASTM STP982*, American Society for Testing and Materials, pp.270-278.

[68] S. J. Hudak, Jr. and D. L. Davidson, (1988), *ASTM STP982*, American Society for Testing and Materials, pp.121-138.

[69] K. Minakawa and A. J. McEvily, (1981), *Scripta Metall.*, Vol.15, pp.633-636.

[70] C. M. Ward-Close and R. O. Ritchie, (1988), *ASTM STP982*, American Society for Testing and Materials, pp.93-111.

[71] D. L. Davidson and L. K. Austin, (1991), *Fatigue & Fracture of Engineering Materials & Structures,* Vol.14, p.939.

[72] J. E. Allison, R. C. Ku, and M. A. Pompetzki, (1988), *ASTM STP982*, American Society for Testing and Materials, pp.171-185.

[73] D. L. Chen, B. Weiss, R. Stickler, and Zhongguang Wang, (1997), *J. Materials Science and Technology*, Vol.13, pp.1-14.

[74] J. K. Donald, (1997), *Int. J. Fatigue*, Vol.19, pp.S191-S195.

[75] J. C. Newman, Jr., (1992), *NASA TM 104159,* Langley Research Center, Hampton, Virginia.

[76] K. T. Venkateswara Rao and R. O. Ritchie, (1988), *Acta Metall.*, Vol.36, pp.2849-62.

[77] E. F. J. von Euw, R. W. Hertzberg, and R. Roberts, (1972), *ASTM STP513,* American Society for Testing and Materials, pp.230-59.

[78] N. A. Fleck, (1988), *ASTM STP924*, American Society for Testing and Materials, pp.157-83.

[79] D. S. Dugdale, (1960), *J. of Mechanics and Physics of Solids*, Vol.8, pp.100-4.

[80] J. C. Newman, Jr., (1981), *ASTM STP748*, American Society for Testing and Materials, pp53-84.

[81] J. C. Newman, Jr., (1999), *NASA TM 209133,* Langley Research Center, Hampton, Virginia.

[82] R. H. Christensen, (1959), *Metal Fatigue*, New York: McGraw-Hill.

[83] J. Lankford and D. L. Davidson, (1981), In: *Advances in Fracture Research (eds. D. Francois)*, Vol.2, pp.899-906, Oxford: Pergamon Press.

[84] J. E. Allison, (1979), *ASTM STP677*, American Society for Testing and Materials, pp.550-62.

[85] S. Taira and K. Tanaka, (1979), *Transactions of the Iron and Steel Institute of Japan*, Vol.19, pp.411-8.

[86] J. D. Willenborg, R. M. Engle, and H. A. Wood, (1971), *AFFDL-TM-FBR-71-1.*

[87] O. E. Wheeler, (1972), *J. Basic Engng., Trans. of ASME*, Vol.94, p.181.

[88] Masahiro Toyodada and Toshio Niwa, (1993), *Fatigue '93*, pp.681-86.

[89] R. C. McClung, B. H. Thacker, and S. Roy, (1991), *Int. J. of Fracture*, Vol.50, pp.27-49.

[90] J. Wu and F. Ellyin, (1996), *Int. J. of Fatigue*, Vol.82, pp.43-65.

[91] L. W. Wei and M. N. James, (2000), submitted to *Engineering Fracture Mechanics.*

[92] S. Suresh, (1983), *Engineering Fracture Mechanics*, Vol.18, pp.577-93.

[93] J. Schijve, (1974), *Engineering Fracture Mechanics*, Vol.6, pp.245-52.

[94] I. Trockels, A. Gysler, and G. Lutjering, In: *The fourth Int. Conf. On Aluminium Alloys*, pp717-24.

[95] F. J. Gran, A. Gysler, and G. Lutjering, (1993), *Fatigue '93, (eds. J. P. Bailon and J. I. Dickson),* p.623.

[96] T. C. Lindley and C. E. Richards, (1974), *Materials Science and Engineering*, Vol.14, pp.282-93.

[97] H. L. Ewards and R. T. Furnee, (1978), *Int. J. of Fracture,* Vol.14, pp281-93.

[98] A. J. McEvily,(1977), *Fatigue 1977 Conf.*, University of Cambridge, UK.

[99] L. B. Vogelesang and J. Schijve, (1980), *Fatigue & Fracture of Engineering Materials & Structures*, Vol.3, pp.85-98.

[100] R. J. Bucci, A. B. Thakker, T. H. Sanders, R. R. Sawtell, and J. T. Staley, (1980), *ASTM STP 714*, American Society for Testing and Materials, pp41-78.

[101] S. Suresh and A. K. Vasudevan, (1984), In*: Fatigue Crack Growth Threshold Concepts (eds. D. L. Davidson & S. Suresh)*, The Metallurgical Society of the American Institute of Mining, pp.361-78.

[102] J. F. Knott and A. C. Pickard, (1977), *Metal Science*, Vol.11, pp.399-404.

[103] M. Skorupa, (1999), *Fatigue & Fracture of Engineering Materials & Structures*, Vol.22, pp.905-926.

[104] R. E. Jones, (1973), *Engineering Fracture Mechanics*, Vol.5, pp.585-604.

[105] J. Petit, R. Tintillier, N. Ranganathan, M. Ait Abdedaim and G. Chalant, (1988), In: *Fatigue Crack Growth Under Variable Amplitude Loading,* (Edited by J.

Petit, D. L. Davidson, S. Suresh and P. Rabbe), Elservier Applied Science, London, pp.162-179.

[106] J. Schijve, (1976), *Engineering Fracture Mechanics*, Vol.8, pp.575-581.

[107] L. Legris, M. H. El Haddad and T. H. Topper, (1981), *Materials, Experimentation and Design in Fatigue, Proc. Fatigue'81*, Society of Environmental Engineers Conference, (Edited by F. Sherratt and J. B. Sturgeon), Westbury House.

[108] G. H. Jacoby, H. Nowack and H. T. M. van Lipzig, (1976), *ASTM STP595*, American Society for Testing and Materials, pp.172-183.

[109] S. Matsuoka and K. Tanaka, (1980), *Engineering Fracture Mechanics*, Vol.13, pp.293-306.

[110] R. C. McClung, (1992), In: *Theoretical Concepts and Numerical Analysis of Fatigue*, (Edited by A. F. Blom and C. J. Beevers), University of Birmingham, UK, pp.153-171.

[111] C. Bathias and R. M. Pelloux, (1973), *Metall. Trans.,* Vol.4, pp.1265-1273.

[112] M. A. Miner, (9145), *J. of Applied Mechanics*, Vol.67, pp.A159-A164.

[113] E. Gassner and W. Schutz, (1969), *Fatigue Design Procedures* (eds. E. Gassner and W. Schutz), Pergamon, pp.291-307.

[114] J. Schijve, (1970), *NLR MP70012,* Amsterdam.

[115] J. Schijve, (1971), *6th ICAF Symp.,* Miami, USA.

[116] P. C. Paris, (1960), *Ph. D. Thesis*, Bethlehem: Lehigh University.

[117] J. M. Barsom, (1976), *ASTM STP595*, American Society for Testing and Materials, pp.217-35.

[118] J. Schijve, (1973), *Engineering Fracture Mechanics*, Vol.5, pp269-80.

[119] W. Elber, (1976), *ASTM STP595*, American Society for Testing and Materials, pp.236-50.

[120] J. C. Newman, Jr., (1995), *J. of Engineering Materials and Technology, Transactions of ASME*, Vol.117, pp.433-39.

[121] M. Kikukawa, M. Jono, Y.Kondo, and S. Mikami, (1982), *Trans. Japan Soc. Mech. Engrs.*, Vol.48, pp.1496-504.

[122] M. Jono, J. Song, and M. Kikukawa, (1984), *Proc. ICM,* Vol.6, pp.1735-42.

[123] Chung-Youb Kim and Ji-Ho Song, (1994), *Engineering Fracture Mechanics*, Vol.49, pp.105-20.

[124] R. Sunder, (1992), *ASTM STP1122*, American Society for Testing and Materials, pp.161-75.

[125] B. Budiansky and J. W. Hutchinson, (1978), *J. of Applied Mechanics*, Vol.45, pp.267-76.

[126] K. K. Lo, (1980), *J. of Applied Mechanics*, Vol.47, pp.811-815.

[127] Steven G. Russell, (1989), *Engineering Fracture Mechanics*, Vol.33, pp.839-854.

[128] A. U. De Koning, (1981), *ASTM STP743*, American Society for Testing and Materials, pp.63-85.

[129] J. C. Newman, Jr., (1983), *AGARD CP-328* (ed. H. Zocher), pp.6.1-6.26.

[130] J. C. Newman, Jr., (1992), *NASA TM 104159.*

[131] J. C. Newman, Jr., (1999), *NASA TM 209133.*

[132] H. D. Dill and C. R. Saff, (1976), *ASTM STP595*, American Society for Testing and Materials, pp.306-319.

[133] H. Furing and T. Seeger, (1979), *ASTM STP677*, American Society for Testing and Materials, pp.144-167.

[134] A. Blom, G. Wang, and R. G. Chermahini, (1990), *Localised Damage: Computer-aided Assessment and Control*, M. H. Aliabadi et al Eds., Computational Mechanics Publications, Springer-Verlag, Berlin, pp.57-68.

[135] S. R. Daniewicz, J. A. Collins, and D. R. Houser, (1994), *Int. J. of Fatigue,* Vol.16, pp.123-133

[136] D. -H. Chen and H. Nisitani, (1988), *JSME Int. J., Ser 1,* Vol.31, pp.598-605.

[137] D. -H. Chen and H. Nisitani, (1991), *Engineering Fracture Mechanics,* Vol.39, pp.287-298.

[138] D. Nowell, (1998), *Fatigue & Fracture of Engineering Materials & Structures,* Vol.21, pp.857-871.

[139] C. Atkinson and M. F. Kanninen, (1977), *Int. J. of Fracture,* Vol.13, pp.151-163.

[140] E. A. Starke, Jr., *Treatise on Materials Science and Technology*, Vol.31, pp.35-63.

[141] E. A. Starke, Jr. and J. T. Staley, (1996), *Proc. Aerospace Sci.*, Vol.32, pp.131-172.

[142] M. J. Starink, P. Wang, I. Sinclair, and P. J. Gregson, (1999), *Acta Metallurgica,* Vol.47, pp.3841-3853.

[143] S. P. Ringer, S. K. Caraher, and I. j. Polmear, (1998), *Scripta Mater.*, Vol.39, p.1559.

[144] S. P. Ringer, K. Hono, K. I. J. Polmear, and T. Sakurai, (1996), *Appl. Surf. Sci.,* Vol.94/95, p.253.

[145] P. Gomiero, F. Livet, Y. Brechet, and F. Louchet, (1992), *Acta Metall. Mater.*, Vol.40, p.847.

[146] H. C. Shih, N. J. Ho, and J. C. Huang, (1996), *Metall. Mater. Trans. A,* Vol.27, p.2479.

[147] P. J. Gregson, *Aluminium Alloys*, Chapter 2, pp.49-84.

[148] G. T. Hahn and R. Simon, (1973), *Eng. Fract. Mech.*, Vol.5, p.523.

[149] T. J. Warner, R. A. Shahani, P. Lassince and G. M. Raynaud, (1998), Research report of Pechiney.

[150] I. J. Polmear, (1995), *Light Alloys, Metallurgy of the Light Metals*, 3rd Edition, (Eds. Robert Honeycombe and Peter Hancock), Published by Arnold, a division of Hodder Headline PLC., p.92.

[151] J. T. Staley, (1975), *ASTM STP 605*, American Society for Testing and Materials, p.71.

[152] W. E. Quist, (1963), *M. Sc. Thesis*, University of Washington.

[153] R. K. Smith, (1991), In: *Milestones of Aviation* (ed. J. T. Greenwood), Crescent Books, New York, pp.222-296.

[154] R. H. Van Stone and J. A. Psioda, (1975), *Met. Trans.*, A6A, pp.668-670.

[155] G. Lutjering, H. Doker, and D. Munz, (1973), In: *Proc. 3rd Conf. On Struct. Metals*, Cambridge.

[156] J. T. Staley, (1976), *ASTM STP 605,* American Society for Testing and Materials, pp.71-103.

[157] I. Sinclair and P. J. Gregson, (1998), *Oxford-Kobe Materials Seminar on Aerospace Materials*, 22-25 Sept. 1998.

[158] E. A. Starke, Jr. and G. Lutjering, (1979), In: *Fatigue and Microstructure*, American Society for Metals, Metals Park, pp.205-243.

[159] K. T. Venkateswara Rao and R. O. Ritchie, (1988), *Acta Metall.,* Vol.36, pp.2849-2862.

[160] X. Su, J. M. Larsen, and J. R. Jira, (1990), "*Fatigue 90",* pp.1049-1054.

[161] R. Hermann and D. L. Bartlett, (1993), "*Fatigue 93*", pp.1855-1861.

[162] G. R. Chanani, G. V. Scarich, P. E. Bretz, and A. A. Sheinker, (1984), *ICF6.*

[163] W. G. Truckner, J. T. Staley, R. J. Bucci, and A. B. Thakker, (1976), U.S. *Air Force Materials Laboratory Report AFML-TR-76-169.*

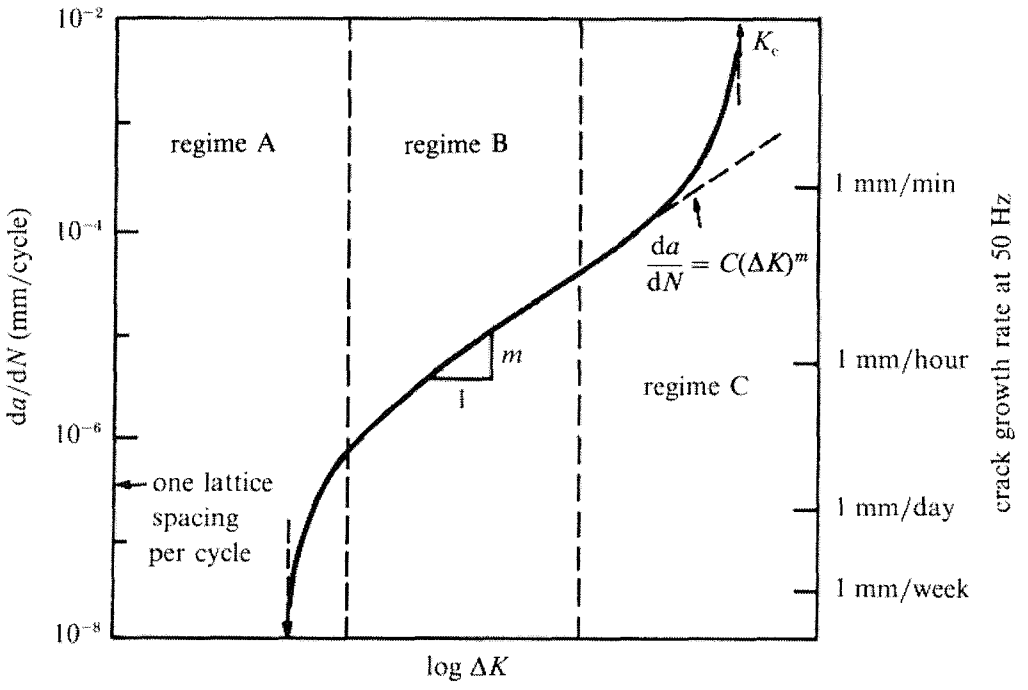

Figure 2.1 *Schematic illustration of the different regimes of stable fatigue crack propagation [6].*

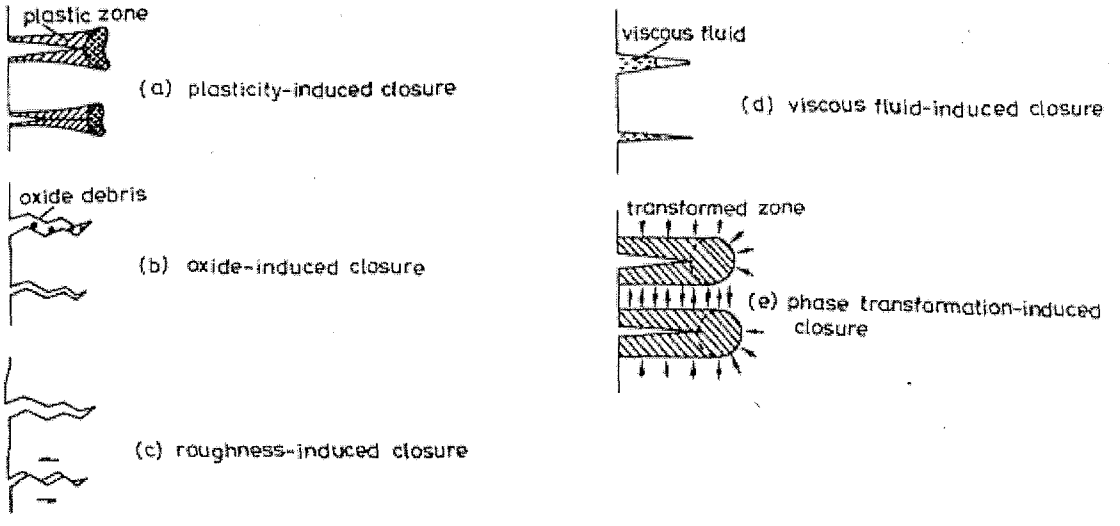

Figure 2.2 *Basic closure mechanisms [31].*

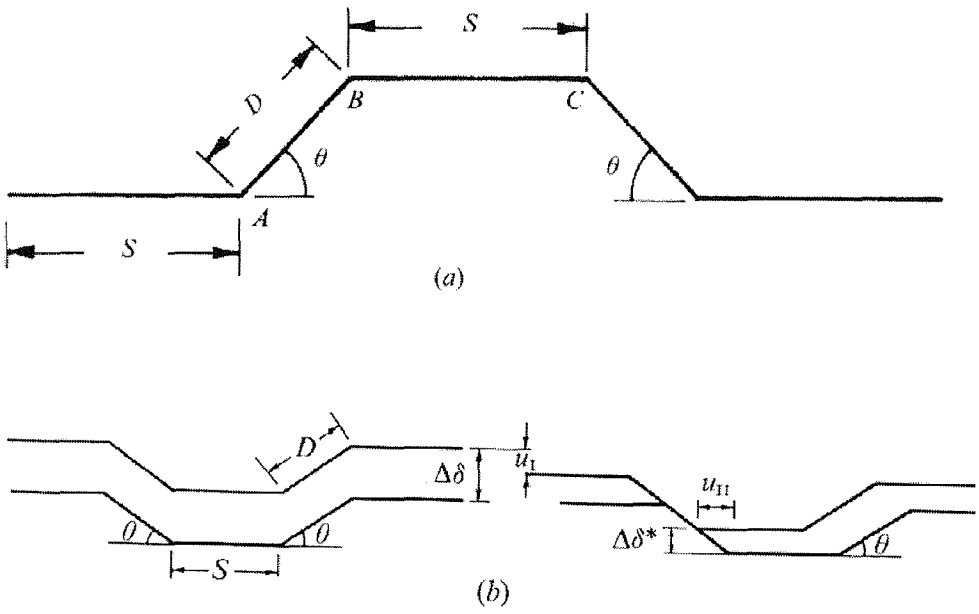

Figure 2.3 *(a) Idealisation of a segment of a deflected crack with periodic tilts, (b) Schematic representation of a deflected crack in the fully opened condition at the peak load of the fatigue cycle (on the left) and relative mismatch between the crack faces leading to premature crack closure during unloading (on the right)[6].*

3. MATERIALS AND EXPERIMENTS

— *This chapter presents the microstructural features and general mechanical properties of the two high strength heat-treatable airframe aluminium alloys tested: AA2024-T351 & AA2024A-T351. The experimental techniques employed in the project are also described.*

3.1. Materials

Two high strength heat-treatable airframe aluminium alloys, *AA2024-T351,* and its advanced variant *AA2024A-T351*, were supplied by Pechiney Centre de Research de Voreppe as 40*mm* thick plates. All work reported here was carried out on the materials from the central part (*t/2*) of the plates. Table 3.1 shows the contents (in wt%) of the major alloying elements for the materials supplied. The reduced *Mn, Fe*, and *Si* contents are as expected for the *2024A*, however, the *Cu* content is relatively high for this batch (specified *Cu* range for 2024A is ~3.7-4.5 wt%).

Table 3.1 Compositions (wt%) of the major elements in Pechiney 2024- & 2024A-T351.

Alloy	*Si*	*Fe*	*Cu*	*Mn*	*Mg*
2024	0.121	0.203	4.065	0.537	1.360
2024A	0.049	0.160	4.510	0.330	1.440

Grain structures were revealed by etching with Keller's reagent (see Figure 3.1), with Table 3.2 showing the measured mean linear intercept grain dimensions. It may be seen that the grain structure of the 2024A is coarser than the 2024 by a factor of approximately 2, with the mean of the *L, T* and *S* dimensions corresponding to 163μm and 328μm for the 2024 and 2024A respectively.

Given the difficulties associated with transmission electron microscopy (*TEM*) imaging of the strengthening precipitates in such naturally aged alloys, differential scanning calorimetry (*DSC*) measurements were used to quantify the *GP(B)* contents of the alloys. Figure 3.2 shows the *DSC* curves for 2024- and 2024A-T351. Baseline and heat capacity corrections were carried out before the interpretation of the *DSC* results.

During the heating process, *GP(B)* dissolution took place from 150°C to 250°C. There was little difference in the *GPB* dissolution for these two materials, indicating that their respective *GP(B)* contents were identical (to the resolution of this method at least). The only obvious difference in these two *DSC* curves occurred at high temperature (505°C) where incipient melting took place, with 2024A exhibiting a stronger peak than 2024. This may be linked to the liquation of *Cu* containing phases in the quaternary *Al-Cu-Mg-Mn* phase diagram [1] associated with the higher *Cu* content of this particular 2024A-T351.

Table 3.2 Mean linear intercept grain dimensions (λ_L, λ_T, and λ_S, corresponding to the L, T, and S directions, respectively), taken at the t/2 plate position.

Materials	λ_L (μm)	λ_T (μm)	λ_S (μm)
2024-T351	312	121	57
2024A-T351	690	216	78

A high-resolution field emission gun *SEM (FEG-SEM)* in back-scattered mode was used to image the *Mn* containing dispersoids. A similar elongated particle morphology was seen in both alloys, as shown in Figure 3.3. However, marked variations in local dispersoid distribution were evident in both alloys, making it difficult to quantify the difference of dispersoids in the materials, though it is of course clear from the associated compositions that the total dispersoid content in 2024A will be lower due to the lower *Mn* content of the alloy. The heterogeneity in dispersoid distribution is attributable to solute segregation on casting [2]. Measurements from representative images show that the nearest separation of dispersoids in the *L-T* plane of these materials is of the order of $0.5\mu m$, based on $\Delta_2 = 1/\left(2\sqrt{N_a}\right)$ (where Δ_2 is the nearest separation and N_a is the dispersoid number per unit area) for random point distributions, whilst mean free paths (in two dimensions) between dispersoids is of the order of $3 - 4\mu m$.

The area fraction, length, breadth, and aspect ratios of constituent phases in both 2024- and 2024A-T351 were characterised by digital image analysis by optical microscopy (using a high-resolution digital camera for image acquisition). To obtain representative

area fraction values of the constituent particles, area fractions for each material were measured from 18 random sites for each of the three surface orientations (*i.e. L-T, L-S, & T-S*). Results in Table 3.3 show that area measurements for the three orientations were reasonably consistent, with 2024A having a slightly higher constituent content, contrary to the basic design of this alloy [3]. The higher constituent level in 2024A may be attributed to the relatively high *Cu* content in this particular batch of 2024A (*i.e.* coarse *S* and/or θ phase may be expected to be present [3]).

Table 3.3 Constituent particle area fraction (%) results.

Materials	*L-T*	*L-S*	*T-S*	All Data
2024-T351	3.0±0.15	2.6±0.11	2.7±0.07	2.8±0.08
2024A-T351	3.2±0.06	3.2±0.11	3.3±0.24	3.2±0.09

Different areas on the specimen surfaces were selected to identify the existing constituents. Constituent length, breadth, and aspect ratios were measured and averaged from over 1000 particles at a magnification of 500x for each material in the *L-T* orientation (see Table 3.4). Overlapping particles were separated manually whenever possible. Figures 3.4 (a) & (b) show representative constituent particles of both alloys. Since there are several types of constituents and each of them has its own characteristic size, results in Table 3.4 represent only a broad average of all the particles in the materials, which is only marginally smaller for the 2024A, compared to the 2024.

Table 3.4 Constituent particle length, breadth, and aspect ratios.

Materials	Length *(μm)*	Breadth *(μm)*	Aspect Ratio
2024-T351	2.9	1.9	1.5
2024A-T351	2.5	1.6	1.6

Chemical compositions of various constituents in the materials were analysed using *SEM* & energy dispersive spectroscopy (*EDS*). Carefully polished flat specimen surfaces were used for the *EDS* analyses, with a final finish of 0.25μm. *EDS* analyses of the two alloys showed that large (~5μm long) *S* phase particles and *Cu-Fe-Mn* rich agglomerates made up the majority of the constituent population in both materials. The

S particles were generally rounded, with aspect ratios < 1.5 (compositions were measured as around *Cu*-46%wt% and *Mg*-16wt%). The *Cu-Fe-Mn* rich clusters were made up of individual particles of ~ 0.1 μm diameter, with overall compositions being measured as around *Cu*-35wt%, *Fe*-11wt% and *Mn*-2.5wt% (rem. *Al*). In the 2024 these clusters were distinctly compact compared to those in the 2024A. Based on known common constituent phases in 2024-type materials, these clusters may be identified in the first instance as a mixture of $Al_7Cu_2Fe + Al_{20}Cu_2Mn_3$, with Al_7Cu_2Fe in the majority. In the 2024 plate, minor constituents were identified as *Fe-Cu-Mn-Si* rich clusters (compositions measured as around *Cu*-13wt%, *Fe*-16wt%, *Mn*-10wt% and *Si*-4wt%) and occasional 1-2μm *Si*-rich particles. In the 2024A distinct *Cu-Fe-Mn* rich rod shaped particles were seen (aspect ratios >5, lengths 2-5μm); these exhibited similar composition measurements to the *Cu-Fe-Mn* rich clusters noted above. Some essentially binary *Al-Cu* particles were seen at the boundaries of other phases in the 2024A.

3.2. Monotonic Tensile Testing

Static mechanic properties in both longitudinal and transverse directions were measured according to *ASTM E8M-96* [4]. The cross-head speed of the machine was set at 1*mm/min*. Both strain and load calibrations were carried out before the test. Multiple specimens were used for each material in each tensile direction and the test results were averaged. Elongation was based on a 25*mm* gage length. Figure 3.5 shows the typical monotonic tensile $\sigma \sim \varepsilon$ curves of the alloys in the longitudinal direction. Test results for the two materials are listed in Table 3.5, showing that 2024A has a generally lower yield strength and ultimate tensile strength in the longitudinal direction compared to the 2024.

Table 3.5 Monotonic tensile test results.

Material	Tensile direction	$\sigma_{ys}(0.2\%)$ *(MPa)*	σ_{UTS} *(MPa)*	$\delta(\%)$
2024-T351	L-direction	372	483	21.4
2024-T351	T-direction	313	474	17.6
2024A-T351	L-direction	345	434	25.2
2024A-T351	T-direction	312	449	13.4

3.3. Cyclic Stress-Strain Testing

The multiple-step test (*MST*) method was used to determine cyclic stress-strain curves of the two alloys. A zero backlash rig was specifically designed and made for these tests. In the multiple-step test, a single specimen is tested at a number of different alternating plastic strains. First, a specimen is cycled between constant strain limits until a fully saturated loop is obtained. Then, the strain limits are increased, and cycling continues until another fully saturated loop is obtained. The cyclic stress-strain curve is the locus of the apexes of the saturated loops. Both alloys saturate quite quickly (by about fifty cycles) for the total strain range tested (from 0.1% to 2%). As such, constant total strain limits were used in the test due to the fact that the differences between total and plastic strain limit tests are usually small when materials behave in this manner [5]. Figure 3.6 shows the cyclic stress-strain curves of 2024- & 2024A-T351 tested in the longitudinal direction. Monotonic and cyclic hardening test results are listed in Table 3.6, showing a marginally greater extent of cyclic strain hardening in 2024A compared to 2024, whilst a slight decrease in monotonic work hardening exponent was seen in the 2024A.

Table 3.6 Cyclic tensile testing results of 2024- & 2024A-T351.

Alloys	$(\sigma_y)_c$ *(MPa)*	$(\sigma_y)_m$ *(MPa)*	n_c	n_m
2024-T351	408	372	0.18	0.10
2024A-T351	366	345	0.20	0.085

3.4. Fatigue Crack Growth Testing

Figure 3.7 shows the fatigue test set-up. Centre-cracked tension (*CCT*) specimens of 2024-T351 and 2024A-T351 were tested at stress ratios (R) of 0.1 and 0.7 according to *ASTM Standard E647* [6]. All specimens were machined from the plate mid-section ($t/2$) in the *L-T* orientation. The width of the *CCT* specimen was 150*mm*, with a gauge length of about 300*mm* and thickness of 12*mm* for thick samples and 2*mm* for thin samples. Side grooved thick *CCT* specimens, with side-grooving to a depth of 1*mm*

and an internal angle of 30° on both faces of the specimen, were used to evaluate stress state effects on crack growth and closure in both alloys [7]. Step load shedding methods were used to obtain baseline $da/dN \sim \Delta K$ curves for the two materials. The reduction in P_{max} (with fixed stress ratio) of adjacent load steps was about 9% of the previous P_{max}. Upon adjustment of maximum load from P_{max1} to a lower value, P_{max2}, a minimum crack extension of 0.50*mm* or 5 times the previous monotonic plastic zone size was used (whichever is greater), to enable a steady state growth rate to be established. The two-probe potential drop (*PD*) technique was used to monitor crack length and control the *CA* fatigue loading tests automatically (see Chapter 5). Single overload tests were carried out under different baseline ΔK levels as well as different overload ratios (see Chapter 6). A four-probe *PD* system was used in single overload tests to monitor the physical crack length increments more accurately. Four strain gauges (two on each face of the specimen at symmetrical positions) were used to obtain good alignment of the test machine. Near-tip strain gauges and a conventional crack mouth clip gauge were used to record local and global compliance curves which are later used to define crack closure points. Detailed information on closure measurements is given in Chapter 4. Features of the fatigue surfaces under low, intermediate, and high ΔK levels were studied in an *SEM* (see Chapters 5 & 6). Three-dimensional reconstruction of fracture surfaces in the two alloys were made via Talysurf Profilometry (see Chapters 5 & 7).

3.5. Summary

1. Microstructures of the Pechiney 2024- & 2024A-T351 materials have been quantified. The supplied 2024A-T351 exhibits twice the grain size of the 2024-T351. *GPB* contents are equivalent in both alloys based on the *DSC* results. Elongated *Mn* contained dispersoids were detected in both alloys, although there was difficulty in quantifying the material differences due to the marked local variations in dispersoid distributions. Area fractions and the average sizes of the coarse intermetallic particles in these two alloys are similar based on optical image analysis results.

2. Static tensile properties of both alloys were determined. Lower yield strength in the longitudinal direction and generally lower ultimate tensile strengths were found in the 2024A-T351. Cyclic tensile test results show that 2024A has a marginally higher cyclic strain hardening exponent than 2024.

References

[1] L. F. Mondolfo, (1976), *Aluminium Alloys*, Butterworth & Co Ltd, London.

[2] T. J. Warner, (1999), private communication with T. J. Warner, Pechiney, France.

[3] T. J. Warner, R. A. Shahani, P. Lassince and G. M. Raynaud, (1998), *Pechiney Report,* Pechiney: CRV, France.

[4] Annual Book of ASTM Standards, (1996), Vol.03.01, *ASTM E8M*, pp.76-96.

[5] A. C. Pickard and J. F. Knott, (1988), *ASTM STP 942*, pp.58-76.

[6] Annual Book of ASTM Standards, (1996), Vol.03.01, *ASTM E647-95a*, pp.565-601.

[7] J. P. Hess, A. F. Grandt Jr. and A. Dumanis, (1983), *Fatigue & Fracture of Engineering Materials & Structures,* Vol.6, pp.189-199.

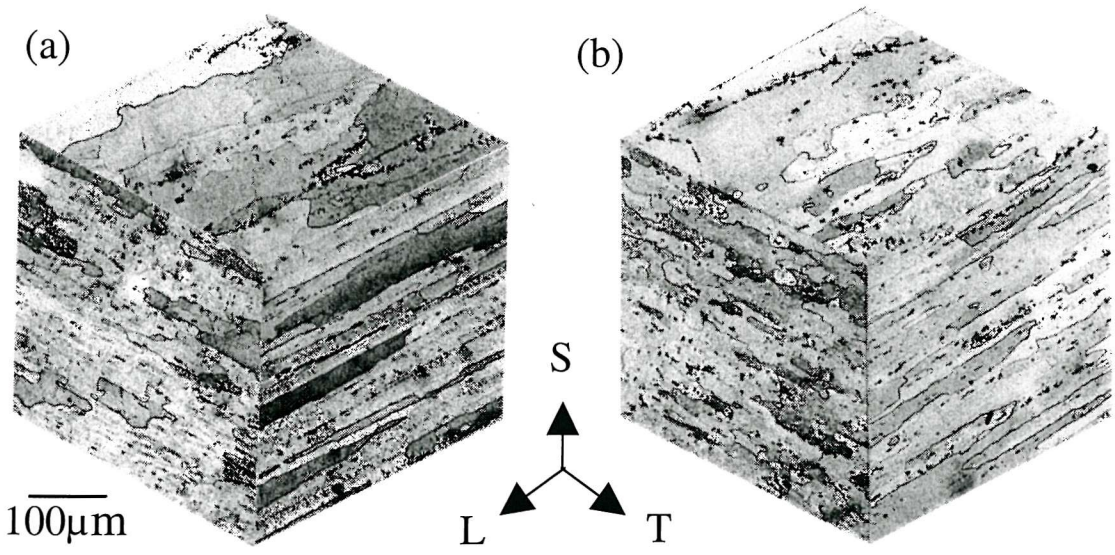

Figure 3.1 *Grain structures of: (a) 2024A-T351, and (b) 2024-T351.*

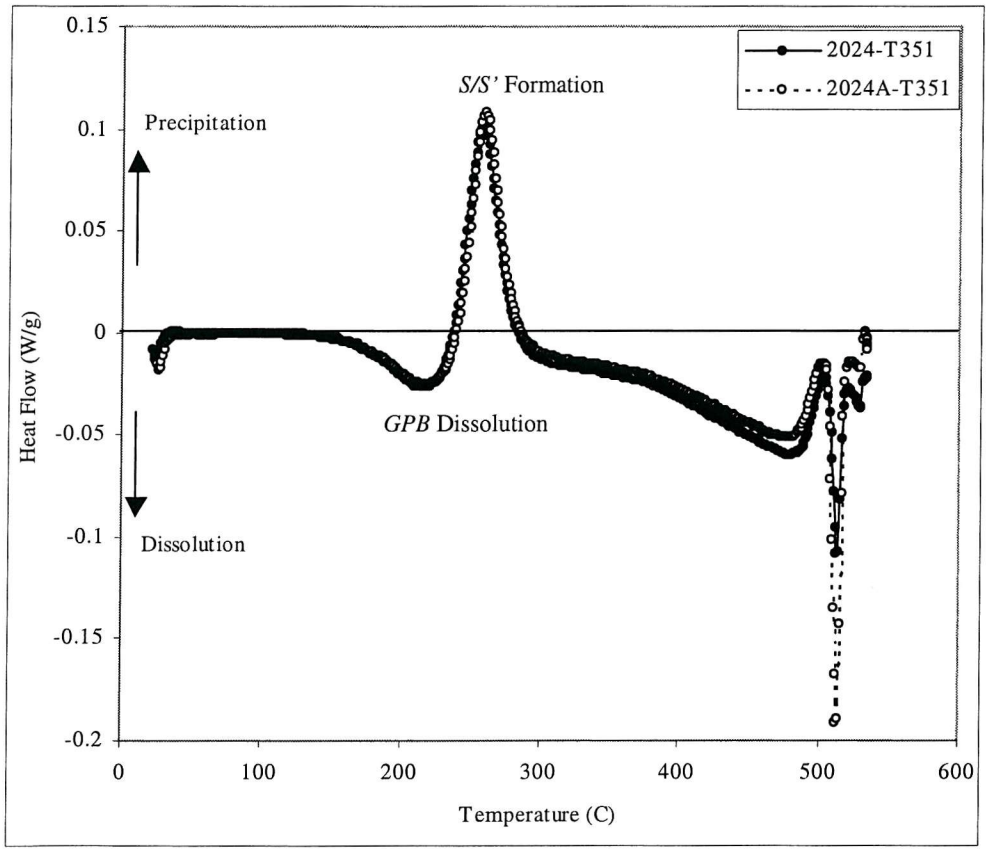

Figure 3.2 *DSC thermograms for 2024- & 2024A-T351.*

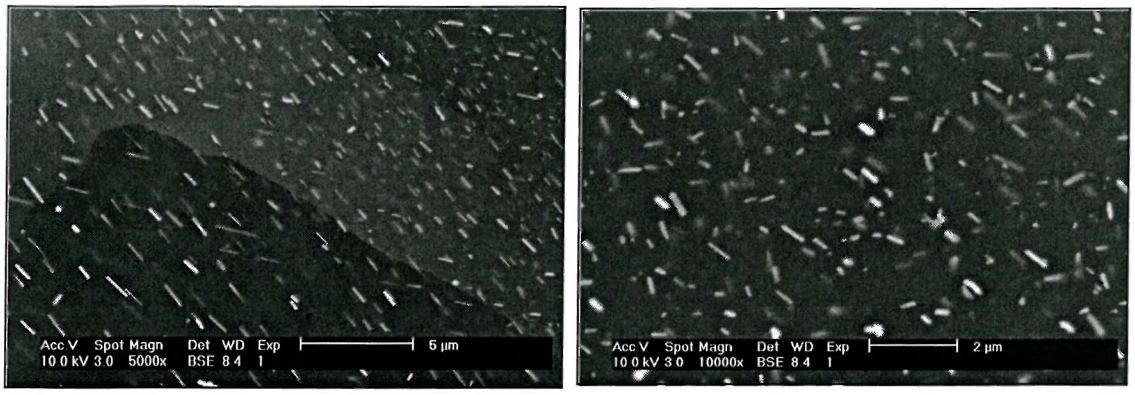

•2024-T351

•2024A-T351

Figure 3.3 *Dispersoid morphology (FEG-SEM) in 2024- & 2024A-T351 (back scattered electron images).*

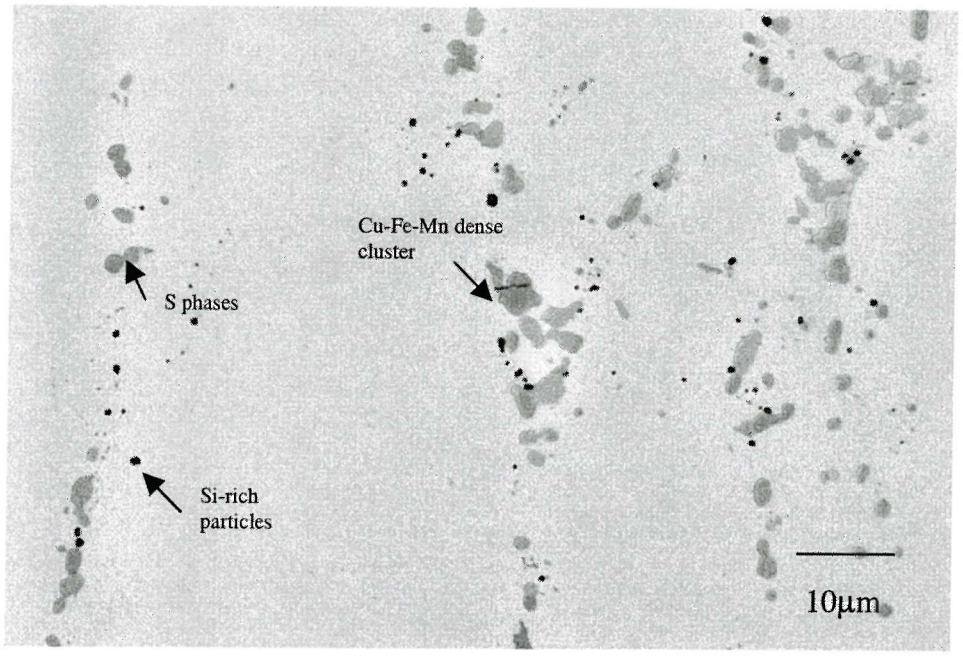

(a)

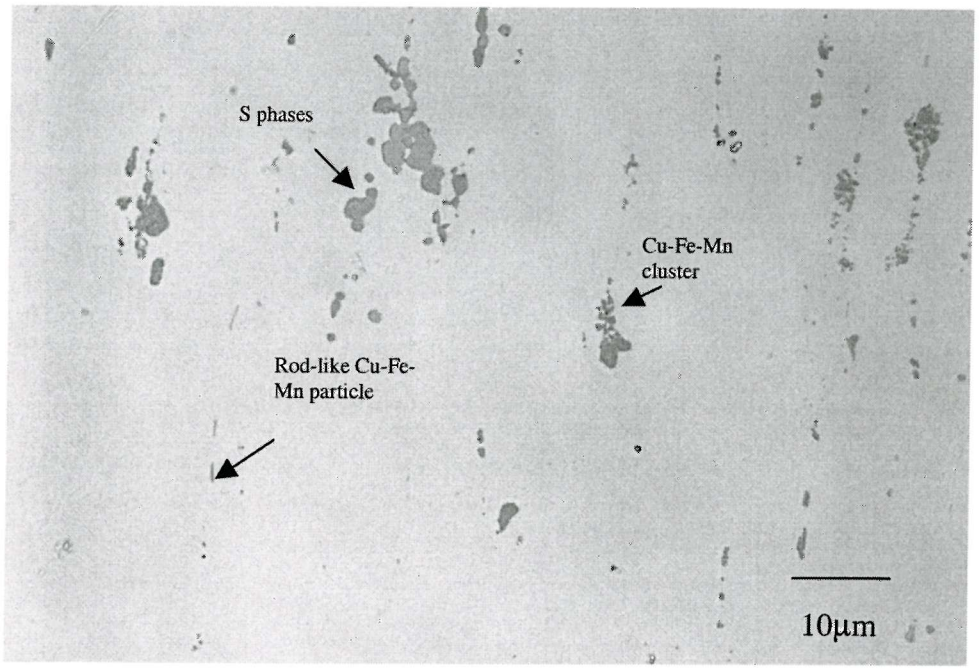

(b)

Figure 3.4 Representative constituents in (a) 2024-T351 and (b) 2024A-T351.

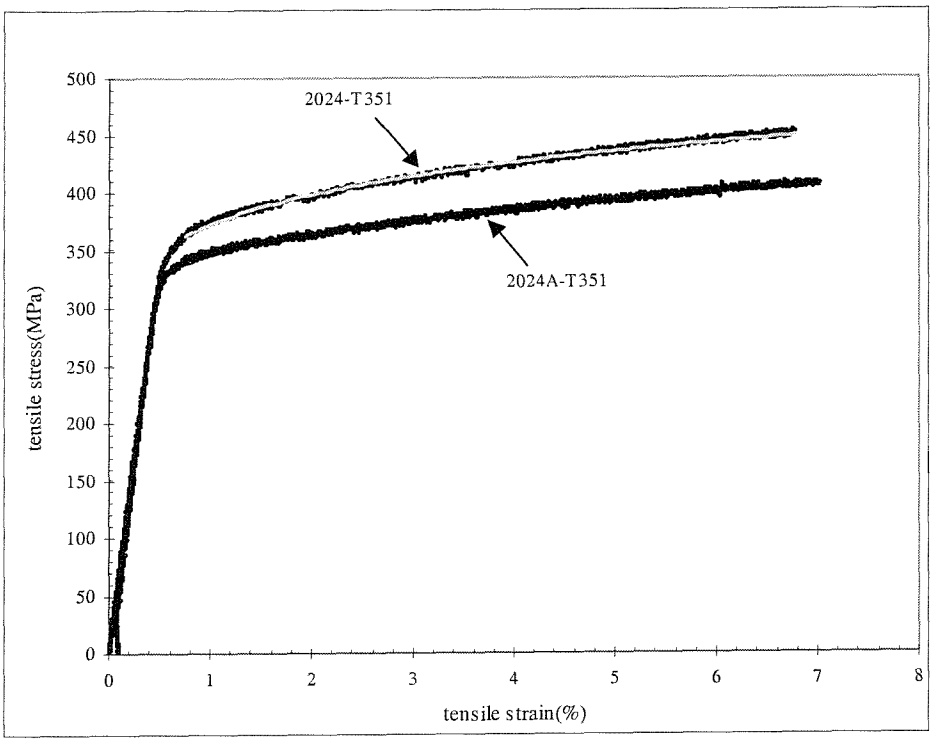

Figure 3.5 *Monotonic tensile σ ~ ε curves for 2024- & 2024A-T351 in the longitudinal direction.*

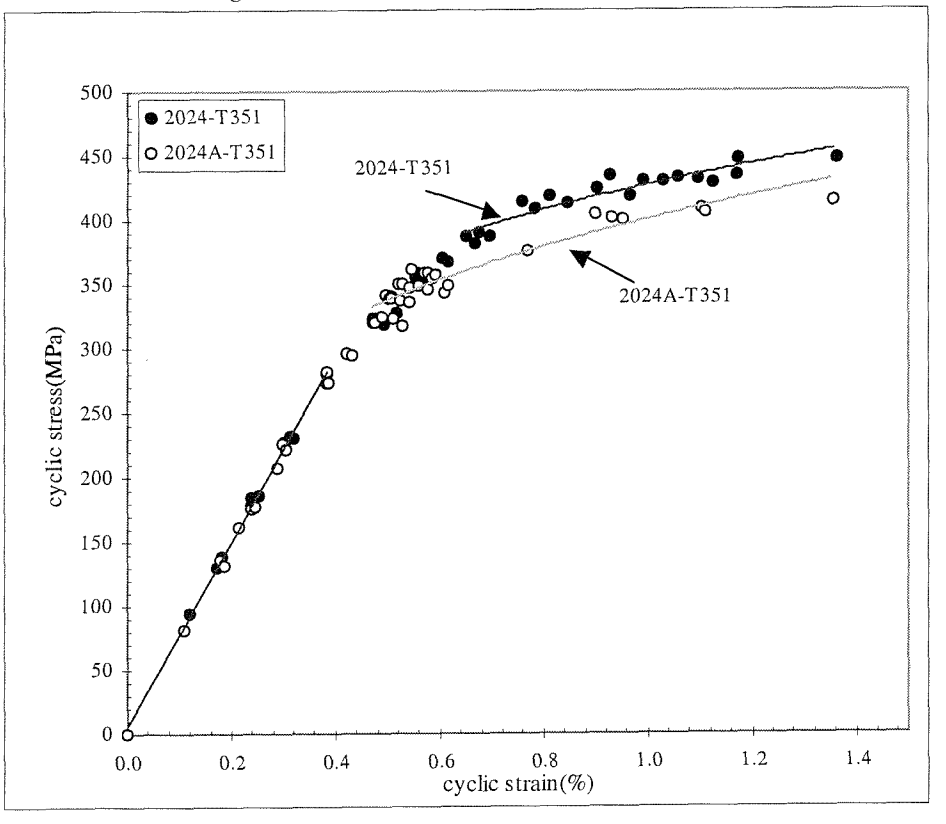

Figure 3.6 *Cyclic σ ~ ε curves for 2024- & 2024A-T351 in the longitudinal direction.*

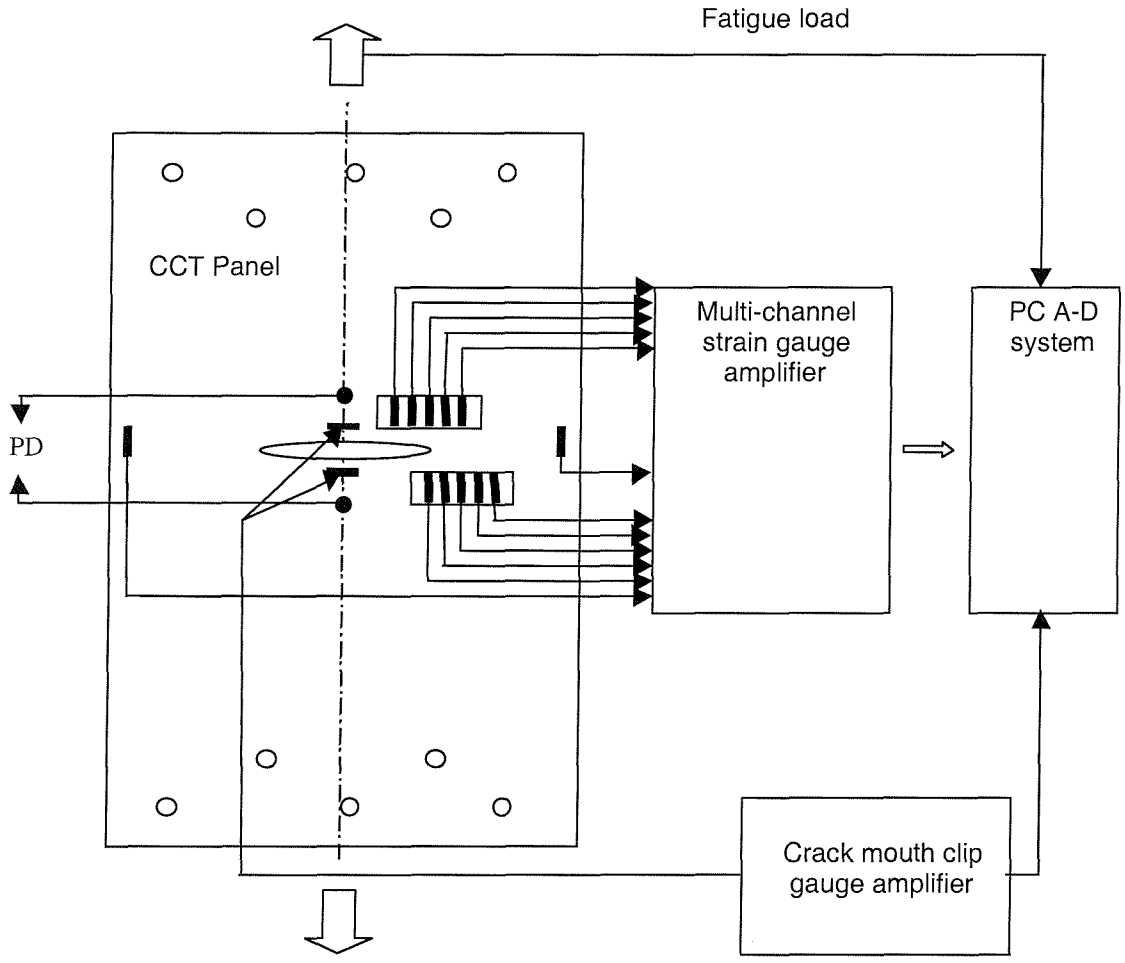

Figure 3.7 Schematic diagram of the fatigue test set-up.

4. SYSTEMATIC ASSESSMENT AND VALIDATION OF COMPLIANCE-BASED CRACK CLOSURE MEASUREMENTS

— *The following chapter describes a specific detailed study of closure measurement methods, with a view to providing a sound experimental basis for subsequent work.*

4.1. Introduction

Closure determination methods within the literature fall into a variety of categories (see Chapter 2). Among them, mechanical compliance measurements are the most widely used methods in detecting crack closure. Closure loads are associated with the initial deviation from the linearity in a given compliance curve when unloading, with Figure 4.1 illustrating the variety of methods used to obtain mechanical compliance data. Being based on specimen deformation, such measurements may be expected to be directly related to load take-up in the crack wake. Global mechanical compliance curves can be obtained from crack mouth clip gauges and back face strain gauges (*BFS*). Near-tip strain gauges can give local mechanical compliance curves, which may be used to identify local closure levels. The push-rod compliance gauge developed by Fleck *et al.* [1] has been used for three-dimensional crack closure measurements.

Detailed evaluation of current closure measurements is given in Chapter 2. Overall it is clear that the identification and interpretation of P_{cl} remains debatable at the moment. Closure concepts are, however, a critical aspect of crack growth understanding, forming the key element of important contemporary fatigue lifing models such as *FASTRAN II* [2]. In the absence of consensus on crack closure assessment, this chapter reports a detailed analysis of crack closure effects in commercial *Al* airframe material, focusing on more reliable interpretation of essentially standard mechanical compliance measurements.

4.2. Closure Measurements

To obtain detailed crack closure information, a crack mouth clip gauge was used to obtain conventional compliance curves (and thus '*global*' closure information), along with arrays of near-tip strain gauges with a spacing of *2mm* (along the crack growth direction) to obtain local crack closure levels. A gap of *1mm* was set between the edge of the strain gauges and the crack plane to avoid the influence of plastic deformation (plane stress plastic zone sizes for the highest K levels tested here corresponded to *~0.4mm*). Gauge position effects ahead of and behind the crack tip (along the crack growth direction) were studied by sampling several strain gauges simultaneously. Finally, replicas were made during the load cycle in *10%* decrements of P_{max} from the peak load for different ΔK levels and studied in the *SEM*.

A computer-based data acquisition system was set up to obtain 600 load ~ displacement data pairs during each unloading cycle. Three basic approaches were used to detect the closure point from the corresponding compliance curves: (i) visual subjective observation, (ii) slope variation analysis, and (iii) curve fitting.

4.2.1. Visual Observations

Two methods were used in the visual determination of closure points:

(a) Direct observation, where closure points were identified by deviation from linearity in the unprocessed unloading compliance curves (Figure 4.2(a)). A rough estimate of closure level is obtained, which is of course quite subjective. Curves were plotted to equivalent scales in all cases to provide a degree of consistency.

(b) Offset observation (Figure 4.2(b)), in which compliance curves were recorded as an offset value from a straight line fit to the upper part of the curves. The offset method (as recommended by *ASTM E647* [3]) may improve the sensitivity to the non-linearity of the compliance curves, however, it is still subjective in identifying the closure point, and there is a degree of uncertainty in selecting the upper portion of the curve for the linear fit [4].

4.2.2. Slope Variations

Closure points were determined non-subjectively via variations in the local slope of the compliance curves [5], see Figure 4.3. Three methods (for corresponding *Matlab* programs see *Appendixes A-C*) were used in this case:

(a) Slope variation 1: starting from the upper part of the compliance curve, the closure point was defined when the local slope, m_{local}, differed from the slope m_o from the upper part of the compliance curve by a certain amount (*5%* in this case). m_{local} was obtained by a linear fit of the local data segment (50 data points, which was about *8 ~ 10%* of the total curve in the present study) around the assumed closure point. m_o was obtained from a linear fit of the top of the compliance curve to the assumed closure point.

(b) Slope variation 2: the compliance curve was divided into segments of equal length (50 data points again). The closure point was defined when the slope difference between adjacent segments first exceeded a pre-set limit (also *5%*).

(c) Slope variation 3: the closure point was determined in a similar way to slope variation 1 except that the length of the upper part for m_o was set to *150* data points (*~25%* of the total curve) from the top of the compliance curve regardless of the presumed closure point, *i.e.* similar to the principle used in the second round robin study of *ASTM Task group E24.04.04* [6].

4.2.3. Curve Fitting

As an alternative to local slope calculation, 'global' curve fitting may be used (see Figure 4.4). Two methods (corresponding *Matlab* programs see *Appendix D*) were considered in this study:

(a) Curve fitting 1: compliance curves are divided into a linear part (upper part) and a second order polynomial curve (lower part) about the assumed closure point along the curve. The closure point is obtained when the absolute difference in co-ordinates between the straight line and the second order polynomial sections at this point reaches a minimum.

(b) Curve fitting 2: the closure point was defined when the difference between the slopes of the straight line and the second order polynomial sections at this point reaches a minimum.

4.3. Results and Discussions

Given the confusion that exists in closure measurement methodologies, it is critical that a consistent and reliable method is identified and verified. Figure 4.5 shows a typical set of compliance curves from the crack mouth clip gauge and strain gauges located near the crack tip for a given ΔK level. Closure transitions are reasonably apparent in all three curves. Near-tip wedging due to crack closure is apparent from the gradient changes for gauges ahead of and behind the crack tip. The decrease rate of the strain of the strain gauge ahead of the crack tip during unloading becomes smaller when crack closure occurs (Figure 4.5 (a)), which is due to the wedge open effect. Greater strain decrease rates were however observed for the strain gauge behind the crack tip (Figure 4.5 (b)), which was caused by the premature crack surface contact. Figure 4.6 shows the offset compliance curves based on the data in Figure 4.5. Closure results derived from the various methods in section 4.2 are shown in Figures 4.7-11 for the full range of stress intensity levels tested.

Figure 4.7 shows closure results from the crack mouth clip gauge using the visual, slope variation and curve fitting methods. Reasonable agreement was seen between the two visual subjective methods, with the offset method giving slightly higher closure levels at higher ΔK levels in particular. The results agree reasonably well with data reported by Yu and Ritchie [7] for *2124-T351* using back face strain gauges on compact tension samples. Closure results given by the slope variation methods are somewhat lower than those from the other two approaches. The difference is affected by the relative strain gauge position to the crack tip. Different slope variation methods also yield somewhat different results. Since this approach detects only local changes in compliance, very gradual initial changes in compliance slope may be missed for any given variation limit. In this case closure points were not detected via slope variation method 2 in certain

cases due to the shape of the crack mouth compliance curves. Both curve fit methods gave relatively high closure levels which are quite stable and consistent for both fitting methods.

Figure 4.8 shows closure results from strain gauges just at the crack tip. Reasonably consistent trendlines are again observed in the visual observation results, with the offset method exhibiting consistently higher closure levels (particularly at higher stress intensity levels). Closure levels for the near-tip strain gauge data are higher than those using the crack mouth clip gauge (particularly for the offset results). Closure results from the slope variation methods are again found to be sensitive to the different methods used. The results are relatively low compared to the other two approaches, but are increased in relation to equivalent crack mouth data. The near-tip strain gauge curve fit results are again quite consistent for both fitting methods, and are very close to the curve fitting data obtained from the clip gauge data in Figure 4.7.

Figure 4.9 shows closure results from strain gauges 1*mm* behind the crack tip. Whilst reasonable general trends are evident, these results show the visual assessment of near-tip behaviour to be sensitive to the positions of the strain gauges. The slope variation results in Figure 4.9 show similar features to Figure 4.8, although significant shifts in closure trends are evident for the individual versions of this method. Curve fit closure results are again stable and reasonably consistent with the previous results in Figures 4.7-8.

Figure 4.10 shows closure results from strain gauges 1*mm* ahead of the crack tip. Both the direct and offset observation results agree well with those taken at the crack tip. The slope variation results shown in Figure 4.10 appear more linear than those taken at the crack tip or 1*mm* behind the tip, particularly for slope variation methods 1 and 2. The results from curve fitting remain high with method 2 agreeing well with the previous results, although the results from curve fitting 1 diverge to an extent at higher ΔK levels. The closure results from strain gauges farther away from the crack tip were generally seen to be noisy and irrational, see Figure 4.11.

In establishing a closure measurement method, two criteria should be identified:

(a) The physical significance of the method, e.g. is the earliest onset of closure detected or may a build-up of loading occur throughout the specimen, and

(b) How experimentally consistent and convenient is the method.

The present results show a considerable range in closure levels at any given ΔK level, with K_{cl}/K_{max} commonly varying by ± 0.2. Such a range may arise from three sources:

(a) Variations in crack closure levels through the thickness of specimens, with surface plane stress effects being expected to dominate near-tip strain gauge results,

(b) Scatter in the raw physical data, and

(c) The sensitivity of the different non-linearity detection methods.

Figure 4.12 illustrates schematically the effect of stress state on closure measurements in a real three dimensional specimen. It is well established in the literature (*e.g.* [1,9-10]) that closure occurs earlier near the free surfaces of a specimen (*i.e.* under plane stress conditions), than at the centre (approaching plane strain conditions). In the three dimensional situation a two stage closure process must then occur, although the distinction between stages will be masked by the gradual transition between plane stress and plane strain conditions that occurs between a specimen surface and its centre. Depending on the thickness of the sample, some interaction between the surface and centre closure processes may also be expected as early fracture surface contact at the specimen surfaces will tend to wedge open the crack at the centre, lowering the closure load at the centre. An ideal closure measurement method will therefore be non-subjective in character and be physically understandable in terms of the processes shown in Figure 4.12.

Of the current closure results, the curve fit measurement methods may intuitively be expected to produce relatively high closure values, as the methods do not rely on achieving a set degree of non-linearity in the compliance data. This is seen in the results, particularly for the crack mouth clip gauge measurements. The physical relevance of such higher measured closure levels may be assessed against the replica

observations of the crack tip closing process, as shown in Figure 4.13 for an applied ΔK of 4.3 $MPa\sqrt{m}$. The first distinct incidence of surface contact in this case is seen on unloading to $0.8P_{max}$, with more extensive contact occurring on further unloading to $0.7P_{max}$. Given the apparent gradual build up of closure and the subjectivity of replica observations, specific closure values were not considered justifiable from such observations. Overall however, replicas consistently showed closure occurring at the highest levels indicated by the various compliance curve methods, *i.e.* the curve fitting methods applied to the crack mouth clip gauge, and the offset observation and curve fitting methods applied to the near-tip strain gauge data.

In terms of surface and bulk specimen effects on apparent closure point, the crack tip strain gauges are of course expected to be more generally sensitive to near-tip surface phenomena than the crack mouth compliance measurements, and hence give higher closure levels. The consistency of the curve fitting method between global (crack mouth clip gauge) and near-tip strain gauge results is then attributable to improved sensitivity of the curve fitting method to the onset of closure in the global compliance data, *i.e.* the curve fit closure results for the crack mouth clip gauge are reasonably sensitive to surface/plane stress closure processes. To illustrate this point, side-grooved specimens with $1mm$ deep sharp side-grooves introduced along the nominal crack growth plane on each face of the $12mm$ thick *CCT* specimens were investigated. It is expected that closure levels should drop as the plane stress regions at the specimen surface are effectively removed. This is indeed confirmed in the curve fitting closure data for the crack mouth clip gauge, as shown in Figure 4.14. It may then be seen that the application of curve fitting methods to crack mouth displacement data from plain and side-grooved samples provides an important potential for separating and quantifying surface and bulk contributions to closure and corresponding influences on crack growth behaviour. The importance of this is emphasised by absence of a side grooving effect on measured crack growth rate results (see details in Chapter 5). This is in itself quite consistent with the plane strain dominance expected for specimens at this thickness at the low load levels used [8]. Any closure measurement method that is based on a nominal '*average*' closure measurement must therefore carefully assess the nature of

this averaging and its relevance to the actual crack growth behaviour as detectable plane stress closure effects in the present study had no appreciable effect on crack growth. This situation may contribute significantly to the discrepancies in closure results and their interpretation that exists within the literature.

In terms of stability and consistency of closure measurement methods, it is clear that the slope variation results were generally the most noisy and were sensitive to different types of implementation. Noisy results may be most directly attributed to the local measurements of slope that are involved (*i.e.* using only small portions of the data at a time), rather than the overall averaging effect that is obtained when applying the curve fits. Reductions in the slope variation threshold for closure detection (*e.g.* from 5 to 1%) may be expected to increase the sensitivity of the methods to the closure process, but will increase the sensitivity of the results to noise in the raw data. It is clear that for the present results, curve fitting methods are able to achieve a greater sensitivity to closure events, with less noise or variability compared to the slope variation methods. Multiple tests show reproducibility in P_{op}/P_{max} of the order of ± 0.05 for the curve fitting methods. Although efforts may always be made to reduce noise in the raw data, it should be noted that the current measurements were well within the data quality criteria of the second *ASTM* round robin exercise [6] (specifically assessing compliance linearity in the test set-up before crack growth occurs).

Whilst the curve fitting methods appear to produce the most consistent results, a potential cause for concern is of course the choice of function to reproduce the non-linear region and how well it approximates the transition point. In reality, the exact shape of the compliance curve may be expected to be a function of:

(a) The operative closure mechanisms and the associated patterns of surface contact and load transfer due to wake plasticity, asperity sliding, crushing, cold welding, *etc.*

(b) The sensitivity of the chosen measurement location to through-thickness closure variations.

Although the true functionality of the non-linear region of any given compliance curve is essentially unknown, the fact that the gradient and co-ordinate matching methods used in the present curve fitting produced similar results for both crack mouth clip gauge and near-tip strain gauges implies that the *linear + quadratic* approximation is reasonable in these cases, as may be seen qualitatively in Figure 4.15. It is further suggested that the comparison of the two fitting criteria be included in any closure measurement exercise to provide a quantitative check that the *linear + quadratic* approach has produced a reasonable fit to the raw compliance data.

4.4. Conclusions

1. Non-subjective curve fitting methods based on linear and quadratic functions have been shown to provide particularly consistent closure measurements from conventional crack mouth clip gauges and properly located near-tip strain gauges. This method improves upon current *ASTM* suggested methods in terms of sensitivity, consistency and noise in the measurements.

2. Separation of surface and bulk closure effects has been achieved via global and near-tip measurements, along with the use of side-grooved specimens. Direct crack tip observation results further validate the sensitivity of curve fitting methods in detecting the onset of closure.

References

[1] N. A. Fleck and R. A. Smith, (1982), *Int. J. of Fatigue*, Vol.4, pp.157-160.

[2] J. C. Newman, Jr., (1995), *J. of Engineering Materials and Technology*, Transactions of ASME, Vol.117, pp.433-439.

[3] ASTM E647, (1995), *Annual Book of ASTM Standards,* Section 3, Vol.03.01, pp.578-614.

[4] J. J. Lee and W. N. Sharpe, Jr., (1988), *ASTM STP982*, American Society for Testing and Materials, pp.270-278.

[5] W. Yisheng and J. Schijve, (1995), *Fatigue Fract. Engng. Mater. Struct.*, Vol.18, pp.917-921.

[6] E. P. Phillips, (1993), *NASA Technical Memorandum 109032*, Langley Research Centre, Hampton, Virginia.

[7] W. Yu and R. O. Ritchie, (1987), *J. of Engineering Materials and Technology*, Vol.109, pp.81-85.

[8] S. T. Rolfe and S. R. Novak, (1970), *ASTM STP463*, American Society for Testing and Materials, pp.124-159.

[9] R. G. Chermahini, K. N. Shivakumar, J. C. Newman, and A. F. Blom, (1989), *Engineering Fracture Mechanics,* Vol.34, pp.393-402.

[10] A. J. McEvily, (1977), *Fatigue 1977 Conf.,* University of Cambridge, UK.

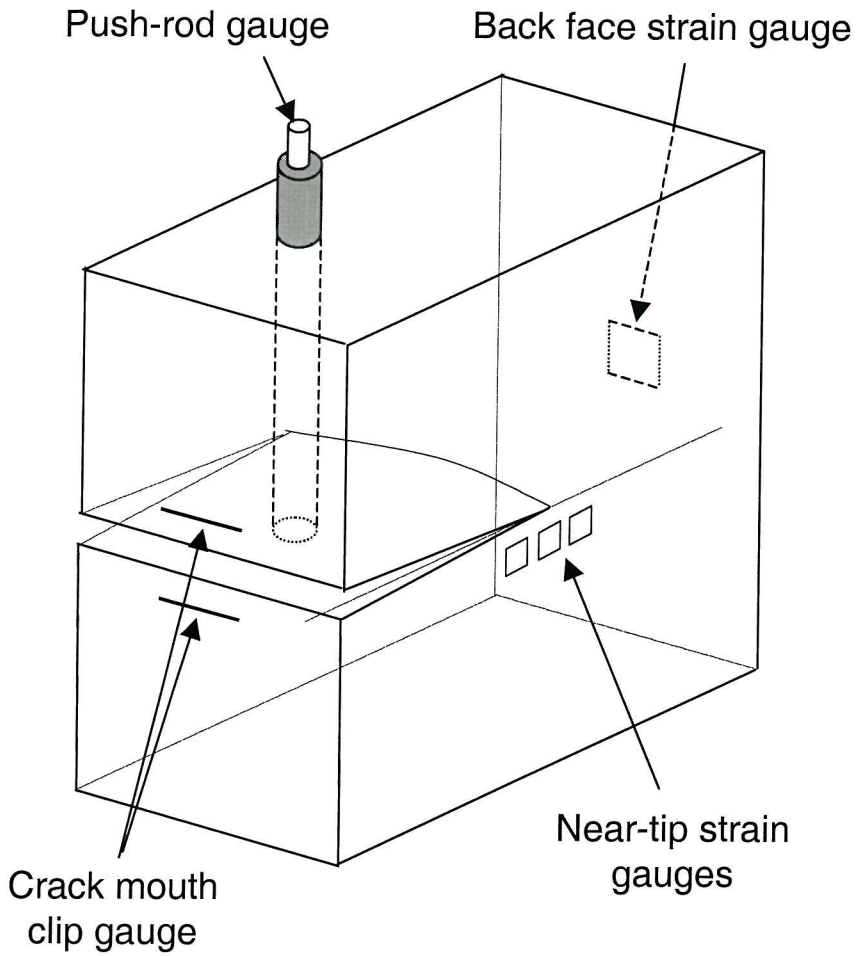

Figure 4.1 Mechanical compliance measurements.

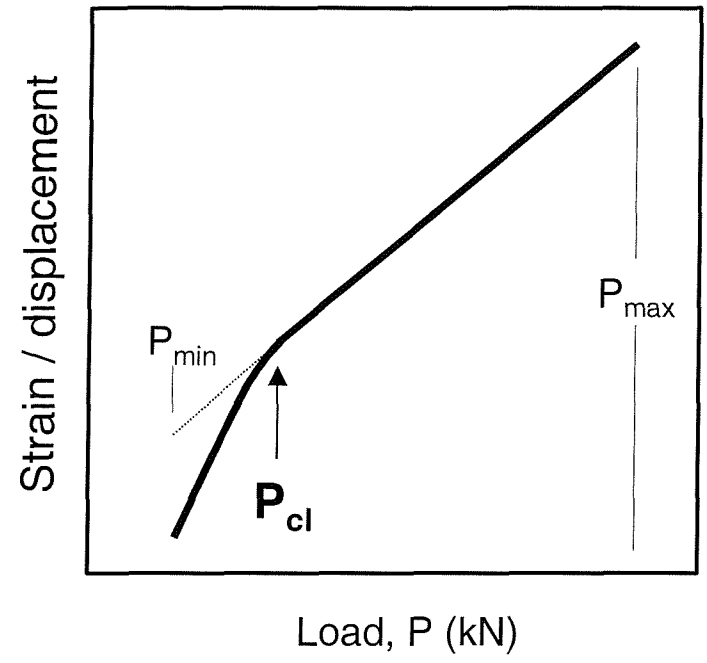

(a)

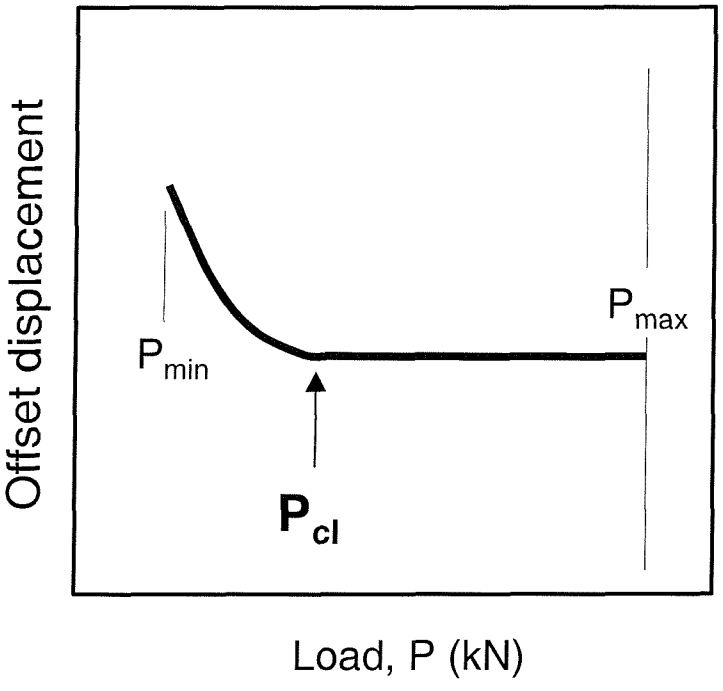

(b)

Figure 4.2 Schematic illustration of visual observations: (a) direct observation and (b) offset method.

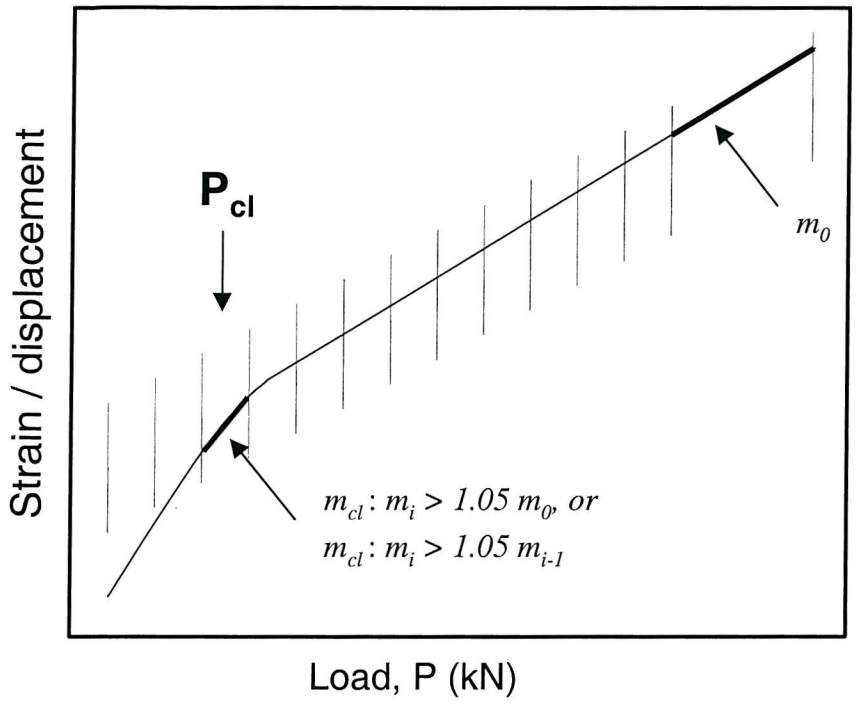

Figure 4.3 *Schematic illustration of slope variation methods.*

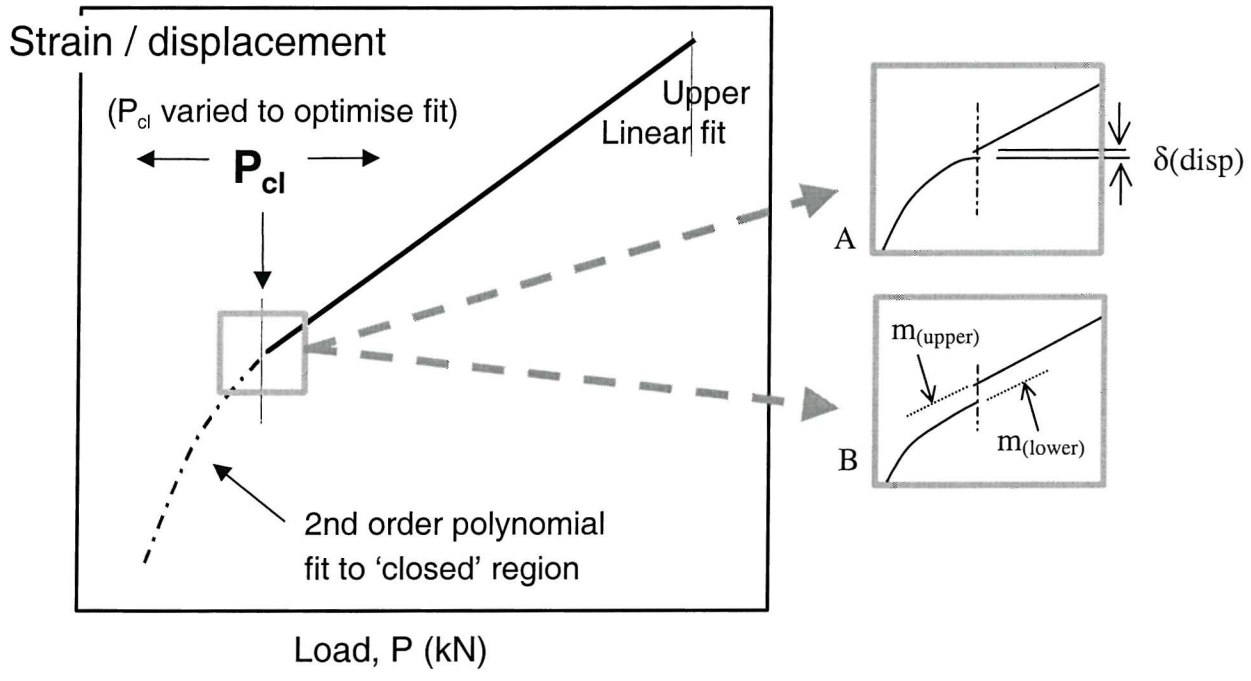

Figure 4.4 *Schematic illustration of curve fitting methods. Highlighted region shows alternative upper-lower curve matching criteria to determine P_{cl}: (A) minimum co-ordinate difference, and (B) minimum slope differences.*

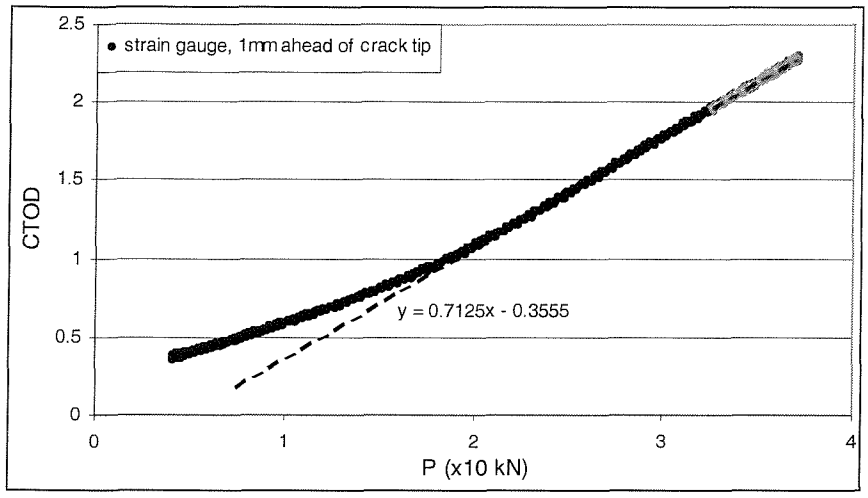

(a)

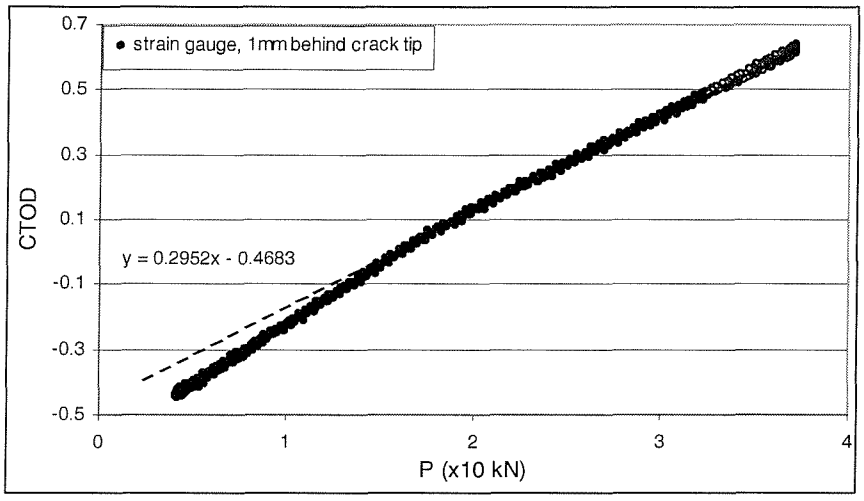

(b)

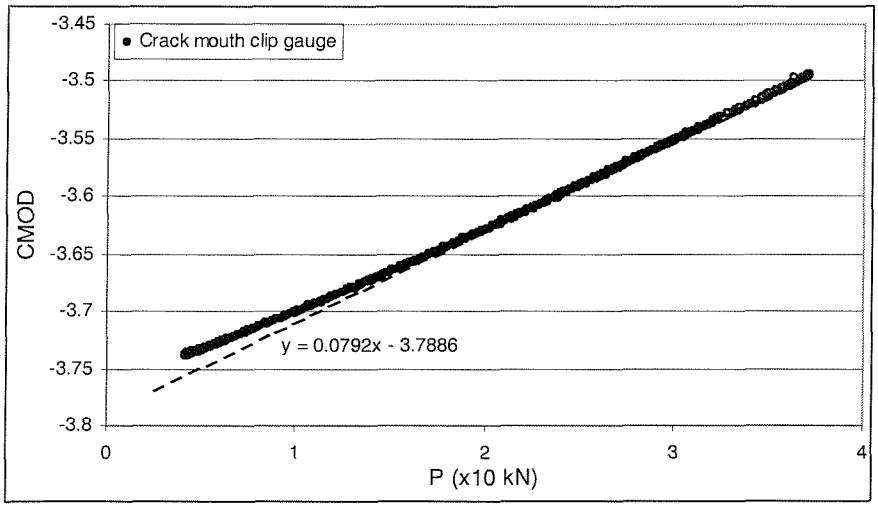

(c)

Figure 4.5 Compliance curves from near-tip strain gauges and crack mouth clip gauge (CTOD & CMOD units are nominal).

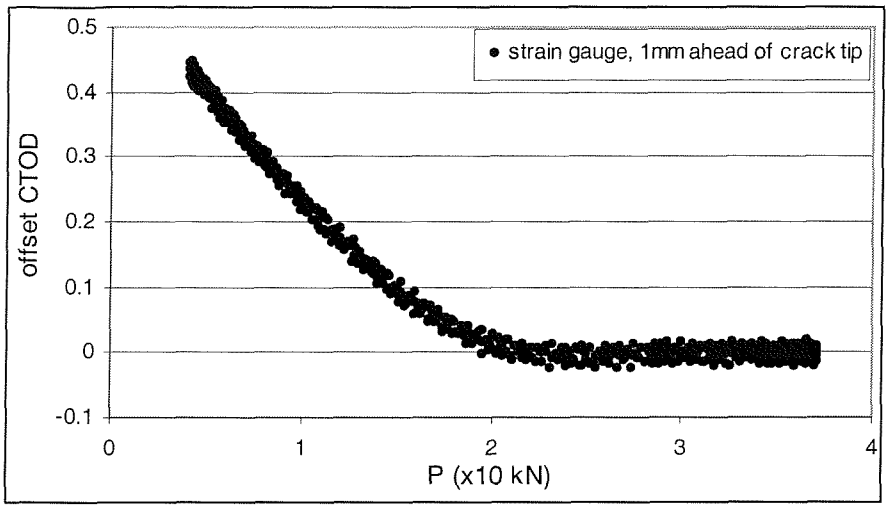

(a)

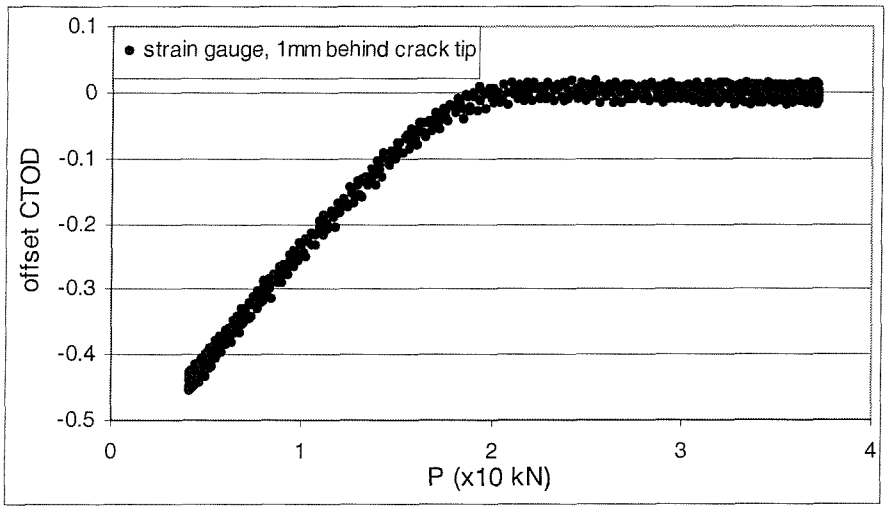

(b)

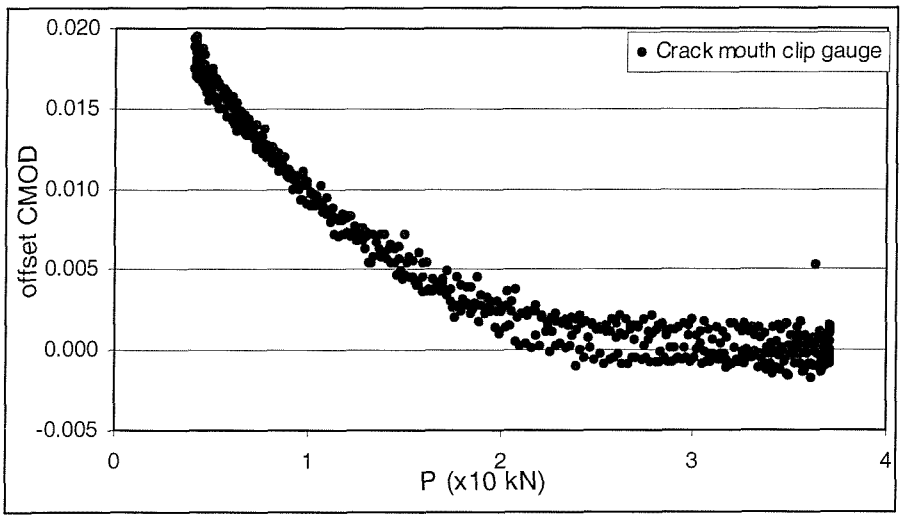

(c)

Figure 4.6 Offset compliance curves from near-tip strain gauges and crack mouth clip gauge.

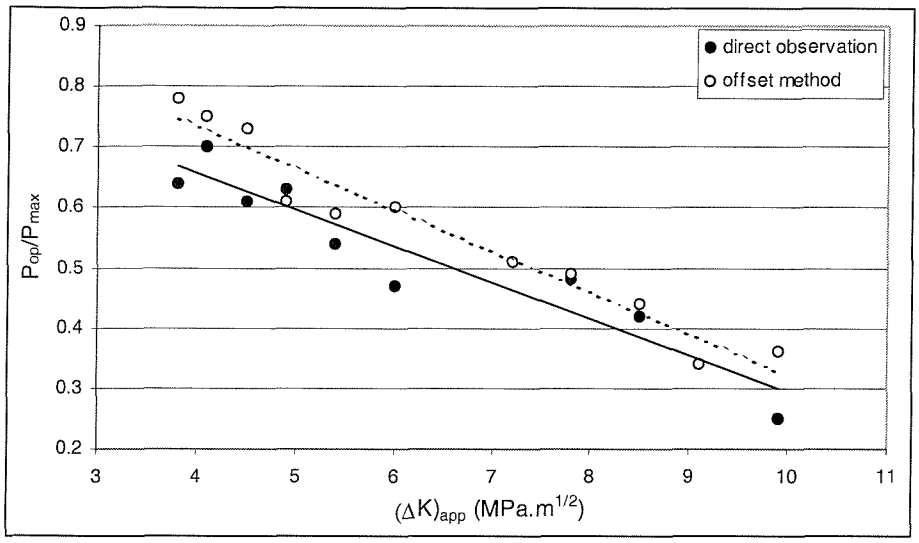

(a)

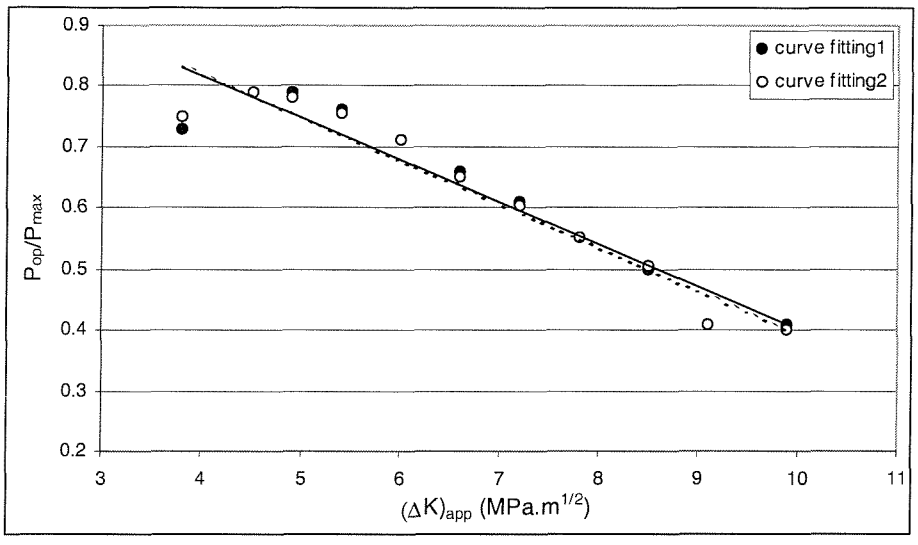

(b)

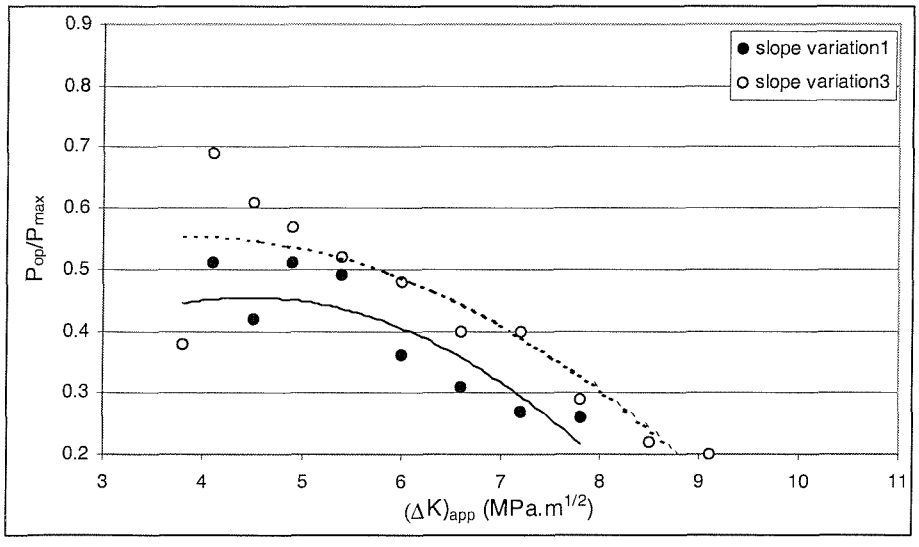

(c)

Figure 4.7 Closure results from crack mouth clip gauge.

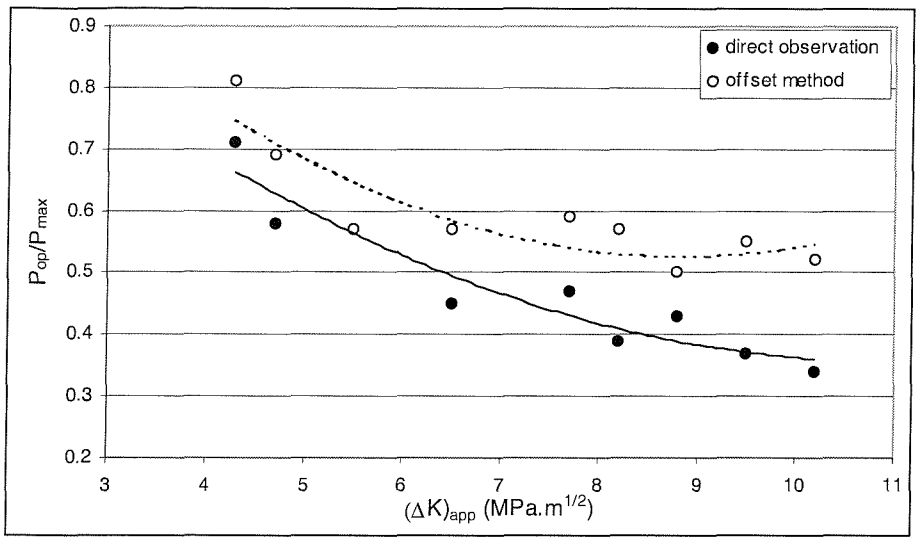

(a)

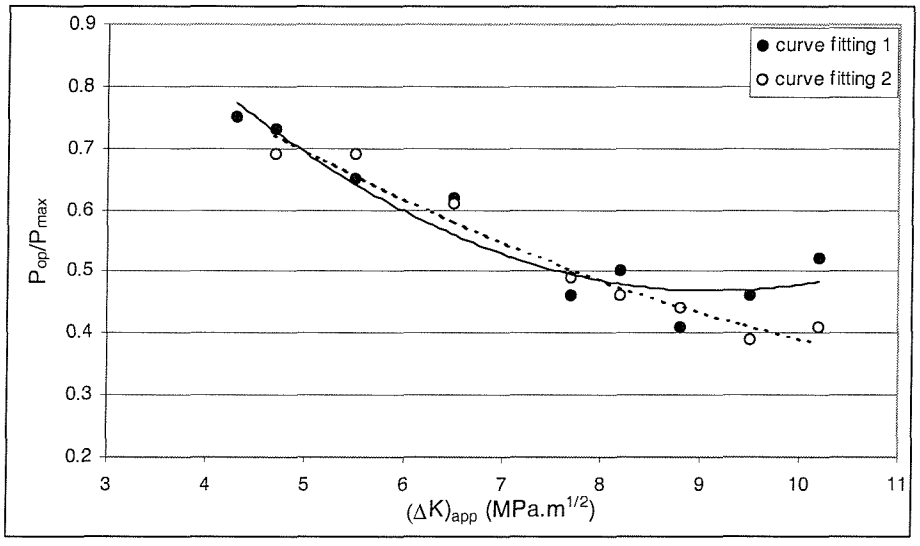

(b)

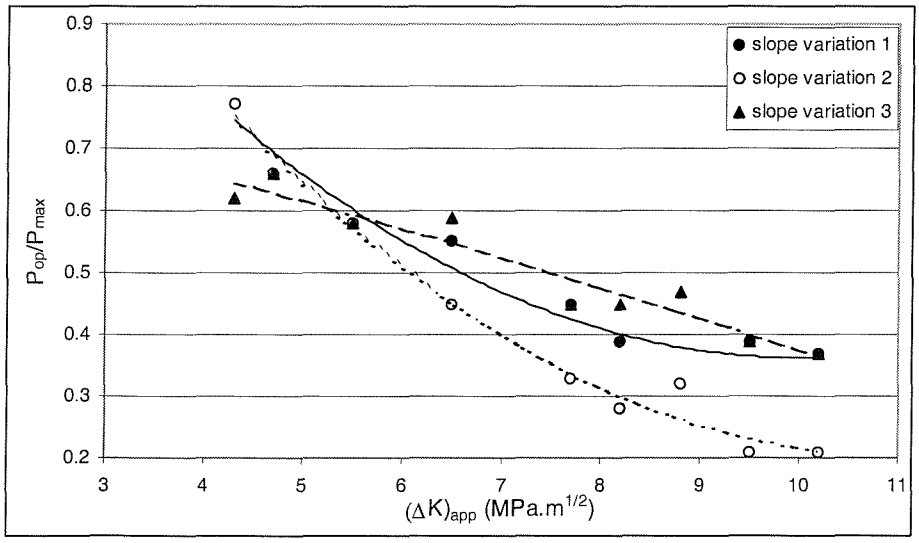

(c)

Figure 4.8 Closure results from strain gauges at the crack tip.

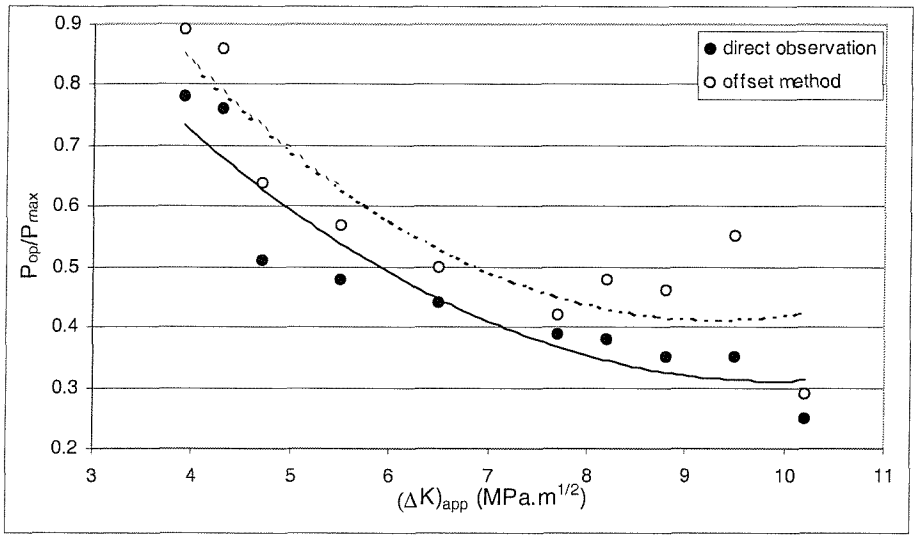

(a)

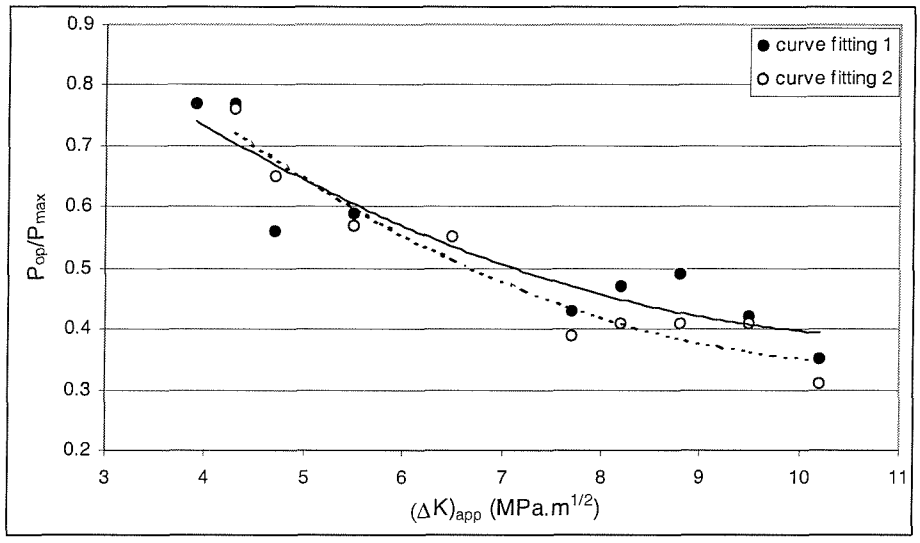

(b)

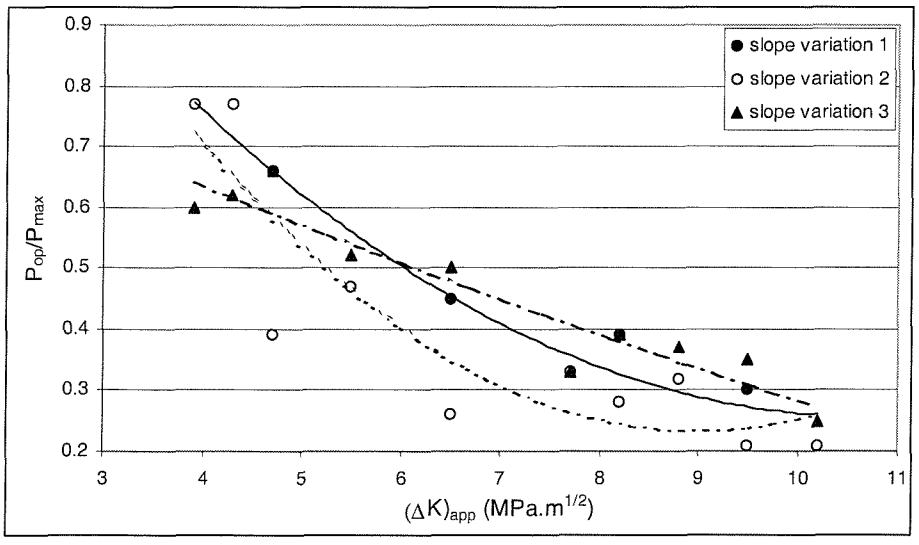

(c)

Figure 4.9 Closure results from strain gauges 1mm behind the crack tip.

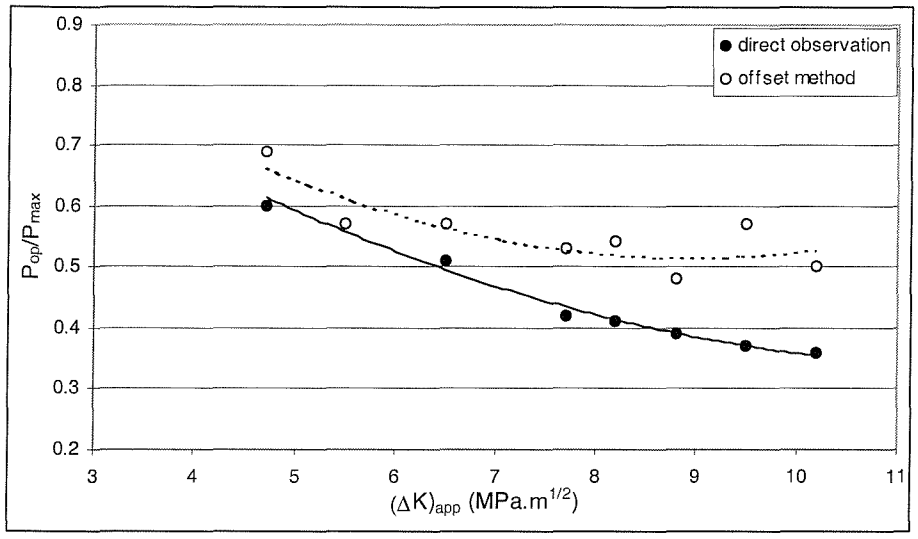

(a)

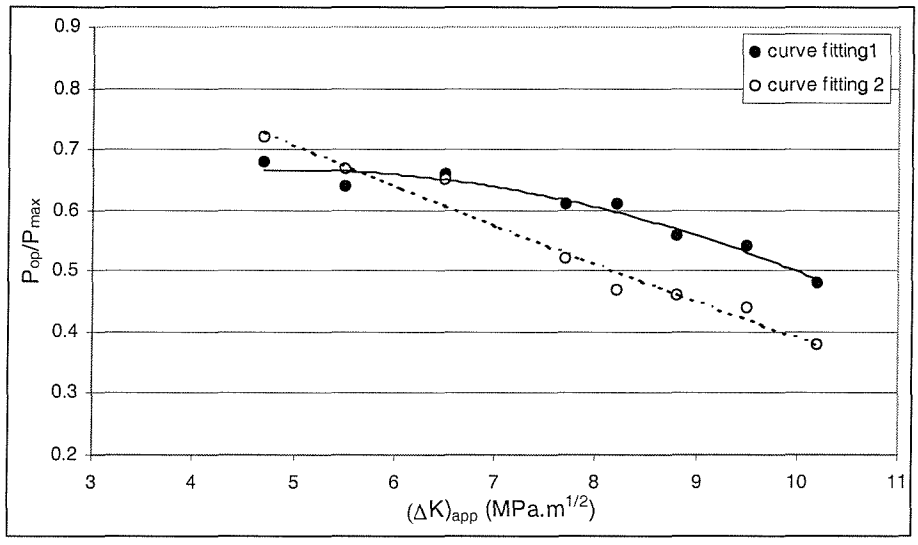

(b)

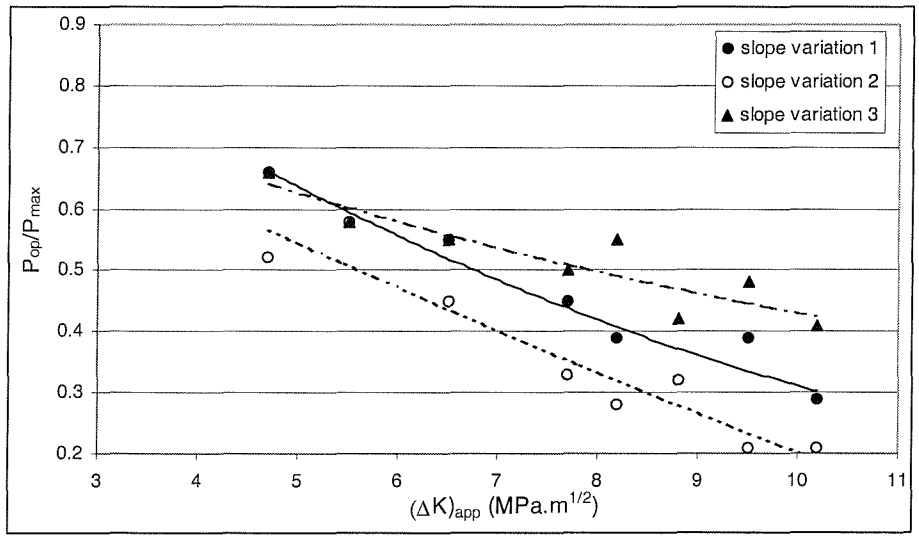

(c)

Figure 4.10 Closure results from strain gauges 1mm ahead of the crack tip.

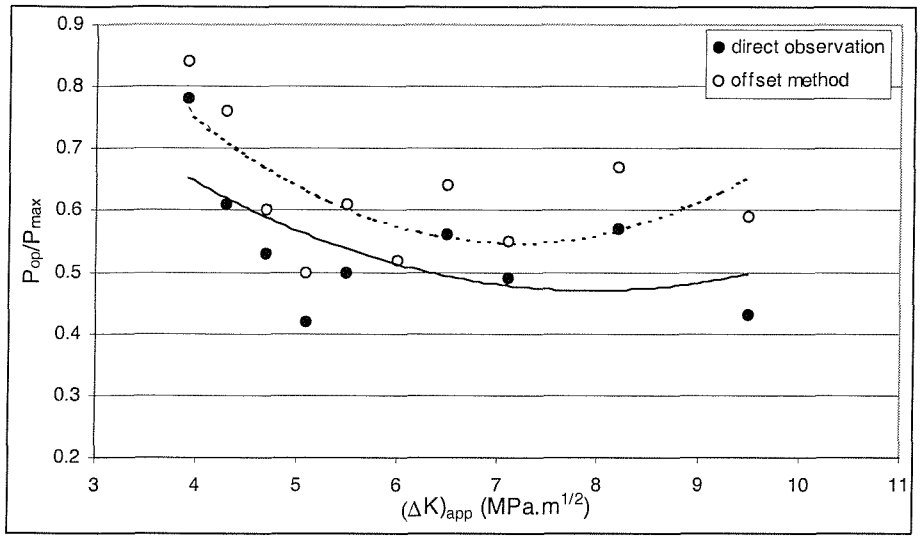

(a)

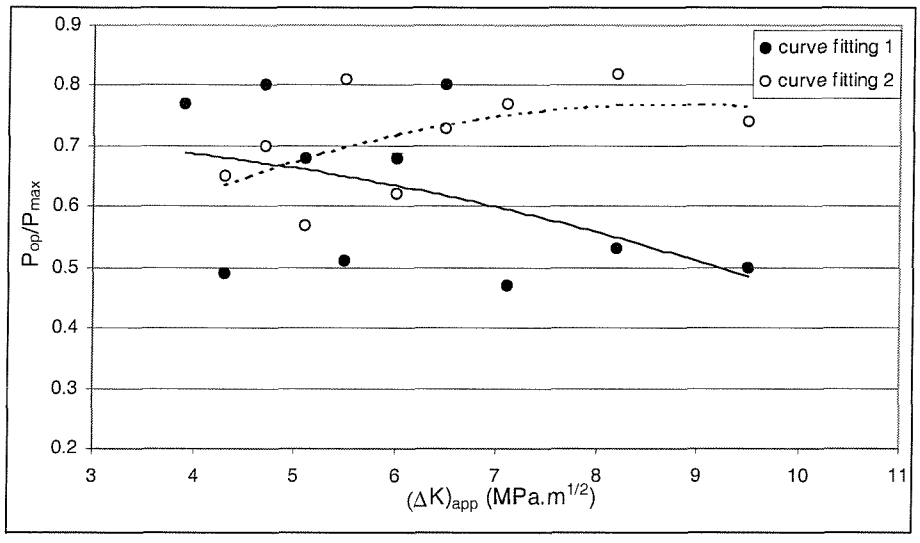

(b)

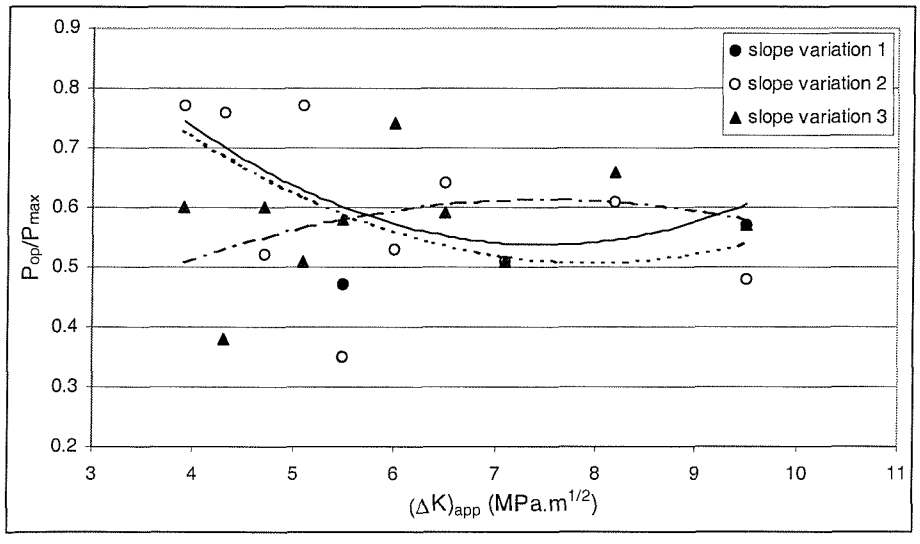

(c)

Figure 4.11 Closure results from strain gauges 2mm behind the crack tip.

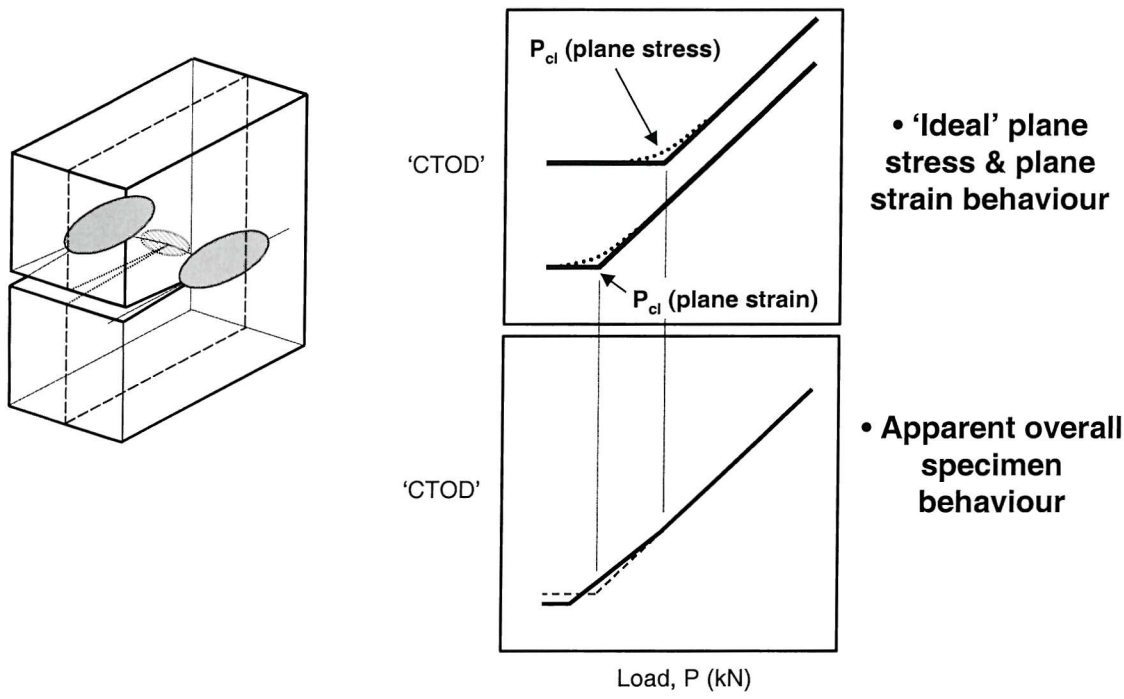

Figure 4.12 Stress state effect on closure measurements in terms of nominal crack tip opening.

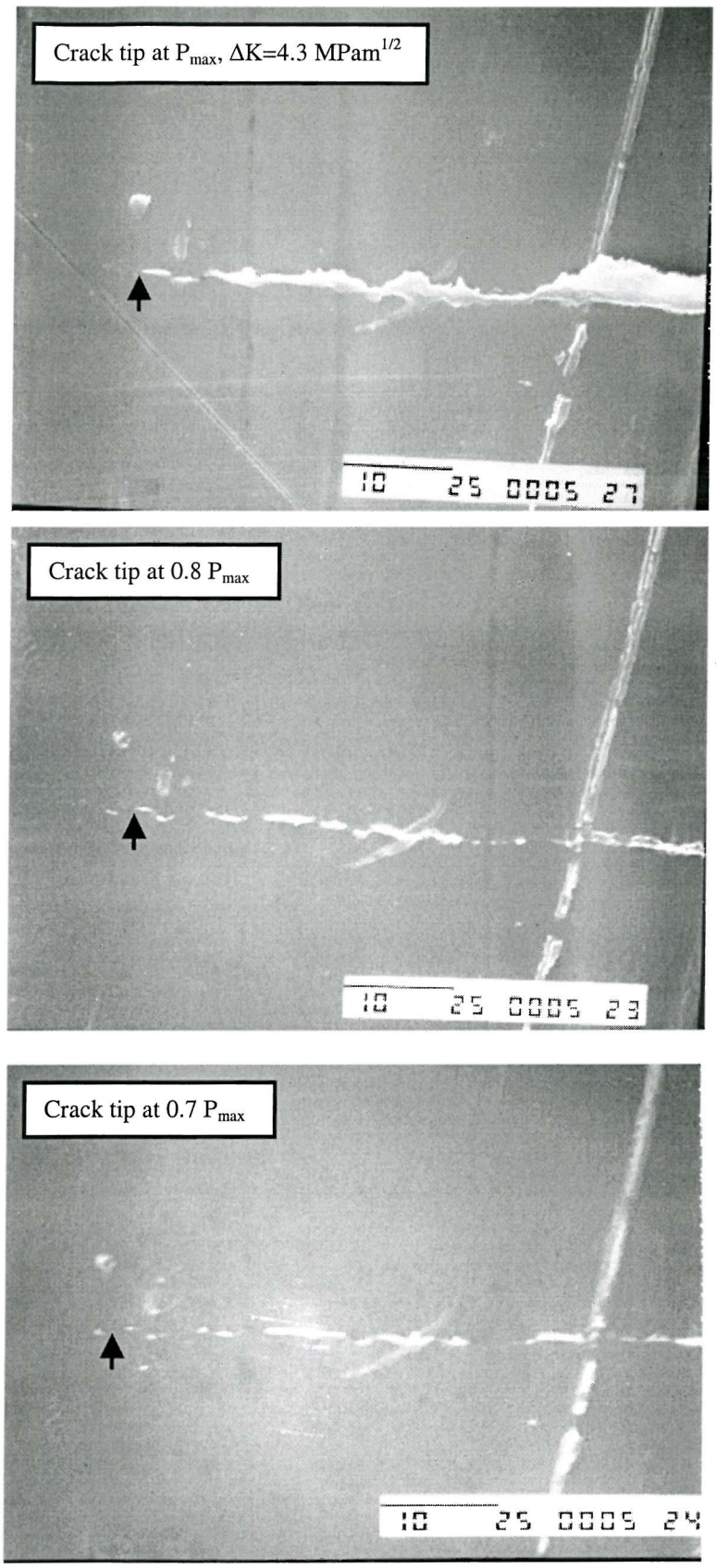

Figure 4.13 Crack tip profiles from replicas at different load levels.

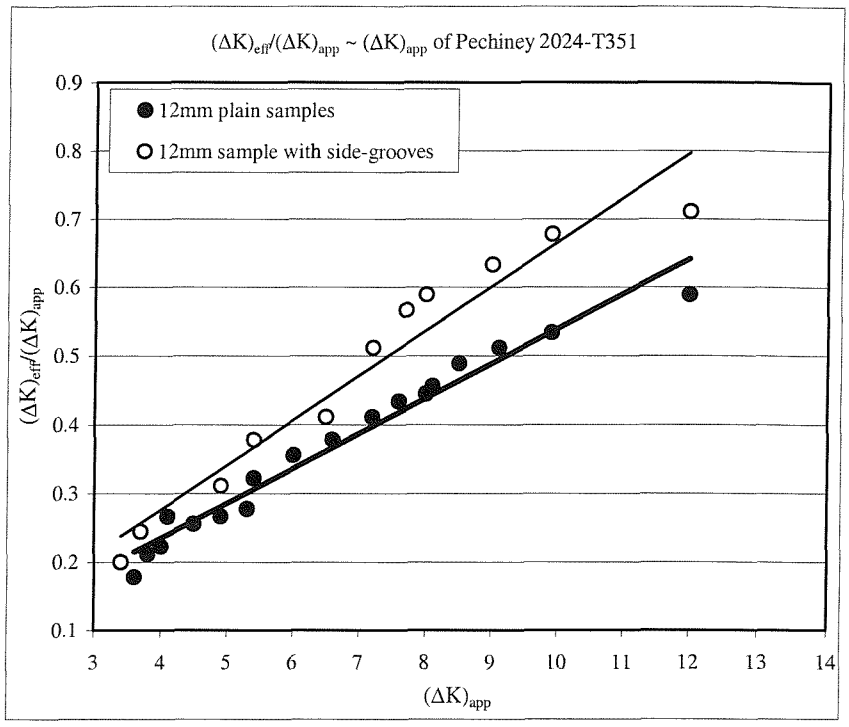

Figure 4.14 Side-groove effects on closure results.

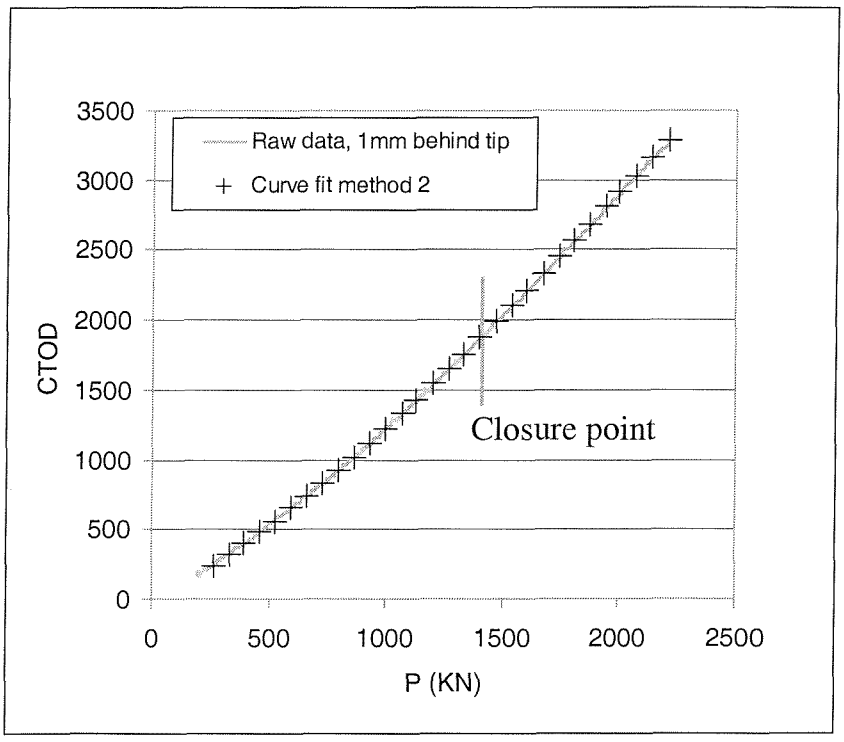

Figure 4.15 Experimental compliance data and corresponding linear + quadratic curve fit.

5. FATIGUE BEHAVIOUR OF 2024- & 2024A-T351 UNDER CONSTANT AMPLITUDE (*CA*) LOADING

— *This chapter describes a study of CA crack growth behaviour in 2024 & 2024A materials, specifically using the crack closure methods described in Chapter 4. The influences of microstructure and stress state on crack growth behaviour are particularly considered.*

5.1. Introduction

Fatigue crack growth resistance is known to be influenced by a combination of intrinsic materials behaviour and crack shielding processes (see Chapter 2). Intrinsic behaviour represents the inherent material resistance to propagation at a crack tip, which may then vary with parameters such as deformation heterogeneity, environment and the extent of crack tip plasticity in relation to characteristic micro-structural dimensions such as grain size, secondary phase particle separation and/or dislocation cell size. Shielding processes (or '*extrinsic*' behaviour) are localised mechanical influences tending to attenuate the crack driving force experienced at a crack tip, which may or may not be dependent on microstructure [1]. The separation of intrinsic and extrinsic contributions to crack growth resistance is a major theme of fatigue research in the last 30 years. It is well established that an accurate quantitative understanding of intrinsic and extrinsic effects on crack growth is essential to directed alloy development for fatigue resistance, and/or improved fatigue life predictions. This chapter addresses this issue through the application of detailed, non-subjective closure measurement methods in the last chapter [2] to the study of crack growth resistance in conventional and advanced variants of AA2024-T351 plate. Stress state effect on crack growth behaviour is addressed using side-grooved thick samples and 2*mm* thick samples to simulate plane strain and plane stress conditions respectively, with microstructural influence on crack growth resistance being considered as well.

5.2. Materials and Experimental

Detailed characterization on the materials tested is given in Chapter 3. Key points are as follows: (1) the supplied 2024A-T351 exhibits twice the grain size of the 2024-T351, (2) *GPB* contents were identical in both alloys, (3) dispersoid content in 2024A is lower

than that in 2024 due to the lower *Mn* content in 2024A, (4) inter-metallic content was found to be very similar for the two alloys, (5) 2024A has a lower monotonic yield strength in the longitudinal direction and generally lower monotonic ultimate tensile strength in longitudinal and transverse directions, and (6) cyclic tensile test results show that 2024A has a marginally higher cyclic strain hardening exponent than 2024.

Crack growth tests were carried out via load shedding in the *LT* orientation at an *R*-ratio of 0.1 using 150*mm* wide centre cracked tension (*CCT*) panels according to *ASTM Standard E647* [3]. The test set-up is shown in Chapter 3. Tests were carried out on three types of samples: 12*mm* thick plain samples, 12*mm* thick samples with 1*mm* deep side-grooves along the nominal crack growth plane on each face, and 2*mm* thick samples. A conventional modification factor was used to calculate stress intensity factors in the side-grooved samples [4]. Repeated tests on 12*mm* thick samples with and without side-grooving confirmed that side-grooves had no effect on growth rates (plane strain conditions should predominate in both cases). Fractographic studies were carried out via *SEM*, with fracture surface roughness also being quantified by 3-D Talysurf Profilometry.

5.3. Results

5.3.1. Stress State Effects on *CA* Crack Growth Behaviour of 2024- & 2024A-T351

A change of stress state typically occurs for a fatigue crack in a plate of intermediate thickness, with the stress state at the crack tip being mainly determined by the relative ratio of the crack tip plastic zone size and the plate thickness. Stress state has a significant influence on fatigue crack growth behaviour via its effects on crack tip plastic zone sizes, crack opening displacements, and associated potential crack closure mechanisms. To most directly study stress state effects on *CA* fatigue crack growth behaviour, 12*mm* thick side-grooved and 2*mm* thick samples are tested to simulate uniform plane strain (in the 12*mm* thick side-grooved case) and plane stress (the 2*mm* thick case should at least tend towards plane stress conditions with increasing K levels[1]) conditions, respectively. Figure 5.1 shows the *CA* crack growth behaviour of 2024- & 2024A-T351 plotted in terms of applied stress intensity range, $(\Delta K)_{app}$. Similar sample

[1]It should be aware that there is no pure plane stress state in the component due to the stress gradient in the thickness direction, as mentioned in Chapter 2

thickness (*i.e.* stress state) effects on crack growth were observed in both alloys. 2*mm* thick samples have clearly increased crack growth resistance at higher ΔK levels, with growth behaviour in 2 & 12*mm* samples converging towards the near-threshold regime.

Figure 5.2 shows crack closure variations (based on the curve fitting methods outlined in Chapter 4) against $(\Delta K)_{app}$ in these two alloys. Closure levels are expressed as the effective stress intensity range over the applied stress intensity range. Consistently higher shielding was measured in thin samples at high ΔK levels in both alloys, with 2024A exhibiting generally higher shielding than 2024. Similar trends in closure variations between the different sample thickness were observed in both alloys.

Crack growth behaviour is plotted in terms of effective stress intensity range, $(\Delta K)_{eff}$, in Figure 5.3. *da/dN* curves for side-grooved samples and 2*mm* thick samples collapse together when plotted in this manner, indicating that sample geometry effects on fatigue crack growth in 2024- & 2024A-T351 are rationalised well by extrinsic processes (*i.e.* closure).

5.3.2. Material Effects on *CA* Crack Growth Behaviour in 2024- & 2024A-T351

A material comparison for *CA* crack growth behaviour of 2024- & 2024A-T351 was particularly established for 12*mm* thick plain- and side-grooved samples. Multiple repeated tests were carried out to ensure that a reasonable statistical representation was obtained. Figure 5.4(a) shows the $da/dN \sim (\Delta K)_{app}$ curves of both alloys. Consistent improvement in crack growth resistance for the 2024A material was observed across most of the ΔK range tested, with results for the two materials showing some convergence towards threshold. Figure 5.4(b) shows the closure variations for side-grooved samples of both alloys. Higher shielding effects in 2024A were measured at high ΔK levels, with both alloys exhibiting similar closure levels approaching threshold.

Figure 5.5 shows the crack growth behaviour of side-grooved samples of 2024- & 2024A-T351 after taking into account of closure effects (note that the crack growth behaviour for thick samples are plane strain dominated). Both alloys exhibit very similar crack growth resistance, indicating that the growth rate difference between the

2024 and the 2024A is largely attributable to closure processes (*i.e.* extrinsic crack growth resistance).

To investigate the micro-structural effects on *CA* crack growth behaviour, features on the fatigue surfaces at different ΔK levels were examined by *SEM*. Figure 5.6 shows the fatigue surfaces of both alloys in the near-threshold regime. Both alloys show a typical '*feathered*' crystallographic crack growth mode in this regime, with 2024A exhibiting a coarser grain structure. Figure 5.7 shows the features of the fatigue surfaces at a $(\Delta K)_{app}$ of 5.1 $MPa\ m^{1/2}$. An obvious shift from crystallographic surface features to more ductile fracture surfaces was observed for 2024 at this ΔK level. The fatigue surfaces of 2024A, however, still exhibited mainly crystallographic features at the same ΔK level as the 2024. Figure 5.8 shows the surface features of the materials at a $(\Delta K)_{app}$ of 12 $MPa\ m^{1/2}$. Both alloys exhibit more ductile surface features at this higher ΔK level, with some crystallographic features still remaining in the 2024A. It is worth noting that crystallographic features were evident in $2mm$ thick samples of both alloys at ΔK of 12 $MPa\ m^{1/2}$ (see Figure 5.9), which was reasonably distinct from the thick samples.

Figure 5.10 shows three-dimensional reconstructions of fracture surfaces in the 2024 & 2024A using Talysurf Profilometry measurements at ΔK of 8 $MPa\ m^{1/2}$. A generally increased size and height of surface features in 2024A is observed, which was in fact quite clear from visual inspection.

5.4. Discussions

The present crack growth results and detailed closure measurement methods indicate a predominantly extrinsic effect of microstructure on crack growth behaviour in these materials. Three main sources of crack closure may be expected to apply to these alloys: (a) *PICC*, (b) *RICC*, and (c) *OICC*.

In terms of *PICC*, it is important to note that the closure results from thick, side-grooved test samples should closely represent pure plane strain behaviour in both alloys. Whilst some debate remains as to the possibility of *PICC* occurring to any significant extent under plane strain conditions (*e.g.* see [5]), various authors that have advocated its

significance in plane strain (*e.g.* see [6]) indicate that closure levels are significantly lower than those observed here. In terms of *OICC*, there was no particular evidence of the build-up of an extensive oxide layer when approaching threshold in these tests. Furthermore, the fact that *OICC* must be an increasing effect when approaching threshold is not consistent with the differences in crack growth/closure behaviour in the two materials (*i.e.,* differences diminished towards threshold, where oxide effects would be expected to be more significant). Given the differences in fracture surface morphology that were observed in the two materials, differences in closure behaviour are therefore most directly attributable to roughness induced closure processes. In the present tests the 2024A alloy exhibited both an increased susceptibility to crystallographic crack growth and a generally increased size of fracture surface features. For a given crack propagation mode such an increase in scale of surface feature is attributable to the larger grain size of the 2024A. In terms of the alloying effects on propagation mode, important micro-structural interactions associated with the present materials include:

(a) Their underaged condition, giving an intrinsic propensity for slip band formation and hence crystallographic crack growth, and

(b) The distribution of slip band blocking features in the materials.

It was clear from the fractography that the 2024A was more susceptible to crystallographic crack growth. This effect was quite evident from relatively low ΔK levels where the crack tip plastic zone sizes are appreciably smaller than the main grain size but are of the order of the dispersoid spacings. As such, these differences are most directly attributable to the reduced dispersoid content of the 2024A material, rather than the grain size – it is only at the highest ΔK levels tested here that even the monotonic plastic zone size begins to approach the in-plane grain dimensions in these materials. Based on comparisons of re-crystallised and unrecrystallised materials, Wanhill [7] has indicated that the presence of sub-grains does not have an appreciable influence on such transitions. Wanhill and other workers [7, 8] have however also suggested that there is a correlation between the various changes in slope that occur along the crack growth curves for these materials and key microstructural dimensions, with the lowest slope change (T_1 in Figure 5.5) being linked to the cyclic plastic zone size exceeding the spacing of dispersoid particles. In the present work, ΔK_{eff} results for the two alloys, which should control the true cyclic plastic zone size at the crack tip, show a reasonably

clear T_1 transition. Whilst there is a small shift in the data for the 2024 and 2024A at this point, there is no particular indication from the 2024A data that the local change in slope was at a higher ΔK than in the 2024 (as might be expected if T_1 is linked to dispersoid content), particularly compared to the differences in crack growth mode that were observed as a function of ΔK. In this respect it is interesting to note that previous work by Slavik *et al.* [9] has suggested that such growth curve transitions do not occur in high strength aluminium alloys (including 2024) when tested under true high vacuum conditions. The transitions are therefore attributable to environmental interactions, which would be consistent with the apparent de-coupling of the crack growth curve transitions and the influence of microstructure on fracture surface morphology in the present tests. It is interesting to note that the influence of dispersoids on crack growth mode may be expected to decrease at very low/threshold conditions as plastic zone dimensions (particularly the cyclic plastic zone size) fall below the dispersoid spacing (for a measured $\Delta K_{th.eff}$ of 0.6 $MPam^{1/2}$, the cyclic plastic zone size will be of the order of 0.1 μm). Convergence in closure levels was evident towards the crack growth threshold in the present tests, implying that, in this regime at least, the grain size (and hence the scale of asperity) was not critical in determining closure levels; rather it is the incidence of crystallographic deflection. Such behaviour may then be consistent with the analytical modelling of *RICC* by Suresh [10], the finite difference modelling of Llorca [11] and the *FE* modelling of Parry *et al.* [12] showing the primary sensitivity of *RICC* to asperity angles rather than height. Further detailed quantification of fracture surface morphology would of course be required to confirm this issue (particularly in terms of identifying and measuring characteristic crack deflection angles in each alloy).

In terms of specimen geometry/stress state effects, it would appear that the novel closure measurement methods developed in this project provide quite clear rationalisation of observed crack growth behaviour. It may be noted that:

(a) The materials in both sample geometries should be quite homogeneous through their thickness given that the samples were machined from the centre of relatively thick plates (40*mm*),

(b) Residual stress differences between the samples should be minimised by the fact that the original materials were stress relieved (*i.e.* Tx51 condition) and samples were relatively thin sections from the parent plate.

As such, a pure mechanics effect is identified between the thick and thin samples, confirming various suggestions (see Chapter 2) that crack closure levels are indeed higher in the plane stress state. As ΔK levels increase, plane stress influence on *PICC* levels will of course increase as the crack tip plastic zone size approaches the specimen thickness (more thorough-thickness relaxation can occur), consistent with the observed divergence of the thick and thin specimen growth rates with increasing stress intensity levels. It is interesting to note that closure levels in the $2mm$ samples at high ΔK levels were higher in 2024A than 2024. Whilst increasing *RICC* contributions to closure might still be identified for the 2024A, the lower flow stress levels (yield and *UTS*) might also contribute to greater through-thickness stress relaxation in the 2024A (*i.e.* enhanced plane stress conditions). Microstructural contributions to closure levels are therefore more difficult to identify than those noted earlier in relation to the thick specimen/side-grooved sample results.

It is also interesting to note that for both alloys the crack growth behaviour for thick and thin samples starts to diverge when ΔK is above ~ 7 $MPa.m^{1/2}$, giving an indication of a transition point for the onset of plane stress closure effects. The monotonic Dugdale plastic zone size is ~ $0.2mm$ on each side of the sample at this ΔK level, *i.e.* relatively small compared to the thickness of the samples ($2mm$). This suggests that a significant extent of overall crack tip shielding may be achieved via the incomplete closure of the crack surfaces across the sample thickness. The fact that differences in the onset of crack closure in plane-sided and side-grooved, $12mm$ thick samples could be identified in specimen compliance data (*e.g.* see Chapter 4, Figure 4.14), yet crack growth rates were not influenced by the side-grooving highlights the fact that investigating and quantifying crack closure and growth rate behaviour in plane-sided samples, as widely carried out in the literature, is fundamentally problematic. The careful analysis of closure behaviour in relation to more controlled stress state conditions is therefore considered a vital part of any attempt to resolve the conflicts and controversies that exist in the closure analysis of fatigue, as has indeed been pursued in this work.

5.5. Conclusions

1. Using the crack closure assessment methods outlined in Chapter 4 microstructure and test specimen geometry effects were found to be closely attributable to extrinsic closure effects, even though differences in crack propagation mode were evident in the two alloys

2. Reduced dispersoid content is considered to promote crystallographic growth in 2024A, since differences in growth mode were evident from stress intensities when plastic zone sizes are relatively small compared to the primary grain size.

3. Links between intrinsic crack growth curve transitions and distribution of slip blocking features are not directly supported. There was no clear evidence of shifts in transition points between the alloys, consistent with the influence of environmental effects on such growth curve transitions, as identified previously by Slavik *et al* [9].

4. Crack closure behaviour, approaching threshold at least, appears to be insensitive to the absolute scale of the surface asperities – other characteristics such as deflection angle may therefore be more significant in controlling K_{cl}.

References

[1] I. Sinclair and P.J. Gregson,, (1998), Proc. ICAA6, Toyohashi, JILM, vol. 4, pp.2091-2104.

[2] Yigeng Xu, P.J. Gregson and I. Sinclair, (2000), *Mater. Sci. Eng. A.*, vol.284, pp.114-120.

[3] Annual Book of ASTM Standard(1996), Vol.03.01, *ASTM E647-95a*, pp.565-601.

[4] S.T. Rolfe and S.R. Novak, (1970), *ASTM STP982*, American Society for Testing and Materials, 124.

[5] N.A. Fleck and J.C. Newman, (1988), *ASTM STP982*, American Society for Testing and Materials, 318.

[6] F.O. Riemelmoser and R. Pippan, (1998), *Fat. Frac. Eng. Mater. Struct.*, vol.21, 1425.

[7] R.J.H. Wanhill, (1988), *Eng. Frac. Mech.*, vol.30, 233.

[8] G.R. Yoder, L.A. Cooley and T.W. Crooker, (1982), *NLR Report 4787,* Naval Research Laboratory, Washington DC.

[9] D.C. Slavik, C.P. Blankenship, E.A. Starke and R.P. Gangloff, (1993), *Metall. Trans. A*, vol.24A, 1807.

[10] S. Suresh, (1985), *Mater. Trans. A*, vol.16A, 249.

[11] J. Llorca,(1992), *Fat. Frac. Eng. Mater. Struct.*, vol.15, 655.

[12] M. R. Parry, S. Syngellakis, and I. Sinclair, (2000), *Materials Science and Engineering A,* Vol.291A, pp.224-234.

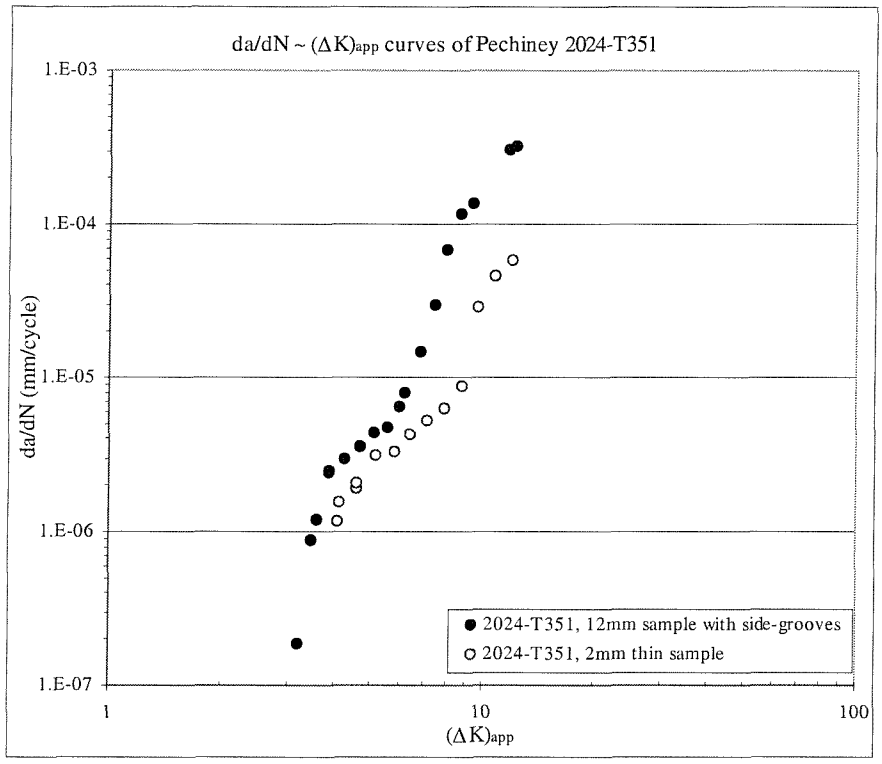

(a)

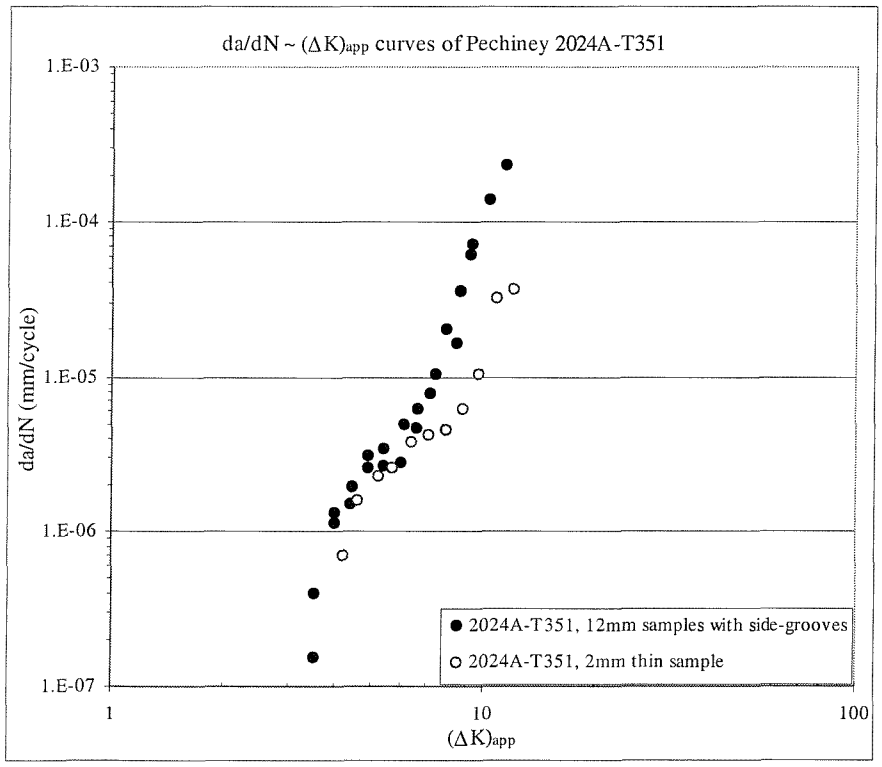

(b)

Figure 5.1 $da/dN \sim (\Delta K)_{app}$ curves at R=0.1: (a) 2024-T351 and (b) 2024A-T351.

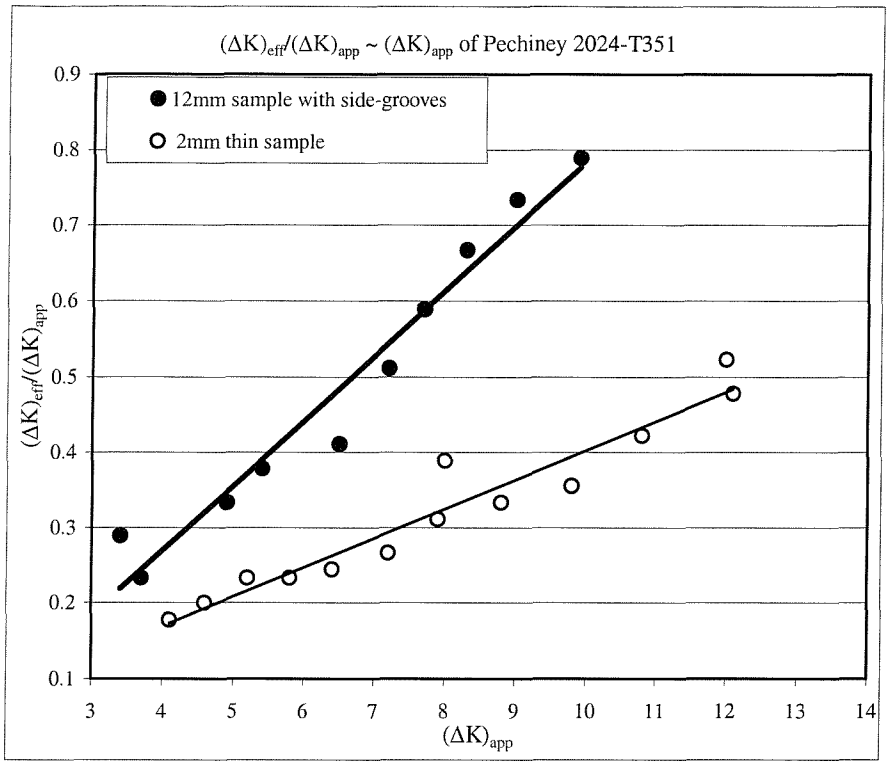

(a)

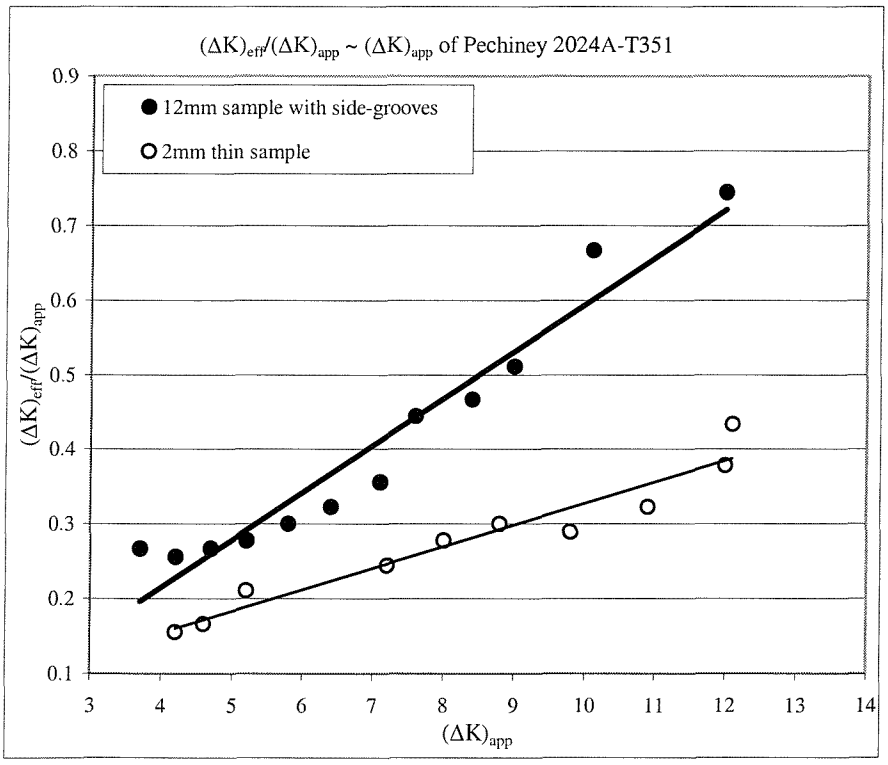

(b)

Figure 5.2 *$(\Delta K)_{eff}/(\Delta K)_{app}$ verses $(\Delta K)_{app}$ at R=0.1: (a) 2024-T351 and (b) 2024A-T351.*

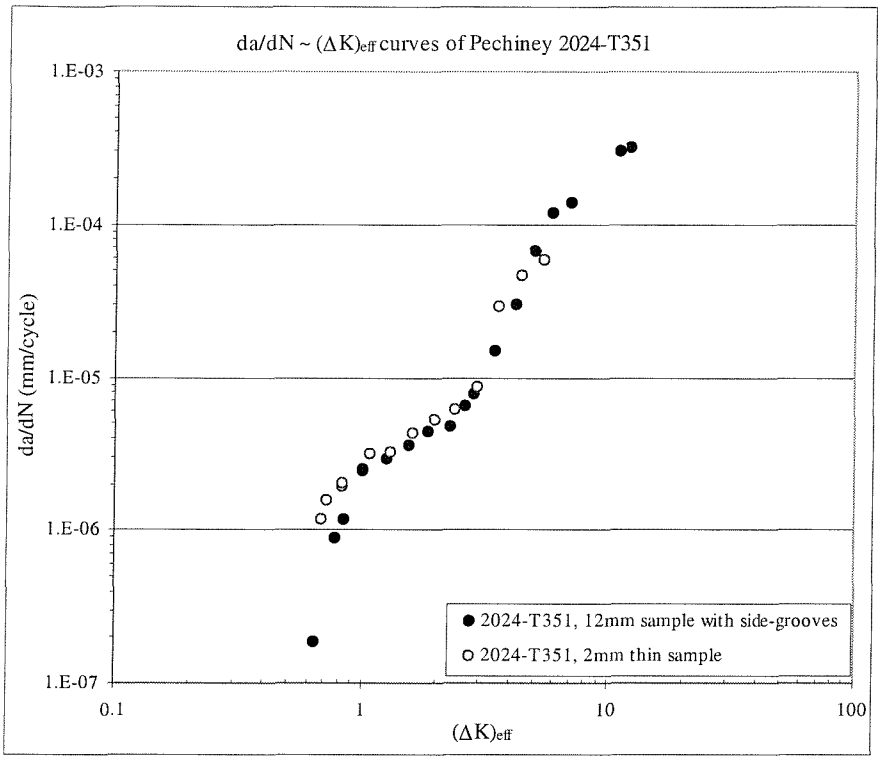

(a)

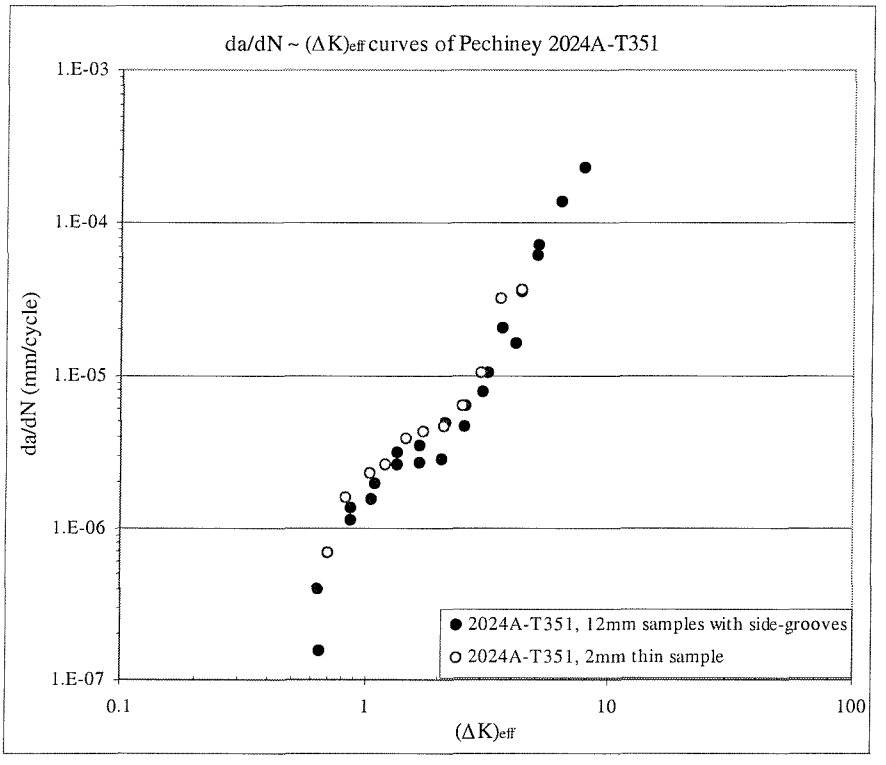

(b)

Figure 5.3 da/dN verses $(\Delta K)_{eff}$ curves at R=0.1: (a) 2024-T351 and (b) 2024A-T351.

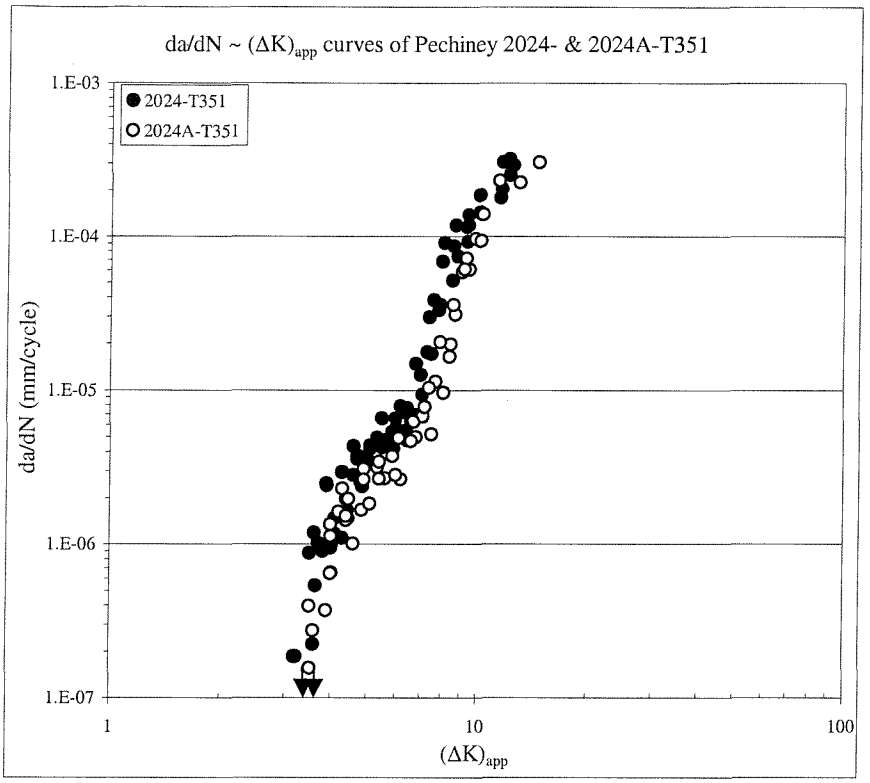

(a)

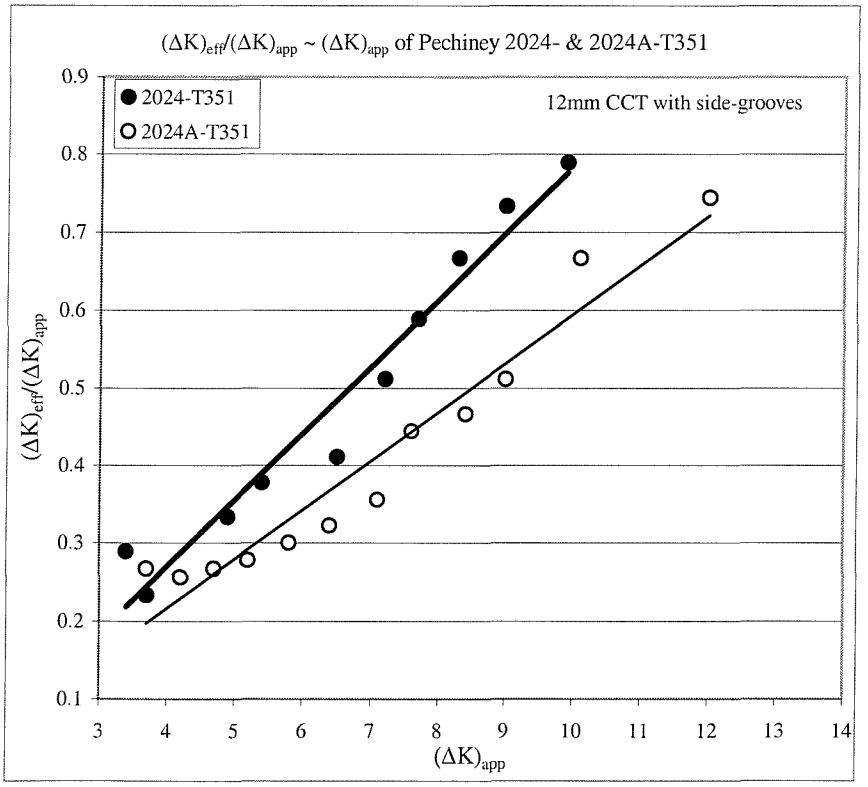

(b)

Figure 5.4 *(a) Crack growth behaviour of 12mm plain- & side-grooved samples and (b) Closure variations of 2024- & 2024A-T351at R=0.1.*

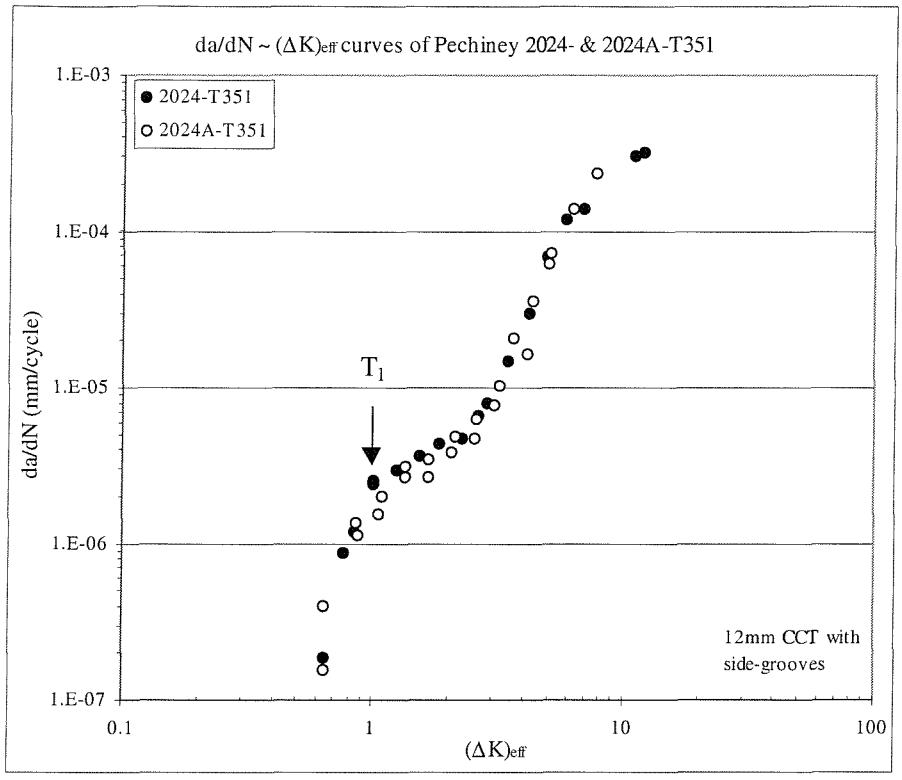

Figure 5.5 da/dN verses $(\Delta K)_{eff}$ curves of 2024- & 2024A-T351at R=0.1.

•2024, ΔK=3.4 MPam$^{1/2}$

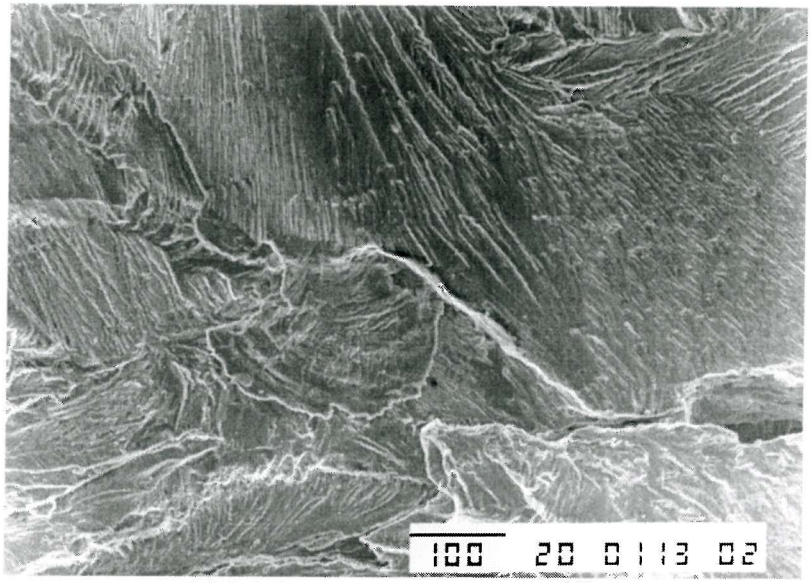

•2024A, ΔK=3.4MPam$^{1/2}$

Figure 5.6 *Fractographic features of 2024- & 2024A-T351 at $(\Delta K)_{app}$=3.4 MPa m$^{1/2}$ of R=0.1.*

•2024, ΔK=5.1 MPam$^{1/2}$

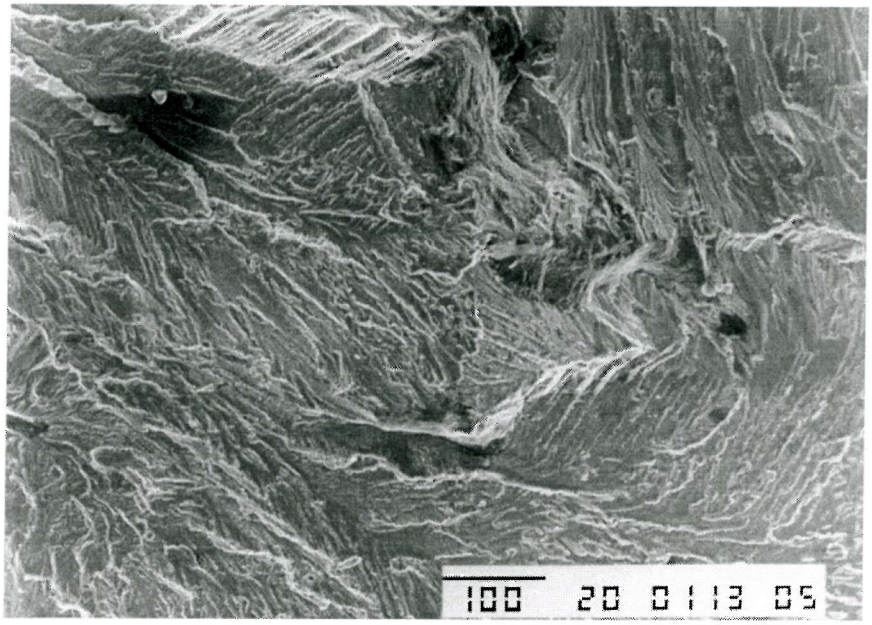

•2024A, ΔK=5.1 MPam$^{1/2}$

Figure 5.7 *Fractographic features of 2024- & 2024A-T351 at $(\Delta K)_{app}$=5.1 MPa m$^{1/2}$ at R=0.1.*

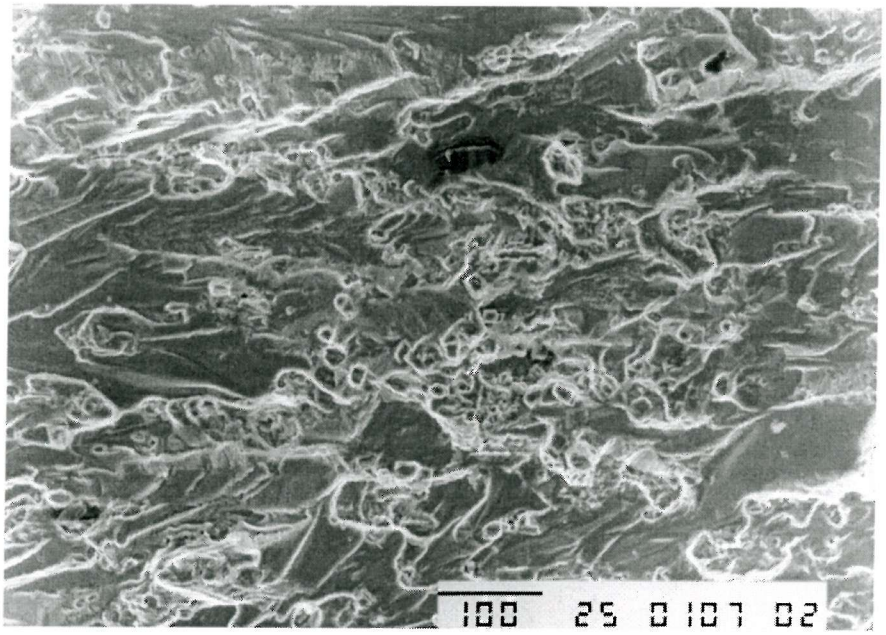

•2024, ΔK=12 MPam$^{1/2}$

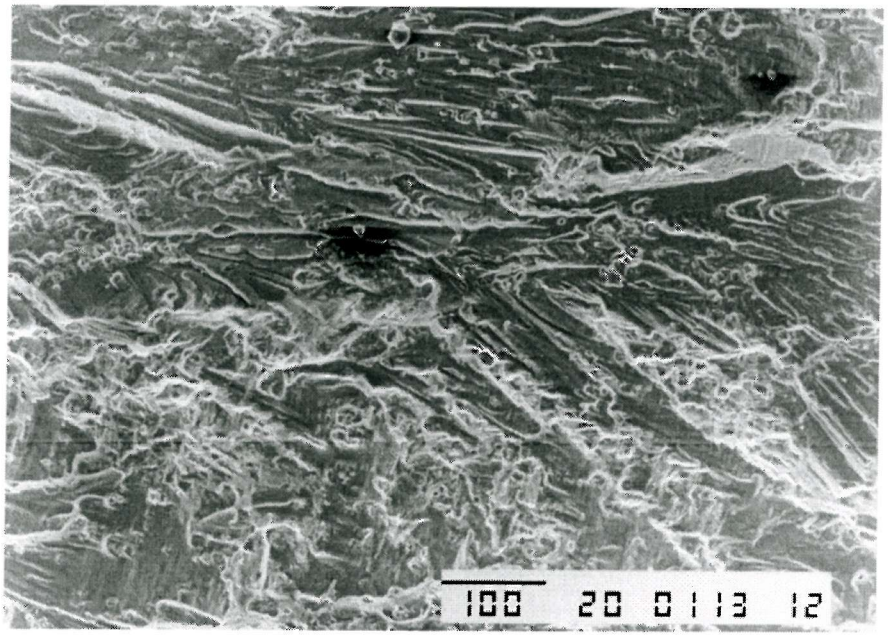

•2024A, ΔK=12MPam$^{1/2}$

Figure 5.8 *Fractographic features of 2024- & 2024A-T351 at $(\Delta K)_{app}$=12 MPa m$^{1/2}$ at R=0.1.*

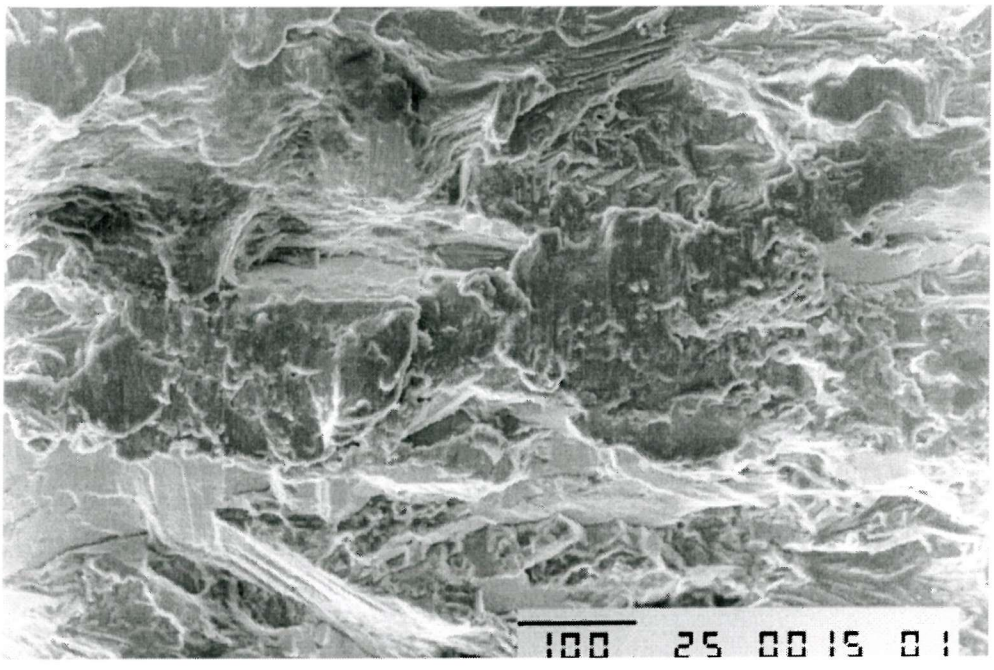

•2024, 2mm thin sample, ΔK=12 MPam$^{1/2}$

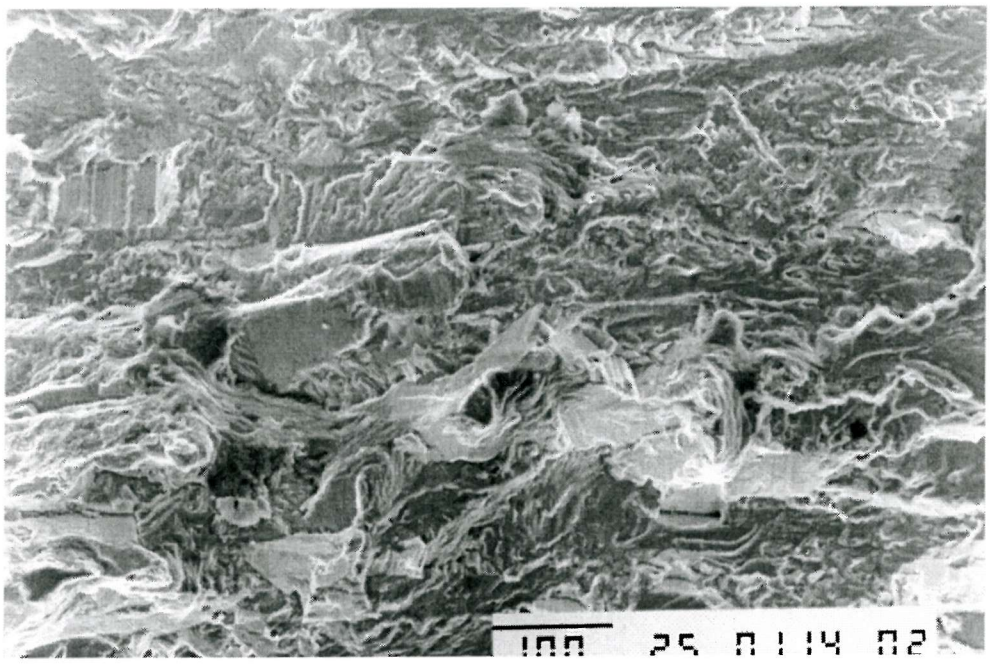

•2024A, 2mm thin sample, ΔK=12 MPam$^{1/2}$

Figure 5.9 Fractographic features of 2mm thick samples of 2024- & 2024A-T351 at $(\Delta K)_{app}$=12 MPa m$^{1/2}$ at R=0.1.

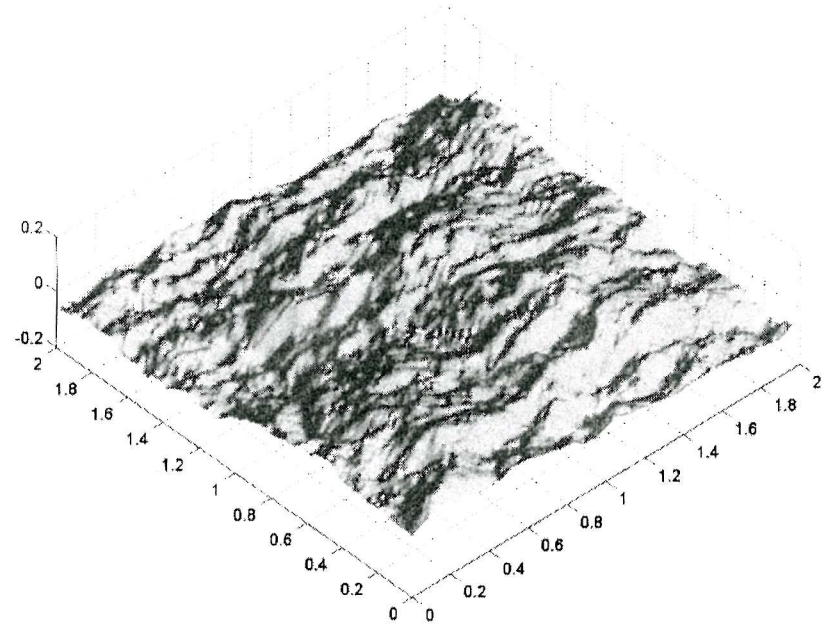

•2024, ΔK=8 MPam$^{1/2}$

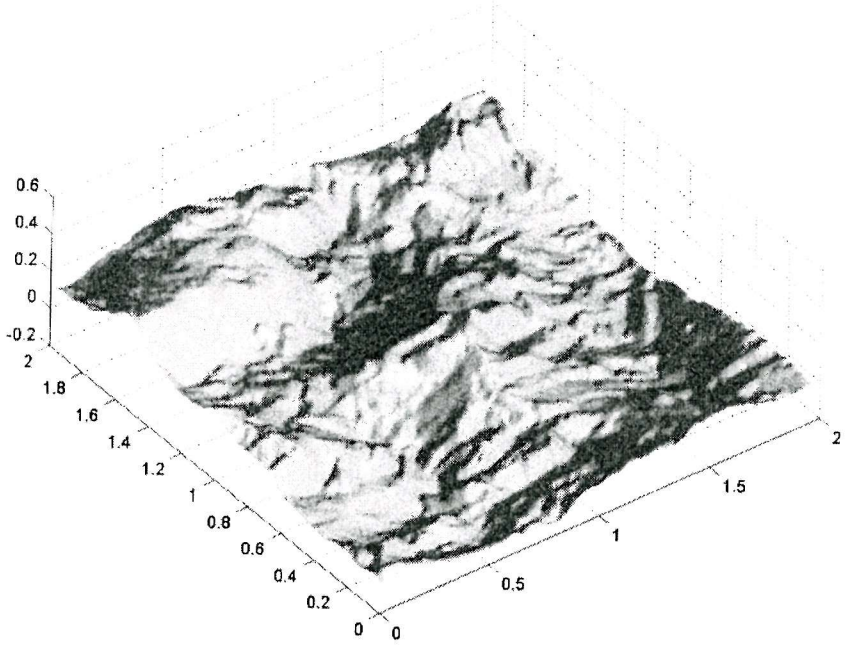

•2024A, ΔK=8 MPam$^{1/2}$

Figure 5.10 3-D reconstruction of fracture surfaces of 2024- & 2024A-T351 at $(\Delta K)_{app}$=8 MPa m$^{1/2}$ at R=0.1.

6. TRANSIENT CRACK GROWTH BEHAVIOUR OF 2024- & 2024A-T351 AFTER SINGLE OVERLOADS

— *This chapter presents predominantly experimental results on single overload tests under various loading and specimen geometry conditions. Post-overload closure variations were carefully assessed. Good correlation between the crack growth behaviour and near-tip closure results was established after a close assessment of compliance curves obtained from near-tip strain gauges essentially using the closure detection methods outlined in Chapter 4. The influence of sample geometry and fatigue surface features on post-overload crack growth is examined. The data are further assessed in relation to the modelling in Chapter 7.*

6.1. Introduction

A substantial part of the service life of aerospace structures is spent under highly variable loading conditions. Prediction of the fatigue life of flawed structural components requires an adequate understanding of the transient behaviour of fatigue crack growth after a change in loading conditions. The application of overloads to an engineering structure before and during service has in fact been considered as a method of extending the service life of components. It has however rarely been used due to an insufficient understanding of the transient processes occurring during and after the overload [1]. In some cases, the classical retardation in crack growth observed after an overload may be completely negated by the acceleration which may also occur, depending on the exact load conditions & material characteristics. Given the complexity that may be involved in real load spectra, it is clear that detailed understanding of the transient fatigue crack growth behaviour following single overloads forms a starting point for understanding variable amplitude fatigue behaviour.

Various mechanisms [2, 3] have been proposed for transient crack growth behaviour after overloads, as discussed in Chapter 2. Among the various mechanisms that may operate, the crack closure concept (particularly plasticity-induced crack closure) is widely recognised, being able to rationalise the three main stages of post-overload fatigue crack growth. Initial crack growth acceleration can be explained by reduced crack closure levels due to the overload-induced tensile plastic deformations ahead of the crack tip. Delayed

crack growth retardation is attributable to subsequently increased closure due to the gradual introduction of enhanced plastic deformation into the crack wake when propagation occurs. Pre-overload crack growth behaviour is recovered when the crack grows beyond the influence zone of the overload plasticity. As noted in Chapters 2 & 4, the interpretation of closure measurements from the literature is far from clear. Given the variability of the information available within the literature, it is clear that careful analysis of closure assessment for the conditions tested is essential for the present thesis, both for qualitative assessment of micromechanisms and for the modelling described in the following chapter.

The present chapter reports experimental results on transient crack growth behaviour in 2024- & 2024A-T351, focusing on the separation of the intrinsic and extrinsic contributions to the post-overload crack growth behaviour in both alloys via detailed crack closure measurements. All overload tests were conducted under essentially the same conditions (in terms of specimen geometry, closure measurement facility, etc) as the previous constant amplitude fatigue tests (see Chapter 3 & 5), with the overload ratio referring to the ratio of the maximum load in the overload cycle to the maximum load in the baseline cycle. Post-overload crack growth rate and closure level variations were carefully measured and analysed as a function of alloy, sample geometry & load conditions. Fractographic features associated with post-overload crack growth were also examined.

Table 6.1 shows the complex overload test matrix. Single overload tests with 50%, 100%, and 150% overload ratios were conducted on 2*mm CCT* samples, and on 12*mm* thick *CCT* samples with and without side-grooves. Three baseline ΔK levels, namely, 6.0, 8.0, and 12.0 $MPam^{1/2}$, were originally used. A pulsed four-probe *PD* system was used to monitor the crack length for the overload study [4]. The main advantage of the pulsed four-probe *PD* system over the two-probe *PD* system (used in the constant amplitude fatigue tests) is the minimisation of the possible influence of crack closure on crack length measurements by applying electrical current at the maximum load of the loading cycle. Pulsed *PD* measurements may therefore eliminate the influence of crack surface contact on the

electrical signal, which was considered significant in the present overload tests given the potentially enhanced crack closure levels and the quite detailed, small crack increments required to describe the post-overload transient. Furthermore, the self-referencing nature of the four-probe system will generally reduce system instability and noise levels.

Table 6.1 Overload Test Matrix for 2024- & 2024A-T351 CCT Panels.

		2024-T351			2024A-T351		
		12*mm* plain sample	12*mm* side-grooved sample	2*mm* sample	12*mm* plain sample	12*mm* side-grooved sample	2*mm* sample
ΔK_b=6.0 *MPam*$^{1/2}$	50% OL	✔			✔		
	100% OL	✔	✔		✔		
	150% OL	✔					
ΔK_b=8.0 *MPam*$^{1/2}$	50% OL	✔	✔	✔	✔	✔	✔
	100% OL	✔	✔	✔	✔	✔	✔
	150% OL	✔			✔	✔	
ΔK_b=12.0 *MPam*$^{1/2}$	50% OL	✔	✔	✔	✔	✔	✔
	100% OL	✔	✔	✔	✔	✔	✔
	150% OL			✔	✔		

✔: *Single overload test was carried out at the prescribed testing condition.*

While the present experimental system was carefully optimised to minimise the effects of electrical and thermal noise (*i.e.* using the four-probe *PD* system) it was still found difficult to reliably clarify differences in transient growth behaviour at a ΔK_b of 6.0 *MPam*$^{1/2}$. Higher resolution in the *PD* system for crack measurement would be required to resolve the necessarily very small post-overload crack length increments associated with such low ΔK_b overload tests. For the sake of simplicity and clarity in the discussions on the effects of material, sample geometry, baseline loading level, and overload ratios on transient crack growth behaviour, only the ΔK_b of 8.0 and 12.0 *MPam*$^{1/2}$ tests are particularly considered hereafter. For 150% overloads, crack growth arrests were observed at a ΔK_b level of 8.0

$MPam^{1/2}$ in 12*mm* plain *CCT* samples of both alloys. Furthermore, in a 12*mm* side-grooved *CCT* sample of 2024A-T351, crack growth arrest was observed at a ΔK_b of $8.0MPam^{1/2}$ after a 150% single overload. No further 150% overload tests were therefore performed on the plain sided *CCT* samples at a ΔK_b of $8.0MPam^{1/2}$, as crack arrests were strongly expected with the increased plane stress influence of the 2*mm* & 12*mm* plain sided samples, as shown later in this chapter (full crack retardation & recovery events were considered the most significant for detailed analysis of the transient phenomena). At a ΔK_b of $12.0MPam^{1/2}$, whilst crack growth arrests were observed in 2*mm CCT* samples of both alloys, conventional transient retardation events occurred after 150% overloads in 12*mm* plain *CCT* samples.

6.2. Closure Measurements after Single Overloads

6.2.1. Compliance Curve Assessment and its Relevance to Post-Overload Closure Measurements

It is widely accepted that the crack closure concept may provide a basis for rationalising post-overload crack growth behaviour. The ability of crack closure to explain various fatigue phenomena is of course dependent upon the reliable and meaningful measurement of the closure point. Inconsistent results for closure loads may arise depending on the measurement location and the data interpretation method [5, 6]. Non-subjective curve fitting methods based on linear and quadratic functions have been discussed in Chapter 4 & Reference [5] after systematic assessment and validation of compliance-based closure measurements. These methods were seen to provide reasonably consistent results using conventional crack mouth clip gauges and properly located near-tip strain gauges under constant amplitude (*CA*) loading condition. It is however expected that under variable amplitude (*VA*) loading conditions reliable closure measurements may become more difficult. Alexander and Knott, in Reference [7] on the ability of closure to explain overload effects, state, "*Much of the confusion and controversy appears to arise from the wide variety of techniques employed, and the different sensitivities of these techniques.*

When the possible effects of different specimen geometries and different materials are added, it is perhaps not surprising that the role of closure is ambiguous." It is therefore important for us to carry out further detailed compliance curve assessment and investigate its relevance to post-overload crack closure measurements for the particular experimental conditions used here (*i.e.* specimen geometry, sensor accuracies, *etc.*).

To minimise the experimental complexity in closure measurement, mechanical compliance curves were used to define closure points in the current investigation, in keeping with the work discussed in Chapter 4. Compliance curves were obtained in the same way as described in Chapter 4 & reference [5].

Figure 6.1 shows the typical shapes of compliance curves (under *CA* loading conditions) from strain gauges behind and ahead of a *CA* crack tip, respectively. During unloading the slope of the compliance curve from the strain gauge behind the crack tip may be seen to become lower when crack closure occurs. An opposite trend is observed in the compliance curve from the strain gauge ahead of the crack tip. The position-dependence of the compliance curve shape is entirely consistent with compressive forces acting through the fracture surfaces once closure occurs as noted in Chapter 4. Both compliance curves clearly exhibit an upper linear part and a lower non-linear part, with a simple single transition point (indicated by the arrows) being consistently detected by the curve fitting methods discussed in Chapter 4. After the application of a single overload, however, a complex evolution of compliance curve shape is observed as the crack propagates into the overload affected zone. Figure 6.2(a) shows 16 compliance curves measured before, during and after the application of a 100% single overload on a *2mm CCT* sample of 2024-T351[1]. The first 15 curves are from one strain gauge initially located ahead of the crack tip (the tip is within ±1mm of the gauge position at all points). The 16th curve was obtained at the same time as the 15th curve but from a gauge ahead of the current tip. Figure 6.2(b) shows the corresponding measuring positions on a diagram presenting the transient fatigue crack growth rate behaviour. Transient crack growth rates, $(da/dn)_t$, are normalised by the baseline crack growth rate, $(da/dn)_b$, and the crack length increment, Δa, is normalised by

[1]For the purposes of this subsection, results are focused on 2024: results obtained for 2024A showed essentially equivalent trends. Relevant differences are discussed later in this chapter.

the monotonic *plane strain* plastic zone size, $r_{p.OL}$, at the maximum load of the overload cycle. The same approach is used to present post-overload transient behaviour throughout this chapter. The use of plane strain condition to calculate $r_{p.OL}$ is mainly due to the difficulties in reliably defining the real stress states of the current overload tests carried out under various conditions. The relevance of this parameter to individual tests will be discussed where relevant. Figure 6.3 shows plastic zone boundaries under plane stress and plane strain (Shih [8]) based on near crack tip stress field solutions derived by Hutchinson [9] and Rice & Rosengren [10] (so-called *HRR* solutions). The stresses, strains and displacements in the near tip '*HRR fields*' exhibit $r^{-1/(n+1)}$, $r^{-n/(n+1)}$ and $r^{1/(n+1)}$ singularities respectively and vary with the polar angle θ, the strain hardening exponent n and the state of stress. A strain hardening exponent, n, of 13 is identified as approximately appropriate for the alloys of interests. Projected dimensions of the plastic zone in the crack growth plane were used to represent the plastic zone size throughout the chapter. As such, the plane stress plastic zone size is larger than plane strain one by approximately a factor of three.

Curve 1 in Figure 6.2(a) was measured before the application of the overload where the strain gauge was situated ahead of the current crack tip. Like the curves in Figure 6.1, there is a single transition point (indicated by the arrow) which can be detected by the curve fitting method. Curve 2 was taken when the crack tip had just propagated into the overload plastic zone by ~ 0.09 $r_{p.OL}$. A reduced closure level was measured by the curve fitting method, which would appear to be consistent with the observed growth acceleration in Figure 6.2(b). Curves 3 and 4 were taken after the crack had propagated into the overload plastic zone by ~ 0.27 $r_{p.OL}$ and 0.37 $r_{p.OL}$, respectively. Their shapes are similar to that of curve 2, although difficulties arose in detecting reliable closure points from these curves. A wide distribution of closure points was seen in analysing such data by the curve fitting method: some results indicated relatively low closure levels, whilst others indicated a relatively high closure points. Gradually increased closure levels may be expected with further penetration of the crack into the overload plastic zone if crack closure is indeed a primary mechanism for rationalising post-overload crack growth. Careful examination of

subsequent compliance curves indicated the presence of two transition points (clear by eye in the later curves in Figure 6.2(a) and 6.4(a)). Similar phenomena have been reported by Paris and Hermann [11] and Ranganathan [12]. These authors attribute the lower transition point to far-field crack opening and the upper transition point to near-tip crack opening. In terms of the present work, qualitative correlation of the closure results with the transient crack growth behaviour is apparent when the upper transition point is defined as the closure point during unloading (*i.e.* closure loads increase as overload retardation occurs). Curve 5 in Figure 6.2(a) shows the compliance curve when the crack penetrated into the overload plastic zone by ~ 0.46 $r_{p.OL}$. The highest closure level (~ 0.86) was detected from this curve, which agrees well with the position of the maximum crack growth retardation point in Figure 6.2(b).

In terms of variability in measured closure levels determined by the curve fitting method, this is clearly consistent with there being more than one transition point on the curves and the fact that current curve fitting methods use only a simple quadratic polynomial to represent non-linearity in the lower part of the compliance curve (*i.e.* only one transition point can be meaningfully detected by the curve fitting methods). Such dual transition behaviour in the compliance data may be one of the reasons for the confusions and controversies in the role of crack closure explaining post-overload crack growth behaviour as pointed out by Alexander and Knott [7]. In the present study, modified curve fitting methods were applied to the dual transition curves where the second order polynomial fitting was not applied to the whole range of the lower part of the curve; rather, the non-linear part was truncated to remove the lower transition based on visual assessment of where the lower transition point lies. This clearly introduces an unwanted arbitrary component to the closure measurement process in defining the truncation point. In most instances this was considered acceptable as the dual transitions were quite clear for much of the overload transients though some difficulties exist at the very early stages (*e.g.* curves 3 & 4 of Figure 6.2(a)) of post-overload crack growth, especially for thick samples under lower baseline ΔK level and smaller overload ratios. Visual checks on the first transition point were carried out for 'difficult' cases to qualitatively confirm the curve fitting closure measurements. Although a certain degree of uncertainty must still be attached to these

points, it should be noted that by the time crack growth rates reached their minimum in a given transient, dual transitions were usually well established in the associated compliance curves, hence the main features of the overload transient may be considered to be captured in the present work.

Curves 6 to 13 in Figure 6.2(a) were measured after the crack had propagated into the overload plastic zone by ~ 0.55 $r_{p.OL}$ to 3.49 $r_{p.OL}$. The upper non-linear process appears to dominate the non-linearity of the compliance curve, with decreasing closure levels being measured with ongoing crack growth. The closure results appear to be in good agreement with the length of the crack growth transient after the overload (again see Figure 6.2(b)). Curves 14 and 15 were obtained when the crack had propagated into the overload plastic zone by ~ 4.60 $r_{p.OL}$ and 4.96 $r_{p.OL}$, respectively. It is clear that pre-overload closure levels are recovered at this stage and the result correlates well with the crack growth behaviour in Figure 6.2(b).

Similar observations were made for the other single overload tests for the different sample geometries and loading conditions. Figure 6.4(a) shows the evolution of compliance curves of 12*mm* side-grooved *CCT* sample of 2024-T351 after the application of a 100% single overload at ΔK_b =12 $MPam^{1/2}$. Figure 6.4(b) shows the corresponding closure measurement positions on the diagram presenting the transient fatigue crack growth behaviour. The compliance curves were obtained in a similar manner to those in Figure 6.2(a). Measured closure variations (upper closure point) appear to correlate well with the general crack growth rate variations after the overload, again suggesting a significant role of crack closure in post-overload fatigue behaviour. It should be noted that more difficulty was encountered in obtaining reliable closure levels at the early stage of post-overload crack growth in the side grooved 12*mm* samples since the first transition point on the compliance curves was less obvious than in 2*mm* samples under the same loading condition.

In terms of baseline load effects, similar conclusions were drawn from the single overload test of 2*mm* thick *CCT* sample of 2024-T351 after a 100% overload under ΔK_b of 8

$MPam^{1/2}$. Figures 6.5(a) & (b) show the same pattern of changes in the shape of the compliance curves and crack growth rates after overload. Whilst similar behaviour was apparent, it was generally noted that changes in compliance curve shapes became more subtle with decreasing $(\Delta K)_b$ and/or smaller overload ratios, and/or increasing sample thickness.

Figure 6.6 shows 15 global compliance curves obtained with a conventional crack mouth clip gauge at the same time as the 'local' compliance curves in Figure 6.2(a). Little disturbance of the compliance curves can be seen during the overload transient. It is clear that crack closure results based on such curves may then be problematic for overload analysis, even if the curve fitting method is employed (curve fitting actually showed no appreciable variation in closure levels from such crack mouth compliance data). This is consistent with results reported in the first round robin exercise of *ASTM TASK GROUP E24.04.04* on crack closure measurement and analysis [13].

6.2.2. Results and Discussions: Post-Overload Crack Closure Behaviour

6.2.2.1. Closure Measurements

It is clear from the above experimental observations that the post-overload crack closure process is more complicated than that under *CA* loading conditions. After the application of a single overload crack closure might, in the first instance, be expected to come from both the pre-overload crack conditions and the overload effects near the crack tip. Such duplex crack contact is then qualitatively consistent with the complex evolution of the shapes of the compliance curves illustrated in Figures 6.2, 6.4 and 6.5 (the phenomenon of complex/multiple closure events is considered further in Chapter 7)[2]. The early stage contribution of overload plastic deformation to the change in sample compliance is initially very limited of course and local to the crack tip. It is the local stresses and strains at the

[2] It may be noted that whilst Figures 6.2, 6.4 & 6.5 may intrinsically involve a change in the sign of the compliance slope changes due to closure (since the strain gauges involved go from being ahead of the current crack tip, to being behind the crack tip), the distinct changes in closure point and the double curvature are not present in non-overloaded crack growth.

crack tip however that may be expected to be controlling factors in terms of crack growth (*i.e.* it is only cyclic plastic strains at the tip that can contribute to crack extension). The fact that the influence of a contact force on the near-tip stress and strain intensification increases exponentially as the distance to the crack tip decreases ($K_P \propto P \cdot r^{-1/2}$, where K_P is the stress intensity caused by the contact force P acting at distance r behind the crack tip) illustrates the importance of the detection of the local closure events. It is therefore clear that far-field closure measurements via crack mouth clip gauges, back-face strain gauges, *etc.* need not reflect the shielding effects on crack growth after the single overload, especially in the early stages of post-overload crack growth. The present work may be seen to confirm various reported comparisons between crack closure results from mechanical compliance, where commonly used remote (global) techniques are seen to yield closure levels that are lower than near-tip derived data [4, 13-15]. As a result, the closure results discussed here are specifically from local compliance curves obtained with near-tip strain gauges unless otherwise specified.

6.2.2.2. Closure Behaviour

Figure 6.7 shows the apparent closure variations in 2024- & 2024A-T351 after a 100% single overload at a baseline ΔK of $12.0 MPam^{1/2}$. Closure level is presented as the ratio of effective ΔK over applied ΔK. The crack length increment is again normalised by the monotonic plastic zone size in plane strain at the maximum load of the overload cycle, $r_{p.OL}$. Figure 6.7(a) shows the results for the $2mm$ thick *CCT* samples of both alloys tested, whilst Figure 6.7(b) shows the results of $12mm$ thick *CCT* samples with side-grooves. Both alloys show similar basic patterns in the variation of crack closure after the overload. After the overload there is a brief decrease in closure level. The closure level then reaches its maximum after the crack has propagated into the overload plastic zone by approximately 0.5 $r_{p.OL}$. Pre-overload closure levels are eventually recovered with ongoing crack propagation.

The observation that maximum retardation occurred after the crack had propagated into the overload plastic zone by ~ 0.5 $r_{p.OL}$ (monotonic plane strain overload plastic zone size) for both alloys for different sample geometries suggests that maximum retardation actually occurred relatively earlier under plane stress conditions in relation to the actual overload plastic zone size (*i.e.*, since plane stress plastic zones are larger than those in plane strain). It is difficult to identify the exact degree of plane stress or plane strain in a real sample. In the ΔK_b=12.0$MPam^{1/2}$/100% overload case, it may be noted that the maximum extent of the surface plastic zone is of the same order as the smaller sample thickness (~1.7mm), and, as such, significant through-thickness stress relaxation may be expected to occur [16]. Also worth noting is that under the same loading and sample geometry conditions, the normalised overload affected distances in Figure 6.7 for both alloys are quite close. For 2*mm* thick samples it is about 4.5 to 5.0 $r_{p.OL}$. For side-grooved 12*mm* thick samples, it is about 3.0 to 4.0 $r_{p.OL}$. Since the parameter $r_{p.OL}$ takes into account of the difference in yield strength in the two alloys, it may be concluded that the scale of the overload plastic zone controls the transient behaviour, with clear implications for the role of *PICC* in controlling the post-overload closure variations in the two alloys (*i.e.*, transient effects scale simply with plastic zone size). It may be noted that the difference in r_p values will be off the order of 20% based on σ_y values. Whilst there is clearly ambiguity in establishing overload distances, the current results were consistent over multiple tests. The overload distance observations for the two alloys must be considered against the sample thickness effects, *i.e.* the actual overload plastic zone will have been larger in the 2*mm* sample than the 12*mm* side groove one for the load conditions indicated (ΔK_b=12.0$MPam^{1/2}$). On the assumption that the 2*mm* sample approaches plane stress conditions during the overload, the actual normalised retardation distance is of the order of 1.6 plane stress overload plastic zone dimensions. The overload plastic zone size is therefore not a unifying scaling factor between plane stress and plane strain conditions, with the overload transient being effectively much longer in plane strain (*i.e.* 3-4 $r_{p.OL}$). Given a generally acknowledged reduction in *PICC* effects in plane strain, this effectively extended overload transient is clearly of interest. A change in predominant closure mechanism between the stress states is of particular interest in the first instance, as *RICC* processes might be expected to make a

more significant contribution to closure behaviour in the more plane strain samples (*i.e. PICC* is reduced by in-plane flow constraint and *RICC* is enhanced by reduced crack flank opening displacements). Both Carlson *et al* [17] and Suresh [18] have previously suggested that microstructural effects on closure (such as *RICC*) during overload events are required to explain the extension of growth rate transient effects beyond the nominal plastic zone size. *RICC* (and indeed other mechanisms such as *OICC*) need not necessarily be the cause for retardation, but they may effectively prolong retardation, (*i.e.* increase total number of delay cycles) once typical near-threshold mechanisms are activated in the post-overload growth region. Analytical support for the role of *RICC* in post-overload transients is considered in Chapter 7.

In terms of differences in behaviour between the two alloys, it was evident that closure benefits evident in *CA* loading of 2024A were carried over into the overload transients. This may be seen more clearly in Figure 6.8 for the two alloys at ΔK_b=8.0$MPam^{1/2}$, where baseline closure differences were more pronounced than at ΔK_b=12.0$MPam^{1/2}$ in Figure 6.7. Slightly shorter overload-affected distances were observed under ΔK_b=8.0 $MPam^{1/2}$ than for a ΔK_b of 12.0 $MPam^{1/2}$. These were about 3.0-4.0 $r_{p.OL}$ for the 2*mm* samples and 2.5-3.0 $r_{p.OL}$ for the 12*mm* side-grooved samples. In the first instance the overload distances for the two sample formats may be seen to be proportionally closer for the lower ΔK_b case, consistent with decreasing plain stress influences.

6.3. Transient Crack Growth Behaviour

6.3.1. Post-Overload Growth Rates

Figure 6.9-12 show the transient crack growth behaviour of 2024 & 2024A after 50% & 100% overloads at baseline ΔK_b of 8 & 12 $MPam^{1/2}$. For the convenience of comparison, the crack length increment, Δa, is normalised by the maximum monotonic plane strain plastic zone radius, $r_{p.OL}$ (in keeping with the previous section). The measured transient

crack growth rate, $(da/dn)_t$, is also normalised, using the baseline crack growth rate, $(da/dN)_b$, which takes into account of the material difference in baseline crack growth rates at the same ΔK_b level. Whilst some differences in alloy behaviour may be identified in Figure 6.9 for example, the differences are relatively small and are non-systematic when considered against the various other load conditions plotted in Figures 6.10-12. As such it may be said that the material influence on the transient crack growth behaviour of the two alloys can be well accounted for by the difference of the *CA* baseline crack growth behaviour and yield strengths, *i.e.* no marked difference in the transient crack growth behaviour was seen when data are plotted in a normalised manner.

Table 6.2 Main Features of Post-Overload Crack Growth Tests of 2024- & 2024A-T351.

Main Features	Sample Geometry	Alloy	$(\Delta K)_b$=8$MPam^{1/2}$		$(\Delta K)_b$=12$MPam^{1/2}$	
			50%OL	100%OL	50%OL	100%OL
Retardation Distance ($r_{p.OL}$)	12*mm* plain *CCT*	2024-T351	~2.0-2.2	~3.0-3.5	~1.7-2.3	~3.5-4.0
		2024A-T351	~1.5-2.2	~3.0-3.5	~1.8-2.3	~3.5-4.0
	12*mm CCT* with side-grooves	2024-T351	~1.5-2.2	~2.5-3.0	~1.5-2.0	~2.8-3.5
		2024A-T351	~1.4-2.0	~2.5-3.0	~1.5-2.0	~2.8-3.5
	2*mm CCT*	2024-T351	~2.0-3.0	~3.5-4.5	~2.5-3.2	~4.0-5.0
		2024A-T351	~1.7-2.3	~3.5-4.5	~2.5-3.2	~4.0-5.0
Retardation Magnitude $(da/dn)_t/(da/dn)_b$	12*mm* plain *CCT*	2024-T351	~1/2.5	~1/10	~1/3	~1/35
		2024A-T351	~1/2.5	~1/10	~1/3	~1/35
	12*mm CCT* with side-grooves	2024-T351	~1/2.5	~1/10	~1/3	~1/25
		2024A-T351	~1/2.5	~1/10	~1/3	~1/25
	2*mm CCT*	2024-T351	~1/3.5	~1/15	~1/5.5	~1/60
		2024A-T351	~1/3.5	~1/15	~1/5.5	~1/60
Location of Maximum Retardation ($r_{p.OL}$)	12*mm* plain *CCT*	2024-T351	~0.7	~0.5-0.7	~0.5	~0.4-0.5
		2024A-T351	~0.4	~0.5-0.7	~0.3-0.4	~0.2-0.3
	12*mm CCT* with side-grooves	2024-T351	~0.6	~0.4-0.6	~0.5	~0.4-0.6
		2024A-T351	~0.4	~0.4-0.6	~0.5-0.6	~0.4-0.6
	2*mm CCT*	2024-T351	~0.3-0.5	~0.4-0.6	~0.4-0.5	~0.4-0.5
		2024A-T351	~0.4-0.5	~0.4-0.6	~0.5	~0.4-0.5

Figure 6.9(c) shows the post-overload crack growth behaviour of the 2*mm* CCT samples of 2024- & 2024A-T351 after a 100% overload at ΔK_b =12.0 $MPam^{1/2}$. This is the closest case to plane stress among the tests reported here ($r_{p.OL}$/sample thickness of approximately unity). Enhanced overload effects were observed in these thin samples for both alloys when compared with 12*mm* plain *CCT* results in Figure 6.9(a). The growth rates were decreased by about 60 times at their lowest levels as opposed to ~35 times in the thick samples. Compared with the 12*mm* plain and 2*mm* thick *CCT* samples, the weakest overload effects were consistently observed for 12*mm* side-grooved *CCT* samples of the two alloys, as shown in Figure 6.9(b). The growth rates were decreased by about 25 times at their lowest levels when the crack had propagated into the overload plastic zone by about 0.4-0.6 $r_{p.OL}$.

Figure 6.10 shows post-overload crack growth results in the three *CCT* sample geometries after a 100%OL at ΔK_b =8.0 $MPam^{1/2}$. Very similar sample geometry and material effects on transient crack growth behaviour were seen to those in Figure 6.9, except that the overload effect is generally less in this case. For the 12*mm* plain *CCT* samples (Figure 6.10(a)), the normalised overload affected distance is about 3.0-3.5 $r_{p.OL}$ (~ 0.7 - 0.8*mm* for 2024-T351 and ~ 0.8-1.0*mm* for 2024A-T351). The growth rates were decreased by about 10 times at their lowest levels for both alloys. For the 2*mm* samples (Figure 6.10(c)), marginally stronger overload effects were observed, with the lowest growth rates being about 18 times less than the pre-overload level. Again, the weakest overload retardation effects occurred in the 12*mm* samples although little distinction was evident between the side grooved and non-side grooved cases.

Figures 6.11-12 show the transient crack growth results for the two alloys after 50% single overloads at baseline ΔK levels of 12.0 and 8.0 $MPam^{1/2}$ respectively. The influences of different materials, sample geometry, and the baseline ΔK levels were investigated in the same way as those in the 100% single overload tests. Decreasing relative overload effects were observed with decreased overload ratios in particular, and decreased baseline ΔK levels.

6.3.2. Correlation Between Crack Growth Transients and Measured Closure Levels

Good qualitative agreement was observed between the transient crack growth behaviour (Figures 6.9-12) and the measured post-overload variations (Figures 6.7-8). To further assess this point, quantitative correlation between the transient crack growth and the measured crack closure results have been made, see Figures 6.13-14. These '*predicted*' crack growth transients were based on closure measurements presented earlier in this chapter and Figure 5.5 in Chapter 5 (see also [19]), where $(\Delta K)_{eff}$ was used to account for closure effects (see Figures 6.7-8), based on crack growth from the *CA* fatigue tests of 12*mm* side-grooved samples (minimising mixed stress state effects on the closure measurements).

Figure 6.13 shows the transient crack growth predicted by the closure results (Figure 6.7) taken after a 100%OL at ΔK_b=12.0$MPam^{1/2}$ in 2*mm CCT* and 12*mm* side-grooved *CCT* samples of the two alloys (the samples closest to ideal plane stress and strain, respectively). Very similar post-overload crack growth behaviour is predicted for both alloys. For 2*mm CCT* samples (Figure 6.13(a)), maximum retardation occurred after the crack had propagated into the overload plastic zone by about 0.5 $r_{p.OL}$. The size of the overload-affected zone is about 4.5 $r_{p.OL}$. These results are consistent with measured crack growth results in Figure 6.9. The predicted magnitude of the retardation is however smaller than the measured crack growth results. As mentioned earlier in the last section, the predicted growth rates for the 2*mm* sample were decreased by about 35 times at their lowest levels, as opposed to 60 times in Figure 6.9(c). For 12*mm* side-grooved *CCT* samples (Figure 6.13(b)), the predicted location of the maximum retardation was about 0.5 $r_{p.OL}$, with the growth rates being predicted to decrease by ~ 17 times at their lowest levels. The retardation distance was about 3.0 $r_{p.OL}$. These results are again consistent with the measured crack growth results (Figure 6.9(b)), although the maximum predicted retardation magnitude is again under-predicted.

Figure 6.14 shows the transient crack growth predicted from closure results (Figure 6.8) after a 100%OL at ΔK_b=8.0$MPam^{1/2}$ in 2*mm CCT* and 12*mm* side-grooved *CCT* samples of the two alloys. Again it may be seen that the general overload transient behaviour is well captured by the predictions, with total overload retardation distances and position of the maximum retardation being quite accurately represented. In terms of exact growth rate values, the predictions are less consistent than those for the ΔK_b=12.0$MPam^{1/2}$ data, with peak retardation levels in particular being more variable between the two alloys and in relation to actual measured *da/dN* values. The magnitude of the differences must however be considered against the greater experimental uncertainty in the ΔK_b=8.0$MPam^{1/2}$ data (both in closure and *da/dN* determination); as such the present closure data are still considered to provide a predominant explanation of the measured transient behaviour. The present results therefore confirm the work of Ranganathan [12] in noting that the evolution of the upper crack opening level in complex post-overload compliance curves was consistent with the crack growth evolution.

6.3.3. Sample Geometry Effects on Post-Overload Crack Growth

It is well recognised that different overload retardation effects may be observed on samples of different geometry [20-22]. Sample geometry effects will also vary with the overload ratio and the baseline ΔK level. This kind of sample geometry-dependence is easily attributed to the stress state influence on post-overload fatigue behaviour. In the present study, 2*mm* sample tests are carried out to simulate plane stress state under test conditions of higher baseline ΔK levels and overload ratios. 12*mm* side-grooved samples are used to simulate the plane strain condition: combined plane stress/strain state effects will be expected on 12*mm* plain *CCT* samples and the 2*mm* samples at lower ΔK_b and overload ratios.

Consistent experimental observations on the sample geometry effects on post-overload fatigue behaviour were observed (Figures 6.7-14). For higher ΔK_b conditions particularly 2*mm CCT* samples exhibit the strongest overload effects on both crack closure and crack

growth rate variations, with the 12*mm* side-grooved samples exhibiting the weakest overload effects. Increased overload effects were also observed with increase in overload ratio and/or baseline ΔK level. There seems however to be no systematic sample geometry influence on the relative locations of the maximum retardation point from the present experimental work. The maximum retardation happened after the crack had propagated into the overload plastic zone by about 0.5 $r_{p.OL}$. The uncertainty regarding the maximum retardation position may be related to insufficient stability of the current *PD* system. Repeated test interruptions due to the closure measurements in the middle of the overload period may cause some fluctuations of the *PD* signals, which will shift the transient crack growth data to some extent.

6.3.4. Fractographic Features After Single Overloads

Figure 6.15 shows fractographic features of 2024- & 2024A-T351 after 100% overloads at a baseline stress intensity range of 12.0 $MPa\ m^{1/2}$. Both alloys show a similar ductile-to-crystallographic crack growth mode transition after overload. Some interactions with inter-metallic particles were observed in the vicinity of where the overload was applied, which may therefore contribute to the brief crack growth acceleration due to the application of the overload. There is clear evidence of post-overload oxide debris, consistent with the role of crack closure in post-overload crack growth (*i.e.* local fretting effects) (see Chapter 2).

Figure 6.16 illustrates the transition in crack growth modes during post-overload crack growth in a 12*mm* thick *CCT* sample of 2024A alloy after a 100% single overload at a baseline ΔK of 12 $MPa\ m^{1/2}$. Figure 6.16(a) was taken 0.5 *mm* away from the position of overload application. A typical crystallographic crack growth mode is shown clearly on the fracture surface, indicating the activation of near-threshold growth modes. Figure 6.16(b) shows the surface features 2*mm* away from the position of overload application. Pre-overload crack growth is mostly recovered although it is not easy to quantify the retardation distance accurately from the *SEM* images only. It was however found that

fracture mode transition distances were qualitatively consistent with the crack growth results (*i.e.* growth mode had returned to 'normal' once growth rates were recovered).

Figure 6.17 shows 3-D reconstructions of the fatigue surfaces after a 100% single overload under ΔK_b of 12 $MPam^{1/2}$ on 12*mm* plain *CCT* samples of 2024- & 2024A-T351. Rougher fatigue surfaces were clearly observed on both alloys after the overload, which may be associated with more crystallographic crack growth noted above.

6.4. Conclusions

1. Detailed assessment of compliance curves is necessary to obtain crack closure measurements during the overload tests, particularly in relation to complex curve shapes found post-overload. Local compliance curves from near-tip strain gauges would appear to be able to detect post-overload closure variations while global compliance curves from a crack mouth clip gauge cannot.

2. It is found that the evolution of the upper transition points on post-overload compliance curves correlates well with transient post-overload crack growth, consistent with near-tip closure processes dominating overload behaviour. The curve fitting method described in Chapter 4 may still be used to detect this first transition point (with subjective data '*trimming*').

3. Close correlation between transient crack growth and measured closure variations has been observed when used in conjunction with *CA* '*intrinsic*' crack growth data. Apparent post-overload crack growth behaviour in 2024 and 2024A is very similar, particularly if normalised retardation distances and crack growth rates are considered. The *CA* closure benefit identified in 2024A is essentially carried through to overload behaviour.

4. Sample stress state conditions clearly influence post-overload behaviour in the tests. Enhanced post-overload retardation effects have been observed on samples closer to plane stress conditions. It is clear that, in terms of the operative maximum plastic zone dimension for a given overload and stress state, plane strain overload transients are however longer than those seen under plane stress conditions. Overload severity (in terms of maximum retardation and transient distance) are reduced for decreasing ΔK_b.

5. Post-overload crack growth is clearly influenced by growth mode transitions. Classical activation of near-threshold mechanisms is observed.

References

[1] J. F. Knott and A. C. Pickard, (1977), *Metal Science,* pp.399-404.

[2] K. T. Venkateswara Rao and R. O. Ritchie, (1988), *Acta Metall.,* Vol.36, pp.2849-2862.

[3] M. Skorupa, (1999), *Fatigue Fract Engng Mater Struct.,* Vol.22, pp.905-926.

[4] C. M. Ward-Close and R. O. Ritchie, (1988), *ASTM STP 982*, pp.93-111.

[5] Y. Xu, P.J. Gregson and I. Sinclair, (2000), *Materials Science and Engineering A*, Vol.284, pp.114-120.

[6] R. Kumar, (1992), *Eng. Fract. Mech.,* Vol.42, pp.389-400.

[7] D. J. Alexander and J. F. Knott, (1987), *Proc. Third Int. Conf. Fatigue and Fatigue Thresholds,* Charlottesville, Virginia, pp.395-406.

[8] C. F. Shih, (1973), *Elastic-Plastic Analysis of Combined Mode Crack Problems,* Ph.D Thesis, Cambridge, Mass.: Harvard University.

[9] J. W. Hutchinson, (1968), *J. of the Mechanics and Physics of Solids,* Vol.16, pp.13-31.

[10] J. R. Rice and G. F. Rosengren, (1968), *J. of the Mechanics and Physics of Solids,* Vol.16, pp.1-12.

[11] P. C. Paris and L. Hermann, (1981), *Fatigue Thresholds*, J. Backlund, et al., Eds., EMAS Publications, Wareley, UK, p.11.

[12] N. Ranganathan, (1999), *ASTM STP 1343*, pp.14-38.

[13] E. P. Phillips, (1989), *NASA Technical Memorandum 101601*, Langley Research Centre, Hampton, Virginia.

[14] J. D. Dougherty, T. S. Srivatsan and J. Padovan, (1997), *Engng. Fract. Mech.*, Vol.56, pp.167-187.

[15] J. C. Newman, Jr., (1981), *ASTM STP 748,* J. B. Chang and C. M. Hudson, Eds., American Society for Testing and Materials, pp.53-84.

[16] S.T. Rolfe and S.R. Novak, (1970), *ASTM STP982*, American Society for Testing and Materials, 124.

[17] R. L. Carlson, G. A. Kardomateas, and P. R. Bates, (1991), *Int. J. Fatigue*, Vol.13, pp.453-460.

[18] S. Suresh, (1985), *Engineering Fracture Mechanics*, Vol.21, pp.1169-1170.

[19] Y. Xu, P. J. Gregson, and I. Sinclair, (2000), *Materials Science Forum,* Vols. 331-337, pp. 1525-1530.

[20] F. J. McMaster and D. J. Smith, (1999), *ASTM STP 1343,* pp.246-264.

[21] J. P. Hess, A. F. Grandt Jr., and A. Dumanis, (1983), *Fatigue of Engineering Materials and Structures,* Vol.6, pp.189-199

[22] C. Hsu, K. K. Chan, and J. Yu, (1999), *ASTM STP 1343*, pp.285-303.

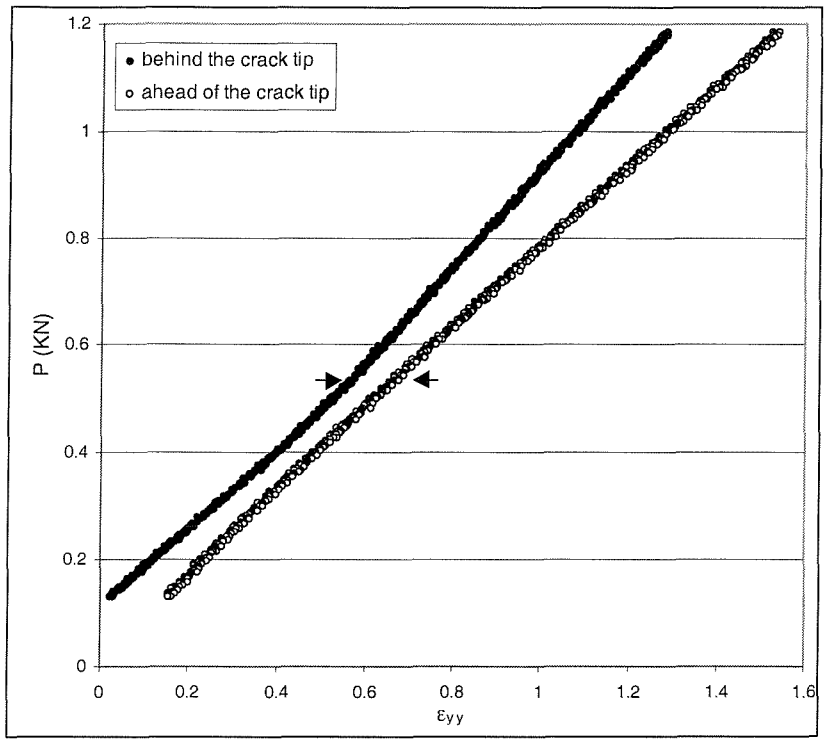

Figure 6.1 *Compliance curves from near-tip strain gauges behind and ahead of the crack tip (under CA loading condition).*

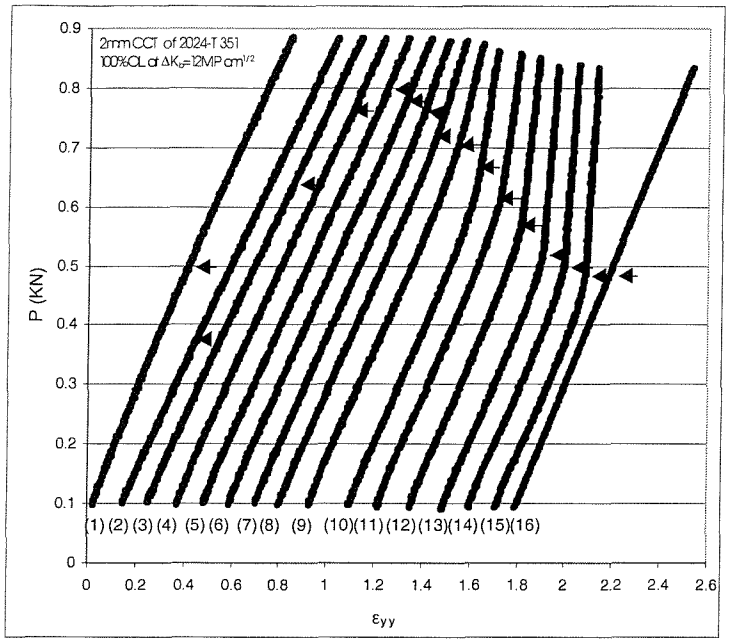

(a)

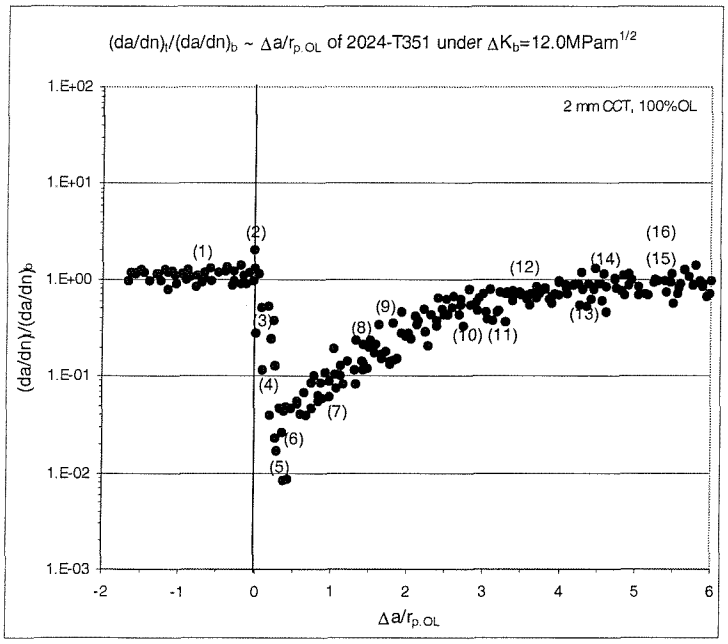

(b)

Figure 6.2 100%OL on 2mm CCT of 2024-T351 at ΔK_b=12.0MPam$^{1/2}$: (a) Evolution of near-tip post-overload compliance curves and (b) corresponding closure measuring positions in the transient crack growth process.

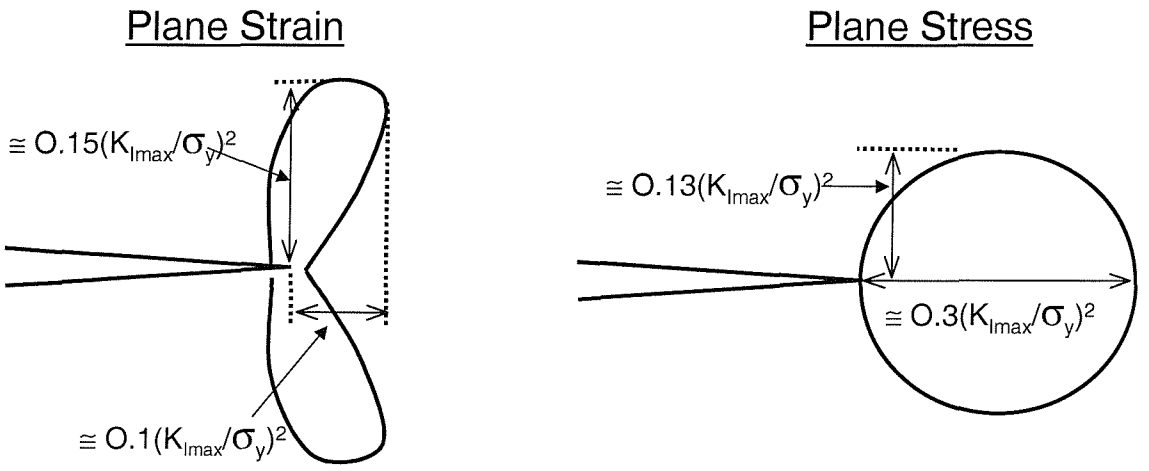

Figure 6.3 Definition of plastic zone size under plane stress and plane strain.

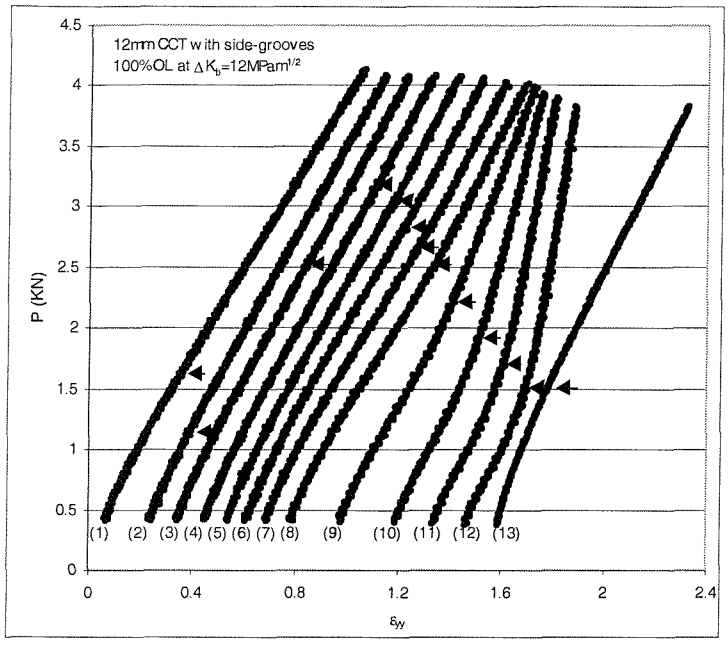

(a)

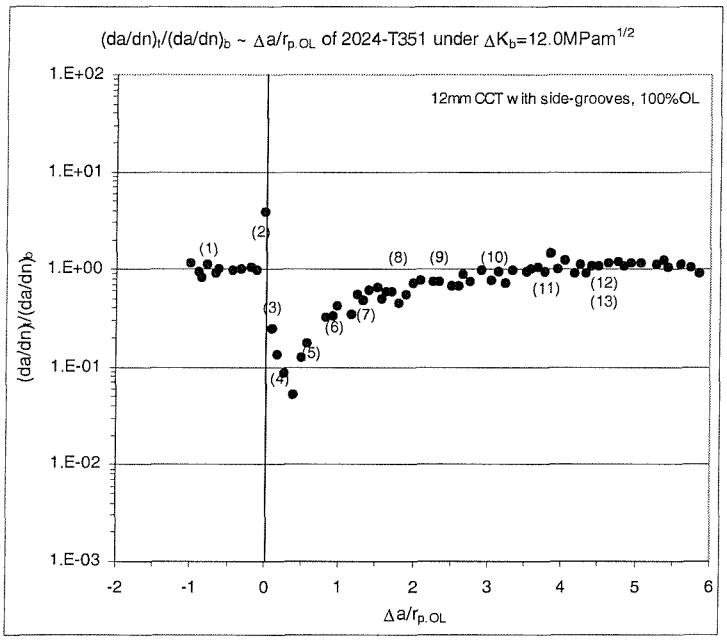

(b)

Figure 6.4 *100%OL on 12mm side-grooved CCT of 2024-T351 at ΔK_b=12.0MPam$^{1/2}$: (a) Evolution of near-tip post-overload compliance curves and (b) corresponding closure measuring positions in the transient crack growth process.*

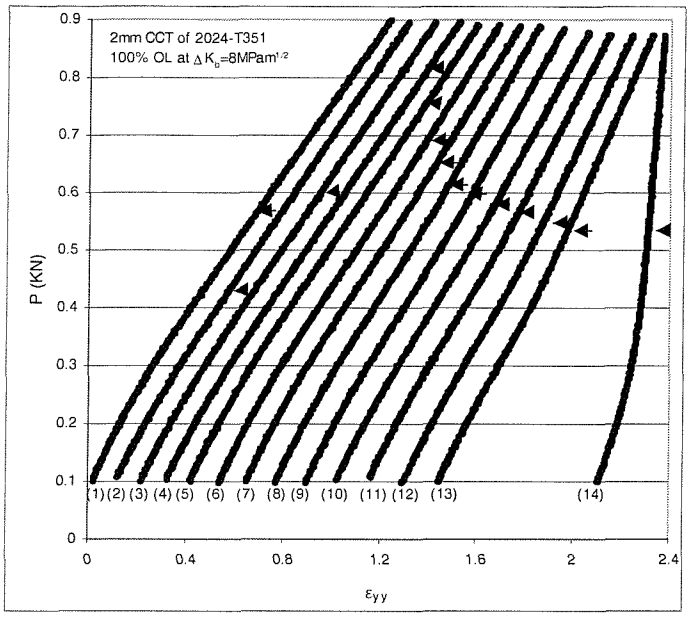

(a)

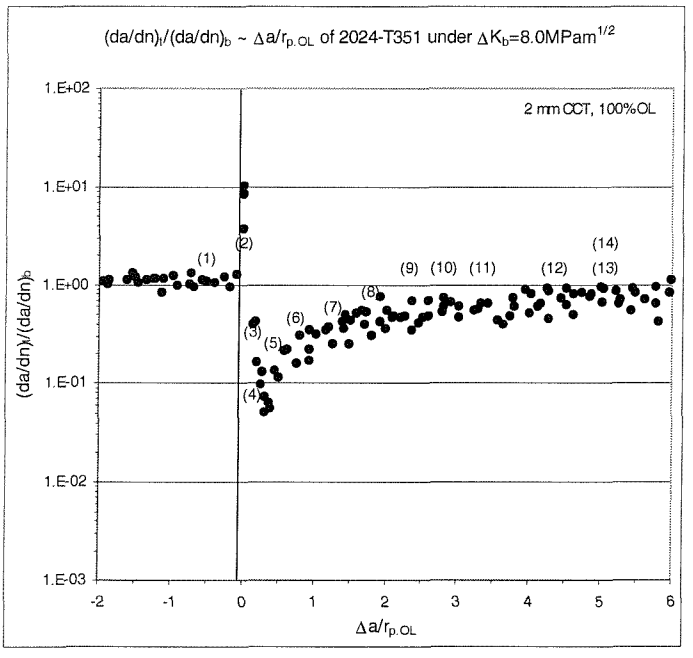

(b)

Figure 6.5 *100%OL on 2mm CCT of 2024-T351 at ΔK_b=8.0MPam$^{1/2}$: (a) Evolution of near-tip post-overload compliance curves and (b) corresponding closure measuring positions in the transient crack growth process.*

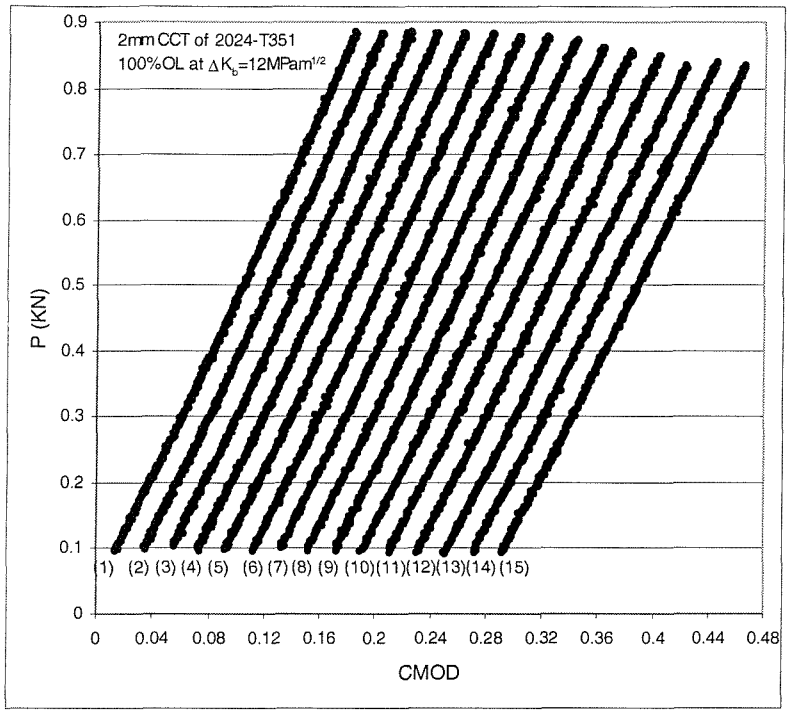

Figure 6.6 Evolution of global compliance curves from the crack mouth clip gauge after a 100%OL on 2mm CCT of 2024-T351 at ΔK_b=12.0MPam$^{1/2}$ with the same measuring positions as those in Figure 6.2.

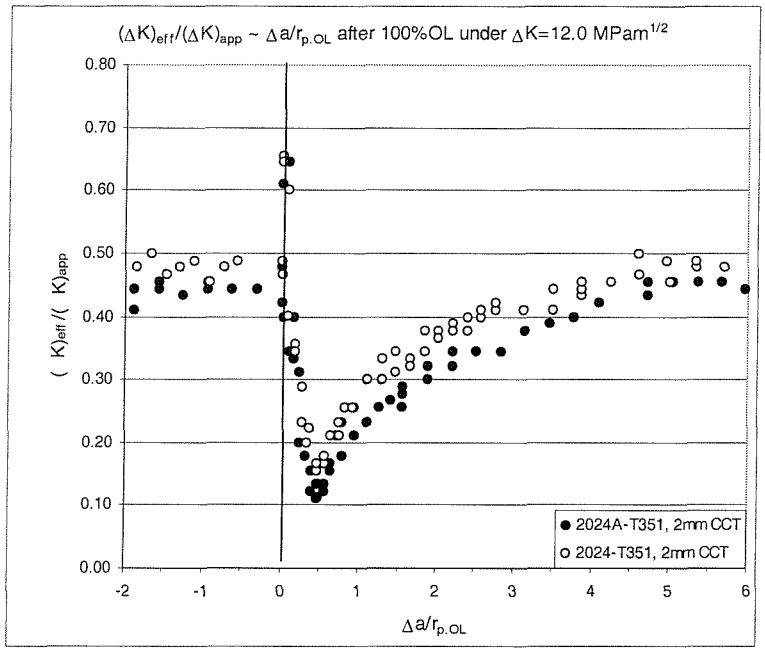

(a)

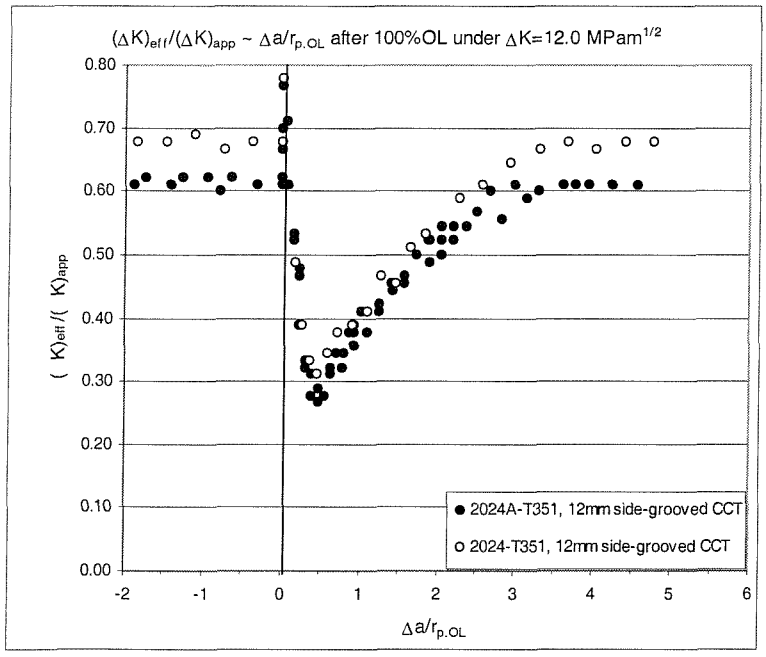

(b)

Figure 6.7 *Closure variations of 2024- & 2024A-T351 after a 100%OL at ΔK_b=12.0 MPam$^{1/2}$: (a) 2mm CCT samples and (b) 12mm thick CCT samples with side-grooves.*

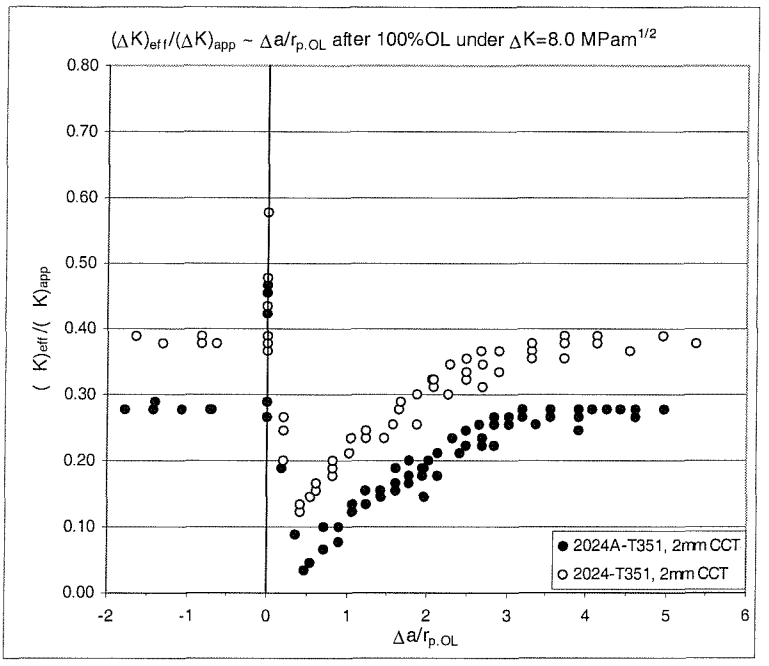

Figure 6.8 *Closure variations of 2024- & 2024A-T351 after a 100%OL at ΔK_b=8.0 MPam$^{1/2}$.*

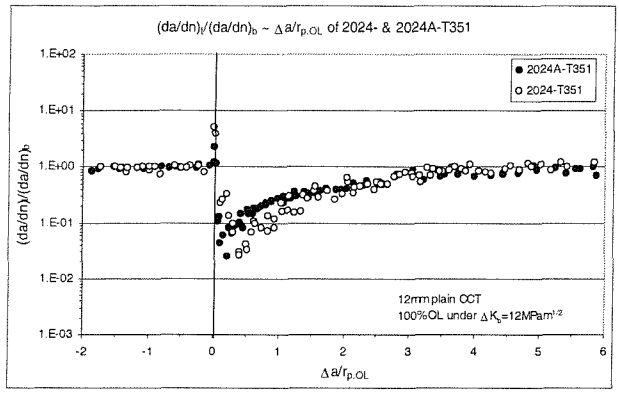

(a)

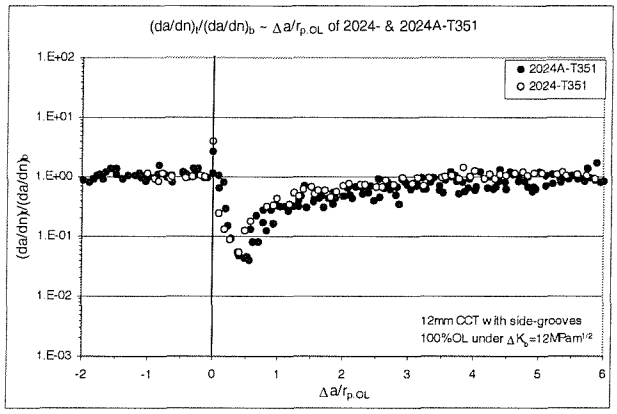

(b)

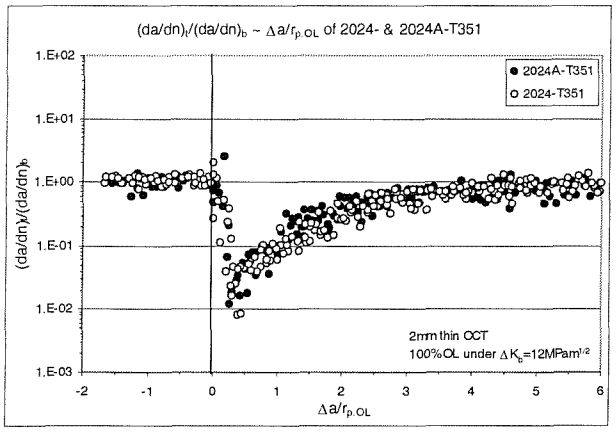

(c)

Figure 6.9 Transient crack growth behaviour after a 100%OL at ΔK_b=12.0MPam$^{1/2}$ on: (a) 12mm plain CCT, (b) 12mm CCT with side-grooves, and (c) 2mm CCT samples.

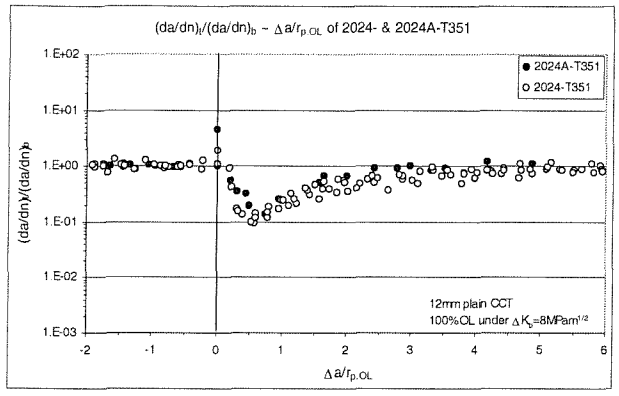

(a)

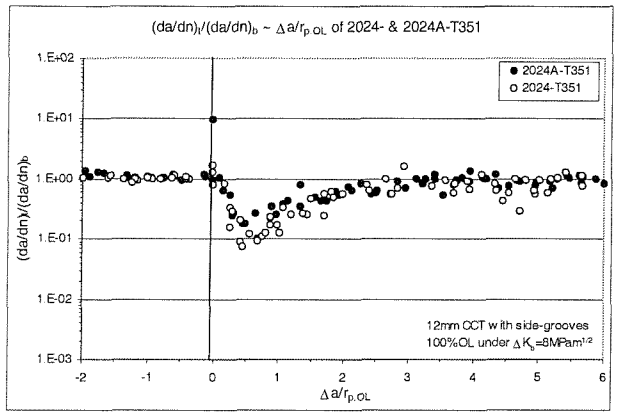

(b)

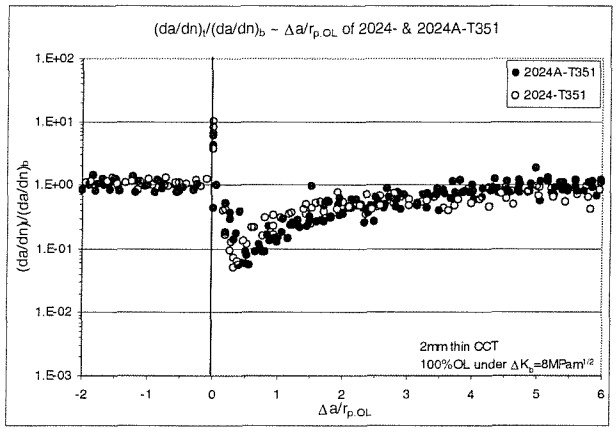

(c)

Figure 6.10 *Transient crack growth behaviour after a 100%OL at ΔK_b=8.0MPam$^{1/2}$ on: (a) 12mm plain CCT, (b) 12mm CCT with side-grooves, and (c) 2mm CCT samples.*

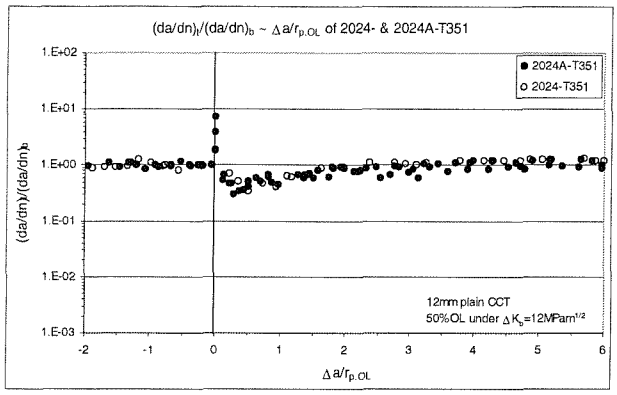

(a)

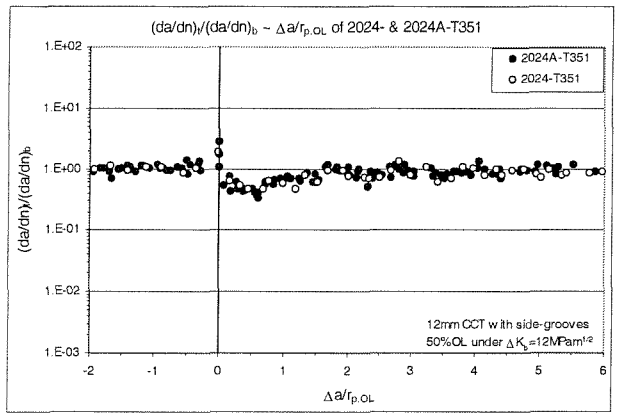

(b)

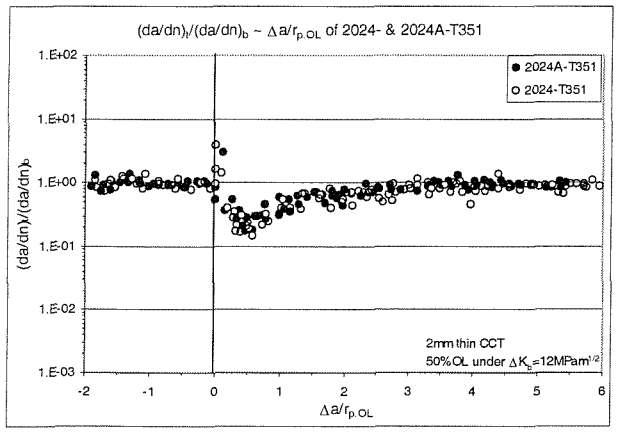

(c)

Figure 6.11 *Transient crack growth behaviour after a 50%OL at ΔK_b=12.0MPam$^{1/2}$ on: (a) 12mm plain CCT, (b) 12mm CCT with side-grooves, and (c) 2mm CCT samples.*

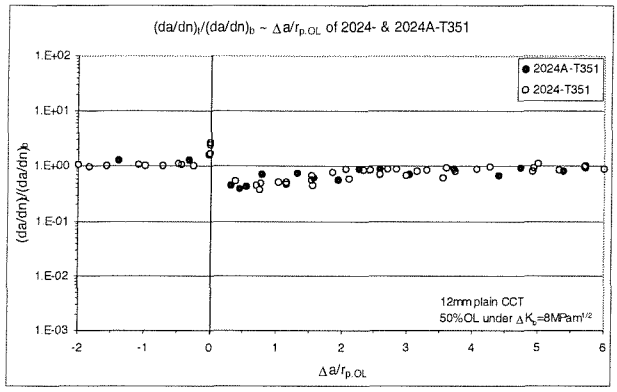

(a)

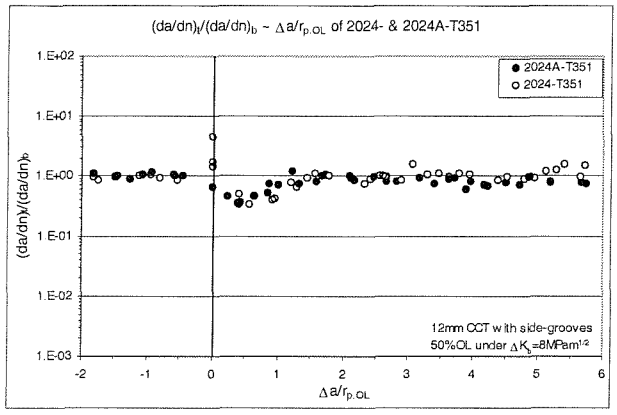

(b)

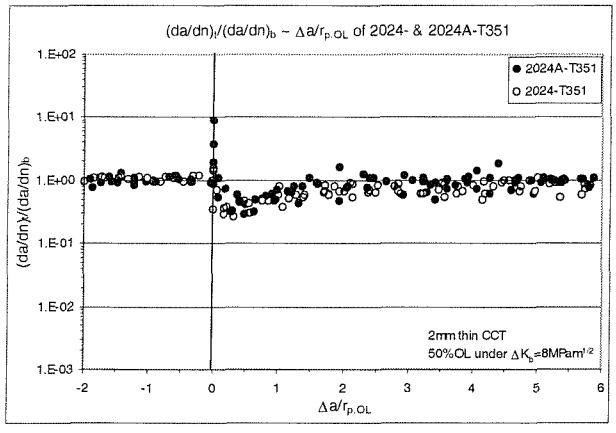

(c)

Figure 6.12 Transient crack growth behaviour after a 50%OL at ΔK_b=8.0MPam$^{1/2}$ on: (a) 12mm plain CCT, (b) 12mm CCT with side-grooves, and (c) 2mm CCT samples.

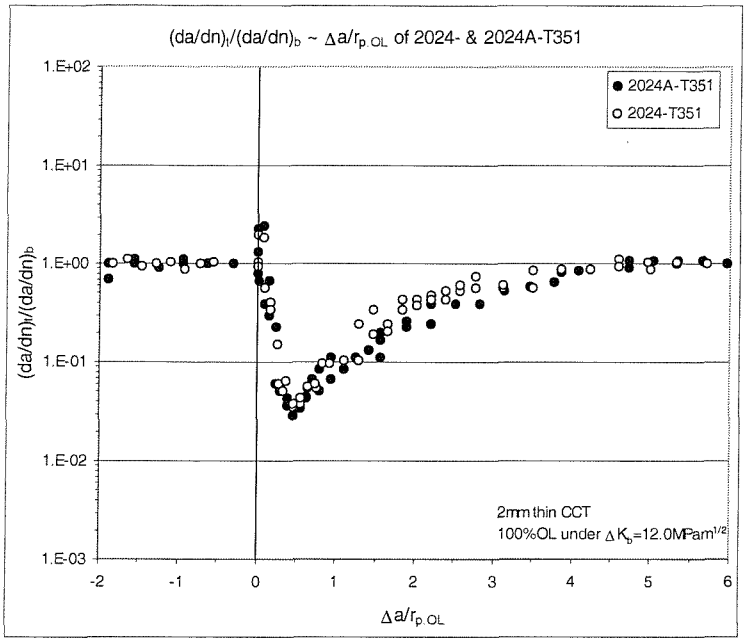

(a)

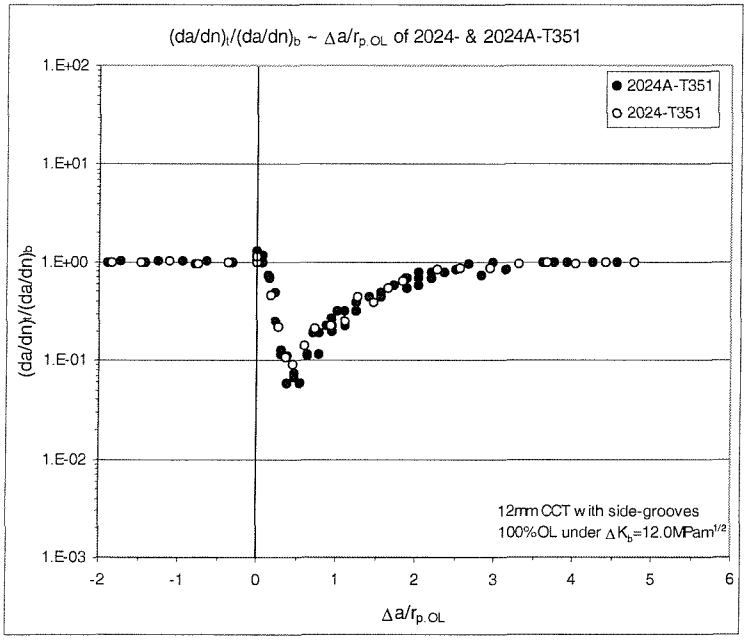

(b)

Figure 6.13 Transient crack growth predicted with closure results measured after a 100%OL at ΔK_b=12.0 MPam$^{1/2}$: (a) 2mm CCT samples and (b) 12mm thick CCT samples with side-grooves.

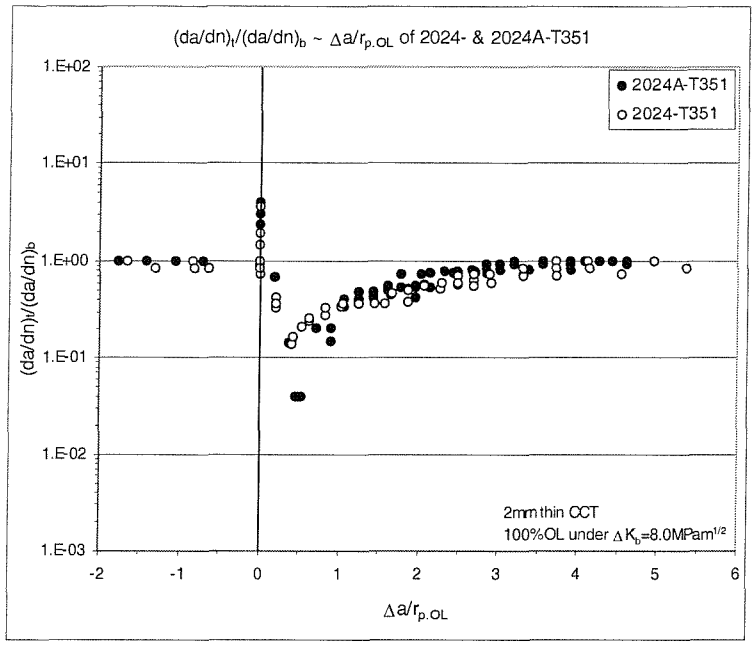

(a)

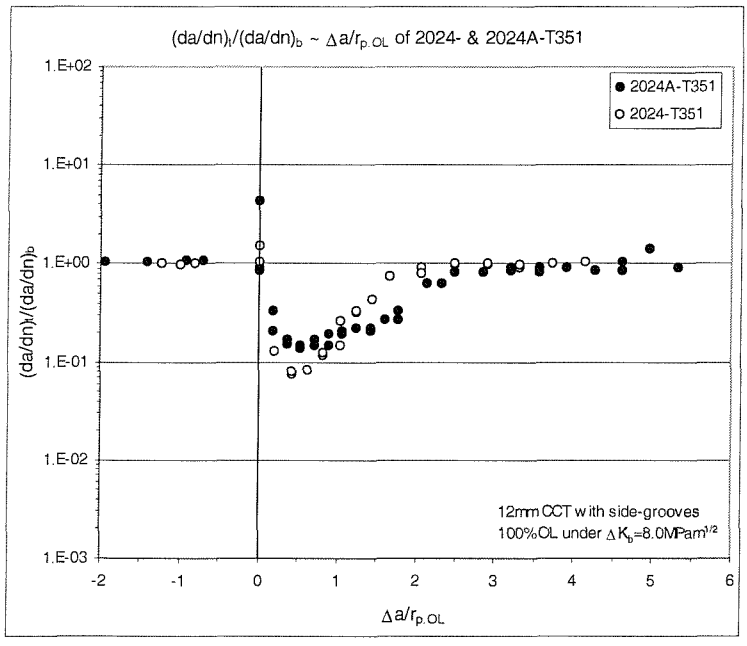

(b)

Figure 6.14 Transient crack growth predicted with closure results measured after a 100%OL at ΔK_b=8.0 MPam$^{1/2}$: (a) 2mm CCT samples and (b) 12mm thick CCT samples with side-grooves.

•2024-T351

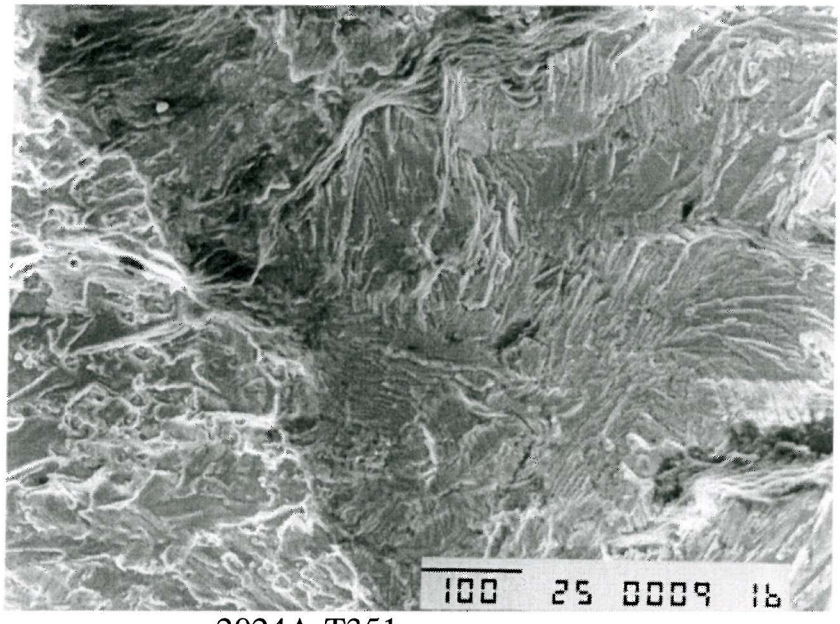

•2024A-T351

Figure 6.15 Fractographic features after 100% single overloads at $(\Delta K)_b$=12 MPa $m^{1/2}$.

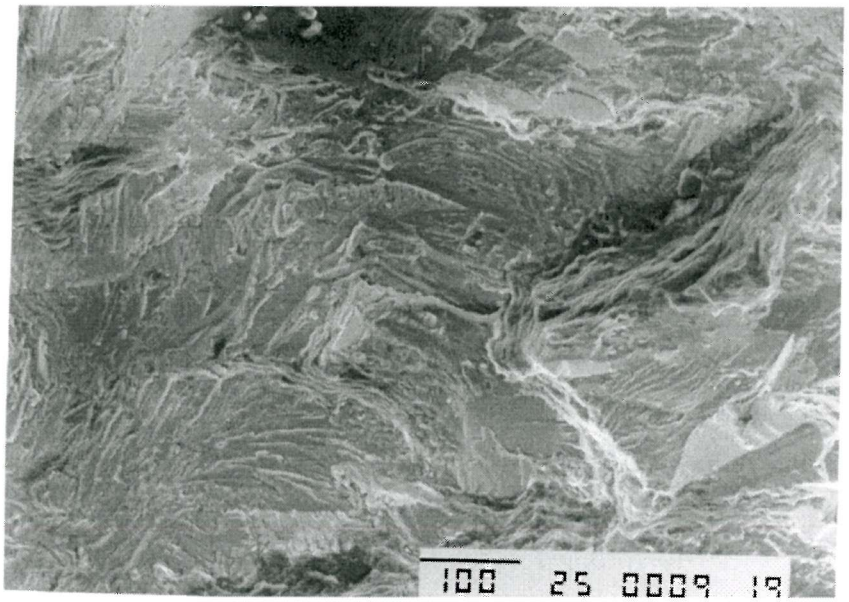

(a)

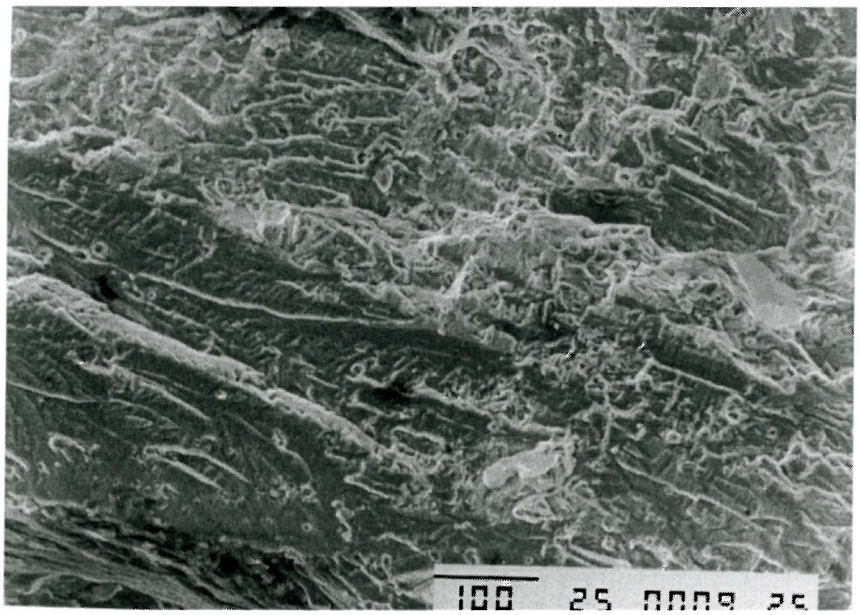

(b)

Figure 6.16 *Fractographic features in 2024A-T351 after 100% overloads at $(\Delta K)_b$=12 MPa $m^{1/2}$: (a) 0.5mm away from the overload and (b) 2mm away from the overload.*

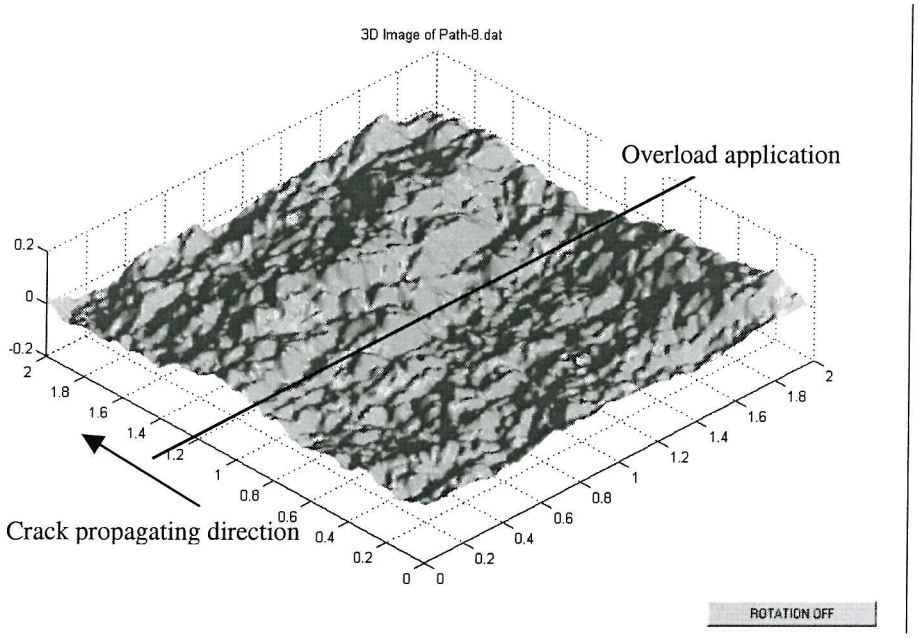

Figure 6.17 *3-D reconstruction of fatigue surfaces after a 100%OL at ΔK_b =12MPam$^{1/2}$ on 12mm plain CCT samples of 2024-T351.*

7. ANALYTICAL MODELLING OF CRACK CLOSURE

— *A modified Dugdale-type strip-yield analytical model has been developed to simulate plasticity-induced crack closure under both the CA and VA loading conditions. The model was established in a similar spirit to Newman's "FASTRAN" model. Good agreement was found between the current modelling results and the theoretical & experimental results in the literature. To reflect realistic material performance, microstructural influence was introduced in the model, extending it into a multi-mechanism formulation. As such further improvements in model predictions were achieved.*

7.1. Introduction

In the context of intrinsic and extrinsic contributions to fatigue resistance, reliable fatigue life prediction may be seen to depend heavily on the accurate estimation of effective crack propagating driving force. It is widely accepted that various micro-structural and micro-mechanical factors may influence the premature contact of the crack surfaces and hence potential closure contributions to fatigue behaviour. Numerous efforts have been made theoretically and experimentally to investigate closure effects on fatigue behaviour. Various causes, such as residual plastic deformation, crack surface roughness, and oxide debris have been proposed to account for the incidence of premature crack face contact (see Chapter 2).

In terms of the analytical modelling of closure processes, much work [1-15] has been carried out, as detailed in Chapter 2. The principles of these models are generally similar, with many being based on a Dugdale [16] or 'strip yield' model, modified to leave plastic deformed material in the wake of the crack to simulate propagation. Such models are mainly appropriate for plane stress crack closure simulation. As noted previously, the main disadvantage of such models is that they are fundamentally single-mechanism-based (*PICC*) and may not fully represent conditions of real engineering components/materials.

This chapter presents a further modified Dugdale-type strip-yield analytical model to simulate crack closure under both the *CA* and *VA* loading conditions. While the main features of Newman's approach [6] have been implemented, an attempt has been made to

incorporate more material behaviour into the model to extend the model into a multi-mechanism form.

7.2. Model Construction

7.2.1. Outline of the Model

In keeping with the previous experimental work [17,18, and Chapter 6], a centre-cracked tension (*CCT*) specimen with the same dimensions of the actual test samples was modelled (Figure 7.1). The body of interest consists of three regions. Region (a) is a linear elastic region with elastic modulus E containing a fictitious crack of length $2(a_o+r_p)$, where a_o is half the physical crack length and r_p is the crack tip plastic zone diameter length. Region (b) is a plasticity region of length r_p directly ahead of the physical crack, and region (c) is the area along the crack surfaces right behind the physical crack tip. A major advantage in the formulation of this model is that the plastic zone size and crack surface displacements are simply obtained by the superposition of two elastic problems of a *CCT* sample subjected to: (i) remote uniform tensile stress, σ_∞, and (ii) uniform stress, σ_i, on a segment of the crack surface (Figure 7.2). The segment stress, σ_i, reflects the effects of premature contact of the fatigue crack surface when the crack propagates into the plastic zone ahead of the crack tip. σ_i may however also be caused by crack surface roughness and oxide debris (especially at the near-threshold regime), as considered later. To facilitate the analysis of the plastic deformation, crack surface opening displacements, and the subsequent crack opening loads, a modified strip-yield model was employed. A series of bar elements was used to model region (b) and (c). Plastic deformations of the bar elements and residual stresses ahead of and behind the crack tip were calculated with a compatibility requirement between the elastic plate and all of the bar elements along the crack surface. The crack opening stress, σ_{op}, is normally calculated from the contact stresses behind the crack tip by equating the applied stress intensity factor at σ_{op} to the stress intensity factor caused by the contact stresses at the minimum stress, σ_{min} [5-9, 11-

13]. The crack opening stress may also be calculated from a displacement analysis: the applied stress required to fully open the crack surfaces is defined as σ_{op} in this case [10].

In the present model, strain-hardening is approximately accounted for by taking the flow stress of the bar element as the average of the yield strength and the ultimate tensile strength. More realistic evaluation on the strain-hardening effect can be made by introducing measured constitutive relations. Strain hardening/softening can also be accounted for by using Hutchinson [19] and Rice & Rosengren [20] singularity solutions ('*HRR* fields'). It is expected however that the improvement to the modelling results will be second order [1]. Three-dimensional constraint effects are simulated by the same method Newman employed, *i.e.*, a constraint factor, α, is introduced (one for plane stress and three for plane strain). It has been reported that this three-dimensional constraint effect can be alternatively evaluated by using an out-of-plane stress constraint factor, T_z $(=\sigma_{zz}/(\sigma_{xx}+\sigma_{yy}))$, and an in-plane stress ratio, k $(=\sigma_{xx}/\sigma_{yy})$ if 3-D *FE* analyses are used [12, 21], although this has not been utilised here.

Unlike the common practice in the literature where a lumping procedure was used to keep the number of elements to a reasonable size in models of this type (30-60) [6, 22], region (b) and region (c) were modelled using a fixed number (100) of elastic-perfectly plastic bar elements, as shown in the enlarged near crack tip area (*A-A* in Figure 7.1). 40 elements were used in region (b), with the remaining 60 elements being used in the region (c). Element widths vary with their relative locations, with the smallest elements being located around the physical crack tip and behind the fictitious crack tip. The advantage of fixing the bar element number during the process of crack propagation modelling is that more reliable and consistent crack opening behaviour will be predicted: while computer time is saved with the element lumping procedure by merging elements far from the crack tip into a single element, sharp changes in crack opening loads at certain crack lengths are sometimes observed [6,23]. Accuracy in crack closure predictions is clearly the most important issue to the current study and the processing cost in not using lumping is really not a major consideration given currently available computer capacity. The length of the 60 bar elements in region (c) is initially set to zero and is updated with crack propagation.

This differs from conventional models where bar elements in region (c) exist only after residual plastic deformation has been passed into the wake. The initial length of the 40 bar elements in region (b) is decided by the opening displacements of the fictitious crack surfaces at the maximum load of the first cycle. To accurately calculate the length and the stress of these bar elements, both elastic and plastic deformations are considered in the fatigue process.

Under constant amplitude loading the size of region (b) is obtained from Dugdale's non-singularity assumption at maximum load. Region (c) is five times larger than region (b). The widths of the bar elements are decided based on the region size and their relative positions within the region. Under variable amplitude loading (single overload in present study), region (b) is from the current physical crack tip to the farthest elastic/plastic boundary introduced by the load history so far. The size of region (b) is updated accordingly with the crack propagation. The size of region (c) is set to five times the maximum size of region (b) so far. The widths and the co-ordinates of these elements are calculated based on the current sizes of these two regions and the position of the physical crack tip.

The model is further extended into a multi-mechanism form by introducing *'effective surface roughness'* in region (c) as an additional residual strain in region (c). The effective surface roughness may be related to crack surface roughness and/or crack surface oxide debris, which are clearly material-related, and also load dependent. As such, the model is capable of evaluating combined effects of plasticity-induced crack closure, roughness-induced crack closure, and oxide-induced crack closure under both the *CA* and *VA* loading conditions. The details of this are considered later.

7.2.2. Governing Equations and the Coding of the Model

The crack tip plastic zone size is determined by Dugdale's approach. Dugdale assumed that there would be no stress singularity physically existing at the fictitious crack tip. This means that the stress intensity factor, K_{σ_∞}, due to the remote tensile stress, σ_∞, will

numerically be equal to the sum of the stress intensity factor, K_{σ_i} due to the uniform tension on element *i* in region (b), *i.e.*

$$K_{\sigma_\infty} + \sum_{i=1}^{40} K_{\sigma_i} = 0 \tag{7-1}$$

The equations for stress-intensity factors for a crack in an infinite plate are given in reference [24]. For the solutions corresponding to Figures 7.2(a) and (b) below, approximate finite-width corrections verified with boundary-collocation analyses [25] must be used. The stress intensity factor for Figure 7.2(a) is:

$$K_{\sigma_\infty} = \sigma_\infty \cdot \sqrt{\pi(a_O + r_P) \cdot \sec\left(\frac{\pi(a_O + r_P)}{W}\right)} \tag{7-2}$$

where a_o is the half physical crack length, r_p is the monotonic plastic zone dimension projected in the crack propagation direction at the maximum load of the fatigue cycle, and W is the width of the plate.

The stress intensity factor for Figure 7.2(b) is:

$$K_{\sigma_i} = \frac{2\sigma_i}{\pi}\sqrt{\pi(a_O + r_P)} \cdot \left[\sin^{-1}\left(\frac{\sin\left(\frac{\pi b_2}{W}\right)}{\sin\left(\frac{\pi(a_O + r_P)}{W}\right)}\right) - \sin^{-1}\left(\frac{\sin\left(\frac{\pi b_1}{W}\right)}{\sin\left(\frac{\pi(a_O + r_P)}{W}\right)}\right)\right] \cdot \sqrt{\sec\frac{\pi(a_O + r_P)}{W}} \tag{7-3}$$

where b_1 and b_2 are the distances of between the centre point of the crack and the two ends of the stressed segment in the model.

For the crack closure modelling, only one quarter of the plate was analysed due to the symmetry of the problem. Figure 7.3 shows a schematic of the loading and co-ordinate system used in the model. Element *j* is connected to the linear elastic region (region (a)) at

point j and subjected to a uniform stress σ_j over the element width $2\omega_j$. L_j is the length of element j. Vj is the crack surface opening displacement at point j, which is caused by the remotely applied load and the stresses from the bar elements. The crack surface opening displacement at point i is given by:

$$V_i = \sigma_\infty \cdot f(x_i) - \sum_{j=1}^{100} \sigma_j \cdot [g(x_i, x_j) + g(-x_i, x_j)] \qquad \text{for } i=1 \text{ to } 100 \tag{7-4}$$

$f(x_i)$ and $g(x_i, x_j)$ are given by:

$$f(x_i) = \frac{2(1-\eta^2)}{E} \cdot \sqrt{[d^2 - x_i^2] \cdot \sec\frac{\pi d}{W}} \tag{7-5}$$

$$g(x_i, x_j) = \frac{2(1-\eta^2)}{\pi E}\left\{(b_2 - x_i)\cosh^{-1}\left(\frac{d^2 - b_2 x_i}{d|b_2 - x_i|}\right) - (b_1 - x_i)\cosh^{-1}\left(\frac{d^2 - b_1 x_i}{d|b_1 - x_i|}\right)\right.$$
$$\left. + \sqrt{d^2 - x_i^2}\left[\sin^{-1}\left(\frac{b_2}{d}\right) - \sin^{-1}\left(\frac{b_1}{d}\right)\right]\right\}\left[\frac{\sin^{-1} B_2 - \sin^{-1} B_1}{\sin^{-1}\left(\frac{b_2}{d}\right) - \sin^{-1}\left(\frac{b_1}{d}\right)}\right]\sqrt{\sec\left(\frac{\pi d}{W}\right)} \tag{7-6}$$

where E is the Young's Modulus of the material, η is a material constant (zero for plane stress and ν (Poisson's ratio) for plane strain), $d=a_O+r_P$, $b_1=x_j-\omega_j/2$ and $b_2=x_j+\omega_j/2$. B_1 and B_2 are given by:

$$B_i = \frac{\sin\left(\frac{\pi b_i}{W}\right)}{\sin\left(\frac{\pi d}{W}\right)} \qquad \text{for } i=1 \text{ or } 2 \tag{7-7}$$

The crack surface contact stresses used for the calculation of the crack opening point are solved from the linear system of equations (Eq.7-4) usingthe Gauss-Seidel iterative method

[26] with boundary conditions added. The boundary conditions in region (b) ahead of the current physical crack tip are:

$$\text{If } V_i^{(k)} \geq L_i^{(k-1)} \cdot \left(1+\alpha\frac{\sigma_O}{E}\right) \Rightarrow \begin{cases} L_i^{(k)} = V_i^{(k)}\left(1-\dfrac{\alpha\sigma_O}{E}\right) \\ if\sigma_i^{(k)} \geq \alpha\sigma_O \Rightarrow \sigma_i^{(k)} = \alpha\sigma_O \end{cases} \tag{7-8a}$$

$$\text{If } V_i^{(k)} < L_i^{(k-1)} \cdot \left(1-\alpha\frac{\sigma_O}{E}\right) \Rightarrow \begin{cases} L_i^{(k)} = V_i^{(k)}\left(1+\dfrac{\alpha\sigma_O}{E}\right) \\ if\sigma_i^{(k)} \leq -\alpha\sigma_O \Rightarrow \sigma_i^{(k)} = -\alpha\sigma_O \end{cases} \tag{7-8b}$$

$$\text{Otherwise } \begin{cases} L_i^{(k)} = V_i^{(k)} \\ \sigma_i^{(k)} = \sigma_i^{(k-1)} \end{cases} \tag{7-8c}$$

The boundary conditions in region (c) behind the current physical crack tip are:

$$\text{If } V_i^{(k)} \geq L_i^{(k-1)} \Rightarrow \begin{cases} L_i^{(k)} = L_i^{(k-1)} \\ if\sigma_i^{(k)} \geq 0 \Rightarrow \sigma_i^{(k)} = 0 \end{cases} \tag{7-9a}$$

$$\text{If } V_i^{(k)} < L_i^{(k-1)} \cdot \left(1-\frac{\sigma_O}{E}\right) \Rightarrow \begin{cases} L_i^{(k)} = V_i^{(k)}\left(1+\dfrac{\sigma_O}{E}\right) \\ if\sigma_i^{(k)} \leq -\sigma_O \Rightarrow \sigma_i^{(k)} = \sigma_O \end{cases} \tag{7-9b}$$

$$\text{Otherwise } \begin{cases} L_i^{(k)} = V_i^{(k)} \\ \sigma_i^{(k)} = \sigma_i^{(k-1)} \end{cases} \tag{7-9c}$$

Where σ_0 is the average of the yield strength and the ultimate tensile strength of the alloy and the additional superscripts on σ_i, V_i, and L_i denote the iteration number of the iterative process of solving the linear system of Eq.(7-4). Eq.(7-4) is rewritten in the form:

$$\sigma_i^{(k)} = \left[\sigma_\infty \cdot f(x_i) - V_i - \sum_{j=1}^{i-1} \sigma_i^{(k)} \left(g(x_i, x_j) + g(-x_i, x_j) \right) - \sum_{j=i+1}^{100} \sigma_i^{(k-1)} \left(g(x_i, x_j) + g(-x_i, x_j) \right) \right] \quad \text{for } i=1 \text{ to } 100 \qquad (7\text{-}10)$$

Initial guesses for σ_i are zeros and are inserted into the right-hand side of the linear system of Eq.(7-10). In the Gauss-Seidel iterative method, the newly obtained stress $\sigma_i^{(k)}$ is checked against the boundary conditions of Eqs.7-8 & 9 once it is calculated, and is updated accordingly. The newly obtained stresses $\sigma_i^{(k)}$ are always used in Eq.(7-10) to calculate the remaining unknown stresses, which makes the solving of linear system of Eq.(7-10) more efficient. This process is repeated until the changes in all of the σ_i values are less than 1% of the flow stress of the alloy. The crack opening stress, σ_{op}, is calculated based on the following criteria (as noted earlier): (i) the applied stress increment $(\sigma_{op}\text{-}\sigma_{min})$ is used to effectively remove all the contact stresses ($<1\%\sigma_o$) in the bar elements in region (c), and/or (ii) the applied stress increment $(\sigma_{op}\text{-}\sigma_{min})$ is used to effectively separate the surface contact ($<1\%\delta_{tmax}$, where δ_{tmax} is the physical crack tip opening displacement at the maximum load of the loading cycle) behind the physical crack tip. An iterative procedure is again employed in crack opening stress calculations.

A computer code for the realisation of the analytical modelling has been written in *FORTRAN 90*. Figure 7.4 shows the flow chart of the program. A modular design is used to allow for easier revisions and operation on a personal computer. Global parameters reflecting model geometry, material information, and some commonly used constants are defined in the *'Global-Data'* module. The model is then initialised in sub-routine *'Initialisation'* at the maximum load of the first loading cycle, which gives the initial co-ordinates, lengths, and the widths of all the bar elements. The sub-routine *'Extension'* propagates the physical crack tip by 1% of the current maximum plastic zone size. The co-ordinates and the widths of the bar elements are updated accordingly. Crack profile, plastic zone size, element lengths, and the stresses of the bar elements at the maximum load of the current loading cycle are calculated in sub-routine *'Smax_Data'*. Effective roughness of the crack surfaces are estimated and appended on the bar elements in region

(c) in the sub-routine *'Effective-Roughness'*. The important crack surface contact stresses and the element lengths at the minimum load of the loading cycle are obtained in sub-routine *'Smin_Data'*. Crack opening stress is calculated in sub-routine *'Crack_Opening'*. This process is repeated until enough crack growth has been made and the modelling is ended. Under *CA* loading, the achievement of steady state growth conditions is judged by the stabilisation of the predicted crack opening stresses. Under single overload and/or underload simulations, it is judged by the recovery of the crack opening stress to the pre-overload level. More details of the program can be found in Appendix E.

7.3. Results and Discussions

7.3.1. Non-Propagating Cracks

As a simple, basic validation of the current model, crack opening profiles and the size of plastic zone predicted by the model may be compared with the well-established Dugdale model-based results. No crack closure will be predicted since there is no plastic deformation left in region (c). Figure 7.5(a) shows the crack opening profiles at the maximum and minimum load of a loading cycle (R=0) under plane stress condition. For convenience of comparison, crack opening displacements are normalised by the maximum physical crack tip opening displacement at P_{max}, whilst the x co-ordinates of the crack surface are normalised by the monotonic plastic zone size, r_b, at P_{max}. The physical crack tip is set at x/r_b=0. The predicted physical crack tip opening displacement at minimum load (0 for R=0) is very close to half the physical crack tip opening displacement at maximum load, which is consistent with Rice's stress superposition estimate ($\delta_{min}/\delta_{max}$=0.5) [27]. Figure 7.5(b) shows the stress distributions on the crack surface (physical crack + fictitious crack) along the crack line at P_{max} and P_{min}, respectively. The normal stresses in the loading direction are normalised by the flow stress of the alloy. It is predicted that the reversed plastic zone size at P_{min} (0 for R=0) is about 0.25 of the forward plastic zone size at P_{max}, which is again consistent with Rice's estimate.

7.3.2. Fatigue Cracks under *CA* Loading

Under *CA* (fixed stress intensity factor range) crack growth, residual plastic deformation is built up in the wake behind the physical crack tip. Detailed analysis of this case has been presented by Budiansky and Hutchinson [1] under plane stress condition and can be used to verify present model.

Figure 7.6 shows the crack profiles at P_{max}, P_{min}, and P_{op} of the loading cycle of *CA* loading (R=0) after the crack has propagated a quarter of the initial monotonic plastic zone size. Residual plastic deformation is left behind the physical crack tip (x/r_b=0.0) due to crack propagation. At P_{min}, a smaller reverse crack tip displacement (~$0.25\delta_o$) is predicted than that for the non-propagating crack (~$0.50\delta_o$). This is clearly consistent with the wedge effect of the additional plastic material in the crack wake. Crack closure is observed immediately behind the physical crack tip: Figure 7.6(c) shows crack profiles for when the applied load increment is just sufficient to fully open the physical crack. Figure 7.7 shows the crack surface stress distributions at P_{max}, P_{min}, and P_{op} after $0.25r_b$ of crack growth under *CA* loading at R=0. The physical crack is fully open at P_{max} and the forward plastic zone is $1.0r_b$. At P_{min}, compressive contact stresses are developed in the bar elements both behind and ahead of the physical crack tip. The reversed plastic zone (~$0.15r_b$) is smaller than that ($0.25r_b$) for a non-propagating crack. The residual stress distribution behind the physical crack tip is then used to calculate the crack opening stress. At P_{op}, the contact stress in region (c) is removed and the residual stress in region (b) is raised. The predicted crack opening level (P_{op}/P_{max}) is found to be ~ 0.44.

Figure 7.8 shows the crack profiles at P_{max}, P_{min}, and P_{op} of the loading cycle of *CA* loading (R=0) after the crack has propagated five times the monotonic plastic zone size, where a stabilised crack opening level has been established. Uniform residual plastic deformation is left behind the physical crack tip, leading to crack closure along the crack line at P_{min}. The residual plastic deformation at the physical crack tip is about 0.89 times the physical crack tip opening displacement at P_{max}, which agrees very well with Budiansky & Hutchinson's result (δ_r/δ_o=0.87). Figure 7.9 shows the corresponding crack surface stress

distributions at P_{max}, P_{min}, and P_{op}. The physical crack is fully open at P_{max} and the forward plastic zone is again $1.0r_b$. Similar observations to Figure 7.7 may be made, however, the stabilised reversed plastic zone is smaller (~$0.09r_b$), attributable to the stronger physical crack tip shielding caused by the more extensive load transfer in the wake, with this value being quite consistent with the analysis of Budiansky & Hutchinson (~$0.093r_b$). The predicted crack opening level (P_{op}/P_{max}) is about 0.57, which is similarly close to Budiansky & Hutchinson's result of 0.56 [1].

The current model was further employed to assess plasticity-induced crack closure under *CA* loading for various stress ratios. Figure 7.10 shows the comparison between current modelling results and Elber's experimental results for thin 2024 sheet [28]. The diagram also highlights the similarity in the two P_{op} determination methods that were used here. The second criterion (stress and displacement based) will be used to predict crack opening levels in the following sections unless otherwise stated. Good agreement is observed between the model results and the experimental results, particularly at higher R ratios. There are some differences at low R ratios. The differences are however minor, especially when the difficulty in crack closure measurements is considered. Plasticity-induced crack closure under plane strain state has also been studied by introducing the constraint factor of 3 to region (b). A reduced crack closure level is predicted under plane strain due to reduced plastic deformation in the wake, which is consistent with various literature results [6, 8, 21, 22]. It is clear from the above that the current analytical model and the associated computer code would appear to provide rational results, at least for the simplified framework considered.

7.3.3. Fatigue Crack Behaviour under Single Overloads

Variations in plasticity-induced crack closure after the application of single overloads of various overload ratios have been investigated with the current analytical model. Figure 7.11 shows crack profiles at (a) P_{max}, (b) P_{min}, and (c) P_{op} of a 100% single overload cycle immediately after application of the overload. Overload crack tip blunting is clearly predicted with the physical crack tip opening ~ four times the baseline physical crack tip

opening displacement at P_{max} (Figure 7.11(a)). At P_{min}, the physical crack surfaces appear to be held open by the effect of overload crack tip blunting, with the residual physical crack tip opening being about 1.5 times the baseline physical crack tip opening (Figure 7.11(b)). This means that applied load has to go below the P_{min} to close the crack surface. Figure 7.11(c) illustrates this effect, showing the crack profile when the crack surfaces in region (b) start to touch each other. It may be seen that, unlike *CA* loading where crack closes immediately behind the physical crack tip, crack closure occurs far behind the crack tip due to the blunting (although it must be recognized that the crack has been 'artificially' loaded below P_{min} in this case).

Figure 7.12 shows the crack surface stress distributions at P_{max}, P_{min}, and P_{op} of the 100% overload cycle. The forward plastic zone size at P_{max} of the overload cycle is four times the baseline plastic zone size. The reversed plastic zone size at P_{min} is about a quarter of the forward plastic zone, which is expected since the crack at this moment is similar to a static crack with no residual plastic deformation in the wake. The reversed plastic zone is slightly bigger at P_{op} than at P_{min} since further reduction of the external load was required to close the crack.

As the crack propagates into the overload plastic zone, enhanced plastic deformation is left in the wake behind the physical crack tip. Figure 7.13 shows crack profiles at (a) P_{max}, (b) P_{min}, and (c) P_{op} of a loading cycle after the crack has propagated into the overload plastic zone by ~ $0.53r_{overload}$. Greater opening at the physical crack tip (~$1.2r_b$) is predicted at P_{max} (Figure 7.13(a)) due to enhanced plastic deformation from the overload. This elastic opening is still maintained at P_{min} (Figure 7.13(b)) during unloading since the crack closure level is very high (~0.99) at this point and most of the external load is taken up by the elements behind the physical crack tip. Figure 7.13(c) shows the crack profiles at P_{op}; it is clear from this figure that the first crack surface contact occurs immediately behind the current physical crack tip. The contact spreads over region (c) once the applied load goes below the opening level. Different contact profiles emerge under different loading conditions. Figure 7.14 shows the crack profiles at P_{op} of a loading cycle ~$0.63r_{overload}$ away from the application of a 150% single overload. It is clear from this figure that the

first contact point during unloading is a point removed from the current physical crack tip (corresponds approximately to the point where the overload was applied). A key point is the fact that there is a discrete, near tip closure event associated with the overload. It may be seen that this contact actually wedges open the crack flanks further back along the crack wake. As such it may be seen that '*residual*' closure due to pre-overload deformations further back along the crack wake would be expected to occur at a relatively low load level (*i.e.* lower than the pre-overload P_{cl}), consistent with the low secondary slope change that occurred in the experimental compliance data. This secondary contact is not explicitly seen in the current models due to the limited crack wake ($5r_p$) that is considered, but may be expected given there will be residual plasticity further back in the real crack wake and the fact that the near tip wedging effect can only influence behaviour relatively close to the tip (*i.e.* St. Venants Principle). Figure 7.15 shows the crack surface stress distributions at P_{max}, P_{min}, and P_{op} of the same loading cycle of Figure 7.13. No reversed yielding is observed at P_{min} and P_{op} due to large extent of load transfer behind the physical crack tip.

Figure 7.16 shows crack profiles at (a) P_{max}, (b) P_{min}, and (c) P_{op} of a loading cycle after the crack has propagated some distance from the overload affected zone (~$2.0r_{overload}$). Elastic physical crack tip opening is about $0.90\delta_o$, which is very close to the value predicted under *CA* loading (see Figure 7.8), *i.e.* tending back to the pre-overload state. Two near tip contact areas in region (c) are in fact obvious during unloading. The contact stresses for the further contact point have a limited influence on the near-tip material behaviour in region (b) (immediately ahead of the physical crack tip), although they have an influence on global compliance curve. Figure 7.17 shows crack surface stress distributions at P_{max}, P_{min}, and P_{op} of the same loading cycle. The forward plastic zone size has recovered to 1 baseline plastic zone size and the reversed plastic is about $0.09r_b$, *i.e.* close to the pre-overload state.

Figure 7.18 shows crack closure variations after single overloads of 50%, 100%, and 150% overload ratios under plane stress conditions. Crack growth arrest is predicted after the application of a 150% single overload, which is consistent with the current experimental observations on *2mm CCT* samples. It is of course possible to let the crack artificially

propagate into the overload plastic zone in the model case. Closure levels are essentially recovered to pre-overload levels after the crack tip has grown out of the overload plastic zone (~$6.5r_b$), which is about one overload plastic zone size (based on plane stress zone size calculation). Very high closure levels are predicted after the application of a 100% single overload under plane stress loading conditions. The crack does not arrest in this case however. The retardation distance is again close to one (plane stress) overload plastic zone size. For 50% overloads, the predicted increase in crack closure is much lower than the other two cases, but the retardation distance is still around one overload plastic zone size. The maximum retardation occurred after the crack had propagated into the overload plastic zone by about $0.20r_{overload}$ for all the three overload ratios.

Crack closure variations after single overloads of 50%, 100%, and 150% overload ratios under plane strain condition are shown in Figure 7.19. Similar trends with the increase in overload ratio are predicted under plane strain compared to the plane stress results in Figure 7.18. The overload effect is clearly reduced in plane strain compared to plane stress. No crack growth arrest is predicted after the application of a 150% single overload. Crack growth retardation distance is however comparable to the plane strain overload plastic zone size for all cases and the maximum retardation occurs after the crack has propagated into the overload plastic zone by about $0.4r_{overload}$. It may be seen that the overload behaviour predictions are broadly consistent with the experimental results in Chapter 6, with the following main points of interest:

(i) There are no baseline effects in these plasticity only models. Baseline closure level predictions for the models approach those of the experimental results for the higher $(\Delta K)_b$ level tested (*i.e.* $(\Delta K)_b=12MPam^{1/2}$), consistent with the generally held concepts of when *PICC* may be expected to operate.

(ii) Identifying the $(\Delta K)_b=12MPam^{1/2}$ experiments as the more directly comparable to the modelling results, the following comparisons may be made:

   a. The total overload transient distances predicted for plane strain are much shorter than found experimentally (by a factor of ~ 3 for the 100% overload in the 12*mm* thick side-grooved samples).

b. Total overload transient distances predicted for plane stress are somewhat closer to experimental values (but are still over-predicted by a factor of ~ 1.5 for the 100% overload in the *2mm* thick samples).
c. The maximum shielding effects predicted by the *PICC* models are less than the corresponding experimental data; this is particularly the case for the plane strain condition where approximately double the attenuation in $(\Delta K)_{eff}$ is seen in the 100% overload in *12mm* side-grooved tests compared to the *PICC* plane strain model (for the *2mm* 100% overload sample the attenuation in $(\Delta K)_{eff}$ is ~ 25% greater than in the plane stress model).

7.3.4. Modelling of Combined *PICC* and *OICC* Effects

Whilst satisfactory basic performance characteristics of the model has been observed in the prediction of *PICC* under both *CA* and *VA* fatigue loading, it has been identified in previous chapters that fatigue behaviour is often influenced by several crack closure mechanisms. *RICC* and *OICC* are two key forms of closure that may be considered relevant here, especially in the near threshold crack growth regime and/or under *VA* loading. If only *PICC* is considered by the present models, the predicted crack closure level is only *R* ratio dependent under the same stress state: there is no baseline stress intensity range dependence, as noted above.

RICC mechanism and *OICC* mechanism are not explicitly considered in the present model formation. They may however be introduced via the concept of *effective* roughness. The effect of crack surface roughness or oxide debris on crack closure may then be simulated by appending 'extra' material onto the bar elements (*i.e.* some extra length to the element) in region (c). As such the roughness or oxide effects are related to some equivalent strain in what is fundamentally a *PICC* modelling framework. This is clearly a physically unrealistic approach, however it does present two key attractive features:

(1) It is computationally cheap compared to explicit treatment of crack paths and residual plasticity [29].

(2) By staying with the basic *FASTRAN* framework this approach is readily applied to complex/realistic load spectra of interest in real engineering design.

In the first instance this '*effective strain*' approach will be applied in a semi-empirical manner, with model behaviour being investigated via a combination of parametric analysis and fitting to the available experimental data.

Figure 7.20 shows the variation of combined *PICC* and *RICC* levels with the change of effective roughness of a crack at a $(\Delta K)_b$ of 12.0 $MPam^{1/2}$ and R=0.1: the '*effective roughness*' is expressed a deformation applied uniformly to the crack faces. Increased *PICC+RICC* levels are clearly predicted with increasing thickness of effective roughness. It is worth noting that effective surface roughness (or indeed oxide layer thickness for *OICC*) need not necessarily be at a scale comparable to the crack tip opening displacement to have noticeable effects on crack closure, as is commonly suggested in the literature (*e.g.* [30-31]). As may be seen in Figure 7.20, a few hundredths of a micrometer of extra material can enhance the closure level significantly if it is appended to the existing plastically deformed material left in the wake of the crack, while the crack tip opening is at the scale of a few μm. It may also be seen from Figure 7.20 that increasing effective roughness has a much stronger influence on closure level under plane strain than plane stress conditions.

To simulate the baseline stress intensity factor range dependence of crack closure, effective crack surface roughness may be introduced into the present model. Conventional wisdom would suggest effective surface roughness is $(\Delta K)_b$ dependent, as can be seen from the discussion in Chapter 4 (*i.e. RICC* effects are most significant for crystallographic/stage I type growth near-threshold). Figure 7.21(a) shows a simple empirical relationship for effective roughness versus $(\Delta K)_b$: specifically a linear relationship is assumed between the surface roughness and $(\Delta K)_{eff}$ in the lower part of the Paris regime (consistent with greater fracture surface roughness as the threshold condition is approached). The effective roughness in question is applied to a given element of the crack wake based on the $(\Delta K)_{eff}$

value at which it was passed by the crack tip. It may be seen from Figure 7.21(b) that using this particular relationship, a good approximation of the measured closure characteristics for the *CA* tests may be generated.

In terms of the discrepancies in measured overload retardation distances and *PICC*-based modelling results, different approaches may be considered. One argument that avoids the use of *RICC* effects is that side-grooves do not produce pure plane strain conditions and therefore side-grooved samples cannot be compared directly with the plane strain modelling results. The assumption of a constraint factor of 3 may then be considered suspect for comparison with the side-grooved specimen data. Further *PICC*-based modelling work has therefore been conducted to assess possible stress state effects on post-overload transients. Figure 7.22(b) shows *PICC*-based modelling results using constraint factors of 3.0 and 2.5. It is found that the predicted closure transient curve does indeed move towards the experimental data and the baseline closure levels agree well after the constraint factor is decreased. However, to obtain a closure peak similar to the experimental data, it is clear a significant lower constraint value must be used, if the constraint factor is indeed lowered to a point sufficient to match the closure peak in Figure 7.22(b) (corresponding to $\alpha \sim 1.5$, *i.e.* close to the pure plane stress value), it is found that the overall transient length is still under predicted and the baseline closure levels no longer match.

In keeping with the empirical approximation of effective roughness contributions to crack closure illustrated in Figure 7.21 for constant amplitude conditions, Figure 7.22(a) highlights 2 empirical second-order polynomial relationships for effective roughness, h, and $(\Delta K)_{eff}$ used to generate the *PICC+RICC* curves in Figure 7.22(b). *PICC+RICC* 17 represents a relationship between effective roughness (h) and $(\Delta K)_{eff}$:

$$h = 6.0 * 10^{-5} mm, \quad 0 \le \Delta K_{eff} \le 2MPa \cdot m^{1/2}$$

$$h = (-5.8 * 10^{-5} * \Delta K_{eff}^2 + 2.32 * 10^{-4} * \Delta K_{eff} + 2.32 * 10^{-3}) / 36mm, \quad 2 < \Delta K_{eff} < 7MPa \cdot m^{1/2}$$

$$h = 1.0 * 10^{-5} mm, \quad \Delta K_{eff} \ge 7MPa \cdot m^{1/2}$$

PICC+RICC 22 represents a similar relationship between effective roughness (h) and $(\Delta K)_{eff}$ to *PICC+RICC* 17 with a small shifts in the polynomial coefficients:

$$h = 6.5 * 10^{-5} mm, \quad 0 \le \Delta K_{eff} \le 2MPa \cdot m^{1/2}$$

$$h = (-6.25 * 10^{-5} * \Delta K_{eff}^2 + 2.5 * 10^{-4} * \Delta K_{eff} + 2.09 * 10^{-3}) / 36mm, \quad 2 < \Delta K_{eff} < 7MPa \cdot m^{1/2}$$

$$h = 1.0 * 10^{-5} mm, \quad \Delta K_{eff} \ge 7MPa \cdot m^{1/2}$$

This is based on the consideration that microstructural influence on fatigue may be related to the relative scale of microstructural features and the crack tip plastic zone size, with the plastic zone size being proportional to $(\Delta K)^2$. The assumption is, of course, quite tentative at this stage. For the two curves shown in Figure 7.22(a) it is found that predicted post-overload crack closure variations agree reasonably well with the measured closure variations, especially for the '*PICC+RICC22*' curve. Similar effects are observed in Figure 7.23 where a *sine* relationship is assumed between the surface roughness and $(\Delta K)_{eff}$. This was identified with experimental observations discussed in Chapter 5 suggesting that near-threshold crack deflection angle may be more important than the absolute scale of the deflection distance in determining crack closure. Similar observations have been reported by Parry *et al.* [29] based on *FE* modelling of *RICC*. A *sine* relationship might then be expected in the effective roughness relationship based on the projection of deflected crack tip shear displacements to give shear mismatch of asperities along a crack path.

In the first instance it may be seen that further empirical fitting of *RICC* components may be carried out for experimental results such as those given in Chapter 6. Such nominal *RICC* influences may then rationalise the baseline load amplitude dependence of the measured closure data, as is indeed obvious for the *CA* predictions in Figure 7.21 where variations in closure level would indeed be absent from the pure *PICC* models. Similarly, Figure 7.22(b) and 7.23(b) show that transients of increased severity and overall length are readily generated by the present approach to *PICC+RICC* modelling, with the more limited discrepancy between the plane stress overload data and the pure *PICC* modelling then being consistent with a reduced relative impact of *RICC* in plane stress, as indicated

by Figure 7.20. Within the time available for the current project a empirical investigation of all the overload transient data presented in Chapter 6 has not been possible, and indeed is not considered entirely rational; in the longer term, as more physically-based procedure for generating effective roughness contributions from a quantitative understanding of roughness induced closure processes is clearly more valuable. Such analysis was considered beyond the scope of the current project; for the results currently available however, the following interpretations may be drawn:

(i) Significant quantitative improvements in the accuracy of modelling crack closure in *CA* and single overload fatigue are readily produced by the introduction of *RICC* influence via simple empirical relationships that are consistent with the established dependence of fracture surface features on effective stress intensity conditions.

(ii) The assumption that the effective roughness component of a crack wake element is simply dependent upon the effective crack tip stress intensity range that it experienced is a significant assumption and which is not substantiated by the present work: it can be seen in particular that the maximum effective roughness levels used in Figures 7.22 and 23 to simulate overload behaviour are appreciably higher than those in Figure 7.21 to simulate *CA* crack growth. This is not considered a major flaw in the current approach however, as recent finite element results have for example shown that quite detailed interactions may exist between fracture surface topography and subsequent on crack closure during overload transients [32]; in particular it has been shown that the relative size of fracture surface asperities and the overload plastic zone size may have an influence on crack closure levels that is not evident during *CA* loading. It may also be possible that different asperity crushing and fretting effects occur when a given surface topography arise within an overload event or as part of ongoing *CA* crack growth, although this point is relatively speculative.

7.4. Conclusions

1. A modified strip-yield model has been developed to simulate plasticity-induced crack closure under both *CA* and *VA* loading condition. The model is developed in a similar spirit to Newman's model with some modifications introduced. The predicted results are validated theoretically and experimentally.

2. Important issues regarding crack closure and fatigue behaviour have been addressed through the modelling investigation. The importance of crack closure concept in controlling near-tip material behaviour is demonstrated by the analytic results. The incidence of two transition points on post-overload local compliance curves is consistent with observed near-tip contact behaviour.

3. The potential for multimechanistic modelling has been explored by the introduction of an effective surface roughness concept. Further understanding of the effect of stress state, *RICC*, and *OICC* on fatigue behaviour under *CA* and *VA* loading has been obtained. It is found analytically that *RICC* has a stronger influence in plane strain than in plane stress. It is also seen that *RICC* and *OICC* may play an important role in closure even if the scale of these features is much smaller than the crack tip opening.

4. Essentially simple empirical representations of how roughness induced crack closure may contribute to *CA* and overload crack growth behaviour have been shown to provide marked improvements in closure modelling accuracy. A key methodology for improving closure modelling accuracy with relatively low computational costs has been demonstrated.

References

[1] B. Budiansky and J. W. Hutchinson, (1978), *J. of Applied Mechanics, Trans. Of ASME,* Vol.45, pp.267-276.

[2] K. K. Lo, (1980), *J. Appl. Mech.*, Vol.47, pp.811-815.

[3] Steven G. Russel, (1989), *Engng. Fracture Mech.,* Vol.33, pp.839-854.

[4] H. D. Dill and C. R. Saff, (1976), *ASTM STP 595,* pp.306-319.

[5] H. Fuehring and T. Seeger, (1979), *ASTM STP 677,* pp.144-167.

[6] J. C. Newman, Jr., (1981), *ASTM STP 748,* J.B. Chang and C. M. Hudson, Eds., American Society for Testing and Materials, pp.53-84.

[7] A. Blom, G. Wang, and R. G. Chermahini, (1990), *Localised Damage: Computer-aided Assessment and Control*, M. H. Aliabadi et al Eds., Computational Mechanics Publications, Springer-Verlag, Berlin, pp.57-68.

[8] J. C. Newman, Jr., (1995), *J. of Engng. Mater. Technology, Trans. of ASME,* Vol.117, pp.433-439.

[9] J. C. Newman, Jr., (1992), *NASA TM 104159,* Langley Research Centre, Hampton, Virginia.

[10] J. C. Newman, Jr., (1999), *NASA TM 209133,* Langley Research Centre, Hampton, Virginia.

[11] S. R. Daniewicz, J. A. Collins, and D. R. Houser, (1994), *Int. J. of Fatigue,* Vol.16, pp.123-133

[12] Tianchong Chang and Wanlin Guo, (1998), *Int. J. of Fracture,* vol.91, L45-L50.

[13] R. J. Dexter, S. J. Hudak, Jr., and D. L. Davidson, (1989), *Engng. Fracture Mech.,* Vol.33, pp.855-870.

[14] D. Nowell, (1998), *Fatigue & Fracture of Engineering Materials & Structures,* Vol.21, pp.857-871.

[15] C. Atkinson and M. F. Kanninen, (1977), *Int. J. of Fracture,* Vol.13, pp.151-163.

[16] D. S. Dugdale, (1960), *J. of the Mechanics and Physics of Solids*, Vol.8, pp.100-104.

[17] Y. Xu, P. J. Gregson, and I. Sinclair, (2000), *Materials Science Forum,* Vols.331-337, pp.1525-1530.

[18] Yigeng Xu, P. J. Gregson, and I. Sinclair, (2000), *Materials Science and Engineering A,* Vol.284A, pp.114-120.

[19] J. W. Hutchinson, (1968), *J. of the Mechanics and Physics of Solids,* Vol.16, pp.13-31.

[20] J. R. Rice and G. F. Rosengren, (1968), *J. of the Mechanics and Physics of Solids,* Vol.16, pp.1-12.

[21] Guo Wanlin, (1994), *Engng. Fracture Mech.,* Vol.49, pp.277-285.

[22] J. B. Ibso and H. Agerskov, (1996), *J. Construct. Steel Res.,* Vol.37, pp229-261.

[23] J. C. Newman, Jr., (1999), Engineering Against Fatigue, J. H. Beynon et al Eds, A. A. Balkema Publisher, pp.261-268.

[24] H. Tada, P. C. Paris, and G. R. Irwin, (1973), *The Stress Analysis of Cracks Handbook,* Del Research Corporation.

[25] J. C. Newman, Jr., (1976), *NASA TN D-8268.*

[26] B. Carnahan, A. H. Luther, and J. O. Wilkes, (1969), *Applied Numerical Methods,* Wiley, New York.

[27] J. R. Rice, (1967), *ASTM STP 415*, pp.247-309.

[28] W. Elber, (1970), *Engng. Fracture Mech.,* Vol.2, pp.37-45.

[29] M. R. Parry, S. Syngellakis, and I. Sinclair, (2000), *Materials Science and Engineering A,* Vol.291A, pp.224-234.

[30] S. Suresh, G. F. Zamiski, and R. O. Ritchie, (1981), *Metallurgical Transactions,* Vol.12A, pp.1435-43.

[31] A. K. Vasudevan and S. Suresh, (1982), *Metallurgical Transactions,* Vol.13A, pp.2271-80.

[32] M. R. Parry, (2000), Ph.D. Thesis, School of Engineering Sciences, University of Southampton.

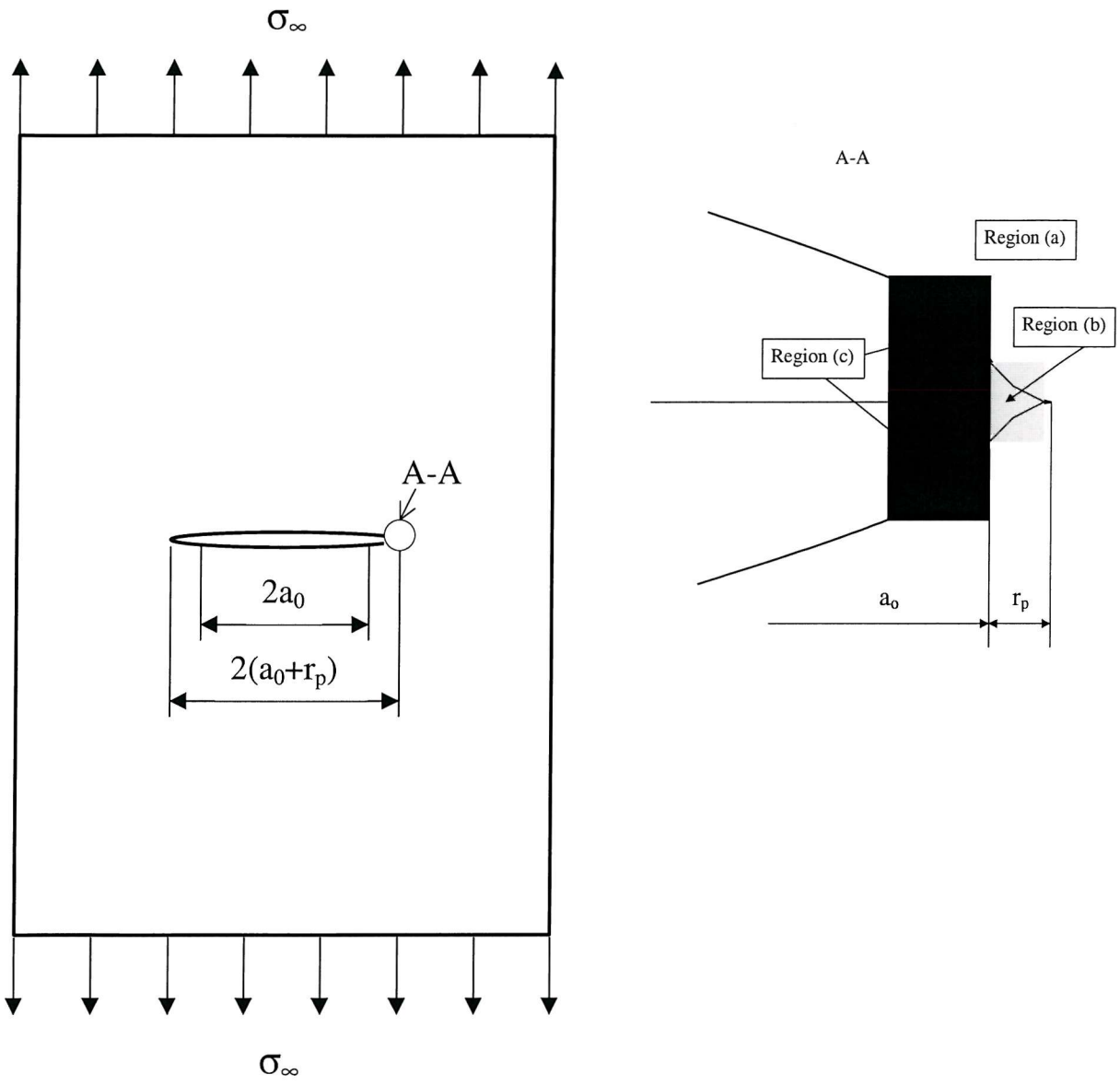

Figure 7.1 Model geometry of the CCT samples.

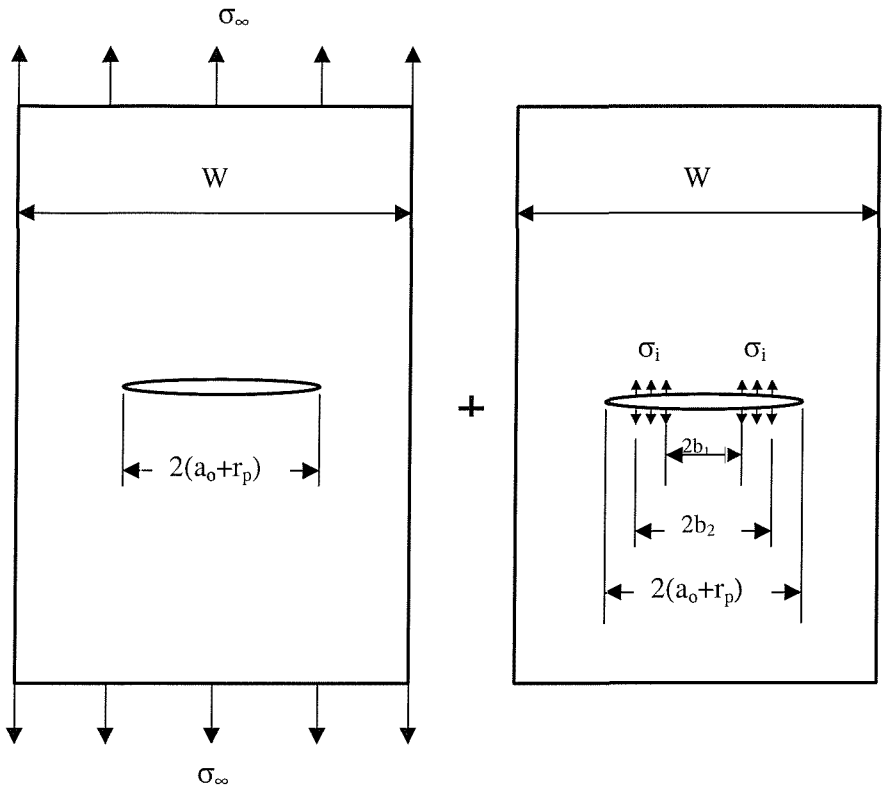

Figure 7.2 *Superposition of two elastic problems of a CCT sample subjected to: (a) remote uniform tensile stress, σ_∞, and (b) uniform stress, σ_i, on a segment of the crack surface.*

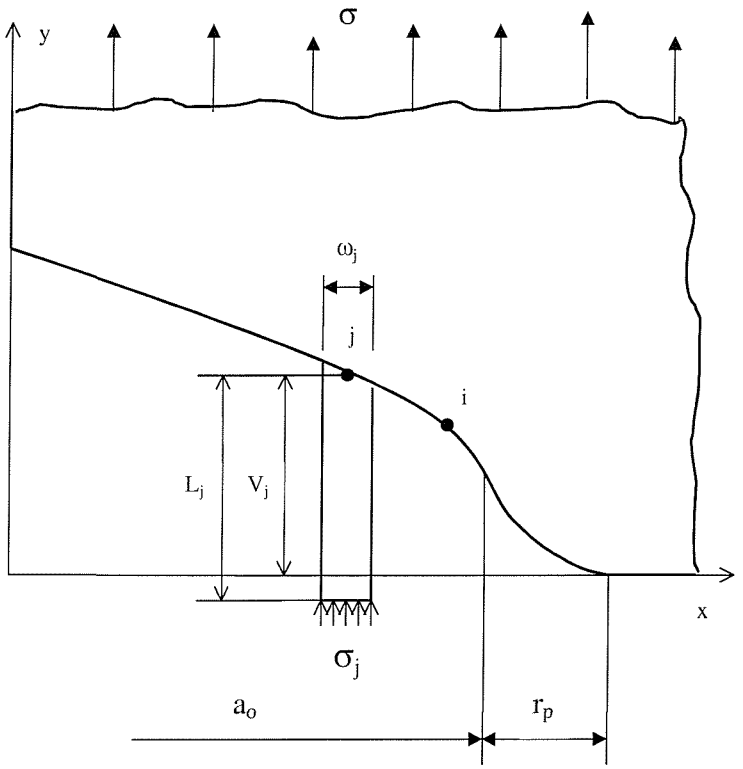

Figure 7.3 *Schematic of loading and co-ordinate system used in the analytical closure model.*

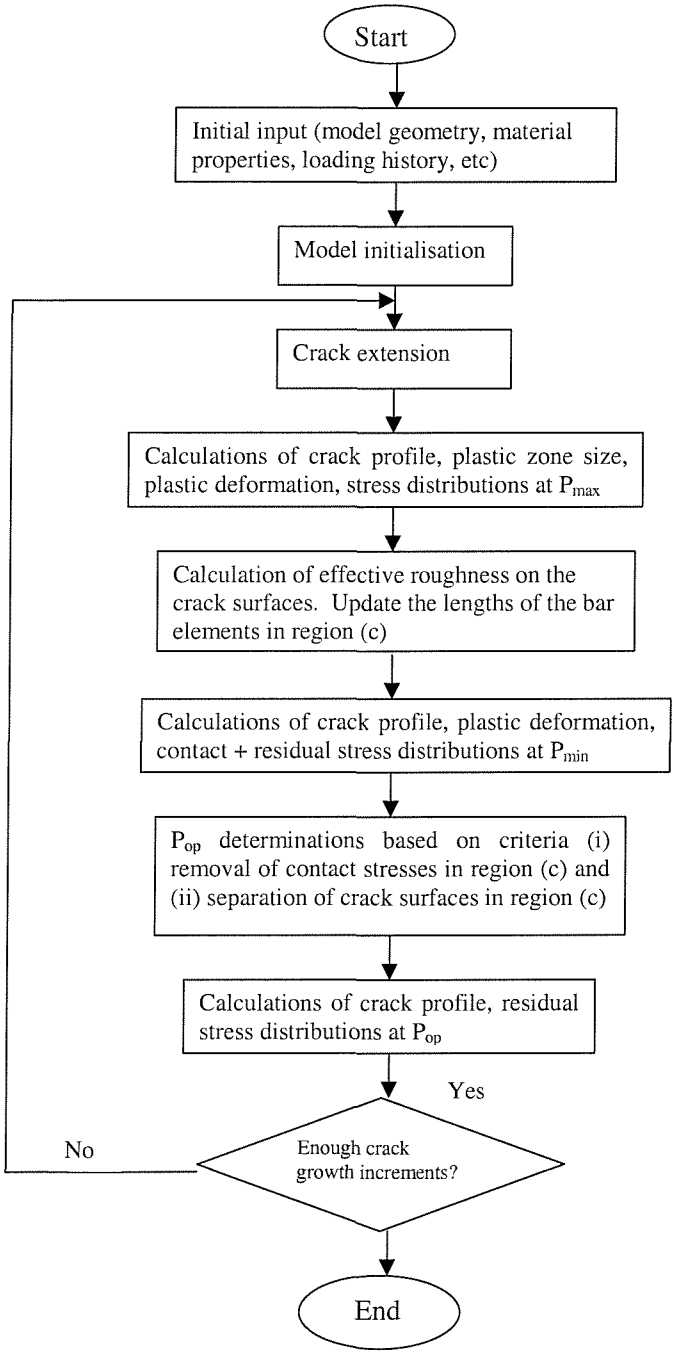

Figure 7.4 Flow chart of the computer program.

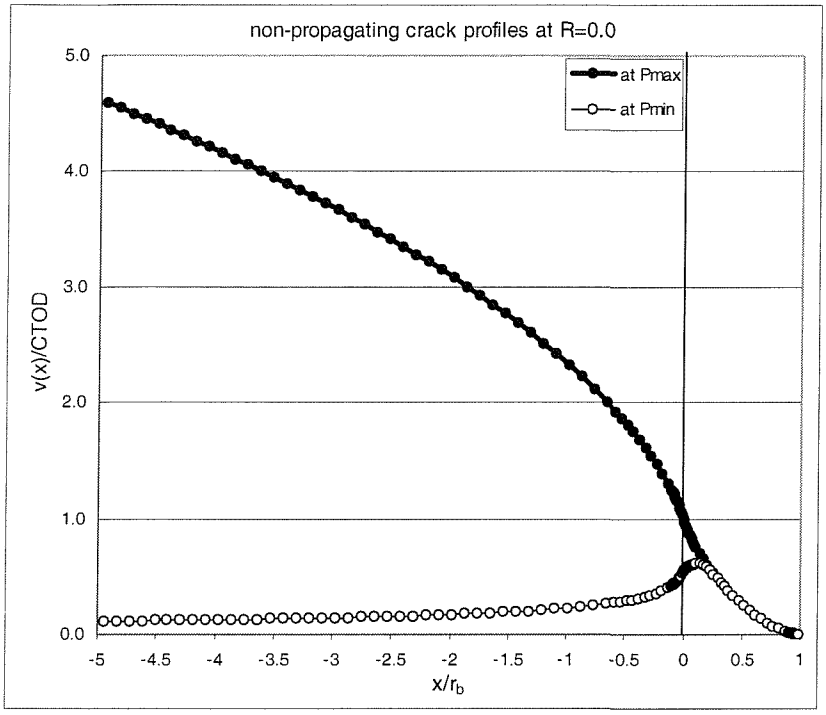

(a)

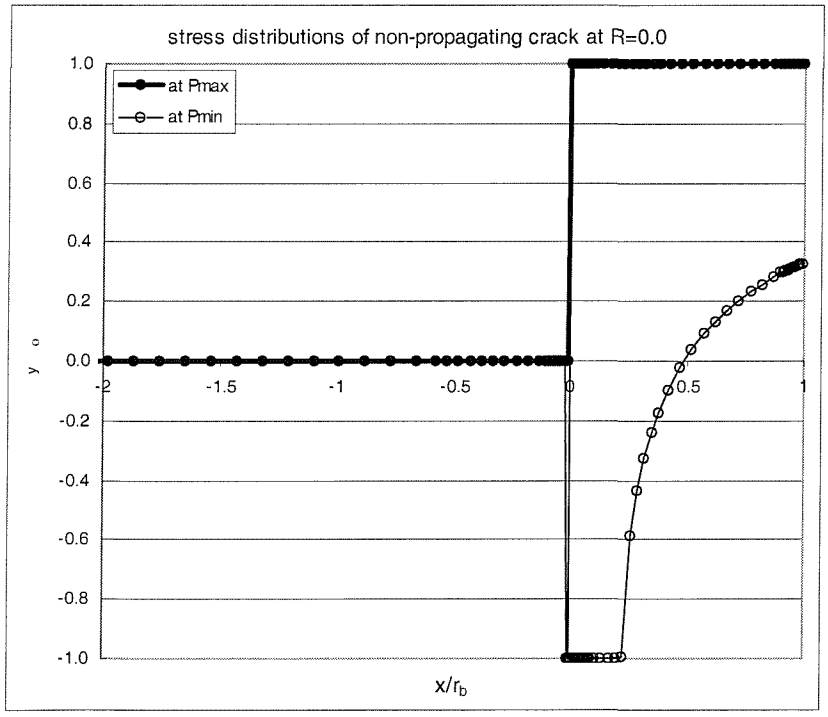

(b)

Figure 7.5 *Crack opening profiles and surface stress distributions of non-propagating crack at R=0.0.*

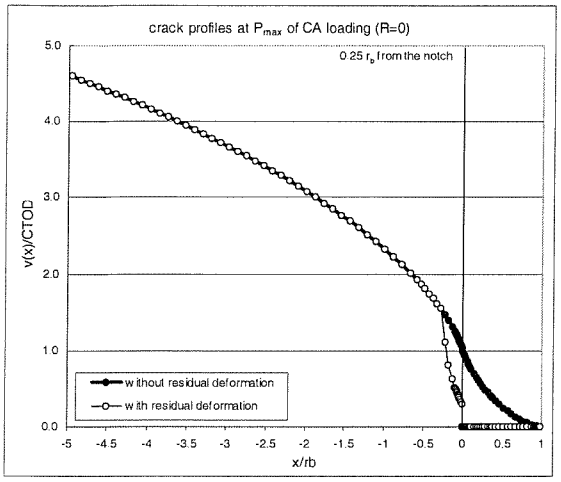

(a)

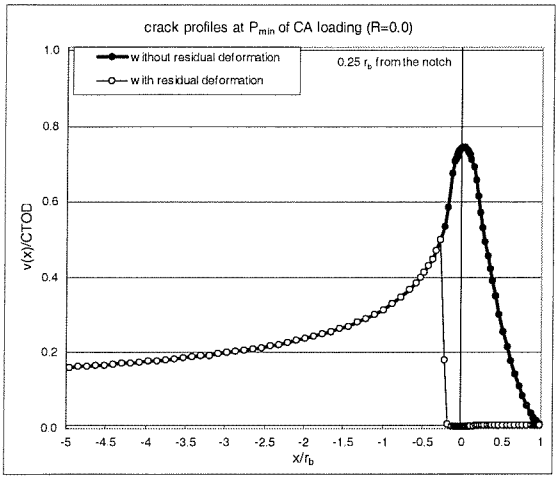

(b)

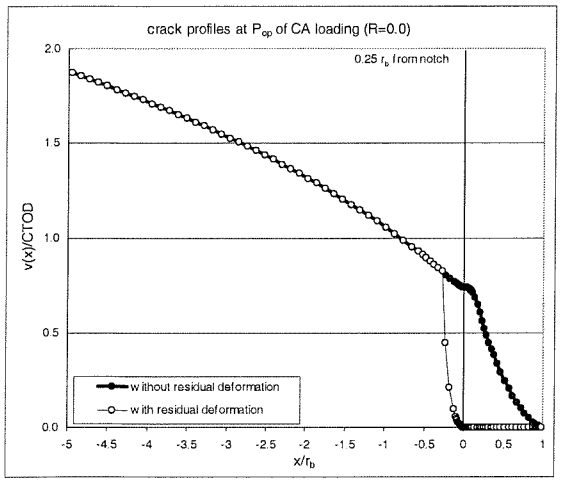

(c)

Figure 7.6 *Crack profiles at (a) P_{max}, (b) P_{min}, and (c) P_{op} after $0.25r_b$ crack growth under CA loading of R=0.*

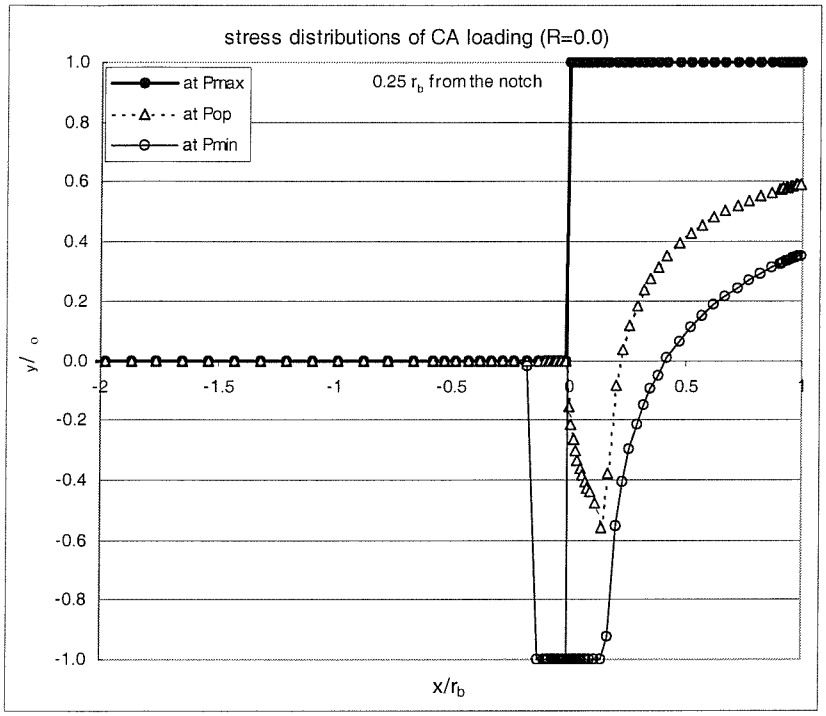

Figure 7.7 Crack surface stress distributions at P_{max}, P_{min}, and P_{op} after $0.25r_b$ crack growth under CA loading of R=0.

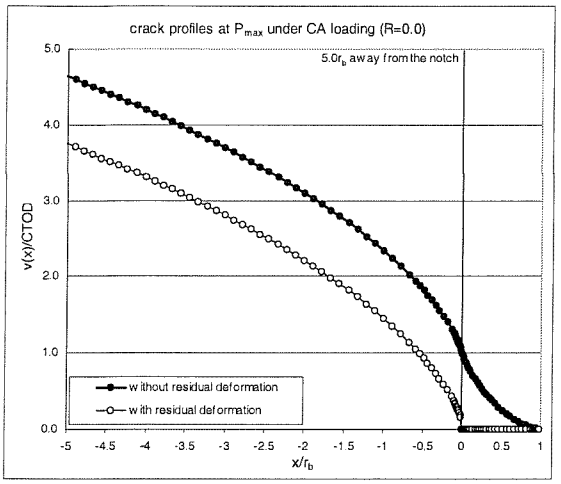

(a)

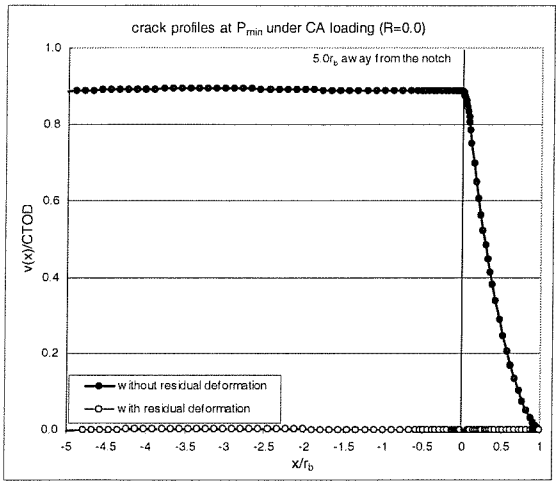

(b)

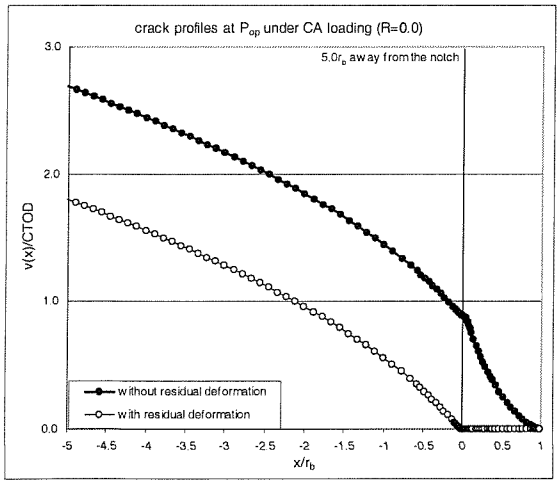

(c)

Figure 7.8 *Crack profiles at (a) P_{max}, (b) P_{min}, and (c) P_{op} after $5.0r_b$ crack growth under CA loading of R=0.*

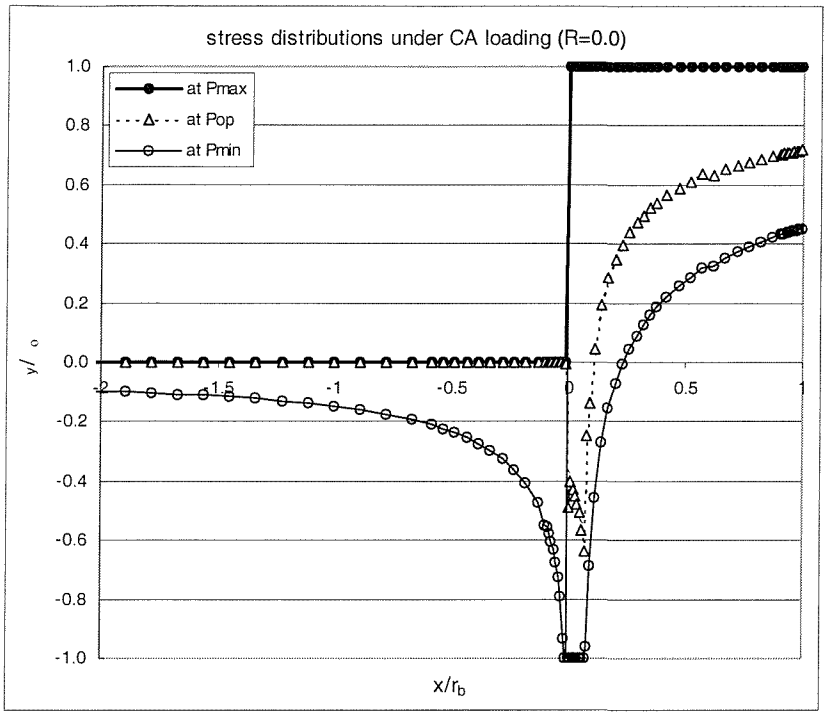

Figure 7.9 *Crack surface stress distributions at P_{max}, P_{min}, and P_{op} after $5.0r_b$ crack growth under CA loading of R=0.*

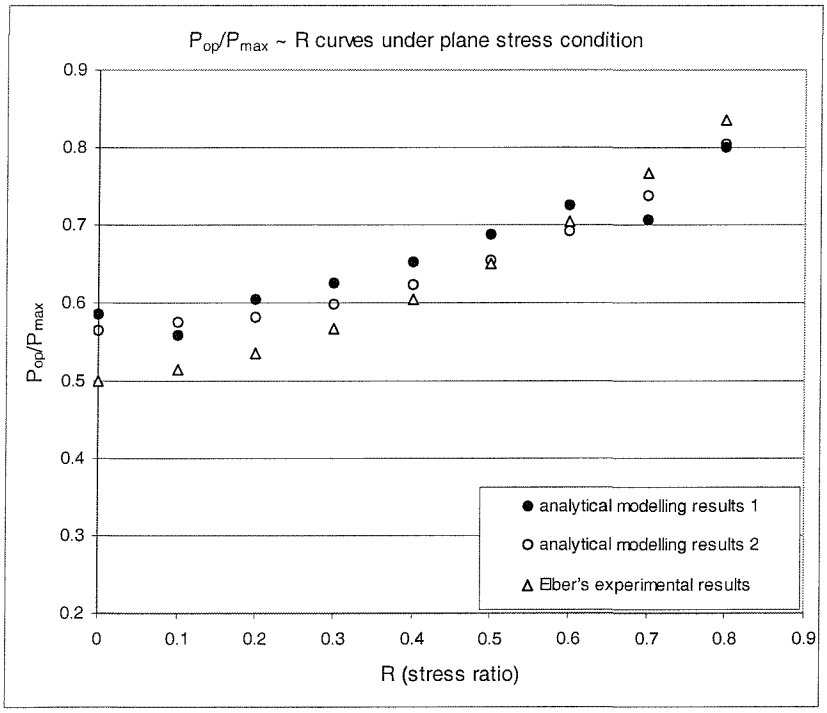

Figure 7.10 *Comparison of current analytical modelling results for plasticity-induced crack closure with Elber's experimental results [28].*

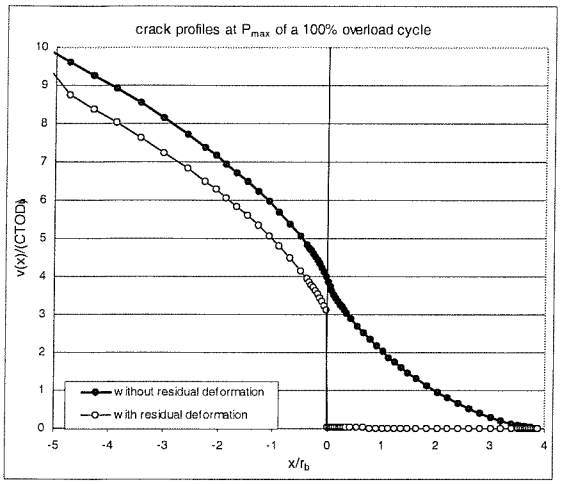

(a)

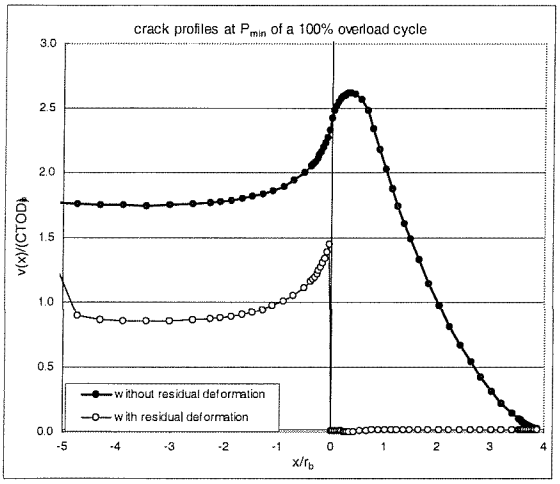

(b)

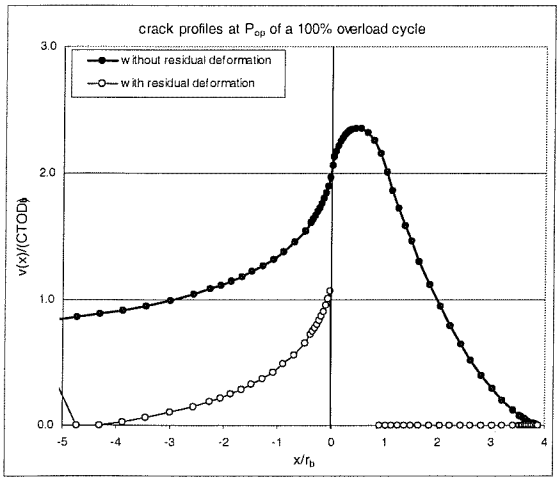

(c)

Figure 7.11 Crack profiles at (a) P_{max}, (b) P_{min}, and (c) P_{op} of a 100% single overload cycle.

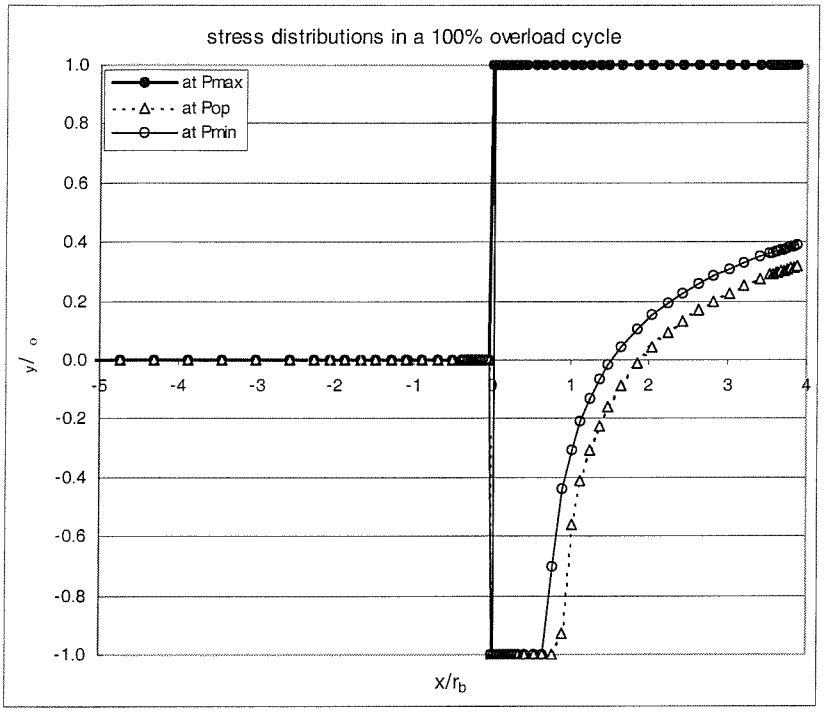

Figure 7.12 Crack surface stress distributions at P_{max}, P_{min}, and P_{op} of the 100% overload cycle.

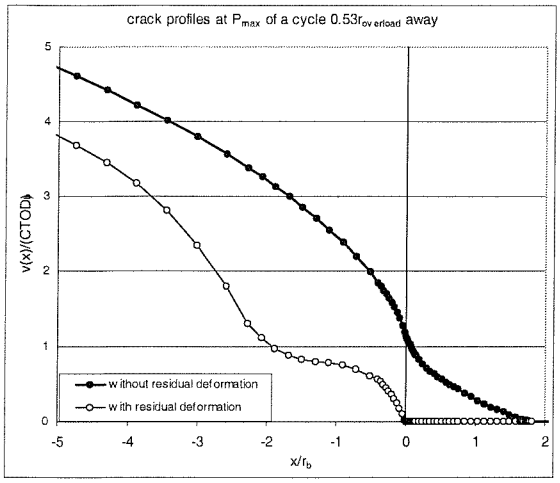

(a)

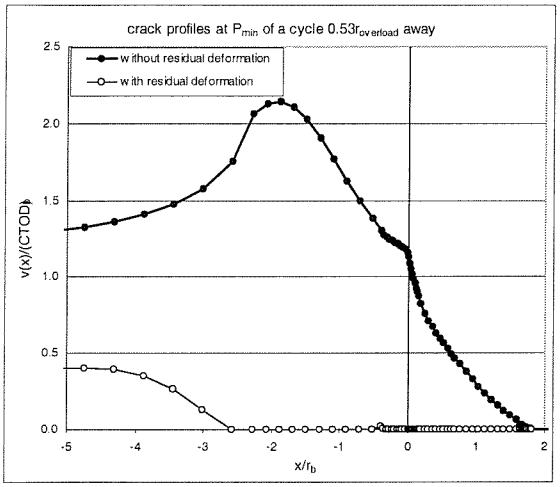

(b)

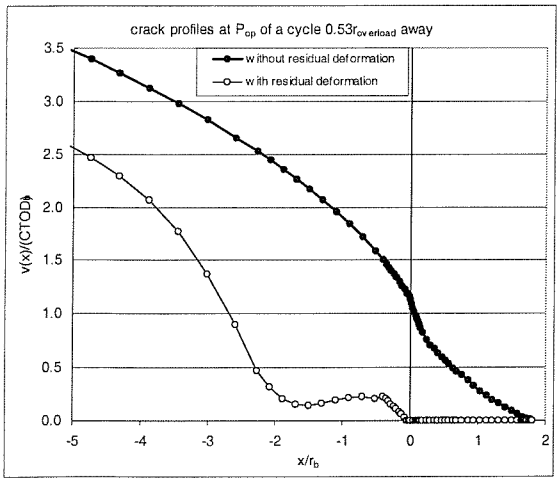

(c)

Figure 7.13 Crack profiles at (a) P_{max}, (b) P_{min}, and (c) P_{op} of a cycle $0.53r_{overload}$ away from the application of a 100% single overload.

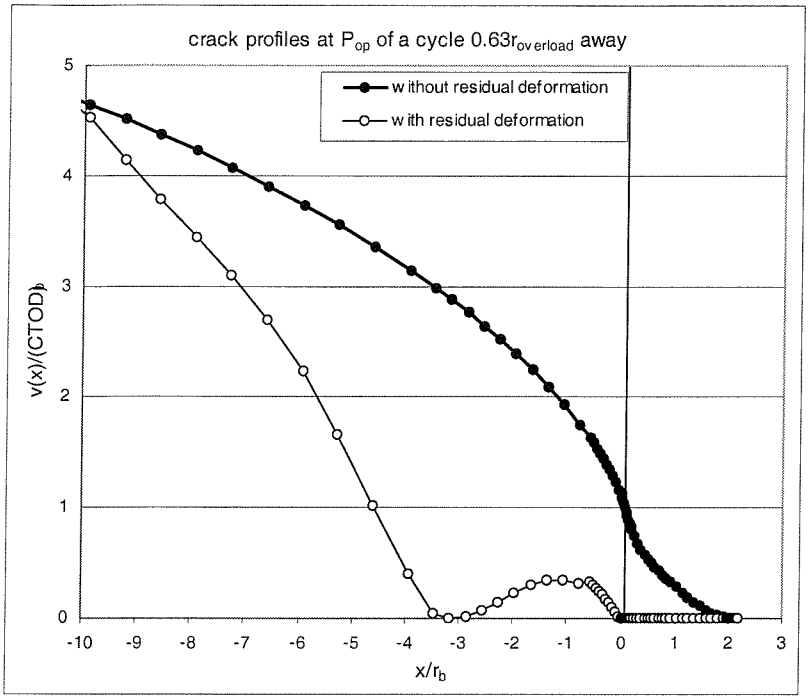

Figure 7.14 Crack profiles at P_{op} of a cycle $0.63r_{overload}$ away from the application of a 150% single overload.

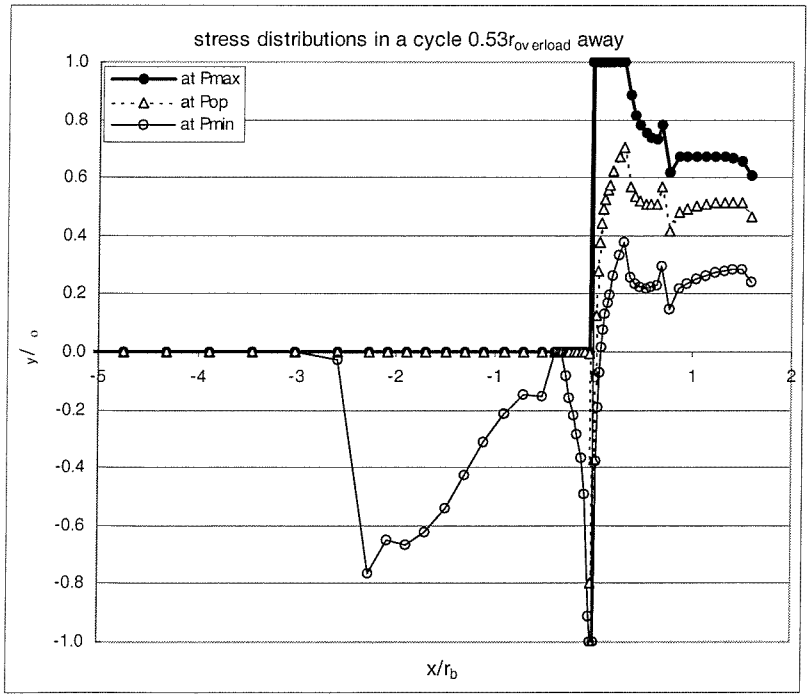

Figure 7.15 Crack surface stress distributions at P_{max}, P_{min}, and P_{op} of a cycle $0.53r_{overload}$ away from the application of a 100% overload.

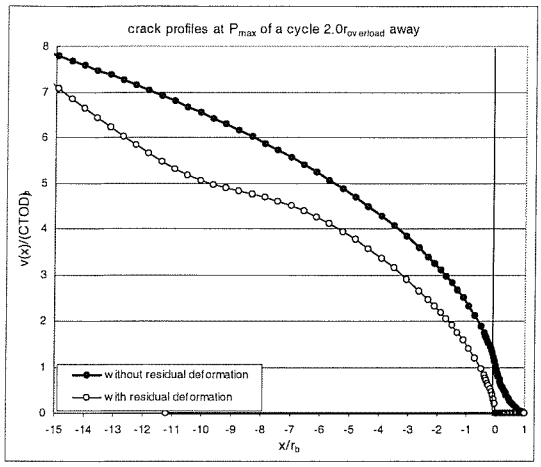

(a)

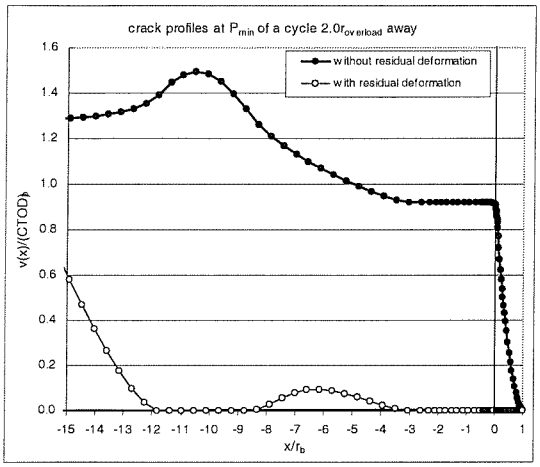

(b)

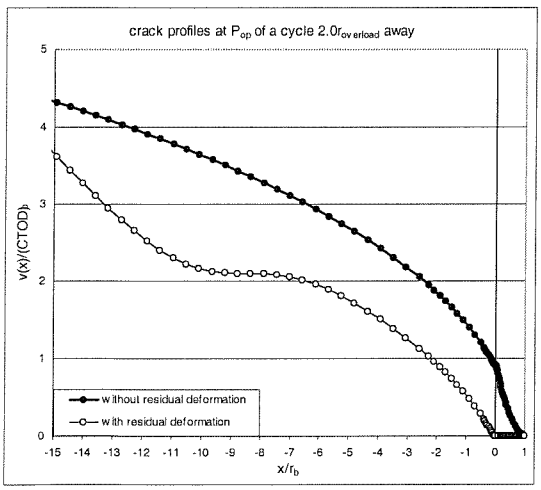

(c)

Figure 7.16 Crack profiles at (a) P_{max}, (b) P_{min}, and (c) P_{op} of a cycle $2.0r_{overload}$ away from the application of a 100% single overload.

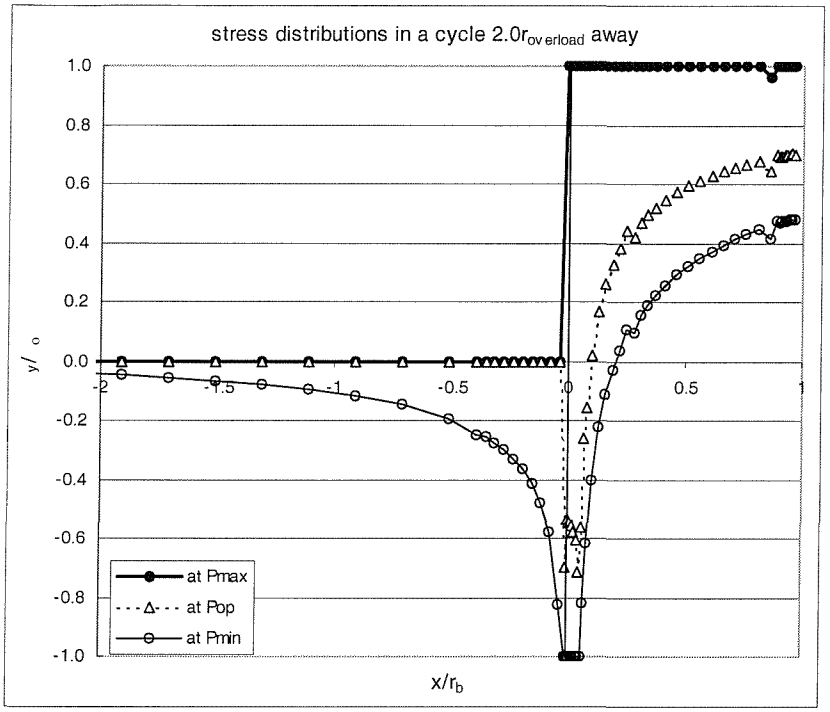

Figure 7.17 Crack surface stress distributions at P_{max}, P_{min}, and P_{op} of a cycle $2.0r_{overload}$ away from the application of a 100% overload.

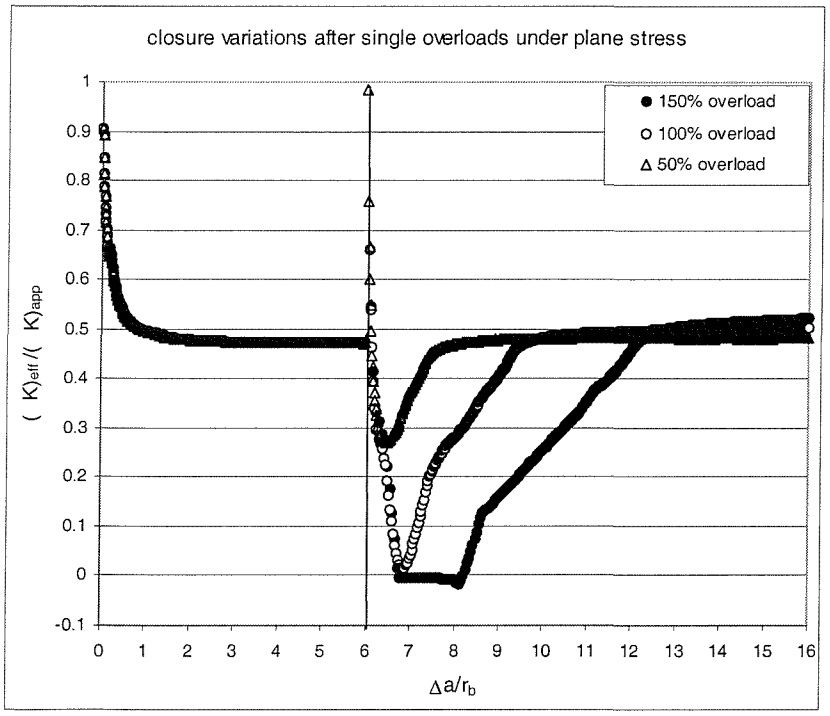

Figure 7.18 Crack closure variations after single overloads of 50%, 100%, and 150% overload ratios under plane stress condition.

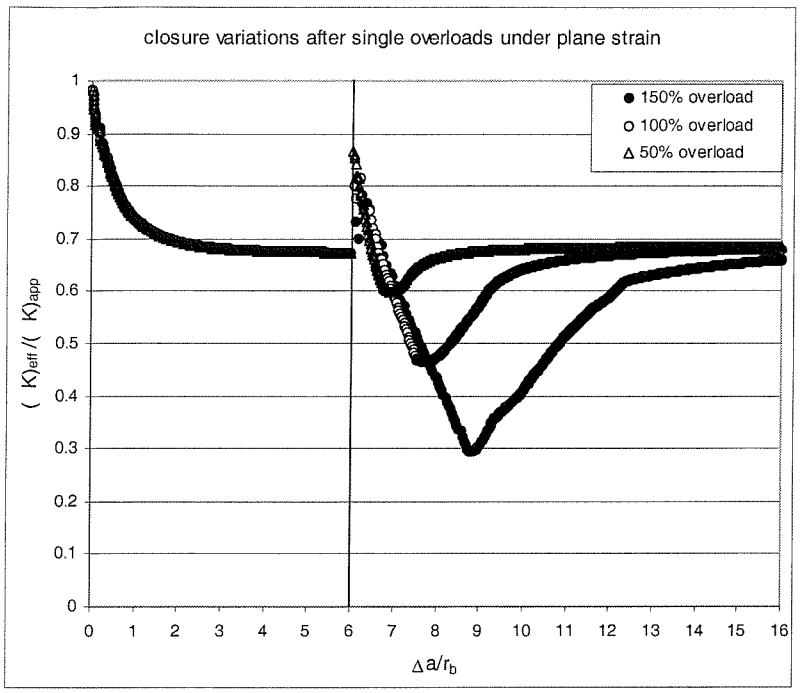

Figure 7.19 Crack closure variations after single overloads of 50%, 100%, and 150% overload ratios under plane strain condition.

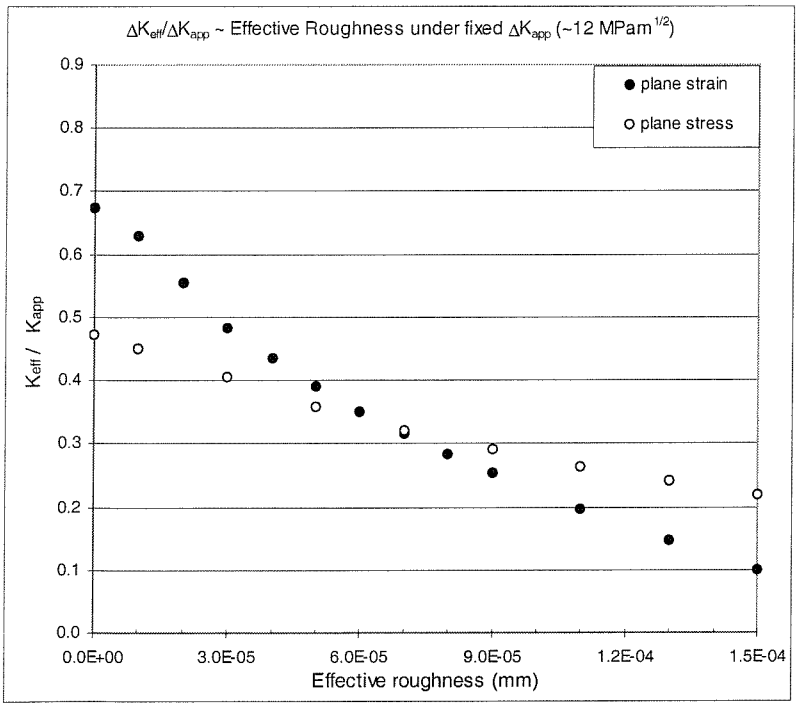

Figure 7.20 Increased PICC+RICC levels with the increase of effective surface roughness.

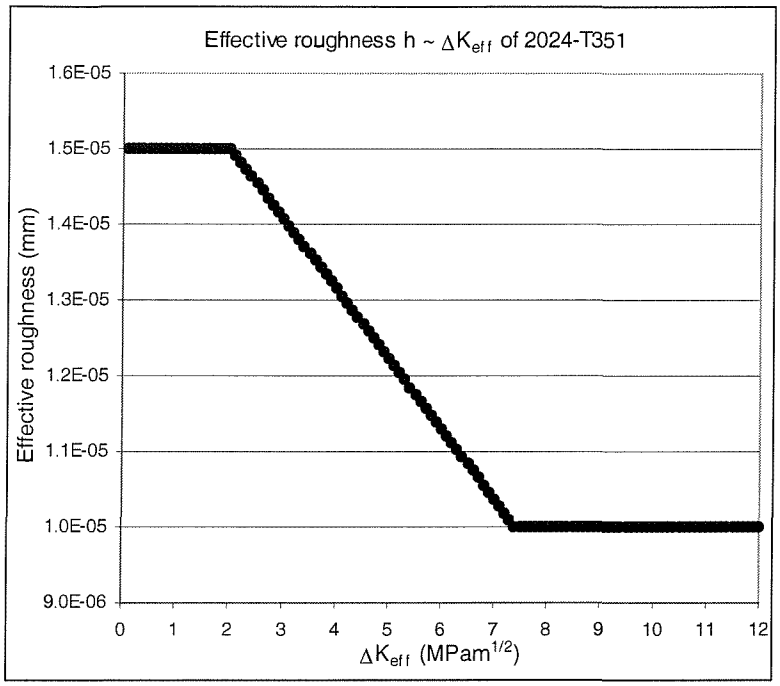

(a)

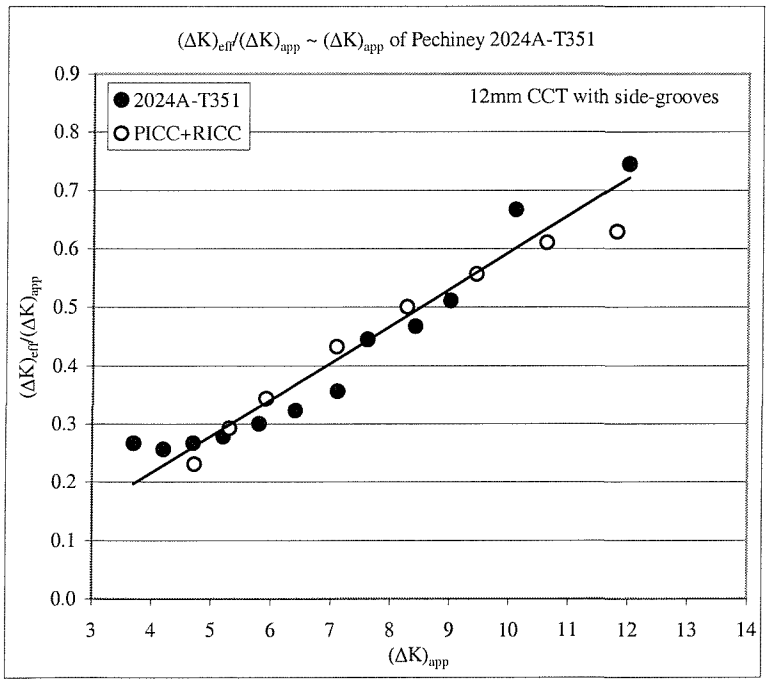

(b)

Figure 7.21 *(a) empirical relationship between effective roughness and $(\Delta K)_{eff}$, and (b) Comparison between predicted and measured closure variations with $(\Delta K)_{app}$ for CA fatigue at R of 0.1 under plane strain conditions.*

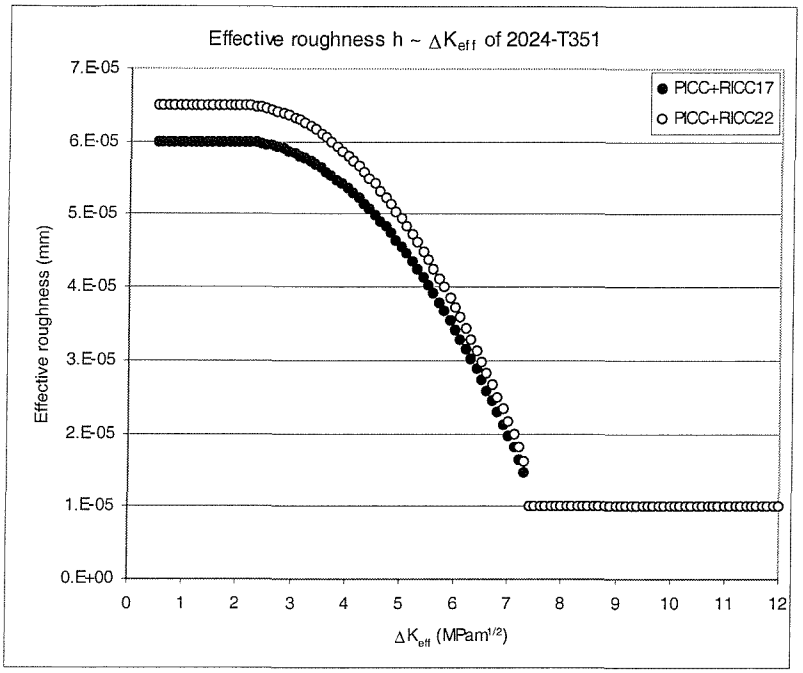

(a)

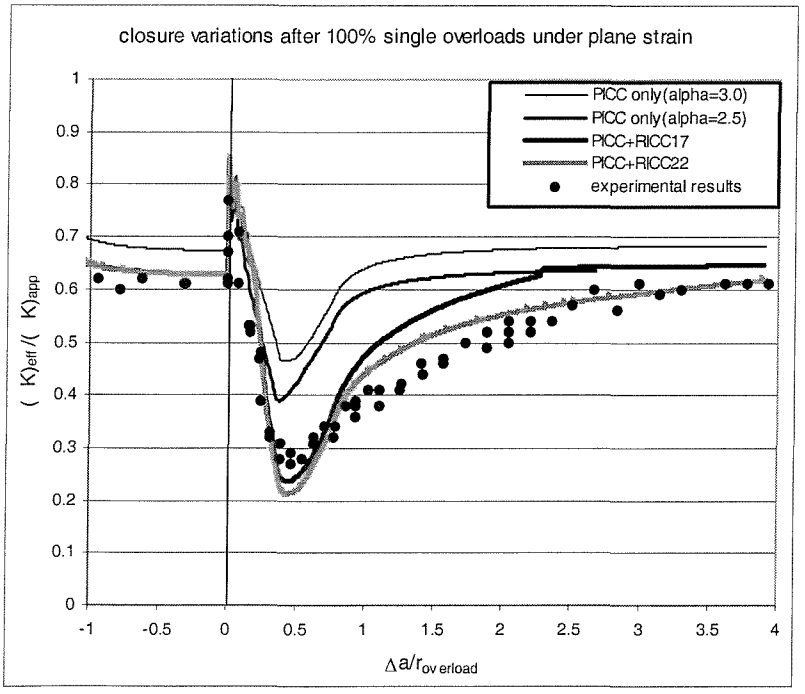

(b)

Figure 7.22 *(a) proposed empirical relationships between effective roughness and $(\Delta K)_{eff}$, and (b) Comparison between predicted and measured post-overload closure transients after a 100% single overload at $(\Delta K)_b$ of 12MPam$^{1/2}$ and R of 0.1and plane strain conditions.*

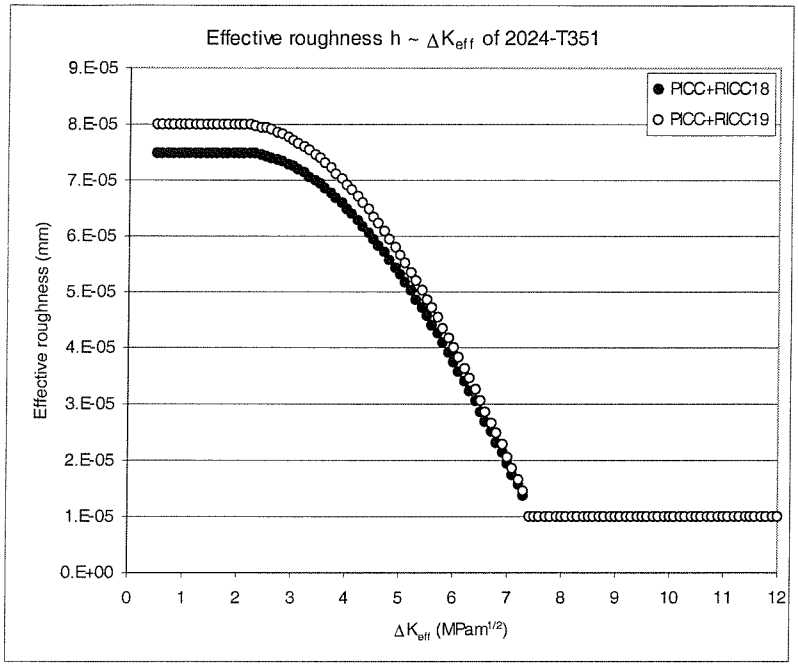

(a)

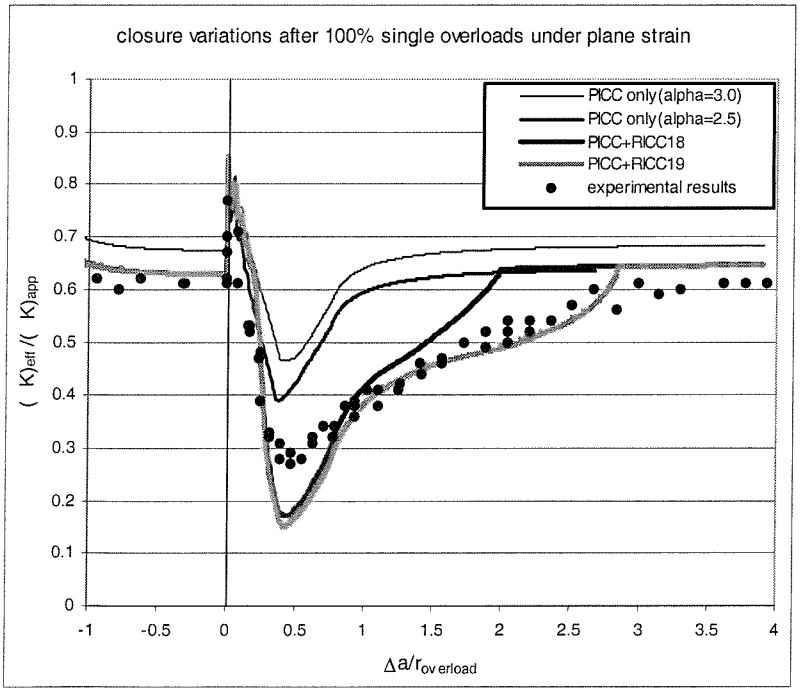

(b)

Figure 7.23 *(a) proposed empirical relationships between effective roughness and $(\Delta K)_{eff}$, and (b) Comparison between predicted and measured post-overload closure transients after a 100% single overload at $(\Delta K)_b$ of 12MPam$^{1/2}$ and R of 0.1and plane strain condition.*

8. CONCLUSIONS AND FURTHER WORK

8.1. Summary & Conclusions

1. Comprehensive literature review has been carried out on following topics: *CA* fatigue behaviour, *VA* fatigue behaviour, and microstructure influence on fatigue resistance of heat-treatable high strength *Al* alloys. A lack of consensus in the role of closure in fatigue behaviour is noted, along with a lack of consistent, non-subjective closure measurements.

2. Systematic material characterisation has been carried out on the alloys 2024-T351 and 2024A-T351. Microstructure, tensile properties, and fatigue behaviour under *CA* and various single overload conditions have been studied.

3. A crack closure measuring system using near-tip strain gauges and conventional crack mouth clip gauges has been established. Sensitive, non-subjective curve fitting methods have been established to measure crack closures under *CA* and *VA* loading conditions. The significance of varying stress states through the thickness of conventional plain-sided test specimens is highlighted, with the current work identifying a combination of thick/side-grooved and thin/non-side-grooved fatigue specimen formats for more systematic analysis of crack growth and closure characterisation.

4. Extrinsic and intrinsic fatigue resistance of the 2024 and 2024A alloys has been investigated via the above closure assessment methods. Alloy influence on crack growth under both *CA* and single overload loading conditions can predominantly be attributable to extrinsic processes, even though differences in crack propagation mode were evident in the two alloys. The *CA* closure benefit in 2024A was seen to be carried over to overload behaviour. Reduced dispersoid content was considered to promote crystallographic growth in 2024A, since differences in growth mode were evident from stress intensities when plastic zone sizes were relatively small compared to the primary grain

size. Crack closure behaviour, approaching threshold at least, was seen to be insensitive to the absolute scale of the surface asperities, suggesting other characteristics such as deflection angle may be more significant in controlling crack closure.

5. Sample stress state conditions clearly influenced post-overload behaviour in the present tests. Enhanced post-overload retardation effects have been observed in samples closer to plane stress conditions. The effect was not seen to scale with the changes in plastic zone size between the two stress states, with overload transients being distinctly longer under plane strain than under plane stress conditions when results are normalised against the relevant plastic zone dimensions.

6. A modified strip-yield analytical model has been developed to simulate *PICC*. The importance of the crack closure concept in controlling near-tip material behaviour is demonstrated by the analytic results. The incidence of two transition points on the post-overload local compliance curves has been analytically recovered and explained by the modelling.

7. An effective surface roughness concept has been introduced to the established *FASTRAN* approach to *PICC* modelling, providing an important initial step in developing more multi-mechanistic approaches to closure and crack growth modelling. Further understanding of the effect of stress state, *RICC*, and *OICC* on fatigue behaviour under *CA* and *VA* loading has been obtained. It is found analytically that *RICC* has a stronger relative influence in plane strain than in plane stress. It is also noted that *RICC* and *OICC* may play an important role even if the scale of these features is much smaller than the crack tip opening. Measured crack closure levels and prolonged post-overload retardations associated with plane strain overloads has been particularly rationalised by the combined effects of *PICC* and *RICC* using the present modified modelling approach.

8.2. Further Work

Based on the current work, areas for further analysis may be identified as:

1. Reliable and non-subjective measurement of crack closure at the very early stages of post-overload crack growth. Further cross-referencing of different closure assessment techniques (*e.g.* interferometry) would be valuable, particular where stress/strain conditions within the bulk of a sample may be examined (e.g. neutron or synchrotron diffraction studies).

2. Further detailed studies on the correlation of following parameters: grain size, surface roughness, crack deflection angles, crack closure, loading condition, and fatigue resistance, to be carried out parallel with the development of a more physically-based estimation process for the 'equivalent roughness' values used in the current modelling.

3. 3-D modelling of crack closure and its relevance to the practical performance of engineering components, *i.e.* addressing the summation of through-thickness stress state effects that inevitably arise across component sections.

APPENDICES

Appendix A.

```
% Closure point determination based on slope variation criterion 1.
clear all;
clc;
pathload=['/home/yx2/'];
filename=['xu05039.txt'];
fid=fopen([pathload,filename]);
sig=fscanf(fid,'%f%f',[7,600]);
status=fclose(fid);
sigfit=zeros(7,600);
for NN=3:7,
d0=100;
d=25;
x1=sig(2,1:d0);
y1=sig(NN,1:d0);
s=polyfit(x1,y1,1);
s0=s(1);
in=d0;
while in<550
x1=sig(2,(in-d):(in+d));
y1=sig(NN,(in-d):(in+d));
s=polyfit(x1,y1,1);
s1=s(1);
delta=abs((s1-s0)/s0);
if delta>0.1,
index=in;
in=600;
else
in=in+d;
x2=sig(2,1:in);
y2=sig(NN,1:in);
s=polyfit(x2,y2,1);
s0=s(1);
index=1;
end
end
%NN
%index
sig(2,index)
%sig(NN,index)
End
```

Appendix B.

```
% Closure point determination based on slope variation criterion 2.
clear all;
clc;
pathload=['/home/yx2/'];
filename=['xu05039.txt'];
fid=fopen([pathload,filename]);
sig=fscanf(fid,'%f%f',[7,600]);
status=fclose(fid);
sigfit=zeros(7,600);
for NN=3:7,
d0=100;
d=25;
x1=sig(2,1:d0);
y1=sig(NN,1:d0);
s=polyfit(x1,y1,1);
s0=s(1);
in=d0;
while in<550
x1=sig(2,(in-d):(in+d));
y1=sig(NN,(in-d):(in+d));
s=polyfit(x1,y1,1);
s1=s(1);
delta=abs((s1-s0)/s0);
if delta>0.1,
index=in;
in=600;
else
in=in+d;
s0=s(1);
index=1;
end
end
%NN
%index
sig(2,index)
%sig(NN,index)
End
```

Appendix C.

```
% Closure point determination based on slope variation criterion 3.
clear all;
clc;
pathload=['/home/yx2/'];
filename=['xu05039.txt'];
fid=fopen([pathload,filename]);
sig=fscanf(fid,'%f%f',[7,600]);
status=fclose(fid);
sigfit=zeros(7,600);
for NN=3:7,
d0=150;
d=25;
x1=sig(2,1:d0);
y1=sig(NN,1:d0);
s=polyfit(x1,y1,1);
s0=s(1);
in=d0;
while in<550
x1=sig(2,(in-d):(in+d));
y1=sig(NN,(in-d):(in+d));
s=polyfit(x1,y1,1);
s1=s(1);
delta=abs((s1-s0)/s0);
if delta>0.1,
index=in;
in=600;
else
in=in+d;
index=1;
end
end
%NN
%index
sig(2,index)
%sig(NN,index)
End
```

Appendix D.

```
% Closure point determination based on curve fitting criterion 1.
clear all;
clc;
figure;
pathload=['/home/yx2/'];
filename=['xu05039.txt'];
fid=fopen([pathload,filename]);
sig=fscanf(fid,'%f%f',[7,600]);
status=fclose(fid);
sigfit=zeros(7,600);
for NN=3:7,
kkmin=50;
for N=100:5:500,
x=sig(2,1:N);
y=sig(NN,1:N);
p=polyfit(x,y,1);
klinear=p(1);
x2=sig(2,N:600);
y2=sig(NN,N:600);
v=polyfit(x2,y2,2);
kcurve=2*v(1)*sig(2,N)+v(2);
kkerror=sqrt((kcurve-klinear)^2+(polyval(p,sig(2,N))-polyval(v,sig(2,N)))^2);
if kkerror<kkmin
kkmin=kkerror;
kkindex=N;
c1=p(1);
c2=p(2);
c3=v(1);
c4=v(2);
c5=v(3);
end
end
p(1)=c1;
p(2)=c2;
v(1)=c3;
v(2)=c4;
v(3)=c5;
sigfit(NN,1:kkindex)=polyval(p,sig(2,1:kkindex));
sigfit(NN,(kkindex+1):600)=polyval(v,sig(2,(kkindex+1);600));
%NN
%kkindex
sig(2,kkindex)
%sig(NN,kkindex)
end
plot(sig(2,:),sig(3,:),'g-',sig(2,:),sig(4,:),'y-',sig(2,:),sig(5,:),'r-',sig(2,:),sig(6,:),'b-
',sig(2,:),sig(7,:),'c-');
```

```
xmax=max(sig(2,:));
ymax=max(sig(3:7,:));
grid on
title('load ~ cod curves');
xlabel('load');
ylabel('cod');
%axis([0:xmax*1.1,0:ymax*1.1]);
zoom;
figure
plot(sig(2,:),sigfit(3,:),'g-',sig(2,:),sigfit(4,:),'y-',sig(2,:),sigfit(5,:),'r-
',sig(2,:),sigfit(6,:),'b-',sig(2,:),sigfit(7,:),'c-');
xmax=max(sig(2,:));
ymax=max(sigfit(3:7,:));
grid on
title('curve fitting');
xlabel('load');
ylabel('fitted cod');
%axis([0:xmax*1.1,0:ymax*1.1]);
zoom
```

Appendix E.

```
      PROGRAM CRACK_CLOSURE_MODELLING
:
:
```
This is the main module of the program. It controls the flow of the model, number of the simulation steps, and load levels, etc.
```
:
:

      Use Global_Data
      Implicit None
      Integer :: N, Loadcycle
      Double Precision :: S1
      Double Precision :: Smax(2000), Smin(2000)
      Loadcycle=2000
      S1=2.5D1
      Smax=S1; Smin=S1*0.1
      Smin(600)=S1*R
      Smax(600)=1.0*S1
      Open  (unit=10, file= "result1.out", status= "old")
      Write (unit=10, FMT=*) "Analytical Crack Closure Modelling"
      Print *, "Analytical Crack Closure Modelling"
100   Format (F10.4, 3(E12.5, 1x))
200   Format (1x, "X(I)", T12, "V(I)", T30, "S(I)", T45, "L(I)")
      Call Initialisation(S1)
      DO N=1, 600
!     Write (unit=10, FMT=*) "*****************************"
!     Write (unit=10, FMT=*) "Results at N=", N
      Print *, "*****************************"
      Print *, "Results at N=", N
      Call Crack_Extension(Smax(N))
      Call Smax_Data(Smax(N), N)
      Call Smin_Data(Smax(N),Smin(N),N)
      Call Crack_Opening(Smax(N),Smin(N),N)
      End DO
      Write (unit=10, FMT=*) "End of the analysis"
      Close (unit=10)
      Print *, "End of the Analysis"
      END PROGRAM CRACK_CLOSURE_MODELLING

:
:
```
Following is Global_Data Module which defines the geometry of the model, material properties used throughout the simulation, and some constant parameters like pi.
```
:
:
```

```
!     Define Module Global_Data
      Module Global_Data
      Implicit None
      Save
!     This module defines sample geometry, materials properties,
!     and some parameters.
      Integer :: N1
      Double Precision :: a0, af, rp0, rpmax, rpmax0, rpmax1
      Double Precision :: Pmax, Pmin, Pmax1, Pmin1
      Double Precision :: S(100),W(100),X(100),F(100),V(100)
      Double Precision :: L(100),L11(100),L22(100),Y(100),G(100,100)
!     width is the whole width while a0 is the half length of
!     the intial physical crack.
      Double Precision, Parameter :: width=15.0D1, T=0.2D1,E=7.0D4
      Double Precision, Parameter :: Poisson=0.03D1, alpha=0.3D1
      Double Precision, Parameter :: epsilon=0.001D1, pi=0.31415926D1
      Double Precision, Parameter :: SYS=37.2D1, UTS=48.3D1, R=0.01D1
      Double Precision, Parameter :: nm=0.01D1, nc=0.018D1, S11=2.5D1
      Double Precision :: roughness, DKapp, DKeff, Kmax
      End Module Global_Data

:
:
```

Following is the definition of the influence functions used in the model.

```
:
:

!     Define influence function F1(X1)
      Function F1(x1)
      Use Global_Data
      Implicit None
                                    :
                                    :
      F1=2.0*(1.0-Poisson**2)*SQRT((af**2-X1**2)/cos(pi*af/width))/E
      End Function F1


!     Define Yield strength function Yield(x1)
      Function Yield(x1)
      Use Global_Data
      Implicit None
      Double Precision :: Yield
      Double Precision, Intent(in) :: x1
      Yield=(SYS+UTS)/2.0
      End Function Yield
```

```
!     Define Subroutine G1
      Subroutine G1
      USE Global_Data
      Implicit None
      Double Precision :: b1,b2,bb1,bb2,a1,a2,a3,a4,a5
      Double Precision :: c1,c2,c3,c4,c5,c6
      Double Precision :: c11,c22,c33,c44,a22,a33,t1,t2
      Integer :: I, J
                                  :
                                  :
                                  :
                                  :
      c22=log(c11+SQRT(c11**2-1.0))
      c33=(af**2+b1*X(I))/(af*ABS(b1+X(I)))
      If (c33<(1.0+1.0D-25)) then
      c33=1.0+1.0D-25
      End If
      c44=log(c33+SQRT(c33**2-1.0))
      a22=(b2+X(I))*c22
      a33=(b1+X(I))*c44
      t2=a1*(a22-a33+a4)*a5
      G(I,J)=t1+t2
      End DO
      End DO
      End Subroutine G1

:
:
```

Following is the Initialisation_Module which calculate initial values of the plastic zone size, element position, element length, etc.

```
:
:

!     Initialisation of the problem
      Subroutine Initialisation(S1)
      Use Global_Data
      Implicit None
!     Variable declarations
      Double Precision, Intent(in) :: S1
      Double Precision :: rp1,t1,t2,sum1,b11,b22,b33,b44
      Integer :: I, J
      Double Precision, External :: F1, Yield

      a0=2.0D1
      N1=0

                                  :
                                  :
```

```
                                :
                                :
      DO J=1,10
      W(J)=0.11*rp0;    X(J)=t1+(real(J)-0.5)*0.11*rp0
      W(J+10)=0.11*rp0; X(J+10)=t1+1.1*rp0+(Real(J)-0.5)*0.11*rp0
      W(J+20)=0.11*rp0; X(J+20)=t1+2.2*rp0+(Real(J)-0.5)*0.11*rp0
      W(J+30)=0.11*rp0; X(J+30)=t1+3.3*rp0+(Real(J)-0.5)*0.11*rp0
      W(J+40)=0.05*rp0; X(J+40)=t1+4.4*rp0+(Real(J)-0.5)*0.05*rp0
      W(J+50)=0.01*rp0; X(J+50)=t1+4.9*rp0+(Real(J)-0.5)*0.01*rp0
      W(J+60)=0.01*rp0; X(J+60)=a0+(real(J)-0.5)*0.01*rp0
      W(J+70)=0.03*rp0; X(J+70)=a0+0.1*rp0+(Real(J)-0.5)*0.03*rp0
      W(J+80)=0.05*rp0; X(J+80)=a0+0.4*rp0+(Real(J)-0.5)*0.05*rp0
      W(J+90)=0.01*rp0; X(J+90)=a0+0.9*rp0+(Real(J)-0.5)*0.01*rp0
      End DO

                                :
                                :
                                :
                                :
!     DO I=1, 100
!     Write (unit=10, FMT=100) X(I), V(I), S(I), L(I)
!     End DO
      Kmax=S11*sqrt(pi*0.001*(a0+rp0)/cos(pi*(a0+rp0)/width))
      DKapp=Kmax*(1-R)
      DKeff=DKapp
      End Subroutine Initialisation

:
:
```

Following is the Crack_Extension Module which let the crack propagate a certain length (~1% plastic zone size) and update the model information such as element position, element length accordingly. Effective roughness is also applied in this module.

```
:
:
      Subroutine Crack_Extension(Smax1)
      Use Global_Data
      Implicit None
!     Variable declarations
      Double Precision, Intent(inout) :: Smax1
      Double Precision rp, rp1, t1, t2, sum1, dmax
      Double Precision b11, b22, b33, b44
      Double Precision d1, d2, d3, d4, d5, d6,d55,d66
      Double Precision W2(100), X2(100), L1(100), L2(100)
      Integer :: I, J, K
      Double Precision, External :: F1, Yield
                                :
                                :
```

```
                    :
                    :
    Else
    DO I=1, 60
    W(I)=W2(I); X(I)=X2(I); L11(I)=L1(I);L22(I)=L2(I)
    End DO
    DO I=1, 100
    X(I)=X(I)+W(61)
    End DO
    L22(61)=roughness
    DO I=6, 1, -1
    DO J=10, 1, -1
    K=J+(I-1)*10
    L11(K)=((W(K)-W(61))*L11(K)+W(61)*L11(K+1))/W(K)
    L22(K)=((W(K)-W(61))*L22(K)+W(61)*L22(K+1))/W(K)
    End DO
    End DO
    a0=a0+W(61)
    af=a0+rp0
    rpmax=rp0
    End If

    DO I=59, 1, -1
    If ((X(I)+W(I)/2.0-20.0)<(W(61)/2.0)) Then
    DO J=1, I
    L11(J)=L1(J)
    L22(J)=L2(J)
    End DO
    Exit
    End IF
    End DO

    L22(61)=0.0D1


    F=(/(F1(X(I)), I=1, 100)/)
    Call G1
    END Subroutine Crack_Extension
```

:
:

Following is the Smax_Data Module which calculate the necessary model information under the maximum load level of this simulation step. Overload effect is introduced in this module.

:
:

```
    Subroutine Smax_Data(Smax1,N)
    Use Global_Data
```

```
      Implicit None
!     Variable declarations
      Double Precision, Intent(inout) :: Smax1
      Integer, Intent(inout) :: N
      Double Precision t1, sum1, dmax
      Integer :: I, J, K
      Double Precision, External :: F1, Yield
100   Format (F10.4, 3(E12.5, 1x))
200   Format (1x, "X(I)", T12, "V(I)", T30, "S(I)", T45, "L(I)")
      S=0.0D1
      L=L11
      DO K=1, 400
      dmax=0.0D1
      DO I=1, 60
      t1=S(I)
      sum1=0.0D1
      DO J=1, I-1
      Sum1=sum1+S(J)*G(I, J)

                                  :
                                  :
                                  :
                                  :
      IF (V(I)<1.0D-25) Then
      V(I)=1.0D-25
!     write (unit=10, FMT=*) "Crack surfaces are closed at Smax"
      Else IF (V(I)<L(I)*(1.0-Y(I)/E)) Then
      L(I)=V(I)*(1.0+Y(I)/E)
!     write (unit=10, FMT=*) "Crack surfaces are closed at Smax"
      Else
      End IF
      End DO

                                  :
                                  :
                                  :
                                  :
      END Subroutine Smax_Data
```

:

:

Following is the Smin_Data Module which calculate the information such as the length of the element and the stresses carried by the element under the minimum load level of the simulation step. Under load effect is introduced in this module.

:

:

```
      Subroutine Smin_Data(Smax1,Smin1,N)
      Use Global_Data
```

```
      Implicit None
!     Variable declarations
      Double Precision, Intent(inout) :: Smax1, Smin1
      Integer, Intent(inout) :: N
      Double Precision :: rp1, t1, Sm, Sa
      Double Precision :: b1, b2, b3, b4, sum1, dmax
      Integer :: I, J, K
      Double Precision, External :: F1, Yield
      Dmax=0.0D1
100   Format (F10.4, 3(E12.5, 1x))
200   Format ( 1x, "X(I)", T12, "V(I)", T30, "S(I)", T45, "L(I)")
      F=(/(F1(X(I)), I=1, 100)/)
      S=0.0D1

      DO I=61, 100
      Sum1=0.0D1
      DO J=1, 100
      Sum1=sum1+S(J)*G(I, J)
      End DO
      V(I)=Pmin*F(I)-sum1
      IF (V(I)<1.0D-25) Then
      V(I)=1.0D-25
                              :
                              :
                              :
                              :

      END Subroutine Smin_Data


:
:
```

Following is the Crack_Opening Module which calculate the load levels required to fully open the crack. Two criteria are used in this model, one is based on the contact stress behind the physical crack tip only, and the other is displacement based.

```
:
:
      Subroutine Crack_Opening(Smax1, Smin1, N)
      Use Global_Data
      Implicit None
      Double Precision, Intent(inout) :: Smax1, Smin1
      Integer, Intent(inout) :: N
      Integer :: I, J, K, M, I1, I2
      Double Precision :: dmax,dmax1, dmin1, sum1, t1, t2
      Double Precision :: Sopen, U1, U2
      Double Precision :: Kop, b1, b2, b11, b22,b3
      Double Precision, External :: F1, Yield
```

```
                    :
                    :
                    :
                    :
If (S(I)>alpha*Y(I)) Then
S(I)=alpha*Y(I)
Else If (S(I)<-alpha*Y(I)) Then
S(I)=-alpha*Y(I)
Else
End If
If (ABS(t1-S(I))>=SYS*epsilon) Then
dmax=ABS(t1-S(I))
End If
End DO
If (dmax<=epsilon*SYS) Then
Exit
End If
End DO

DO I=1, 100


DO I=1, 60
Sum1=0.0D1
DO J=1, 100
Sum1=sum1+S(J)*G(I, J)
End DO
V(I)=Sopen*F(I)-sum1
IF (V(I)<1.0D-25) Then
V(I)=1.0D-25
                    :
                    :

U2=Sopen/Pmax1

DKapp=Kmax*(1-R)
DKeff=DKapp*(1-U2)/(1-R)
print *, "DKapp=",DKapp, "DKeff=",DKeff

                    :
                    :
                    :
                    :
print *, "Crack opening level U2=", U2
END Subroutine Crack_Opening
```